UNIVERSITAT DE LES ILLES BALEARS

Universitat de les Illes Balears

DOCTORAL THESIS

Doctoral programme of physics

Hierarchical data-driven modelling of binary black hole mergers

by

Xisco Jiménez Forteza

Doctor por la Universidad de las Islas Baleares

Supervisors:

Sascha Husa & Alicia M. Sintes Olives

May 2018

"...on a mote of dust suspended in a sunbeam"

Carl Sagan

List of publications derived from this thesis

1. Xisco Jimenez Forteza, D. Keitel et al. Hierarchical data-driven approach to fitting numerical relativity data for non-precessing binary black holes, with an application to final spin and radiated energy. In: Phys. Rev. D95.6 (2017), p. 064024. DOI: 10.1103/PhysRevD.95.064024. arXiv: 1611.00332 [gr-qc] LIGO-P1600270. LIGO Scientific Collaboration and Virgo Collaboration, 2016.
   URL: https://dcc.ligo.org/LIGO-P1600270/

2. D. Keitel, Xisco Jimenez Forteza et al. The most powerful astrophysical events: gravitational-wave peak luminosity of binary black holes as predicted by numerical relativity. arXiv: 1612.09566 [gr-qc]. Accepted for publication in Phys. Rev. D. LIGO-P1600270. LIGO Scientific Collaboration and Virgo Collaboration, 2016.
   URL: https://dcc.ligo.org/LIGO- P1600270

3. Xisco Jimenez Forteza, D. Keitel, Sascha Husa. Phenomenological fit of the peak luminosity from non-precessing binary- black-hole coalescences. Tech. rep. LIGO-T1600018-v4. LIGO Scientific Collaboration and Virgo Collaboration, 2016.
   URL: https://dcc.ligo.org/LIGO-T1600018-v4/public

4. Sascha Husa, Sebastian Khan, Mark Hannam, Michael Pürrer, Xisco Jimenez Forteza, Alejandro Bohé. Frequency-domain gravitational waves from nonprecessing black-hole binaries. I. New numerical waveforms and anatomy of the signal. In: Phys. Rev. D93.4 (2016), p. 044006. DOI: 10.1103/PhysRevD.93.044006. arXiv: 1508.07250 [gr-qc]

5. Sebastian Khan, Sascha Husa, Mark Hannam, Michael Pürrer, Xisco Jimenez Forteza, Alejandro Bohé. Frequency-domain gravitational waves from nonprecessing black-hole binaries. II. A phenomenological model for the advanced detector era. In: Phys. Rev. D93.4 (2016), p. 044007. DOI: 10.1103/PhysRevD.93.044007. arXiv: 1508.07253 [gr-qc]

UNIVERSITAT DE LES ILLES BALEARS

Abstract

Current gravitational wave observations suggest that binary black hole (BBH) systems will be the dominant gravitational waves sources in the frequency range of advanced gravitational waves detectors. The full time-frequency dynamics of these systems have been long known to not be covered accurately by Post-Newtonian (PN) and Effective-One-Body (EOB) formulations of the two body problem. In particular, they fail to reproduce the merger-ringdown regimes where the strong general relativity (GR) effects arise. This involves that any of the quantities computed from the analytic approximants will suffer deviations that may induce an eventual loss of the signal-to-noise-ratio (SNR) and affect the parameter estimation (PE) results. On the other hand, numerical relativity (NR) simulations are thought to provide the most accurate representation of the full evolution thus filling the gap left by the analytic models. Current nonprecessing gravitational wave (GW) models are calibrated to NR data giving name to the so called inspiral-merger-ringdown models (IMR) used in the LIGO template banks. Regarding the strategy they follow in describing the GW strain, they are classified as the EOBNR (time domain) and the Phenom-based models (frequency domain). Both approaches have been mainly calibrated with spin-aligned NR simulations, where the physical information is mostly described by means of the mass-ratio and some effective spin parameter. In this thesis we have developed the framework for a recalibration of the phenomenological models by adding a set of 23 unequal-spin NR simulations to include unequal-spin effects. To this end, we have created a novel fitting strategy that has been particularly well suited for the inclusion of the subdominant effects and the extreme mass-ratio regime. This new fit strategy has been used for the calibration of new and upgraded fits to the final spin, final mass and peak luminosity, being all of them used in the firsts LIGO GW observations. This fitting methodology is currently being tested and adapted for the recalibration of nonprecessing phenomenological models, also showing similar and promising results.

UNIVERSITAT DE LES ILLES BALEARS

Resum (en català)

All llarg de la història, l'ésser humà ha rebut i interpretat la informació arribada del cel per mitjà de les ones electromagnètiques (la llum) provinent dels estels i galàxies més llunyanes. Tant és així, que fins el 2015 aquest hauria sigut pràcticament l'únic mitjà emprat per la comunitat científica per a observar i estudiar els esdeveniment astrofísics que succeeixen en el nostre cosmos. No obstant, el 14 de setembre de 2015 s'obri una nova finestra d'observació a l'univers gràcies a la primera detecció directa de les ones gravitacionals concloent l'esforç perseguit des de fa dècades per les col·laboracions científiques LIGO i Virgo.

Les ones gravitacionals són minúscules oscil·lacions de l'espai-temps que es propaguen a la velocitat de la llum. La seva descripció teòrica sorgeix de la teoria general de la relativitat d'Albert Einstein i degut a la seva feblesa, necessitem dels esdeveniments astrofísics més catastròfics per a poder detectar-les. La primera detecció de les ones gravitacionals fou consistent amb l'aproximació, col·lisió i estabilització de dos forats negres de 36 i 29 masses solars a 1300 milions d'anys llum els quals alliberaren al voltant del 5% de la seva massa en forma de febles ones de l'espai-temps, essent l'event astrofísic més potent mai observat. Aquest event fou anomenat GW150914 d'acord amb la data d'observació i fou anunciat públicament anunciat l'11 de Febrer del 2016 per la col·laboració LIGO-Virgo. No obstant, aquest no ha sigut l'únic event observat en el temps de desenvolupament d'aquesta tesi doctoral. Essent fidel als requeriments estadístics que confirmen o desestimen qualsevol detecció, es pot certificar l'observació d'almenys un event més també compatible amb la col·lisió de dos forats negres anomenat GW151226 i havent-hi un tercer el qual no va arribar als mínims estadístics establerts anomenat LVT151012.

La fusió de sistemes binaris de forats negres són un candidat òptim per a l'observació i estudi de les ones gravitacionals. Les prediccions actuals apunten a aquests tipus d'events com els més freqüents en els detectors terrestres LIGO. Llavors, per a una òptima caracterització de les ones observades es necessiten també dels models teòrics més precisos. En aquesta tesi s'han treballat i millorat els anomenats models fenomenològics d'ones gravitacionals en sistemes no precessants, és a dir, en el que el pla de l'òrbita és fix. Aquests, modelen les ones gravitacionals per mitjà de l'acoblament de les ben conegudes solucions analítiques com les oferides pels models post-Newtonians (PN) i les formulacions *effective-one-body* (EOB) amb els resultats de les computacionalment costoses solucions numèriques de les equacions d'Einstein. Són models d'ona definits a l'espai de freqüència que depenen de la relació de masses dels forats negres així com

de l'anomenat espí efectiu $\chi_{\rm eff}$, que no és més que el resultat de la combinació de les components perpendiculars al pla de l'òrbita dels dos espins reduint així la dimensió de l'espai de paràmetres a sols dues components. Així i tot, malgrat que els models actuals responen prou bé als resultats de les cerques d'ones gravitacionals, no són tan òptims per a la inferència estadística dels espins de cadascun dels objectes degut a la degeneració inherent en la definició de l'espí efectiu.

El focus d'aquesta tesi ha sigut l'extensió dels models fenomenològics d'un sol espí a models de dos espins en els que s'ha afegit la dependència subdominant de la diferència d'espí $\Delta\chi = \chi_1 - \chi_2$. Per a arribar a aquest fi, s'han hagut d'emprar les dades de més de 400 simulacions de sistemes binaris de forats negres de 4 codis diferents (`BAM`, `SpEC`, `LAZEV`, `MAYA`) de les quals 23 s'han obtingut en el transcurs d'aquesta tesi amb el codi `BAM` i que comporta l'àrdua tasca de l'evolució, extracció de les ones gravitacionals i postprocessament de la senyal. Així, i per a millorar els models existents, s'ha redefinit l'estratègia en la construcció i addició d'elements subdominants als *ansaetzë* bidimensionals en els que a més a més s'han inclòs els resultats coneguts del límit en què un forat negre és molt més gran que l'altre. Tot això ha resultat en nous models fenomenològics per a la massa total radiada, l'espí de l'objecte final i el pic de lluminositat. Aquests models han demostrat millorar les descripcions antigues d'aquestes quantitats fent patent de forma clara el possible impacte dels efectes subdominants en els futurs models fenomenològics d'ones gravitacionals.

UNIVERSITAT DE LES ILLES BALEARS

Resumen (en castellano)

A lo largo de la historia, el ser humano ha recibido e interpretado la información recibida del cielo por medio de las ondas electromagnéticas (la luz) provenientes de las estrellas y galaxias más lejanas. Tanto es así, que hasta finales de 2015 este había sido el único medio utilizado por la comunidad científica para observar y estudiar los eventos astrofísicos que suceden en nuestro cosmos. No obstante, el 14 de septiembre de 2015 se abre una nueva ventana de observación al universo gracias a la primera detección directa de las ondas gravitacionales, concluyendo el esfuerzo perseguido desde hace décadas por las colaboraciones científicas LIGO y Virgo.

Las ondas gravitacionales son minúsculas oscilaciones del espacio-tiempo que se propagan a la velocidad de la luz. Su descripción teórica surge de la teoría de la relatividad general de Albert Einstein y debido a su débil interacción con la materia, necesitamos de los eventos astrofísicos más catastróficos para poder detectarlas. La primera detección de las ondas gravitacionales fue consistente con la aproximación, colisión y estabilización de dos agujeros negros de 36 y 29 masas solares a 1300 millones de años luz los cuales liberaron alrededor del 5% de su masa en forma de débiles ondas del espacio-tiempo, siendo el evento astrofísico más potente jamás observado. Dicho evento fue llamado GW150914 de acuerdo con su fecha de observación y fue públicamente anunciado el 11 de Febrero de 2016 por la colaboración LIGO-Virgo. Sin embargo, este no ha sido el único evento observado en el transcurso de esta tesis doctoral. Siendo fiel a los requisitos estadísticos que confirman o desestiman qualquier detección, se puede certificar la observación de al menos un evento más también compatible con la colisión de dos agujeros negros llamado GW151226 y habiendo un tercero el cual no llegaría a los mínimos requisitos estadísticos para ser confirmado llamado LVT151012.

La fusión de sistemas binarios de agujeros negros son un candidato óptimo para la observación y estudio de las ondas gravitacionales. Las predicciones actuales apuntan a este tipo de eventos como los más frecuentes en los detectores terrestres LIGO. Para una óptima caracterización de las ondas observadas necesitamos los modelos teóricos más precisos. En esta tesis se han trabajado y mejorado los llamados modelos fenomenológicos de ondas gravitacionales en sistemas sin precesión, es decir, en el que el plano de la órbita es fijo. Estos, modelan las ondas a través del acoplamiento de las conocidas soluciones analíticas como las ofrecidas por los modelos post-Newtonianos (PN) y las formulaciones *effective-one-body* (EOB) con los resultados de las computacionalmente costosas soluciones numéricas de las ecuaciones de Einstein. Son modelos de onda definidos en el espacio de frecuencias que dependen de la relación de masas de los agujeros negros así

como del llamado espín efectivo $\chi_{\rm eff}$ que no es más que el resultado de la combinación de las componentes perpendiculares al plano de la órbita de los dos espines y con el que se consigue reducir la dimensión del espacio de parámetros a solo dos componentes. Así y todo, a pesar de que estos modelos responden suficientemente bien a los resultados de las búsquedas de las ondas gravitacionales, no son tan óptimos en la inferencia estadística de los espines de cada uno de los objetos debido a la degeneración inherente en la definición del espín efectivo.

El foco de esta tesis ha sido la extensión de los modelos fenomenológicos de un solo espín a modelos de dos espines en los que se ha añadido la dependencia subdominante de la diferencia de espines $\Delta\chi = \chi_1 - \chi_2$. Con este fin, se han tenido que utilizar los datos de más de 400 simulaciones de sistemas binarios de agujeros negros de 4 códigos diferentes (`BAM`, `SpEC`, `LAZEV`, `MAYA`) de las cuales 23 se han obtenido en el transcurso de esta tesis con el código `BAM` y que ha conllevado la difícil tarea de la evolución, extracción de las ondas gravitacionales y postprocesamiento de la señal. Así, y para mejorar los modelos existentes, se ha redefinido la estrategia en la construcción y adición de elementos subdominantes a los *ansaetzë* bidimensionales en los que además se han usado los resultados analíticamente conocidos en los que un agujero negro es mucho mayor que el otro. Todo esto ha concluído en la prescripción de nuevos modelos fenomenológicos para la masa total radiada, el espín final y el pico de luminosidad. Estos modelos han demostrado mejorar las descripciones antiguas para estas cantidades, desvelando de forma clara el posible impacto de los efectos subdominantes en futuros modelos fenomenológicos de ondas gravitacionales.

UNIVERSITAT DE LES ILLES BALEARS

Summary (in English)

Throughout history, human beings have received and interpreted information from distant stars and galaxies through electromagnetic waves (light). Until 2015 this was the dominant way for observing astrophysical events happening in our cosmos. However, on September 14'th 2015 a new window to the universe was opened thanks to the first direct gravitational wave detection, a goal pursued for several decades by the LIGO/Virgo scientific collaboration.

Gravitational waves are tiny space-time oscillations propagating at the speed of light. They are a prediction of the Einstein theory of gravity and we need the most catastrophic astrophysical events to detect them. The first observation of gravitational waves described the inspiral, merger and ringdown of two black holes with 36 and 29 solar masses located at 1300 billion light-years, where about the 5% of the total mass was radiated as gravitational waves and becoming the most powerful astrophysical event ever observed. The event was called GW150914, consistently with its the arrival date and was publicly announced on February 11'th 2016 by the LIGO Virgo collaboration. This has not been the only event observed during this thesis project. Relying on statistical criteria arguments, we can certify the observation of one additional event also compatible with the coalescense of a pair of black holes tagged as GW151226 plus a third one called LVT151012 likely from astrophysical origin but that did not reach the statistical significance required to be confirmed.

The coalescense of binary black hole systems are an optimal candidate for the observation and study of gravitational waves. The current observations suggest that these kind of events could dominate the future ground based detections. Then, we need to optimise the theoretical waveform models to characterise the future observations. In this thesis we have given the first steps towards a new upgrading of the nonprecessing gravitational waves models. These models result from the matching of the well known post-Newtonian (PN) and effective-one-body (EOB) analytic formulations to the computationally expensive numerical solutions of the Einstein equations. They are defined in the frequency domain and depend on the ratio of the two black hole masses (mass-ratio) and some effective spin $\chi_{\rm eff}$ that results from the combination of the components of the spins orthogonal to the orbital plane thus reducing the physical parameter space to only two dimensions. Then, although this current prescription have been demonstrated to be sufficient for the searches of the gravitational waves in the data, they are not so optimal for the statistical inference of the spins of each BH, which is partially caused by the inherent degeneracy introduced by the effective spin.

The focus of this work has been the extension of the one-spin phenomenological models to its two-spin version by adding the subdominant effects carried by the spin difference terms $\Delta\chi = \chi_1 - \chi_2$. To that end, we have employed the data of more than 400 simulations of binary black hole systems generated by four different codes (`BAM`, `SpEC`, `LAZEV`, `MAYA`), 23 of them generated throughout this thesis by means of the `BAM` code. This involved the difficult task of evolving, extracting the waves and the data postprocessing of each case. Then, we have redefined the strategy for building higher than two dimensional *ansaetze* to add subdominant effects and where we have also included the results of the extreme mass ratio limit. All this analysis has resulted in the prescription of new phenomenological models for the final mass, final spin and peak luminosity. The new models have been shown to improve the old descriptions of these quantities while they have clearly revealed the possible impact of the subdominant effects in the near future phenomenological models.

Acknowledgements

In this lines I would like to express my gratitude to all people who has been directly involved in my research during these long four years. Then, in order of importance and presence, I would like to thanks my supervisors Prof. Sascha Husa and Prof. Alicia Sintes for the continuous guidance, help and encouragement received both in science and other professional topics. Thanks to them, I had the unique opportunity of living from inside one of the most outstanding discoveries in science.

I would also like to express my gratitude to Dr. David Keitel for the invaluable lessons, advice and patience dedicated to me during these years. The most relevant results of this work would not have been possible without his support. Also for his exhaustive revision of the text and all the effort devoted on it.

I am specially grateful to Dr. Carlos Palenzuela for his continuous support and advise from both scientific and non-scientific perspective and also for the useful comments on this document. In this line, I also thanks my mates and research colleagues Juan Calderon, Sebastian Khan, Miguel Bezares and Gemma Simó. I know it was boring but I will certainly compensate you. I want also to extend my gratitude to all the members Relativity and Cosmology Group of the Universitat de les Illes Balears and specially to Rafel, Alex, Morate, Miquel and all the other students.

Now it is time to remember my friends and important people who helped me to do more easy handling this task. I begin with my lunch mates, some of them already cited above. Then, thanks to Carlos (Palenzuela), Carles (Bona), Borja, Miguel, Dani and specially to Gemma to be so kind when the dark clouds were around and being the best possible partner during these years, to my research buddies Juan and Sebastian and finally to my group of local and eternal friends Miki, Javi (Pisha), Jose, Angel, Juan y Patrick for tolerating my constant changes of humor of these years. Obviously, I can not forget to express my gratitude to my family; father (Jiménez), mother (Forteza) and brother (Jiménez-Forteza) for pushing me forward to obtain my goals.

This work has been done as a member of the LIGO Scientific Collaboration and supported by the FPI-CAIB grant of the Conselleria d'Educació i Universitats del Govern de les Illes Balears and the Fons Social Europeu, Vicepresidència i Conselleria d'Innovació Recerca i Turisme, Agencia Española de Investigación, the Max Planck Society via the Max Planck Prince of Asturias Mobility Award, the Spanish Ministry of Economy and Competitiveness grants FPA2016-76821-P, CSD2009-00064 and FPA2013-41042-P and the Fondo Europeo de DEsarrollo Regional (FEDER). I also thankfully acknowledge the computer resources at BSC MareNostrum computer under PRACE and RES (Red Española de Supercomputación) grants, 2015133131, AECT-2016-1-847 0015, AECT-2016-2-0009, AECT-2017-1-0017.

Contents

Abstract iii

Resum (en català) iv

Resumen (en castellano) vi

Summary (in English) viii

Acknowledgements x

List of Figures xv

List of Tables xviii

Abbreviations xix

1 Introduction to Gravitational Waves 1
- 1.1 Introduction to GR . . . 2
  - 1.1.1 General principle of covariance in GR . . . 2
  - 1.1.2 Curvature in GR . . . 4
  - 1.1.3 Ricci tensor and Bianchi identities . . . 5
- 1.2 Weak field approximation . . . 6
  - 1.2.1 Linearization of the Einstein field equations . . . 6
  - 1.2.2 Equations of motion in the TT frame . . . 9
  - 1.2.3 Generation of gravitational waves . . . 10
    - 1.2.3.1 Quadrupole formula derivation . . . 11
    - 1.2.3.2 Toy model: BBH system . . . 12
- 1.3 Sources of gravitational waves . . . 14
- 1.4 Gravitational wave detectors . . . 17
  - 1.4.1 Resonant bars . . . 17
  - 1.4.2 Laser Interferometer Gravitational wave Observatory: LIGO . . . 19
  - 1.4.3 Other interferometric detectors . . . 23
  - 1.4.4 Third-generation ground-based gravitational wave detectors . . . 24

1.4.5 Space-based gravitational wave detectors: LISA mission 24
1.5 Prospects on gravitational waves astronomy 26

2 Two body problem overview **28**
2.1 BBH physical parameters 29
2.2 Waveform anatomy 31
2.3 Analytic models 32
2.3.1 Post-Newtonian approximants 33
2.3.2 SEOBNR approximants 35
2.3.3 Phenomenological waveform models 36
2.4 Numerical relativity models 37
2.4.1 ADM 3+1 formalism 38
2.4.2 Space-time 3+1 field equations 40
2.4.3 The BSSNOK formulation 42

3 Simulations of BBH systems with the BAM code **45**
3.1 The BAM code 45
3.2 Derived quantities 51
3.2.1 Gravitational waves 51
3.2.2 Apparent horizons 54
3.2.3 Final spin 55
3.2.4 Final mass 55
3.2.5 Luminosity and peak luminosity 56
3.3 Unequal-spin simulations with BAM 58
3.3.1 Unequal spin simulations 58
3.3.2 Grid configuration 59
3.3.3 Apparent horizon fits for the BAM code 64
3.4 Eccentricity reduction 68
3.4.1 Eccentricity in the Keplerian two body problem 68
3.4.2 NR eccentric waveforms 70
3.4.3 Reducing the eccentricity in a real case 72
3.5 Time and frequency integration of the psi4 76
3.6 Extrapolation 78

4 Hierarchical data-driven fitting of BBH mergers **81**
4.1 Hierarchical data-driven approach 82
4.1.1 Motivation 82
4.1.2 Flowchart 83
4.1.3 NR data as a driver of the phenomenological fits 83
4.1.4 Spin parametrization and unequal-spin motivation 85
4.1.5 Extreme-mass-ratio limit 87
4.1.6 Model selection criteria and ranking statistics 89
4.1.7 Fit uncertainties 91
4.2 Hierarchical data-driven fitting: Application to final spin and energy radiated 92
4.2.1 NR data selection 93
4.2.2 Choice of fit quantity 94

4.2.3 One-dimensional subspace fits . . . 94
4.2.3.1 1D fits: Final Spin . . . 94
4.2.3.2 1D fits: Radiated energy . . . 96
4.2.4 Two-dimensional fits . . . 98
4.2.4.1 Two-dimensional fits: final spin . . . 98
4.2.4.2 Two-dimensional fits: energy radiated . . . 100
4.2.5 Unequal-spin contributions and 3D fit . . . 101
4.2.5.1 Unequal-spin contributions and 3D fit: final spin . . . 102
4.2.5.2 Unequal-spin contributions and 3D fit: energy radiated . . . 105
4.2.6 Fit assessment . . . 108
4.2.7 Precessing binaries . . . 112
4.2.8 Spin parameter selection . . . 113
4.2.9 Apparent horizon and area theorem . . . 115
4.2.10 Data sets and NR uncertainties . . . 116
4.3 Hierarchical data-driven fitting: Application to peak luminosity . . . 120
4.3.1 Astrophysical implications of the peak luminosity . . . 121
4.3.2 NR data . . . 122
4.3.3 Constructing the phenomenological fit . . . 123
4.3.4 One-dimensional subspace fits . . . 124
4.3.4.1 One-dimensional non-spinning fit . . . 124
4.3.4.2 One-dimensional equal-mass-equal-spin fit . . . 125
4.3.5 Two-dimensional fits . . . 126
4.3.6 Unequal-spin contributions and 3D fit . . . 128
4.3.7 Fit assessment . . . 131
4.3.8 Residuals and information criteria . . . 132
4.3.9 Large-mass-ratio and extremal-spin limits . . . 134
4.3.10 NR data investigations . . . 135
4.3.10.1 Comparison between different codes . . . 136
4.3.10.2 Extrapolation . . . 137
4.3.10.3 Mode selection . . . 140
4.3.10.4 Outliers . . . 143

5 A phenomenological frequency-domain model: PhenomD 146
5.1 Overview of the phenom-based models . . . 147
5.1.1 Some notes on the PhenomD construction. . . . 147
5.2 Hybrids . . . 149
5.3 Inspection of the PN approximants . . . 151
5.4 Unequal-spin effects on the PhenomD coefficients . . . 153

6 Conclusions and outlook 155

Bibliography 160

List of Figures

1 GW150914 . . . xxiii

1.1 Parallel transport and Covariant Derivative . . . 5
1.2 Gravitational waves - Matter Interaction . . . 10
1.3 Gravitational wave source . . . 11
1.4 BBH system . . . 13
1.5 GW detectors . . . 17
1.6 Resonant bars . . . 18
1.7 LIGO observatory . . . 20
1.8 Frequency domain GWs . . . 22
1.9 Third-generation gravitational wave (GW) detectors . . . 25
1.10 GW sources and prospects . . . 27

2.1 BBH extrinsic parameters . . . 30
2.2 Time domain hybrid waveform . . . 32
2.3 Space-time foliation . . . 38
2.4 Normal vector to Σ_t . . . 40

3.1 3D visualization of the ψ_4 . . . 53
3.2 $r\psi_{4,22}(t)$ vs $rh_{4,22}(t)$ . . . 54
3.3 Luminosity $L_{lm}(t)$ . . . 57
3.4 Unequal spin simulation plan . . . 59
3.5 BAM Cartesian boxes . . . 61
3.6 Sine waves and grid resolution . . . 63
3.7 Apparent horizons for different η choices . . . 65
3.8 Apparent horizons evolution . . . 66
3.9 Apparent horizons fits . . . 67
3.10 Keplerian orbit . . . 69
3.11 Eccentricity in a Keplerian orbit . . . 70
3.12 CPU hours per cycle . . . 72
3.13 Residual eccentricity . . . 73
3.14 Residual eccentricity correction with Ω . . . 75
3.15 Residual eccentricity correction with the radial coordinate separation r . . . 75
3.16 Eccentricity reduction across the parameter space . . . 76
3.17 Fourier integration with no f_0 cutoff . . . 77
3.18 FFI algorithm vs polynomial fit . . . 79
3.19 Polynomial extrapolation of ψ_4 . . . 80

4.1 Flowchart of the hierarchical fitting methodology . . . 84

4.2 Parameter space coverage: final mass and energy radiated . . . 85
4.3 Unequal-spin effect reflected in the final spin . . . 87
4.4 BIC raking example . . . 91
4.5 Final spin in terms of η and $Seff$ . . . 93
4.6 One-dimensional η-$\widehat{S}$ fits on the final spin . . . 95
4.7 One-dimensional η-$\widehat{S}$ fits on the energy radiated . . . 97
4.8 Extreme-mass ratio limit for the final spin . . . 99
4.9 Extreme mass-ratio limit for the energy radiated . . . 101
4.10 One-dimesional analysis of the unequal-spin effect for the final spin . . . 102
4.11 One-dimesional fits of unequal-spin effect for the final spin . . . 103
4.12 One-dimesional analysis of the unequal-spin effect for the energy radiated 106
4.13 One-dimesional fits of the unequal-spin effect for the energy radiated . . . 107
4.14 Unequal-spin intuition on three-dimensional plots . . . 109
4.15 Residuals distribution for the final spin . . . 110
4.16 Residuals distribution for the energy radiated . . . 111
4.17 Extreme spin limit . . . 112
4.18 Spin parameter dependence . . . 114
4.19 Extreme spin limit for different S_{eff} . . . 114
4.20 Test of the area theorem on the final state fits . . . 115
4.21 Radiation vs. horizon quantities in 2D plots . . . 116
4.22 Residuals vs. horizon/radiation differences . . . 117
4.23 Duplicated NR cases intuition . . . 118
4.24 Duplicated cases in 2D . . . 118
4.25 Outliers form the one-dimensional analysis . . . 120
4.26 Parameter-space coverage of the combined NR data set from BAM, SXS, GaTech, RIT . . . 122
4.27 Two-dimensional space for the peak luminosity . . . 122
4.28 One-dimensional fits of the rescaled non-spinning peak luminosity . . . 124
4.29 One-dimensional fits of the rescaled peak luminosity for equal-mass equal-spin . . . 126
4.30 Two-dimensional equal-spin fit . . . 127
4.31 Spin-difference behavior at fixed mass ratios . . . 129
4.32 Spin-difference behavior of the scaled NR luminosities . . . 131
4.33 Fit residuals of the final 3D peak luminosity fit . . . 133
4.34 Full NR-calibrated fits . . . 135
4.35 Behavior of the full 3D fit in the extremal-spin limit . . . 135
4.36 Relative differences in the peak luminosity for equal-parameter . . . 136
4.37 Comparison of the distribution of relative fit errors . . . 137
4.38 Mon-spinning example of extrapolation from finite radii: SXS-GaTech-BAM 139
4.39 Non-spinning example of extrapolation behavior: SXS/GaTech . . . 140
4.40 Per-mode contributions to the total peak luminosity . . . 141
4.41 Relative loss in the peak luminosity including modes up to $\ell_{\rm max} = 6$ . . . 142
4.42 Comparison of rescaled peak luminosities for non-spinning SXS and BAM and perturbative large-mass-ratio data . . . 143

5.1 PhenomD amplitude and phase derivative . . . 147
5.2 22 mode Hybrid . . . 151

5.3 Parameter plot for the new PhenomD upgrade 151
5.4 Comparison of fully analytic PN and EOB appoximants 152
5.5 Unequal-spin effects on the PhenomD coefficients 153

List of Tables

2.1 $3+1$ Christoffel symbols 41

3.1 New set of BAM unequal spin simulations 60
3.2 Grid setup 61

4.1 Fit coefficients for the one-dimensional nonspinning $L'_{\rm orb}\left(\eta, \widehat{S}=0\right)$ 95
4.2 Fit coefficients for the one-dimensional nonspinning $E_{\rm rad}\left(\eta, \widehat{S}=0\right)$ and equal-mass-equal-spin $E_{\rm rad}\left(\eta=0.25, \widehat{S}\right)$ 97
4.3 Fit coefficients for the extreme-mass-ratio limit of the final spin 99
4.4 Coefficients of the extreme-mass-ratio limit for the energy radiated 101
4.5 Fit coefficients for the final 3D step of the $L'_{\rm orb}$ fit 105
4.6 $E_{\rm rad}$ fit coefficients for the final 3D step 107
4.7 Summary statistics for the various steps of the hierarchical final-spin fit . 109
4.8 Summary statistics for the new final-spin fit compared with previous fits . 110
4.9 Summary statistics for the new radiated-energy fit 111
4.10 Summary statistics for fits with three different choices of effective spin . . 114
4.11 NR cases from the source catalogs not included in the fit calibration . . . 120
4.12 Fit coefficients for the one-dimensional non-spinning $L'_{\rm peak}\left(\eta, \widehat{S}=0\right)$ fit . 124
4.13 Fit coefficients for the one-dimensional equal-mass-equal-spin $L'_{\rm peak}\left(\eta=0.25, \widehat{S}\right)$ fit 126
4.14 Summary statistics for the various steps of the hierarchical fit 132
4.15 Fit coefficients for the final 3D fit stage 132
4.16 Summary statistics for the final 3D peak luminosity fit 133
4.17 NR cases from the source catalogs not included in the fit calibration, for reasons detailed below. 144

Abbreviations

ADM	**A**rnowitt **D**eser **M**isner
AH	**A**pparent **H**orizon
AIC	**A**kaike **I**nformation **C**riterion
AICc	**A**kaike **I**nformation **C**riterion **c**orrected
AMR	**A**daptive **M**esh **R**efinement
BBH	**B**inary **B**lack **H**ole
BH	**B**lack **H**ole
BIC	**B**ayesian **I**nformation **C**riterion
BNS	**B**inary **N**eutron **S**tar
BSSNOK	**B**aumgarte **S**hapiro **S**hibata **N**akamura **O**ohara **K**ojima
CBC	**C**ompact **B**inary **C**oalescence
CMB	**C**osmic **M**icrowave **B**ackground
CE	**C**osmic **E**xplorer
CW	**C**ontinuous **W**aves
EF	**E**xponential **F**it
EH	**E**vent **H**orizon
EM	**E**lectro**M**agnetic
EMRI	**E**xtreme **M**ass **R**atio **I**nspiral
EOB	**E**ffective **O**ne **B**ody
EOS	**E**quation **O**f **S**tate
ET	**E**instein **T**elescope
FFI	**F**ixed **F**requency **I**ntegration
GaTech	**G**eorgi**A** **Tech**
GR	**G**eneral **R**elativity
GRB	**G**amma **R**ay **B**urst

GW	**G**ravitational **W**ave
HM	**H**igher **M**odes
HOM	**H**igher **O**rder **M**odes
HW	**H**ybrid **W**aveform
IH	**I**solated **H**orizon
IMBBH	**I**nter**M**ediate **B**inary **B**lack **H**ole
IMR	**I**nspiral **M**erger **R**ingdown
KAGRA	**KA**mioka **GRA**vitational Wave Detector
LIGO	**L**aser **I**nterferometer **G**ravitational Wave **O**bservatory
aLIGO	**a**dvanced **LIGO**
eaLIGO	**e**arly **a**dvanced **LIGO**
IndIGO	**Ind**ian **I**nitiative in **G**ravitational-wave **O**bservations)
LISA	**L**arge **I**nterferometer **S**pace **A**ntenna
eLISA	european **L**arge **I**nterferometer **S**pace **A**ntenna
LVC	**L**IGO and **V**irgo **C**ollaboration
LSC	**L**IGO **S**cientific **C**ollaboration
MIT	**M**assachusetts **I**nstitute of **T**echnology
NR	**N**umerical **R**elativity
NS	**N**eutron **S**tar
NSF	**N**ational **S**cience **F**oundation
PE	**P**arameter **E**stimation
PDF	**P**robability **D**ensity **F**unction
PN	**p**ost-**N**ewtonian Approximation
PTA	**P**ulsar **T**iming **A**rray
PSD	**P**ower **S**pectral **D**ensity
QNM	**Q**uasi**N**ormal **M**odes
RIT	**R**ochester **I**nstitute of **T**echnology
RMSE	**R**oot **M**ean **S**quare **E**rror
ROM	**R**educed **O**rder **M**odel
RWZ	**R**egge-**W**heeler-**Z**erilli
SMBH	**S**uper **M**assive **B**lack **H**ole
SN	**S**uper **N**ova
SNR	**S**ignal-to-**N**oise **R**atio

SO	**S**pin-**O**rbit
SPA	**S**tationary **P**hase **A**pproximation
SS	**S**pin-**S**pin
SXS	**S**imulating e**X**treme **S**pacetimes
TT	**T**ransverse **T**raceless

Preface

In 1915 Albert Einstein published his magnificent theory of general relativity [1]: a revolutionary theory of gravity conceptually very different from Newton theory of gravity. The new theory merged the concepts of space and time in a unique entity called space-time sculpted by its matter content.

Albert Einstein's new theory was able to reproduce all the old predictions of Newtonian gravity and to answer some of the long-time opened questions of this theory. One of the weak points of Newton's theory concerned the infiniteness of the speed of the propagation of the gravity force. This contrasted with the statements of the special theory of relativity where the maximum allowed speed was set to be the speed of light. Only one year after the publication of his theory, Albert Einstein himself found a solution hidden in his equations in the form of very feeble waves that propagate at the speed of light. They were expected interact so weakly with matter that he did not expect they could be ever discovered [1, 2]. The answer to this question arrived as small, oscillating perturbation on September 14th, 2015 when the two LIGO detectors (Hanford and Livingstone) vibrated at almost the same time consistent with the general relativity predictions [3]. This date is now considered the *birth of gravitational wave astronomy.*

First direct gravitational wave detection was publicly announced on 11th February 2016 by the LIGO and Virgo Scientific Collaboration (LVC). The discovery described the last stages of the evolution of a binary black hole system (BBH) with initial black hole masses of 36^{+5}_{-4} $M_\odot$ and 29^{+4}_{-4} $M_\odot$, which finally merged into a single BH with 62 $M_\odot$ at a estimated distance of 1.3 billion light years. The system was named GW150914, according to the date of its observation. This milestone detection was not only the first direct evidence on the existence of gravitational waves but it also was the confirmation that BHs exist and form binary systems, that they can exist with masses about the $30M_\odot$ and merge to a final object of about $60M_\odot$. The system was observed with a matched-filter signal-to-noise-ratio (SNR) of 24 and with a significance larger than 5.1σ, equivalent to false alarm rate of 1 event per 203000 years. This signal caused a minimal displacement on the LIGO mirrors of about $\sim 10^{-18}$ meters, i.e., a thousand of times

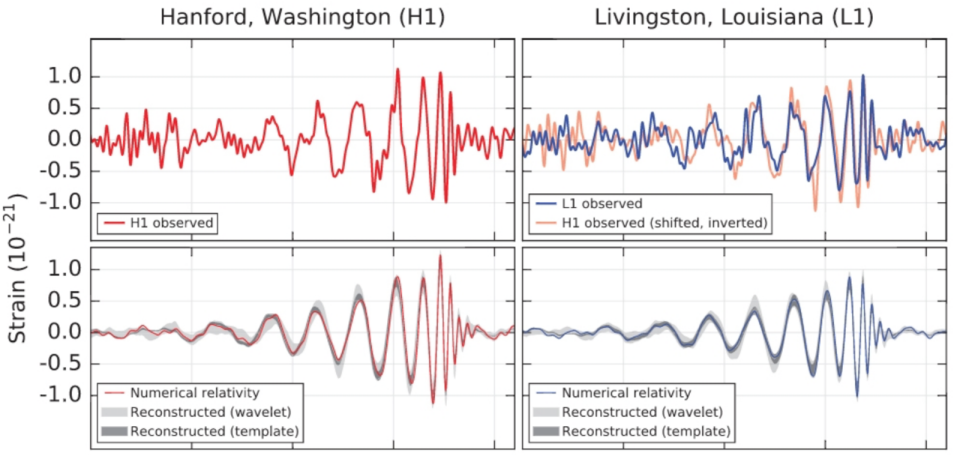

FIGURE 1: First gravitational wave observation reported by the LIGO-Virgo scientific collaboration [3]. Top panel: Minimally filtered strain $h(t)$ corresponding to GW150914. Notice the remarkably nice agreement between the shifted signals in both detectors (right panel). Bottom panel: Numerical relativity prediction for the observed signal compared with the reconstructed wavelet from the detector's data.

smaller than the size of the atomic nucleus. Despite the smallness of the effect caused on the mirrors, its evidence were overwhelming when looking into the data. Figure 1 shows the data segment corresponding to GW150914 [3]. The signal is clearly outlined over a minimally band-filtered noise having a good agreement with GR predictions. This has not been the only event observed by the LIGO detectors during this thesis project. A lower mass system tagged as GW151226 and with masses $14.2M_{\odot}$ and $7.5M_{\odot}$ was also observed during the first LIGO observation run (O1) with a lower SNR of 13 and where the match-filtering techniques were essential to detect it. Moreover, there was a third binary black hole (BBH) candidate called LVT151012 that did not reach the 5σ threshold required to be confirmed although there exist some indications that suggest its astrophysical origin. Then, the era of the gravitational wave astronomy has just started with the hope of having more and more diverse astrophysical observations that help us to better understand our universe.

Structure of this thesis

This thesis talks about the modelling of gravitational waves and final state quantities from binary black hole mergers framed in the context of LIGO detectors. Then, Chapters 1 and 2 introduce the basic context and formalism used in the later ones. Chapter 1 provides a quick review of the basic concepts related to gravitational wave astronomy. We go over the most relevant points of general relativity (GR) and the weak field approximation (gravitational waves (GWs)) to end with a brief overview of the main gravitational

waves (GWs) sources, interferometers and prospects in GW astronomy. Chapter 2 is intended to review the several analytic and numerical solutions to the two body problem focused on BBH mergers. To this end, I first identify the relevant physical parameters in BBH mergers and I describe some aspects of the morphology of the radiation. Then, I give an overview of the different PN and EOB formulations, phenomenological and SEOBNR approximants and NR results putting some more emphasis in describing the Arnowitt-Deser-Misner (ADM) $3+1$ decomposition of the Einstein Field equations and the Baumgarte-Shapiro-Shibata-Nakamura-Oohara-Kojima (BSSNOK) formulation used in the `BAM` code. In Chapter 3 I extend the first results of obtained in this thesis; the numerical setup and simulation of 23 BBH systems with unequal spins and performed with the `BAM` code. In this Chapter we detail the main features of the code, from the initial data to the mesh-refinement structure. Then, we describe all the data post-processing needed to obtain the final products: $\psi_4(t)$, strain $h(t)$ and luminosity $L(t)$ as well as the final mass and final spin. This post-processing involves resolution and extrapolation studies, the analysis of the possible sources of numerical errors and the eccentricity reduction of all the set of cases. Chapter 4 constitutes the original results obtained throughout this thesis project in collaboration with Glasgow University and University of Cardiff. Using the simulations described in Chapter 4 and collecting all the available NR data from the SXS [4], RIT [5], and GaTech [6] waveform catalogs, we have developed a new hierarchical, data-driven fitting methodology that has been applied for a new calibration of phenomenological models for the final mass and final spin [7] and peak luminosity [8] of BBH mergers. In Chapter 5 I give a brief review of the PhenomD model and I show the primary results of the new fitting methodology on the calibration of a three-parameter PhenomD model. Finally, in Chapter 6 I outline the main results and conclusions obtained in this thesis and I analyse the possible ways of extending this research.

Chapter 1

Introduction to Gravitational Waves

Albert Einstein's General theory of Gravity GR [9–12] predicts that any accelerated, non-axisymmetric source of energy emits space-time oscillations that propagate at the speed of light. These oscillations are elusive weakly interacting waves that travel freely through the Universe carrying out physical information about the processes which generate them: scientific community refers to them as gravitational waves [1, 2] and were detected for the first time on 14th of Semptember 2015 by the LIGO/Virgo collaboration [3, 13], almost 100 hundred years after their theoretical description. GR is generally accepted as the best candidate theory of gravity in modern physics. While it provides an extremely accurate description of all the dynamical processes formerly explained through the popular Newton's formulation of gravity, it also expands its horizon to an innumerable new set of physical objects unexplained by this old theory: so much catastrophic and exotic as black hole (BH) , wormholes, the expansion of the universe but also other less dramatic physical situations as the anomalous precession of the planet Mercury and and the correct description of light bending [11]. Contrary to Newton's theory, gravity is no longer viewed as a "force" but as a consequence of the deformation of the space-time fabric. In the words of John Archibald Wheeler:

Space-time tells matter how to move, matter tells space-time how to curve.

GR draws a physical theory of gravity in a fully geometrical scheme that will require us to use the well-known tools of differential geometry to disentangle coordinates effects from the genuine features of the space-time geometry. In this chapter I review the basic GR derivations following [14, 15].

1.1 Introduction to GR

Wheeler's most popular quote is mathematically synthesized through Einstein field equation; a four-dimensional equation given in term of symmetric tensors computed from the metric,

$$G_{\mu\nu} = 8\pi \frac{G}{c^4} T_{\mu\nu} \,, \tag{1.1}$$

where $G_{\mu\nu}$ and $T_{\mu\nu}$ denote the Einstein tensor and the stress-energy tensor of a matter field respectively, and G and c are Newton's gravitational constant and the speed of light. The left hand side of (1.1) encodes the geometrical content of the four-dimensional space-time. In the standard scenario, this space-time is usually depicted as four-dimensional Lorentzian manifold with an underlying smooth background metric tensor $g_{\mu\nu}$ which captures the notion of distance on the manifold and it reads:

$$ds^2 = g_{\mu\nu} dx^\mu dx^\nu \tag{1.2}$$

where the repetition of the indices denotes a summation over twin indices. The element ds^2 defines the infinitesimal displacement between to nearby points on the manifold. It might be seen as the analogous to any purely spatial line element in a given Riemmanian manifold but now considering also displacements in time. The four-dimensional metric tensor $g_{\mu\nu}$ is described as a symmetric 4×4 matrix, that is, with 10 independent components from the total 16 coefficients. Gravitational interactions are thoroughly determined by the metric tensor and is the basis of most of the calculations in GR.

1.1.1 General principle of covariance in GR

The principle of general covariance was formulated by Albert Einstein as one of the axioms of GR (and any other physical law) to be fulfilled. It states that the form of the physical laws must be invariant under any arbitrary change of coordinates or, equivalently, that any physical theory must be expressed in terms of tensor fields. Equation (1.2) is invariant under smooth changes of the space-time coordinates

$$x^\mu = f^\mu(x^\nu) \,, \tag{1.3}$$

keeping constant the space-time interval ds^2 regardless the coordinate system used for labeling the space-time points. This is, the four-dimensional length element ds must be preserved regardless the coordinate choice. Then, the metric tensor $g_{\mu\nu}$ must behave as a covariant tensor field under general coordinate transformations, meaning that any

change of the coordinates is propagated as:

$$g_{\mu'\nu'} = g_{\mu\nu}\left(\frac{\partial x^{\mu}}{\partial x^{\mu'}}\frac{\partial x^{\nu}}{\partial x^{\nu'}}\right) . \tag{1.4}$$

The general covariance of GR also implies that one might freely move from one system of coordinates to another without affecting the underlying space-time geometry inherent to our manifold. Thus, we can always find a coordinate system satisfying:

$$\partial_{\lambda} g_{\mu\nu}|_{P} = 0 \,, \tag{1.5}$$

at any regular space-time point P and where $\lambda = (0, 1, 2, 3)$. This means that it always exists a local inertial system at P described by the rules of special relativity, i.e., the space-time is locally flat at P. However, what would be the result of inspecting the field values at different points P?, how do we measure non-local differences on the field variables? how do we disentangle the coordinate effects from the "isolated" variations of the field variables? The common flat space-time derivative (1.5) does not break up by itself the physical ambiguity driven by the change of the coordinates on a given surface: one has also to compensate for the changes in the coordinate basis from one point to another to recover the same conceptual meaning of the partial derivative in a flat space-time. This is achieved by means of the covariant derivative, which applied to a vector field takes the following form,

$$\nabla_{\mu} v^{\nu} = \partial_{\mu} v^{\nu} + \Gamma^{\nu}{}_{\mu\lambda} v^{\lambda} \,. \tag{1.6}$$

where v is a vector field defined defined in the vicinity of P. The first term of the right hand side of (1.6) is the usual partial derivative used in a flat space-time while Γ accounts for the so called Christoffel symbols which describe the metric connection and give a sense of how the vectors are parallel-transported along any curve. The definition of the covariant derivative is not restricted to vector fields but it is a general operation applicable to any tensor of a given rank with the same philosophical idea; the characterization of the tensor field variations taking into account the changes on the coordinate basis along our manifold. Here we use our rank-two metric tensor to illustrate its formulation,

$$\nabla_{\lambda} g_{\mu\nu} = \partial_{\lambda} g_{\mu\nu} - \Gamma^{\sigma}{}_{\lambda\mu} g_{\sigma\nu} - \Gamma^{\sigma}{}_{\lambda\nu} g_{\mu\sigma} \,. \tag{1.7}$$

At this point, we should recall that the standard prescription of GR must recover locally the special relativity results. This means that we should be allowed to define at any point P a local inertial coordinate system which satisfies (1.5). Thus, it is natural to generalize (1.5) to (1.8) in order to guarantee that special relativity is fully recovered

locally.

$$\nabla_\lambda g_{\mu\nu} = 0\,. \tag{1.8}$$

The tensorial character of (1.8) implies that this equality must be hold in any coordinate system, providing the following familiar relations between the Christoffel symbols and the metric tensor,

$$\Gamma^\lambda{}_{\mu\nu} = \frac{1}{2} g^{\lambda\kappa} \left(\partial_\mu g_{\kappa\nu} + \partial_\nu g_{\kappa\mu} - \partial_\kappa g_{\mu\nu}\right)\,, \tag{1.9}$$

where $g^{\lambda\kappa}$ is the inverse matrix of $g_{\lambda\kappa}$ thus satisfying,

$$g^{\lambda\mu} g_{\lambda\nu} = \delta^\mu_\nu\,. \tag{1.10}$$

1.1.2 Curvature in GR

Equations (1.2) to (1.10) illustrate the profound geometrical character of GR being sometimes difficult to distinguish between geometrical effects induced by some particular coordinate choice and the intrinsic effects of the curvature (gravitation). This well known problem is solved according to the rules of differential geometry and, in particular, through the Riemman tensor which provides a univocal characterization of the curvature of the space-time,

$$\left(\nabla_\lambda \nabla_\sigma - \nabla_\sigma \nabla_\lambda\right) v^\mu = R^\mu_{\beta\lambda\sigma} v^\beta\,. \tag{1.11}$$

Equation (1.11) provides a measure of the non-Euclideanity of our four-dimensional space-time; a flat, gravity free (Euclidean) space-time is the only configuration with a vanishing $R^\mu_{\beta\lambda\sigma}$. To illustrate this, consider the closed curve delimited by the equilateral triangle of Figure 1.1 and imagine we move a vector emanating at the point A along the curved triangle on the sphere. After completing the full path, one realises that we do not get the original vector back. This is a feature of curved space-times, i.e., with non-zero Riemann tensor. Then, combining (1.6) and (1.11) the Riemann tensor reads:

$$R^\mu_{\lambda\sigma\nu} = \partial_\lambda \Gamma^\mu{}_{\sigma\nu} - \partial_\sigma \Gamma^\mu{}_{\lambda\nu} + \Gamma^\mu{}_{\lambda\rho}\Gamma^\rho{}_{\sigma\nu} - \Gamma^\mu{}_{\sigma\rho}\Gamma^\rho{}_{\lambda\nu}\,. \tag{1.12}$$

The tensorial character of (1.12) guaranties that if the Riemman is not zero for a given coordinate system, it will not be zero for any other possible arbitrary choice of coordinates. Thus, it provides a simple way of separating the curvature (gravitation) from other coordinate related effects.

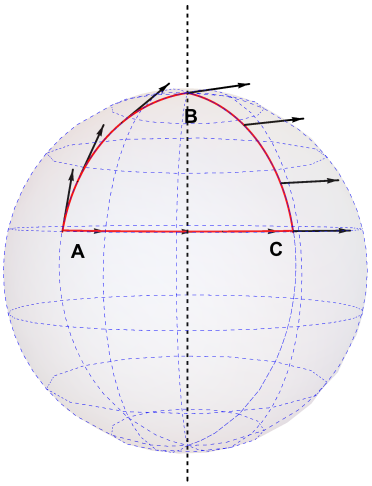

FIGURE 1.1: Illustration of a vector *parallel-transported* from the point A along the close thick curve highlighted in the figure. In a curved space-time the vector does not return to itself.

1.1.3 Ricci tensor and Bianchi identities

The Riemman tensor is a four-rank tensor corresponding to $4^4 = 256$ components. However, from (1.9) and (1.12) one finds a series of symmetries that reduce the number of independent components of the Riemann tensor to only 20. Taking into account all the symmetries, the only way of contracting a pair of indices results in the Ricci tensor, which is naturally related to the Einstein tensor (1.1) through,

$$R_{\mu\nu} \equiv R^{\rho}_{\mu\rho\nu}\,, \tag{1.13}$$

where allowing for (1.9) and (1.10) one finally gets,

$$R_{\mu\nu} = \frac{1}{2}(\partial^{\rho}\partial_{\mu}g_{\nu\rho} + \partial^{\rho}\partial_{\nu}g_{\mu\rho} - \partial^{\rho}\partial_{\rho}g_{\mu\nu} - \partial_{\mu}\partial_{\nu}g)\,. \tag{1.14}$$

Another important relation of the Riemann tensor involves its covariant derivative, and is known as the second Bianchi identity,

$$\nabla_{\rho}R^{\mu}_{\nu\lambda\sigma} + \nabla_{\rho}R^{\mu}_{\nu\sigma\lambda} + \nabla_{\sigma}R^{\mu}_{\nu\rho\lambda} = 0\,, \tag{1.15}$$

Finally, by contracting two pairs of indices one gets the analogous Bianchi identity for the Ricci tensor,

$$\nabla_{\mu}\left[R^{\mu\nu} - \frac{R}{2}g^{\mu\nu}\right] = 0\,, \tag{1.16}$$

which is interpreted as a conservation law for the object enclosed within the brackets. Equation (1.16) is directly related with the first equation shown in this text (1.1) thus

being:

$$G_{\mu\nu} = R_{\mu\nu} - \frac{R}{2} g_{\mu\nu} \,, \tag{1.17}$$

where the bracketed object in (1.16) is nothing more that the contravariant version of the Einstein tensor. Furthermore, coming back to (1.1), from pure geometrical statements and through (1.16) we get the predicted conservation law for the energy momentum tensor which reads:

$$\nabla^{\mu} T_{\mu\nu} = 0 \,. \tag{1.18}$$

Thus, (1.18) is the generalization of the energy and momentum conservation in special relativity $\partial^{\mu} T_{\mu\nu} = 0$ on non-Euclidean space-times.

1.2 Weak field approximation

The gravitational interaction is in general weaker than the other known forces[1] of nature; for instance, while I am writing these lines a pile of molecules can hold me comfortably seated on my chair through their electrostatic repulsion against the total gravitational pull exerted by the whole Earth. This might be qualitatively understood by looking at the strong suppression factor $G/c^4 \sim 10^{-46}$ of (1.1): it takes an enormous amount of energy to deform the space-time geometry.

However, there exist many scenarios in our universe in which large and compact forms of energy are eventually emitted as gravitational waves and also carrying out more power than most of the well known astrophysical electromagnetic events [3, 13]. Those feeble waves propagate at the speed of light and warp our space-time likewise a small stone thrown to a quiescent lake would perturb its surface. They were for the first time formulated by Albert Einstein [1] one year after the publication of GR and are a direct consequence of (1.1) under certain assumptions that we will detail in this chapter. We start our deduction with (1.1) with $c = 1$ and $G = 1$ (geometrical coordinates) to simplify the notation, namely:

$$G_{\mu\nu} = 8\pi T_{\mu\nu} \,. \tag{1.19}$$

1.2.1 Linearization of the Einstein field equations

Gravitational waves arise formally when one considers the effect of a small linear perturbation to the flat background space-time $\eta_{\mu\nu}$. We want to obtain the equations of motion in terms of the linearly perturbed flat metric by computing all the curvature

[1] Recall that we do not longer consider gravity as a force but as an effect of the space-time geometry.

related quantities exposed in Sec. 1.1. Then, we express the perturbed metric as,

$$g_{\mu\nu} = \eta_{\mu\nu} + h_{\mu\nu}, \qquad |h_{\mu\nu}| \ll 1\,, \tag{1.20}$$

where we choose $\eta_{\mu\nu}$ to take its canonical form $\eta_{\mu\nu} = diag(-1,1,1,1)$ and $h_{\mu\nu}$ satisfies the properties of a tensor field on a flat background (Minkowski space-time). Regarding the weakness of the perturbation and ignoring higher than linear contributions in $h_{\mu\nu}$, it is easy to obtain the contravariant form of (1.20),

$$g^{\mu\nu} = \eta^{\mu\nu} - h^{\mu\nu}\,. \tag{1.21}$$

In this scenario, $\eta_{\mu\nu}$ is used for lowering and raising the indices. We begin by computing the expression of the Christoffel symbols in terms of the new metric (1.20) and neglecting higher than linear order terms in $h_{\mu\nu}$:

$$\Gamma^{\lambda}{}_{\mu\nu} = \frac{1}{2}\eta^{\lambda\kappa}\left(h_{\kappa\nu,\mu} + h_{\kappa\mu,\nu} - h_{\mu\nu,\kappa}\right)\,, \tag{1.22}$$

Once computed the connection coefficients in this new frame, we must propagate them through the Einstein field equations to compute the perturbed Riemman tensor (1.12) neglecting higher than linear order terms in $h_{\mu\nu}$. The perturbed Riemann tensor reads:

$$R_{\rho\sigma\mu\nu} = \frac{1}{2}\left(\partial_\sigma\partial_\mu h_{\rho\nu} + \partial_\rho\partial_\nu h_{\sigma\mu} - \partial_\rho\partial_\mu h_{\sigma\nu} - \partial_\sigma\partial_\nu h_{\rho\mu}\right), \tag{1.23}$$

while the perturbed Ricci tensor is computed from the contraction of the ν and ρ indices:

$$\begin{aligned} R_{\mu\nu} &= \frac{1}{2}\left(\partial_\mu\partial^\lambda h_{\lambda\nu} + \partial_\nu\partial^\lambda h_{\lambda\mu} - \partial_\lambda\partial^\lambda h_{\mu\nu} - \partial_\mu\partial_\lambda h\right)\,, \\ R &= \partial^\lambda\partial^\rho h_{\lambda\rho} - \partial^\lambda\partial_\lambda h\,, \end{aligned} \tag{1.24}$$

where $h = h^\lambda_\lambda$ is the trace of the metric perturbation and $R = R^\lambda_\lambda$ is the Ricci scalar.

We can now incorporate the results of (1.24) in (1.17) to get the explicit form of the perturbed Einstein tensor. However, it is convenient for reducing the formal complexity of our equations to define a *trace reversed* metric pertubation tensor such:

$$\bar{h}_{\mu\nu} = h_{\mu\nu} - \eta_{\mu\nu}h/2, \qquad \bar{h} = -h. \tag{1.25}$$

With these modifications the Einstein tensor reads:

$$G_{\mu\nu} = \frac{1}{2}\left(\partial\rho^{\partial}_{\mu}\bar{h}_{\nu\rho} + \partial\rho^{\partial}_{\nu}\bar{h}_{\mu\rho} - \partial^\rho\partial_\rho\bar{h}_{\mu\nu} - \eta_{\mu\nu}\partial^\rho\partial^\sigma\bar{h}_{\rho\sigma}\right)\,. \tag{1.26}$$

According to the Einstein field equations (1.19), (1.26) must be equal to $8\pi T_{\mu\nu}$. This

equality implicitly means that we are taking the zeroth order contribution in $h_{\mu\nu}$ of the energy-momentum tensor, i.e., that the scale of the $T_{\mu\nu}$ is on the same order of magnitude than the perturbation. However, (1.26) can be further simplified taking advantage of the coordinates freedom contemplated by GR. Thus, we are allowed to consider any small but arbitrary change of coordinates, such that:

$$x^{\mu\prime} = x^{\mu} + \epsilon^{\mu}\,, \tag{1.27}$$

where ϵ satisfies $|\partial_{\mu}\epsilon^{\mu}| \ll 1$.

These new coordinates transform our initial metric to first order in ϵ to:

$$(g_{\mu\nu})' = \eta_{\mu\nu} + h_{\mu\nu} - \partial_{\mu}\epsilon_{\nu} - \partial_{\nu}\epsilon_{\mu}\,, \tag{1.28}$$

where the *prime* indicates that we are working in the new coordinates. This coordinate transformation leaves the physical situation intact for any arbitrary but small ϵ^{μ}. Then, after some algebra we identify:

$$\left(\bar{h}_{\mu\nu}\right)' = \bar{h}_{\mu\nu} - \partial_{\mu}\epsilon_{\nu} - \partial_{\nu}\epsilon_{\mu} + \eta_{\mu\nu}\partial_{\lambda}\epsilon^{\lambda}\,, \tag{1.29}$$

$$\left(\partial^{\nu}\bar{h}_{\mu\nu}\right)' = \partial^{\nu}\bar{h}_{\mu\nu} - \partial^{\nu}\partial_{\nu}\epsilon_{\mu}\,. \tag{1.30}$$

At this point, we are allowed to choose any coordinate transformation that satisfies $\partial^{\nu}\bar{h}_{\mu,\nu} = \partial^{\nu}\partial_{\nu}\epsilon_{\mu}$, thus:

$$\left(\partial^{\nu}\bar{h}_{\mu\nu}\right)' = 0, \tag{1.31}$$

which defines the so called harmonic, De Donder or Lorentz gauge (being the analogous condition in electromagnetism). Thus, in these coordinates and after some algebra we get:

$$\Box\bar{h}_{\mu\nu} = 16\pi T_{\mu\nu}, \tag{1.32}$$

where the $\Box = \eta_{\mu\nu}\partial^{\mu}\partial^{\nu}$ is D'Alembertian operator in flat space. Equation (1.32) stands for a wave equation for metric waves propagating at the speed of light ($c = 1$) with a source term $T_{\mu\nu}$. Now, for the sake of simplicity, we set this term to zero (vacuum solution) to study its properties. The general complex solution given in terms of plane waves, namely:

$$\Box\bar{h}_{\mu\nu} = 0\,, \tag{1.33}$$

$$\bar{h}_{\mu\nu} = A_{\mu\nu}e^{ik_{\alpha}x^{\alpha}}\,, \tag{1.34}$$

where k^{μ} is the wave vector and $A_{\mu\nu}$ the amplitude tensor. We can now deduce the usual properties of a plane wave by inspecting the properties of the set of Equations (1.31)

to (1.34). First, notice that inserting the plane wave solution (1.34) in (1.33) we obtain:

$$\eta^{\mu\nu}k_\mu k_\nu = k_\nu k^\nu = 0, \tag{1.35}$$

which describes a null wave vector, i.e., that $\bar{h}_{\mu,\nu}$ propagates at $c = 1$.

Furthermore, combining the Lorentz gauge (1.31) and (1.34) we find the following relation between the amplitude tensor $A_{\mu\nu}$ and the wave vector k^μ:

$$A_{\mu\nu}k^\nu = 0\,. \tag{1.36}$$

This indicates that the amplitude of the oscillation $A_{\mu\nu}$ is *transverse* to the direction of propagation defined by k^ν: the general solution describes a plane wave traveling along null vectors. All the gauge choices and, in particular, (1.25) and (1.36) describe the gravitational waves in the so called *transverse-traceless* (TT) gauge (trace-free and transverse propagation). Notice that the amplitude tensor $A_{\mu\nu}$ (as well as the metric perturbation $h_{\mu\nu}$) has in principle ten independent components because of the symmetry of the metric tensor. On the other hand, the orthogonality condition (1.36) provides a set of four extra equations for the amplitude tensor thus reducing this number to a total of six. This, added to the gauge freedom associated to the four coordinate functions ϵ^μ of (1.29) reduce this number to only two, consistent with the two light polarizations, which we denote by h_+ (plus polarization) and $h_\times$ (cross polarization). Then, these metric waves propagating in the *z-axis* direction turns out to be,

$$h_{\mu\nu} = \begin{pmatrix} 0 & 0 & 0 & 0 \\ 0 & h_+ & h_\times & 0 \\ 0 & h_\times & -h_+ & 0 \\ 0 & 0 & 0 & 0 \end{pmatrix}. \tag{1.37}$$

1.2.2 Equations of motion in the TT frame

The general solution found in (1.37) gives a sense of how a metric wave perturbation propagates. However, we will compute the effect of a passing GW on free particles (for simplicity). This is done by solving the geodesic deviation equation for a non-interacting particle under the effect of a TT plane wave perturbation. This is given by:

$$\frac{\partial^2 x^\mu}{dt^2} = R^\mu_{00\lambda}x^\lambda\,, \tag{1.38}$$

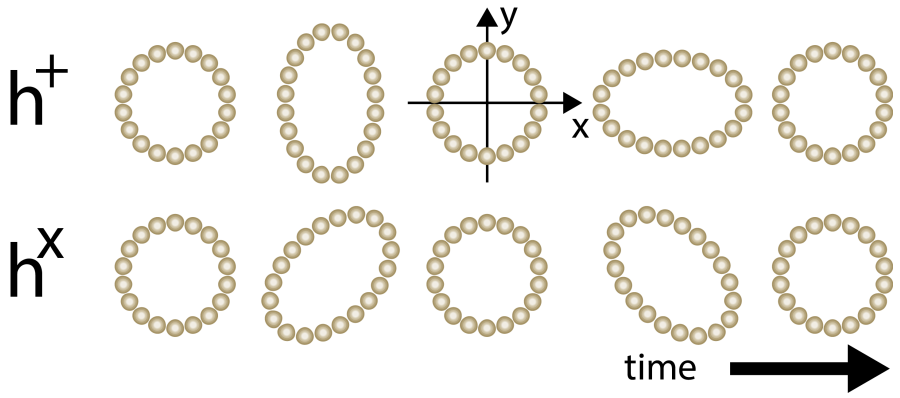

FIGURE 1.2: Effect of a gravitational wave traveling in the *z-direction* (crossing the sheet of paper) on a ring of free particles living on the $x-y$ plane. Top panel: + polarization, bottom panel: x polarization.

and using the results of (1.23) it takes the following form,

$$\frac{\partial^2 x^\mu}{dt^2} = \frac{\partial^2 h_{\mu\lambda}}{dt^2} x^\lambda \,, \tag{1.39}$$

that is nothing more that the acceleration suffered by the free particle to the passage of a metric perturbation $h_{\mu\nu}$. Indeed, it acts like a force to any particle stuck at x^μ. Then, solving (1.39) to leading order in h one gets,

$$x^\mu(t) = \left(\delta^\mu_\lambda + \frac{1}{2} h_{\mu\lambda}(t)\right) x^\lambda_0 \,, \tag{1.40}$$

being $h_{\mu\nu}$ an oscillatory function of time (plane wave) as shown in (1.34). From (1.37) and (1.40) we can have an idea of how a metric plane wave would modify the x^μ positions of a free particle. To make the illustration easier, let us choose a certain orientation such $h_\times = 0$. Equation (1.40) reads:

$$x = \left(1 + \frac{1}{2} h_+(t)\right) x_0 \,, \qquad y = \left(1 - \frac{1}{2} h_+(t)\right) y_0 \,. \tag{1.41}$$

Then, while the wave is shrinking one of the coordinates at the same time is stretching the other coordinate. This oscillatory behavior on test particles is the basis gravitational wave detectors. Figure 1.2 illustrates the separated effect of the two polarizations on a ring of test particles. Notice that $h_\times$ behaves similarly but rotated 45°.

1.2.3 Generation of gravitational waves

We have seen that a small, time dependent metric perturbation to the flat metric $\eta_{\mu\nu}$, under certain gauge considerations and solving the equations with $T_{\mu\nu} = 0$, results on the description of a planar metric wave moving at the speed of light. Now, we consider the

situation one level up by taking a non-vanishing but still small energy-momentum tensor (far-zone solution). Then, each source will described by a different energy distribution (different energy momentum tensor) which will characterise a different wave profile.

1.2.3.1 Quadrupole formula derivation

As it happens in electromagnetism, the general solution of (1.34) is given in terms of the retarded Green function, namely,

$$\bar{h}_{\mu\nu}(t,x) = 4\int \frac{T_{\mu\nu}\left(t',x'\right)}{|x-x'|}d^3x'\,, \tag{1.42}$$

where x accounts for the position of the source in relation to the observer, x' traces the geometry of the source, $t' = r - |x - x'|$ is the retarded time and r is the position of the source center of mass (see Figure 1.3). First, notice that all the objects of astrophysical

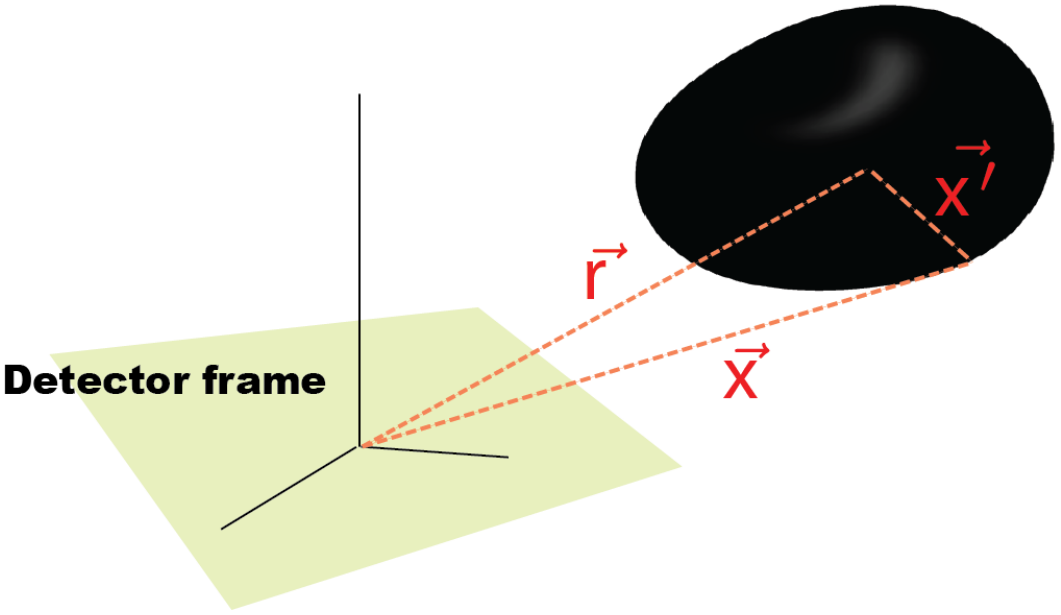

FIGURE 1.3: Reference frame for a given gravitational wave source represented by the black ellipsoid. Objects of astrophysical interest satisfy $\vec{x} \approx \vec{r}$ usually referred as the *far zone regime*.

interest (see Sec. 1.3) are far away from the detector's frame or, in other words, that the intrinsic coordinates x' are negligible compared to the source-detector distance x. This is known as *far-zone* approximation and it is mathematically translated as: $r \approx |x|$. In order to simplify some calculations we can transform (1.42) to the Fourier domain namely,

$$\bar{h}_{\mu\nu}(\omega,x) = \frac{4e^{i\omega r}}{r}\int \tilde{T}_{\mu\nu}\left(\omega,x'\right)d^3x', \tag{1.43}$$

where we have taken advantage of the *far-zone* condition. In addition, the energy-momentum tensor conservation (1.18) translates to: $-\partial_j \tilde{T}^{j\nu} = -i\omega \tilde{T}^{0\nu}$. Thus, taking into account the energy momentum tensor conservation and integrating by parts (1.43) one finally gets,

$$\bar{h}^{ij} = -\frac{2}{r}\partial_0\partial_0 \int x^i x^j T_{00}(t-r,x)d^3x\,, \tag{1.44}$$

where the integrand is nothing more than the mass-quadrupole moment according to the famous Einstein 1916 results [2],

$$\bar{h}^{ij} = -\frac{2}{r}\ddot{I}^{ij}(t-r)\,. \tag{1.45}$$

From the last equation it is clear that any source with a non-vanishing second derivative of the mass-quadrupole moment will emit gravitational waves. This explains why perfectly axisymmetric sources as individual spinning BH, neutron star (NS) are not expected to be GW emitters. Indeed, galactic NSs with a minimal a $1mm$ crust, not aligned with the orbital axis, could be sufficient to generate periodic GW signals detectable by LIGO [16–18].

1.2.3.2 Toy model: BBH system

For the first time in these lines we work out the equations that relate the gravitational waves to BBH mergers which is the main topic of this thesis. It is well known that a complete accurate solution of such systems is only possible when full NR is taken into account. Even the most up to date post-Newtonian [19, 20] and EOB analytic models [21, 22], which account for higher order quadrupolar corrections, breakdown in the late inspiral and merger-rindown regimes[2]. However, it is still possible to obtain an accurate solution when the system is far from the coalescence and the two black holes can be considered as a point-like, slow-moving particles. As a toy example and at zero order we can get an analytic solution for the metric perturbation $h_{\mu\nu}$. For simplicity, it is assumed a quasi circular (zero-eccentric) orbital decay which is equivalent to the formulation of the Kepler two body problem for a circular orbit (with $G = c = 1$),

$$v^2 = M/d\,, \qquad \omega_{orb} = \sqrt{M/d^3}\,, \tag{1.46}$$

where d stands for relative distance between the two particles, v the relative velocity, $M = m_1 + m_2$ is the total mass and ω_{orb} is the angular velocity. Then, we locate the

[2] See Sec. 2.2 for a detailed description of the waveform anatomy.

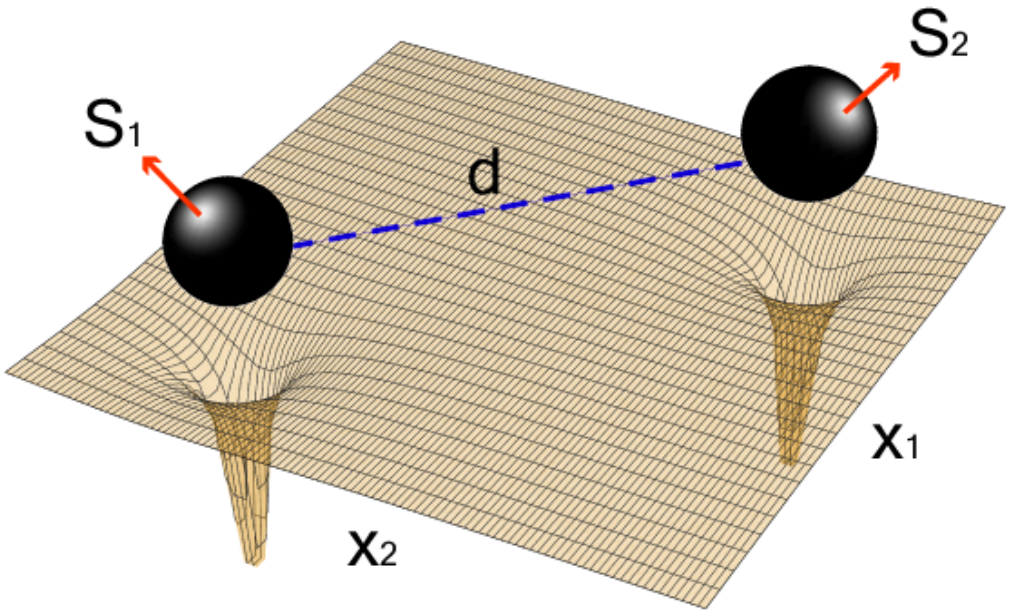

FIGURE 1.4: Artistic representation of the two body orbit for a BBH system in a quasi-circular evolution. The orbital distance $d(t)$ progressively shrinks to eventually merge in a Kerr BH.

two bodies on the $z = 0$ plane as,

$$\begin{aligned} x_1 &= \{d\cos(\omega_{orb}t), d\sin(\omega_{orb}t), 0\} \ , \\ x_2 &= \{-d\cos(\omega_{orb}t), -d\sin(\omega_{orb}t), 0\} \ . \end{aligned} \tag{1.47}$$

From (1.44) is clear that the only relevant energy momentum tensor component is the 00 which in this example takes the following form,

$$T_{00}(t,x) = M\big(\delta(x_1 - d\cos(\omega_{orb}t))\delta(x_2 - d\sin(\omega_{orb}t)) \tag{1.48}$$

$$+ \delta(x_1 + d\cos(\omega_{orb}t))\delta(x_1 + d\sin(\omega_{orb}t))\big) \ , \tag{1.49}$$

where the δ function is used to define the position of each black hole orbiting at an angular frequency ω_{orb}. Then, after integrating (1.44) it is possible to obtain the following expression for the gravitational waves strain,

$$h_{ij} = \frac{8M}{r} d^2 \omega_{orb}^2 \begin{pmatrix} 0 & 0 & 0 & 0 \\ 0 & -\cos(2\omega_{orb}t) & -\sin(2\omega_{orb}t) & 0 \\ 0 & -\sin(2\omega_{orb}t) & \cos(2\omega_{orb}t) & 0 \\ 0 & 0 & 0 & 0 \end{pmatrix} . \tag{1.50}$$

Then, binary systems emit GWs with twice the frequency of the orbital system. This condition is quite well preserved at quadrupole order during the whole evolution, getting only relevant deviations in the merger-ringdown regime of the evolution, where the strong field effects appear. Additionally, notice that (1.50) is written in terms of the geometrical

units with $G = c = 1$. Putting back the physical units to the equation, that is, adding a factor G/c^3 10^{-36} and eventually considering a standard scenario in which two black holes of masses $M = 10M_\odot$ orbit around each other at $100Mpc$ far away from the Earth and at a relative distance of 10^5 km, we get that an estimated strain of $h \sim 10^{-21}$. Thus, such catastrophic configuration only will affect the Earth (detectors) geometry in one part on 10^{21}, that translated to the ground-based detectors implies a variation on the test masses of the order 10^{-18} (Sec. 1.4), i.e, smaller than the size of a proton.

BBH mergers are expected to be not only the dominant source of gravitational wave detections but also the events with highest SNR on the ground based detectors [23, 24]. From the predicted astrophysical sources, only an unlikely supernova (SN) explosion in the Milky Way might generate a compatible amplitude (indeed larger) than the expected far away binary mergers. Then, in order to increasingly constrain the various astrophysical scenarios for BBH mergers, it is essential to gain statistics by performing as many detections as possible with the highest possible SNRs. This motivates the development of increasingly accurate prescriptions of gravitational waveform models and which has been the main topic of this thesis.

1.3 Sources of gravitational waves

Due to the weak nature of gravity and consistently with the numbers and estimates given in the last section, detectable gravitational waves are related to catastrophic, high energy cosmological events such as Compact-Binary-Mergers (CBC) , highly rotating NSs, SN explosions, early universe phase transitions, cosmic strings etc. leaving also some room for non-predicted astrophysical events that may emerge. In this section we describe some of the most promising astrophysical events expected to be gravitational wave emitters.

Compact Binary Coalescences

CBC, and in particular BBH mergers, are the targeted sources of study of this thesis, being the predicted dominant events on ground based detectors. By CBC we mean BH-BH, BH-NS and NS-NS binary mergers. Indeed, the first astrophysical clue on the existence of gravitational waves was the discovery of the Hulse and Taylor pulsar [25] in 1974. Nowadays, the scientific effort in seeking for gravitational waves coming from CBC mergers is overwhelmingly justified: the LIGO detectors have already observed the late inspiral, merger and ringdown of several binary systems compatible with a stellar-mass BH-BH coalescenses [3, 13].

Stellar-mass compact binary mergers are expected to be the dominant source of future detections for ground-based gravitational detectors, as it is being confirmed by the current observations [26]. They describe pairs of old stars that have already gone through all the stages of stellar evolution, have been gravitationally bound and then orbit each other while the orbital distance is shrinking. This stage can last several $Myrs$ until the merger, where the final object definitively settles down to a Kerr black hole[3]. The major fraction of gravitational wave radiation is emitted in the last few orbits (seconds) and it is what we observe in the ground-based detectors. The collection of more events will help to constrain the formation scenarios, stellar evolution models and population distributions [27]. Mergers involving matter are also excellent candidates as an EM counterpart observation. The expected number of detections per year on the upgraded advanced detector era might reach the 1000 events/year [26].

Other sources compatible with the space-based detectors (Sec. 1.4.5) are the extreme mass-ratio-inspirals (EMRI) and the intermediate binary black hole mergers (IMBBH). They are predicted to be large mass compact mergers with frequencies on the order of the mHz, i.e., out of the LIGO frequency band but very relevant for space-based missions as LISA [28].

Continuous gravitational waves

From Sec. 1.2 we have learned that any physical system with a time-varying quadrupole moment is a gravitational wave emitter. This makes of rapidly, spinning and with some degree of asymmetry Milky Way neutron stars, potential gravitational wave candidates [29]. Although they are known to be almost spherically rotating objects, any elastic stress or magnetic field might induce small deformations (ellipticity) on the shell of the neutron star that might be related with the internal equation of state (EOS) of the star. They are expected to be emitters of an almost monochromatic gravitational wave strain (small deviations on the spin rate are also predicted by the theory) thus making possible long time integrations of the data as opposite to BBH mergers. On the other hand, its weak strain limits the searches to the Milky Way, hence reducing a lot the volume coverage in relation to BBH mergers. Current continuous waves (CW) searches are seeking for systems with an ellipticity constrained to be less than $1mm$ for some of the known Milky Way pulsars [29].

[3]This is always true for systems where at least one of the two bodies is a BH. For NS-NS mergers the situation is in general the same, except for low mass mergers, where the remnant mass may not be sufficient to collapse into a BH, thus leaving a remnant NS.

Stochastic sources

Astrophysical models predict a low occurrence of ground-based GW detections from BBH mergers and CW emitters in a sense that they are very unlikely to be found as the superposition of two or more signals. Even the optimistic 1000 detections of BBH systems predicted in the next $\sim 4-5$ years become a small number when one considers the probability of having two events at the same time and ringing at the same frequency [30]. However the situation might be completely different when moving to space missions. One of the considered noise contributions (confusion noise) of the LISA mission (see Sec. 1.4.5) are the galactic binary white-dwarf inspirals. Taking into account that most of Main Sequence (MS) stars end their life as a white dwarf and that about the 50% live in binary systems we could end with $\sim$ 10 million of interacting binaries, being all potential gravitational wave emitters. In this scenario, the chances of having a superposition of more than two signals also increase thus creating an stochastic gravitational wave background hitting continuously the detectors.

The stochastic background may also have a cosmological origin [31]. Some cosmological models predict that the universe passed through an accelerated expansion phase in its initial stages which was related to some hypothetical phase transition. This likely involved a fast warping of the space-time that likely created a relic gravitational wave background (analogous to the electromagnetic cosmic microwave background CMB). If these models come true and recalling that this accelerated expansion happened much before than the recombination era (when the CMB was formed) we will cross the electromagnetic barrier to see farther back into the history of the Universe than ever before.

Burst

The word "burst" in this context collects all the unmodeled gravitational wave sources that emerge as a transient in the data. It is actually a search for the unexpected. Several and completely different scenarios might generate such transients: core-collapse SN, high-mass binary black hole mergers[4], exotic events as cosmic strings and any non-predicted source.

In these type of searches [32] the different pipelines look for similar patterns within the maximum $10ms$ that separate an event from Hanford to Livingstone (which also defines the line that joins the two detectors). Of special interest are the high-energetic

[4]The frequency of the system scales as $1/M$. This effect shifts the signal to the low frequency regime. For some specific high mass configuration all the inspiral may be totally overlapped by the low frequency noise thus just leaving "visible" the short merger-ringdown phase. For a more illustrative picture see Figure 1.8 and imagine what would be the effect of increasing the mass of the most left-shifted waveform.

burst expected from NS-NS and NS-BH mergers. These events could be the source of the gamma ray burst observations by the electromagnetic telescopes. Having its gravitational wave counterpart would also help to locate the system and provide an alternative description to the, up to now, unknown sources. These searches will be obviously optimized when more detectors are added to the net.

1.4 Gravitational wave detectors

Nowadays the physical reality of the gravitational waves is accepted by the vast majority part of the scientific community after the observation of the GW150914, GW151226 and LVT151012 systems by the LIGO detectors. However, this belief was not so uniform until the late 50's. Besides the known weakness of the signals predicted by the equations of GR and which made the researchers doubt about an eventual future detection, it was not even clear whether those space-time wiggles could produce any physical effect when crossing our matter fields. The discussion was solved by Richard Feymann and his famous *sticky bead* argument at the Chapel Hill conference in 1957. He illustrated with a simple though experiment that gravitational waves must carry energy and that it could be transferred to heat the surface of a metallic stick as a consequence of the friction caused by the movement of two beads attached to it.

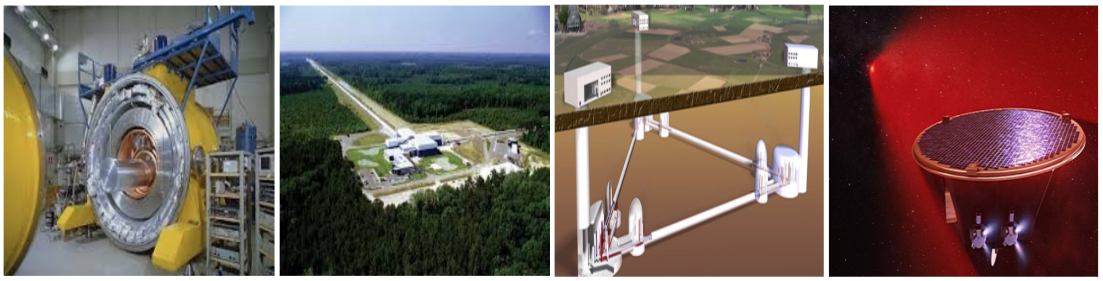

FIGURE 1.5: Pictorial representation of some GW detectors. From left to right: AURIGA [33], LIGO-Livingstone [34], ET [35], LISA [28].

1.4.1 Resonant bars

The Feymman thought experiment was a great boost for the idea of building gravitational wave detectors. Indeed, one of the researchers who attended the Chapel Hill conference, Joseph Weber, was the first scientific to make a real attempt to detect gravitational waves based on the so called resonant bars (see figure on the left of Figure 1.5). The underlying idea of these detectors involved the phenomenon called *sympathetic resonance* that actuates when an external vibration matches the resonance or ringing

frequency of the material (in the same way that a civil engineer must control the ringing frequency of the different structures when building a bridge).

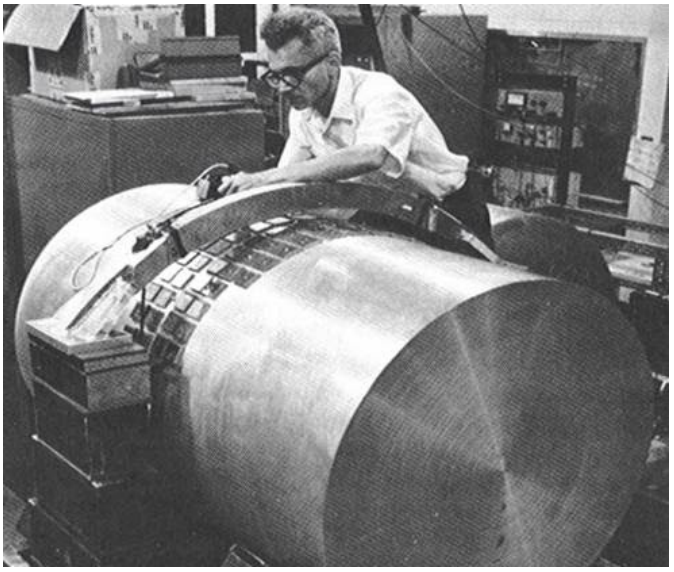

FIGURE 1.6: Joseph Weber working on his resonant bars for detecting gravitational waves. The bars originally consisted of a cylinder of aluminum 2 meters long and 1 meter in diameter.

The characteristic ringing frequency of the Weber's aluminum bars were about the 1600 Hz thus peaking at frequencies consistent with low mass binary systems ($\sim 10M_{\odot}$) and with the not very frequent, at least in the Local Group[5], SN explosions. However, the main problem of the bars was not so much the frequency but the very limited sensitivity achieved. Weber's bars sensitivity was only sufficient to detect signals with a typical strain about $h \sim 10^{-16}$. This magnitude, compared to the estimated zero order quadrupole strain of $h \sim 10^{-21}$ computed in the previous section would be roughly equivalent to detect a BBH merger at a distance of $1kpc$ (in the Milky Way), which is very unlikely considering the current rate estimates and standard astrophysical binary population models.

Despite all the complications described above, Weber claimed having detected gravitational waves in 1969, being just the first of a series of "detections" announced in the following years. However, none of those claims were sufficiently significant to be seriously considered and after years of failed detections the usage of resonant bars became unpopular among the growing gravitational waves community. However, there still remain alive some modern projects as AURIGA [33] which is also being used for research in quantum gravity.

[5]The Local Group comprises more than 54 galaxies including the Milky Way. The raw rate of SN explosions is about 6 per century in the Local Group being this number too low for considering them as likely candidates for an eventual detection.

1.4.2 Laser Interferometer Gravitational wave Observatory: LIGO

In the late 60's and in parallel to the first realizations of resonant bars, a new idea based on the elegant concept of light interferometry emerged as a promising alternative to bar based gravitational wave detectors. This first approach sowed the first seeds of what we know today as the Laser Interferometer Gravitational wave Observatory (LIGO).

The idea of using laser interferometry to monitor the relative motion of two freely hanging mirrors and based on the old idea of a Michelson interferometer were firstly considered in the early 60's by two Russian researchers: M.Gertsenshtein and V. I. Pustovoit [36] although the first tests and designs had to wait until the late 60's when Robert Forward an colleagues at Hughes Research Laboratories (California) built the first small-scale (1 m) prototype. This initial version was later complemented by Weber and Rainer Weiss at Massachusetts Institute of Technology (MIT), Hans Billing and colleagues in the Max Planck Institute for Quantum optics in Garching (Munich) and by Ronald Drever and collaborators in Glasgow University by building new and upgraded prototypes that, at the same time, were growing up in size to achieve more sensitivity (1-40 meters). In parallel, K. Thorne and the new-born gravitational wave group at Caltech started the first investigations on the modelling of the astrophysical sources and their predicted gravitational wave emission. The goal was to envision from a theoretical point of view the different sources that could produce such elusive emission and which ended with a still premature but quite satisfactory description of most of the sources referred to in Sec. 1.3. The combined results of the theoretical modelling and the instrumental performance of these first designs made quickly clear the necessity of kilometer-long observatories to detect gravitational waves; it was born the idea of the LIGO detectors. After years of planning and prototype research now funded by the National Science Foundation (NSF) the MIT and the Caltech groups submitted in 1987 the initial proposal that finally ended in 2002 with the installation and commissioning of LIGO's initial interferometers at Hanford, Washington and Livingston, Lousiana.

Basic design of a LIGO interferometer

The current ground based gravitational wave observatories are based on the old idea of a Michelson-Morley interferometers used in the classical experiment to test the existence of the ether in 1887. The underlying physics of an interferometer rely on the well known physical phenomena called light interference which is nothing more than the pattern resulting from the superposition of two or more light sources of equal or nearly-equal frequency. The basic idea is sketched out in Figure 1.7.

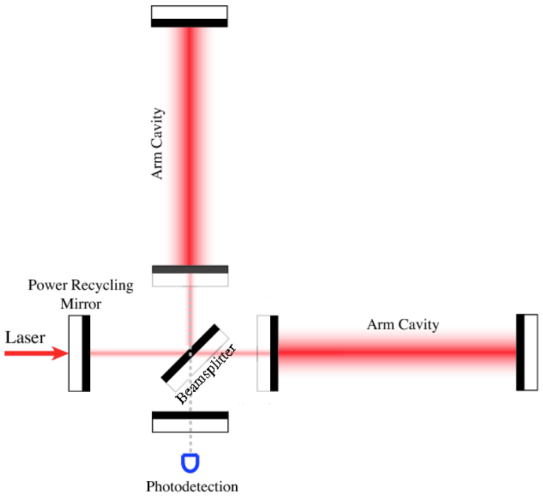

FIGURE 1.7: A simplified design of a LIGO interferometer. The laser hits the beam splitter and then follows perpendicular paths towards the mirrors. Each beam is forced to bounce 280 times in the Fabry-Perot cavities to finally reach the photodetector.

In a Michelson-Morley interferometer, a monochromatic light beam (laser) is emitted towards a mirror (beam splitter) which divides the original beam into two identical but perpendicular beams; one just passing through while the other is redirected (reflected) 90 degrees. Both beams travel towards two reflecting mirrors placed at exactly the same distance from the beam splitter, which in this case (LIGO) are 4-km of ultra-high vacuum arms. In absence of any passing gravitational wave, the two beams travel back the same distance until they reach the photodetector thus being superposed. Then, whenever the distance traveled (optical path) is exactly the same, they cancel each other out in a so called destructive interference. However, imagine a gravitational wave passing through the detectors. As we show in Sec. 1.2, a GW stretches one of the arms while shrinking the other. This induces a variation in the optical path that causes a time delay between two beams when reaching the photodetector; they will not be longer canceled out but instead a constructive interference signature will be recorded, being specific of each astrophysical source.

Main sources of noise acting on a LIGO interferometer

The aim behind its design is now clear; detect variations in the length of the arms on the order of $\Delta L \sim 10^{-18}$m. This astonishingly small magnitude leaves the reader wonder how many possible noise contributions would make vibrate one atom a distance one thousand times smaller than the size of its nucleus (and even larger displacements). However, we are not looking for individual vibrations but for coherent and correlated displacements of all the atoms of the mirror: an eventual gravitational must affects

equally all the atoms of the macroscopic system. Thus, the phase shift produced for a passing gravitational wave in a simple Michelson-Morley interferometer reads [36],

$$\Delta\phi = \frac{4\pi}{\lambda_L} h_0 L \sim 5 \times 10^{-11}\,, \tag{1.51}$$

where $\lambda_L \sim 1\mu m$ is the typical wavelength of the LIGO lasers and where we have taken $h_0 \sim 10^{-21}$. LIGO interferometers are supplemented by Fabry-Perot cavities which force to bounce each laser beam about 280 times before finally merge in the photodetector (illustrated as diffused red beams in Figure 1.7). This increases by about the same factor the estimated phase shift, being now about $\Delta\phi \sim 10^{-8}$. This phase resolution is achievable considering the current performance of the detectors although there still exist several noise contributions that may cause such phase shifts. These noise sources may even simulate the effect GW so it is essential to identify them to avoid any confusion. Each contribution affects the data in a different way depending on the frequency and added together define the sensitivity of the detector $S_n(f)$. They are usually classified as: shot noise, radiation pressure noise, seismic and Newtonian noise and thermal noise. Let us briefly describe the main features of each contribution:

- ***Shot noise.*** The shot noise comes from the quantum character of the light emitted by the laser. The averaged power emitted by a monochromatic laser is nothing more than the sum of the energy of each photon constituting the beam in a given observation time T such $P = 1/TNE_\gamma$, where N is the total number of photons arrived at T and E_γ its energy. The amount of power lost by the counting error is governed by a Poisson distribution which in the limit of high power lasers, i.e., large N, becomes a Gaussian process with $\Delta N = \sqrt{N}$, being $\Delta P/P \sim N^{-0.5}$. Thus, this contribution is reduced increasing the power the laser by re-injecting coherently the partially reflected light through the so called power recycling mirrors.

- ***Radiation pressure.*** The laser itself exerts an extra pressure over the mirrors that affects their position. Intuitively, the higher the power is, the higher the pressure will be. This effect could be easily compensated if the power of the laser were constant by applying the equivalent force in the opposite direction. However, we have seen that the power is described by a Gaussian process thus making fluctuate the pressure impinged to the mirrors. This generates a stochastic pressure that shakes the mirrors thus mimicking an eventual gravitational wave oscillation. This is tackled using squeezed light [37] to reduce the uncertainty in the phase at the cost of increasing the amplitude uncertainty (Heisenberg uncertainty principle).

– ***Seismic and Newtonian noise.*** LIGO detectors are ground based gravitational wave detectors that, inevitably, interact with the surrounding environment. This implies that any external "shake" produced by earthquakes, wind, human activities might affect the position of the mirrors and must be accounted for in the calibration. This type of noise sources affect the low frequency regime of the detector and it is one of the major unsolvable limitations of the ground based detectors, restricting the detections to sources that are, at least, above $\sim 10Hz$.

– ***Thermal noise.*** The inherent fluctuations of the atoms composing the mirrors and suspensions originate oscillations that must be estimated and reduced to a minimum level. It is the dominant source of noise and it is attenuated by materials with low mechanical dissipation factors that are actively monitored to reduce the oscillation of the suspensions.

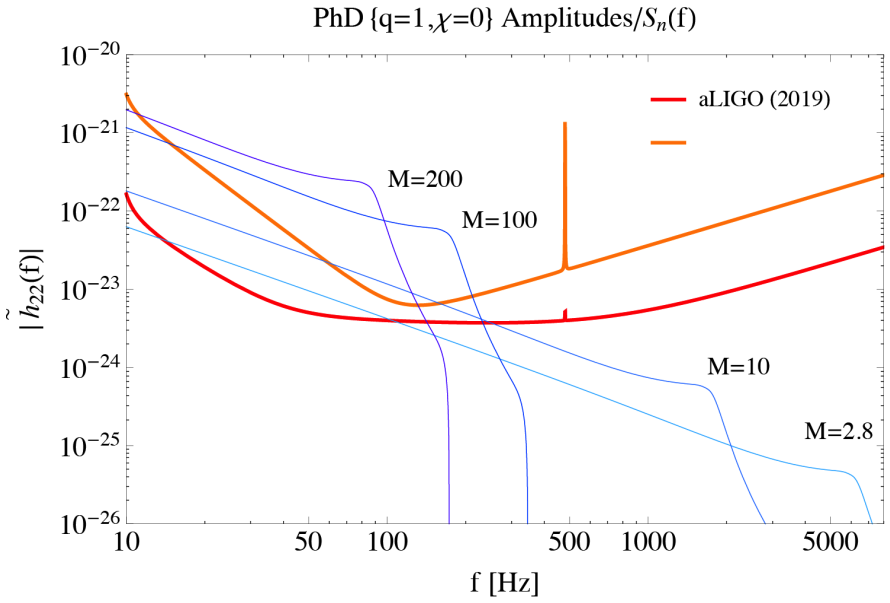

FIGURE 1.8: Illustration of some waveform amplitudes from a mass-ratio $q = 1$ non-spinning system located at a luminosity distance 1.4 Giga-light years superposed to the theoretical predictions of the $\sqrt{Sn(f)}$ for the initial advanced LIGO run (compatible with the first period of data acquisition) and the zero detuned detector scheduled for 2019. The waveforms have been computed with the so called PhenomD model [38, 39].

The combination of all the noise sources draw the current power spectral density $S_n(f)$ or sensitivity of the detector. In Figure 1.8 I illustrate the theoretical prescription of the noise curves in the advanced detector era tagged as aLIGO2015 and aLIGO2019 (upgraded version). They are expected to be dominantly sensitive from about $\sim 10Hz$ (seismic and Newtonian bound) to about a few kHz (shot noise). During the first observation run O1 both detectors achieved a sensitivity approximately equal to the theoretical predictions (orange curve in Figure 1.8) with the now well known results:

the detection of two gravitational waves from BBH systems. Furthermore, the detectors are scheduled to be upgraded in different phases until late 2019-2020 when they will optimally achieve the so called *zero detuned* configuration (red curve), extending the volume coverage to cosmological distances ($D_L \sim 2Gpc$).

1.4.3 Other interferometric detectors

Beyond LIGO, there exist current plans for adding more interferometric detectors to the net in a short time scale. These are:

- GEO-600 consists of two 600 m detector where the light passes twice thus making an effective distance of 1.2 km. Located in Hannover (Germany), it is the result of a collaboration between the United Kingdom and Germany. It is capable to observe GWs from $50Hz$ to $1.5kHz$. Its sensitivity can not compete with the advanced detectors, being more than one order of magnitude lower in the low frequency regime and what have made of GEO-600 a test bank for the technology later implemented in the LIGO-Virgo detectors. On September 18th 2015, it started taking data simultaneously with the LIGO detectors.

- Virgo is built in Cascina (Italy) as a french-italian collaboration. It consist in a $3km$ interferometer with a devising very similar to the LIGO detectors. It is also compatible with the same frequency range but, for the moment, with a bit less sensitivity. During the period 2007-2011, some coincidence runs were performed together with the two LIGO detectors before starting a long term upgrading phase. It is scheduled to join the LIGO detectors by the end of 2017 thus having for the first time the three advanced detectors taking coincident data.

- KAGRA (Kamioka Gravitational Wave Detector) is a project approved on 22 June 2010 for the construction of an underground interferometric detector with two arms, $3km$ long at Gifu (Japan). It uses the same state of art devising of the LIGO-Virgo detectors. The first initial operative phase (iKAGRA) started taking data on March 2016. The baseline design is expected to be online by 2018.

- IndIGO (LIGO-India) was announced on February 12th 2016 one day after the milestone announcement of the first GW observation by LIGO. The proposed detector is a Michelson Interferometer with Fabry-Perot cavities in two enhanced arms of $4km$ length aiming to be sensitive in the frequency range between 30 to $800Hz$. Its design is thought to be identical to that of LIGO detectors thus adding other detector to the net by 2020.

1.4.4 Third-generation ground-based gravitational wave detectors

The current LIGO detectors (status, science and devising) are known as the second-generation or advanced gravitational wave ground-based observatories. Although we can now carry out primary and innovative research on the GWs field, there exist some well known conceptual and devising limitations that constrain the science performance of the second-generation gravitational wave observatories.

One of the major limitations comes from the unavoidable low frequency noise that is generated by a combination of the seismic and thermal noises sources. This frequency regime agree with the frequencies predicted for high-mass and high-mass-ratio events thus making more difficult to separate them from the noise. This is directly translated as a loss of intermediate mass-ratio binary mergers (not yet observed) and an eventual first observation of an intermediate-mass stellar object ($\sim 100 M_{\odot}$). Related to the latter, a better performance of of the low frequency regime will increase the total SNR per observation thus allowing an improved description of the inspiral regime while increasing the physical horizon distance up to cosmological scales ($z \sim 10$) for events compatible with GW150914.

To circumvent these impediments there exist ongoing plans to go one step further in the ground-based gravitational wave astronomy: the Einstein Telescope (ET) [40, 41] and the Cosmic Explorer (CE) [42]. The ET is a design for an underground gravitational wave detector on a Sagnac configuration forming an equilateral triangle with three arms of $10km$ and with two detectors in each corner. It is expected to reduce the seismic and Newtonian noise influence on the data thus opening the GW spectra to the $\sim 1Hz$ astronomy. On the other hand the CE is a project for a $40km$ gravitational wave observatory conceived as the current LIGO-Virgo detectors. The in-band sensitivity may ranges from $10Hz$ to a few kHz. It will be dominantly limited by quantum noise in the high frequency regime and by the Newtonian noise for low frequencies. In figure Figure 1.9 we show the estimated sensitivity for both detectors compared to the current second-generation GW observatories and an eventual 20 reduced km version.

1.4.5 Space-based gravitational wave detectors: LISA mission

In Figures 1.8 and 1.9 is illustrated one the main impediments of the ground-based gravitational wave detectors: the potential growth of the noise when going to frequencies below the $10Hz$. As we mention in Sec. 1.3, it may exist a rich population of gravitational waves sources within a region centered about the mHz. Thus, this unsolvable limitation is inherently attached to the Earth and restricts significantly the sparsity of

the sources that can be detected on the ground. However, it is possible to overcome this issue by building a space-based interferometer: this is the main underlying idea of the LISA mission.

The LISA mission translates the idea of gravitational wave laser interferometry to space. One of the obvious gains, besides avoiding the seismic noise always present in the Earth, is that in space we can attain interferometric distances much larger than for ground-based interferometers. The mission plan is based on the idea using laser interferometry to monitor the position of free flying test masses in a triangular formation and separated 2.5 million km apart. This does not only allows to reach better sensitivities but also shifts the frequency range to the mHz gravitational wave astronomy thus matching the typical frequencies of EMRIS, IMBBH mergers, galactic binary inspirals (white-dwarf and neutron star binaries), cosmological stochastic background and also working as an alarm for the future LIGO-type mergers. All this challenging technology has been successfully tested by the LISA-pathfinder mission [43] which was conceived as a test mission to prove the technology devised for LISA. The LISA team has recently submitted a proposal in response to the ESA call for L3 mission concepts [28].

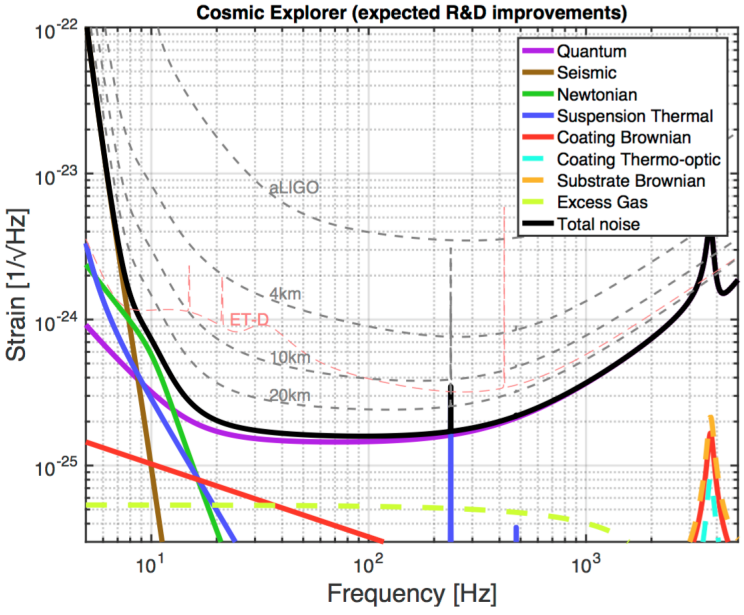

FIGURE 1.9: Figure from [42]. Target sensitivity for the ET and CE projects compared to the current LIGO-Virgo detectors. With these plans, the sensitivity will increase about factor of 10.

1.5 Prospects on gravitational waves astronomy

The groundbreaking GW discovery and the near future predictions about the new detectors and detections offer a unique way of observing our universe in a way never contemplated. Finally, we have (and have had) the opportunity of observing the high frequency range of the gravitational wave spectra and unveil the physics of some of the most powerful, energetic and catastrophic events of the cosmos (GW150914, GW151226, LVT151012). This new innovative science will be first tied to the performance of the operating ground-based gravitational wave detectors and then expanding its horizons thanks to progress in third-generation and space-based gravitational wave detectors. Then, some of the current open physics questions could be further clarified relying on the new GW band. I list below some of them.

Fundamental physics

1. *Is GR the correct theory of gravity?* The final stages of BBH mergers provide a direct window into the behavior of gravity in the strong field regime. While the two events already detected have been identified as compatible with BBH mergers, the SNR of the signal was not high enough to conclude much about the final ringdown, where, for instance, the area theorem and No-Hair theorem can be tested. With more detections we expect to place better constraints on the theory.

2. *How does matter behave under extreme conditions of density and pressure?* Neutron stars are rapidly rotating objects that can emit gravitational radiation through elastic deformations, magnetic deformations, unstable r-mode oscillations, and free precession. All these effects create different waveform patterns that give us information about the stellar interior thus relating them to the still unknown equation of state (EoS).

Astronomy and astrophysics

4. *How abundant and what are the formation channels of stellar-mass black holes?* An increased statistics will help us to constrain the masses and spins of the stellar-mass BHs thus generating the first observable distributions of these objects. Furthermore, as different formation channels predict different parameter distributions we could place better constraints to the stellar initial-mass function.

5. *Do intermediate-mass black hole exist?* One of the current unknowns in astrophysics is the existence of IMBHs ($M \sim 100 - 10^5 M_\odot$). Although there seems to be some evidence [44] there is no unambiguous electromagnetic detection yet.

6. *What is the origin of gamma-ray bursts?* Each LIGO candidate activates an alarm that is sent to the *partner telescopes* to observe large regions of the sky seeking for an electromagnetic counterpart matching the signal detected in the GW spectra. This includes eventual events involving matter as binary neutron star (BBH) mergers, being the latter one possible explanation for the gamma-ray bursts observed.

Cosmology

7. *How was the universe before the formation of the cosmic microwave background (CMB)?* Analogous to what happens with the CMB, there might exists a stochastic gravitational wave background originated from the combination of a large number of random and independent events. However, this spectra is expected to be placed much earlier ($10^{-36} - 10^{-32}s$) than the formation of the CMB layer thus having information of the first stages of the universe.

The first GW observations have only minimally filled a short band of the gravitational wave spectra. In the following years and thanks to theoretical and technological progress in GW wave detectors, we expect to slowly complete the GW spectra by adding the currently unexplored bands. Then, the GW astronomy will not only be an ideal complement of the EM spectra but a completely different way of studying many physical effects never observed in the EM range.

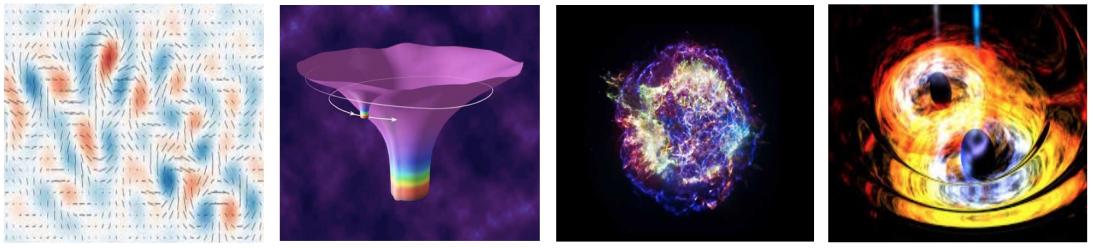

FIGURE 1.10: Artistic representation of some gravitational wave sources to be observed for the second and third generation gravitational wave observatories. From left to right: CMB, EMRI inspiral, SN explosion, BBH mergers. Credits: CalTech, Wikipedia, Scientific American, Physics World.

Chapter 2

Two body problem overview

The main topic of this thesis has been the numerical simulation and modelling of BBH systems, motivated by the recent GWs detections [3, 45] and future predictions [24]. These events will dominantly populate the ground-based GW spectra. To maximise the number of detections and getting an accurate estimate of the BBH physical parameters it is essential to work with the best possible gravitational representations. Current GW models go far beyond the simple example shown in Chapter 1, where we have deduced the GW strain at the zero-order or Newtonian limit. There actually exist analytic representations of the waveforms described by means of the PN and EOB formalisms that solve the dynamics to a much higher level of accuracy. These analytic approaches provide an accurate description of the inspiral and late-inspiral phase although they break down in the merger part of the evolution. In parallel, numerical relativity solutions gained a lot of popularity after the breakthrough in 2005 [46]. Based on the 3+1 formulation of the Einstein field equations, several codes and groups around the globe have succeeded in simulating about the last 20 orbits of the evolution of BBH systems thus becoming the most faithful representation of the physical waveforms [47]. On the contrary and beyond its proven success, the computation of the radiation using NR codes present a series of challenges that we must consider:

- NR simulations are computationally very expensive. A single and not particularly challenging simulation (nonprecessing with low mass-ratio and low spins), can take on the order 10^5 CPU hours. This becomes a strong limitation in order to populate sufficiently the parameter space and calibrate the waveform models.

- As a consequence of the high computational cost, we are constrained to short NR waveforms. The initial physical waveform frequency is usually larger than the corresponding lower frequency cuttoff ($\sim 10Hz$) of the ground-based detectors [48] for high-mass-ratio mergers. This limitation is addressed by building

hybrid waveforms that combine the known analytic results with the NR solutions (see Chapter 5). Generating much longer evolutions is then highly constrained by the performance of NR codes.

- NR waveforms are rather recent in the history of numerical relativity. Nowadays, there exist on the order of 1000 public BBH waveforms unequally distributed across the parameter space. Then, while some regions of the parameter space are quite well covered by the different NR codes, there exists a clear lack of data in high-mass-ratio, high-spin regimes. (see the parameter space plots of Chapter 4 and Chapter 5).

The latter points motivate the use of the two available waveform representations for an optimal modelling of the radiation: through analytic models which accurately describe the low-motion regime and NR codes that model the region where the analytic models fail in its description. Indeed, the combination of the analytic GR-based formulations with the NR results are the basis of the current analytic and semi-analytic Inspiral-Merger-Ringdown (IMR) models used in the template banks of the ground based detectors. In this section we summarise the main features of the formulations considered.

2.1 BBH physical parameters

Before detailing the main features of analytic and NR formulations, we first discuss the relevant physical parameters of standard BBH mergers. A BBH system refers to an object where two black holes are gravitationally bound and orbit each other. These objects emit energy in the form of GWs while the orbit shrinks to eventually merge. In particular, a non-charged black hole is univocally described by its total mass and the three spin components, popularly known as the No-Hair Theorem. Thus, we deal with a system of 8 source-based or intrinsic parameters $\Xi = \left\{m_1, m_2, \vec{S}_1, \vec{S}_2\right\}$, being m_i and $\vec{S}_i$ the masses and the spins of the two particles. For convenience and modelling purposes, they are normally recombined to finally read:

$$\Xi = \left\{M, \eta, \vec{S}_1, \vec{S}_2\right\} , \tag{2.1}$$

where now $M = m_1 + m_2$ is the total mass, $\eta = m_1 m_2/M^2$ is the symmetric mass-ratio. Here, the eccentricity of the orbit is not considered according to the standard astrophysical scenario for BBH LIGO-mergers[1]. Then, with these 8 parameters we can completely describe the evolution, fusion and further stabilization of a BBH system.

[1] At so high frequencies, most of the BBH systems are expected to be circularized by radiating away the eccentricity [49].

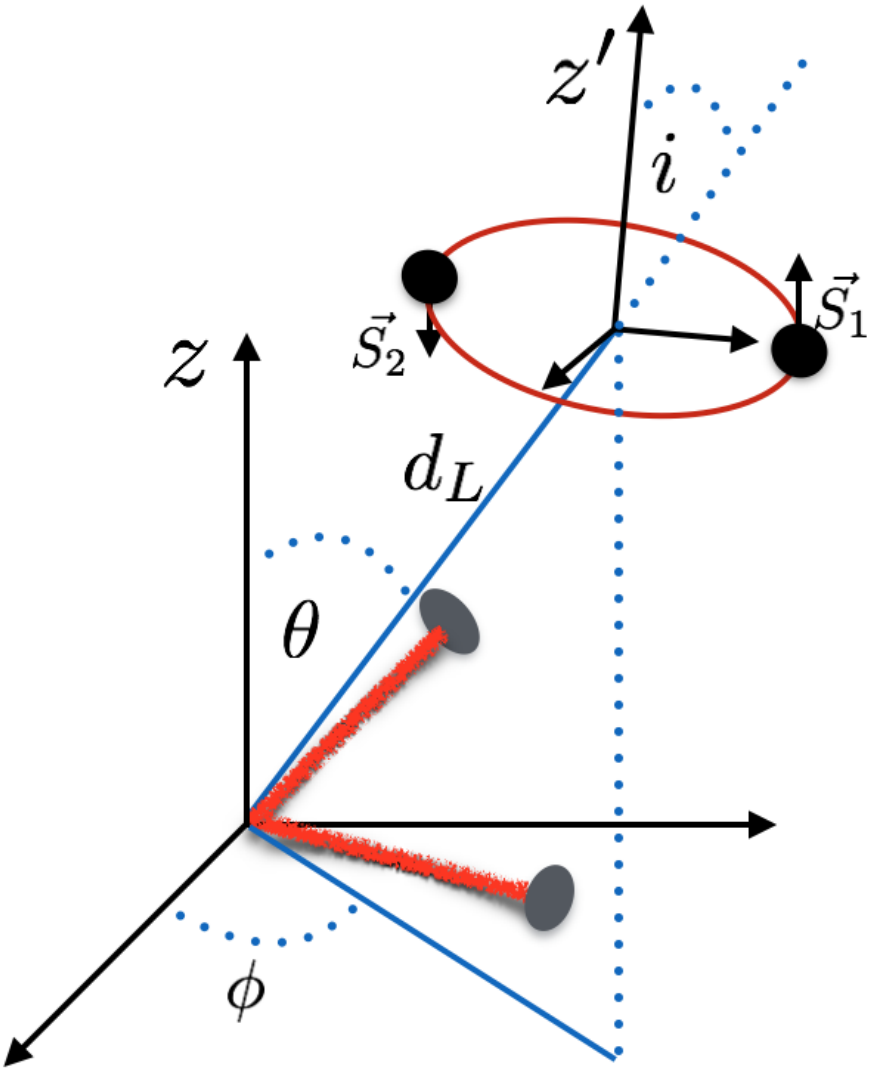

FIGURE 2.1: Representation of the reference frame of the detector (z axes) and its relation to the source frame (z' axes). The angles θ and ϕ locate the source on the sky while i provides the relative orientation of source frame with the line of sight.

The set formed by Ξ is complemented with an additional collection of 7 extra parameters which account for the angular position, polarization and distance to the source. They are known as the extrinsic parameters, namely:

$$\Lambda = \{d_L, \theta, \phi, \psi, i, t_0, \Phi_0\} \tag{2.2}$$

where d_L is the luminosity distance, θ is the polar angle, ϕ the azimuthal angle, ψ the polarization angle, i the inclination, t_0 the reference time and Φ_0 the reference phase (see Figure 2.1).

This way of splitting the parameter space is specially useful since the extrinsic parameters can be normally factored out as independent contributions of the GWs strain.

This property allow us to develop models only based on the intrinsic parameters where the contribution of the extrinsic parameters are trivially added to the models. In this thesis we have restricted our studies to nonprecessing systems meaning that from the initial 6 spin components we are left with only two components aligned with the orbital momentum $\vec{L}$ of the system. Moreover, the total mass acts as a simple scaling factor for the amplitude while it shifts the time and frequency evolution. Then, it is normally set as $M = m_1 + m_2 = 1$ thus not being relevant for the modelling of BBH mergers. Consequently, the physical parameter space that we want to synthetise is reduced to $\Xi = \{\eta, S_{1z}, S_{2z}\}$. In addition, as suggested by the PN results [20, 50–52] and confirmed by many previous studies of NR-calibrated models [38, 53, 54], the dominant parameter dependencies can be reduced to only two, being them the mass-ratio and some appropriate effective spin parameter S_{eff} that results from combination the individual spins of the binary. The phenomenological final state fits, the luminosity fit and the phenomenological models presented in Chapter 4 and Chapter 5 use this $\{\eta, S_{eff}\}$ parametrization. Similarly, the subdominant effects studied in this thesis are added by adding $\Delta\chi = \chi_1 - \chi_2$ corrections to our expressions where $\chi_i = S_i/m_i^2$.

2.2 Waveform anatomy

In this thesis, the targeted result of the BBH dynamics is the gravitational wave strain $h(t)$ (or $\tilde{h}(f)$ if we are in the frequency-domain) as well as other derived quantities as the final mass, final spin and peak luminosity. Indeed, $h(t)$ is the quantity measurable on ground-based GW detectors. As suggested throughout the text, analytic and numerical representations are not equally satisfactory in the modelling of the signal; while the slow-motion is well covered by the analytic models the strong GR regime must be represented by the NR solutions. The limits of the slow-motion regime, i.e., where NR is needed are not uniformly defined and may variate across the parameter space. However, even by eye inspection, we can identify three clear phases in the evolution: the inspiral (INward-Spiral) phase, the merger, and the ringdown. I describe below the basic features of these three regimes.

- Inspiral. It describes the quasi-adiabatic inward evolution towards the coalescense. It represents the far-zone zone solution where the two BHs are far from each other and orbit at low speeds. PN and EOB approximants enable us to represent accurately this evolution even when the speed is no longer *small* ($\sim 0.1c$). In Figure 2.2 the inspiral is framed in red and we see that both the amplitude and the frequency evolution increase smoothly.

- Merger. The merger frames the regime where the most strong GR effects are present. It covers the last orbits $\sim 2-3$ of the evolution although its exact placement is not defined in general. PN approximants breakdown at these stages and full GR is needed for an adequate description (see Sec. 2.4.1).

- Ringdown. The ringdown describes the regime right after the merger, where the two BHs have merged into a final object. Then, the system settles down to a stationary and equilibrium solution of the field equations where any distortion in its shape is radiated through GWs. They are emitted in a well known spectrum of exponentially decaying frequency modes, called the quasinormal modes (QNMs). Their solutions can be modeled analytically and any deviation from their predictions would imply a violation of the No-Hair Theorem. A clean characterization of the ringdown regime could allow us to explore whether other exotic objects could mimic the events observed by LIGO [55].

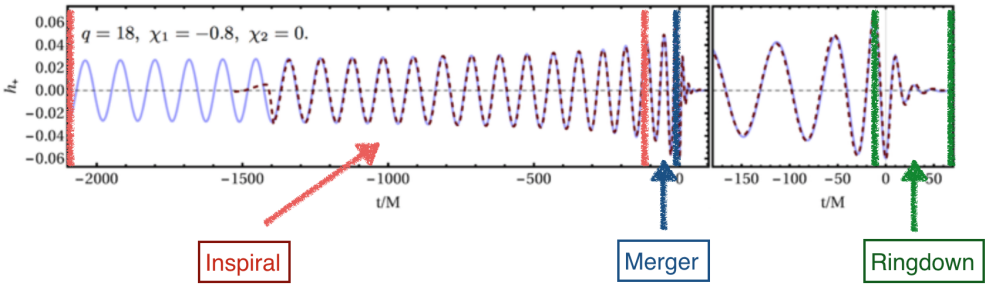

FIGURE 2.2: Time-domain representation of a mass-ratio $q = 18$ system with dimensionless spin $\chi_1 = -0.8$ (biggest BH) and $\chi_2 = 0$. We show the three different phases of the evolution. In the zoomed section we show the ringdown regime, where it is clear the amplitude decay. The modeling and further detection of the ringdown could help in the future to constrain and reject alternative gravity theories.

The three regimes together give name to the so called IMR waveforms [38, 56] which are currently employed as waveform templates for searches and parameter estimation in the LIGO waveform banks.

2.3 Analytic models

Fully analytic gravitational waveform models [19, 22] describe accurately the inspiral phase of the evolution of BBH mergers although they breakdown at the late inspiral and merger-ringdown. Despite this well known limitation, analytic models are still used for many purposes as for calibrating the early inspiral part of the NR calibrated models or as input data for solving the NR initial data. In parallel, NR calibrated models [38, 39, 56] provide a continuous solution on the physical parameter space of the two body problem

that covers the full waveform in both time and frequency domains. In this section we will provide a brief depiction of the main approaches to the two body problem: PN approximants and EOB solutions and phenomenological and EOB-NR models.

2.3.1 Post-Newtonian approximants

In Sec. 1.2.3.2 we have obtained the zero-order solution (Newtonian) of the gravitational waves generated by two point-like masses under the assumptions of weak field and slow motion. These assumptions are mathematically extended through an expansion of the equations of motion in terms of a truncation parameter $\epsilon \sim (v/c)^n$ where v is the speed of the system, c the speed of light and n the order of the PN expansion. In particular, post-Newtonian approximants solve the evolution of the orbital phase $\phi(t)$ by expanding it in terms of $(v/c)^n$, where $\Omega = \dot{\phi}(t)$ [57], namely

$$(\omega d)^2 = \frac{GM}{d} + \sum_n a_n \left(\frac{GM}{dc^2}\right)^n . \tag{2.3}$$

Equation (2.3) is nothing more than the generalization of the Kepler formula for a shrinking evolution, with GM/d the Keplerian orbital speed of the system.

Standard PN approximants solve the dynamics of the system considering quasi-circular and adiabatic orbits; the two bodies move at low speeds compared to the speed of light and the radial velocity is smaller than the tangential one (slowly shrinking). Indeed, (2.3) gives the corrected orbital evolution by means of the quadrupole approximation (1.45), where the orbital frequency satisfies $\Omega = 2\omega$ far from the merger. If higher than quadrupolar corrections are considered (higher modes) the strain can be expanded as,

$$h(t) = \sum_{l=2}^{\infty} \sum_{m=-l}^{l} h_{lm}(t, r)\, {}^2Y_{lm}(\theta, \phi) \tag{2.4}$$

where ${}^2Y_{lm}$ are the spin-two spherical harmonics. In this scenario the frequency evolution of the GWs does not scale so trivially and it results from the superposition of all the terms considered in (2.4). Moreover, each m contribution satisfies, at least in the early inspiral, that $\Omega_m = m\omega_m$ (see Chapter 4).

Equation (2.3) is computed from the total energy of the system E and the energy flux $\mathcal{L} = \frac{dE}{dt}$. The inherent ambiguity of GR in defining the energy of a system arises here. In Chapter 1 we obtained the GWs solution by inserting a linear perturbation to a flat background metric. We can do the same but not restricting the expansions just to linear terms but also considering higher order corrections to the flat metric [19]. Then, in order

to compute the orbital quantities we use:

$$\frac{dE}{dt} = \frac{dE}{dv}\frac{dv}{dt} = \mathcal{L}(v)\,, \quad M\omega = v^3\,, \quad \phi(t) = \int^t \omega dt'\,, \tag{2.5}$$

where v is the orbital speed of the system. The most up to date PN expansions to the energy E and the flux $\mathcal{L}$ are currently known up to v^7 order which translated to the PN nomenclature are the so-called 3.5PN approximants for nonprecessing models (the targeted systems of this work). Then, before giving the explicit expressions let us define some of the variables that appear in them[57]:

$$x = \left(\frac{GM\omega}{c^3}\right)^{2/3}, \qquad M = m_1 + m_2, \tag{2.6}$$

$$\delta M = m_1 - m_2, \qquad \nu = \mu/M = \frac{m_1 m_2}{M^2}, \tag{2.7}$$

$$\vec{S} \equiv \vec{S}_1 + \vec{S}_2, \qquad \vec{\Sigma} \equiv \left(\frac{\vec{S}_2}{m_2} - \frac{\vec{S}_1}{m_1}\right), \tag{2.8}$$

$$S_\ell = \vec{S}_{\hat{\ell}}, \qquad \Sigma_\ell = \Sigma_{\hat{\ell}}. \tag{2.9}$$

where, x is the variable used for the evolution. Then, the expressions for the energy $E(x)$ are [19, 57]:

$$\begin{aligned} E(x) = -\frac{\mu c^2 x}{2}\Bigg\{ & 1 + x\left(-\frac{3}{4} - \frac{1}{12}\nu\right) + x^2\left(-\frac{27}{8} + \frac{19}{8}\nu - \frac{1}{24}\nu^2\right) \\ & + x^{3/2}\left[\frac{14}{3}S_\ell + 2\frac{\delta M}{M}\Sigma_\ell\right] x^3\left(-\frac{675}{64} + \left[\frac{34445}{576} - \frac{205}{96}\pi^2\right]\nu - \frac{155}{96}\nu^2 - \frac{35}{5184}\nu^3\right) \\ & + x^{5/2}\left[\left(11 - \frac{61}{9}\nu\right)S_\ell + \frac{\delta M}{M}\left(b - \frac{10}{3}\nu\right)\Sigma_\ell\right] \\ & + x^{7/2}\left[\left(\frac{135}{4} - \frac{367}{4}\nu + \frac{29}{12}\nu^2\right)S_\ell + \frac{\delta M}{M}\left(\frac{27}{4} - 39\nu + \frac{5}{4}\nu^2\right)\Sigma_\ell\right]\Bigg\}. \end{aligned} \tag{2.10}$$

Note that $\omega \sim v^3$ and $x \sim v^2$, what clarifies the why of the name given to the PN expansion. Of particular note are the terms in S_ℓ and Σ_ℓ and their combinations. As we will see in Chapters 4 and 5 such terms and alternative combinations of them are used for defining the physical parameters of the phenomenological models. Finally, spin-spin corrections to (2.10) have been added in [20]. The corresponding expressions for the GWs flux DE/Dt can be found in Section (9.2) of [19, 57].

Then, there exist different strategies for computing ω and Ω in (2.5). Note that, in summary, one ends up with an equation for dv/dt that can be integrated to obtain $v(t)$. This can be immediately used for solving ω and Ω by means of:

$$\frac{dv}{dt} = \frac{\mathcal{L}(v)}{\frac{dE}{dv}}\,, \tag{2.11}$$

and where other related variables as the quasi-circular linear and angular momentum can be computed through $p_t = \mu v, L = r p_t$, where p_t is the tangential linear momentum. To obtain the radial contribution one has to account for the radiation reaction terms [19] which lead the shrinking of the orbit.

This way of proceeding gives name to the `TaylorT1` approximant [50, 58, 59]. In addition, (2.11) can be inverted in a way such we compute $(\frac{dE}{dv})/\mathcal{L}(v)$ up to 3.5PN order and then to find the corresponding equation for $t(v)$. This result can be directly replaced in the quantity $d\Omega/dv$ and then d compute the phase by analytic integration. This is the so called `TaylorT2` approximant (see [19] for explicit expressions). The `TaylorT3` approximant [60] is obtained from the expressions for `TaylorT2` by first inverting the Taylor expansion and inserting them into the `TaylorT2` phase. Finally, `TaylorT4` is obtained by re-expanding $\mathcal{L}(v)$ and truncating it at the 3.5PN order.

The different solutions for the angular frequency ω (that is trivially deduced from the phase) and the orbital speed v can now be replaced in the zeroth-order GWs solution (Chapter 1) to provide a much better and long-termed approximation to the physical solution while the zero-order amplitude factor is kept the same (which is true since the amplitude A satisfies $\dot{A}/A \ll \dot{\Omega}$):

$$h(t) = \frac{4M\eta v^2}{r} e^{-i(2\omega^{PN} t)} \tag{2.12}$$

although today this result is further improved by also considering higher-order corrections to the amplitude [61, 62].

Alternatively, we can also obtain the equivalent frequency-domain analytic expressions using the Stationary-Phase-Approximation (SPA) [36]. In this approximation, (2.12) is Fourier transformed taking advantage of the slow evolution of the amplitude and expands the phase around a fixed time t_f up to second order. These transformations define the `TaylorF2` approximant [19] which has been longer used in the calibration of the phenomenological IMR models (Sec. 2.3.3).

2.3.2 SEOBNR approximants

The EOB approximants [21, 22] map the dynamic of the two-body system onto an effective one body moving in a background space-time. They were initially proposed for solving equal-mass systems, pushing the PN expressions right up to the merger and where the ringdown is added from the results of perturbation theory. Although they are considered essentially more accurate than the PN prescriptions, they also get relevant deviations in the merger phase. Then, EOB models have given way to NR

calibrated models where the late PN coefficients are adjusted by fitting them to NR simulations; they are the so called `EOBNR` models. Nowadays there exist different versions of these models: `SEOBNRv2` [63], this being a 22 mode, spinning and nonprecessing model, `SEOBNRv3` [64] which also accounts for precession, `EOBNRv2HM` [65], a nonprecessing, non-spinning model including higher harmonics up to $l = 5$ and the latest version `SEOBNRv4` [66] which improves `SEOBNRv2` by increasing the number of the NR points and also including a calibration to the extreme-mass-ratio limit by means of Teukolsky waveforms [56].

In the EOB formalism the full dynamics is described by solving a coupled system of ordinary differential equations for each point of the parameter space. Then, time-domain solutions have to be translated to frequency-domain representations, for searches and parameter estimation purposes. Although this is still a much faster process than the full NR solution ($\sim$ CPU seconds versus 10^{5-6} CPU hours), they are still too slow for searches and parameter estimation studies, where hundreds of thousands of waveforms have to be generated. To resolve this, reduced basis methods or better known as reduced order models (ROM) [67] have been shown essential for its usage in the LIGO data.

2.3.3 Phenomenological waveform models

The alternative to EOB models is given by the phenomenological waveform models [38, 39, 53, 54, 68, 69]. They provide a closed form IMR representation of the quadrupolar strain in the frequency domain by fitting simple polynomial functions and whose coefficients are mapped to the physical parameter space by matching the known PN/EOB results to NR waveforms. Since the 2005 NR breakthrough [46], several versions of the models have been successfully calibrated in parallel to the growth of the BBH simulations field although only the last version presented in [38, 39, 70] is considered suitable for parameter estimation purposes. Here, we summarize the different versions of the phenom-based models:

- PhenomA [68]. Nonspinning phenomenological model calibrated to equal-mass waveforms generated with the CCATIE code [71] and a set of unequal-mass $0.16 \leq \eta \leq 0.25$ performed with the BAM code [72]
- PhenomB [53]. Extension of the PhenomA model to spinning binaries calibrated with NR waveforms contained in $[-0.75, 0.75]$ and mass-ratios in $[0.16, 0.25]$ performed with the LLAMA [73], CCATIE [71] and BAM [72] codes. The spin contribution is motivated by a PN effective parametrization such $\chi = (m_1\chi_1 + m_2\chi_2)/(m_1 + m_2)$.

- PhenomC [54]. Spinning model calibrated to an extended set of NR waveforms contained in $[-0.85, 0.85]$ and mass-ratios in $[0.16, 0.25]$ performed with the LLAMA [73], CCATIE [71], BAM [72] and SPEC [74] codes. The PN model is taken from the TaylorF2 [50, 75] phase and the 3PN amplitude [61, 62] where the late inspiral is also fitted to NR. The spin contribution is fitted by the same effective spin parameter χ as in PhenomB.

- PhenomP [69]. Precessing phenomenological model based on the *twisted* version of the PhenomC and where the spin-precessing effects are fitted by the leading order effective spin contribution called χ_p. An upgraded version based on PhenomD has been used in the first detections for parameter estimation (PE) .

- PhenomD [38, 39]. Latest version of the non-precessing equal-spin version of the phenomenological models. This model extends the calibration region to mass-ratio $q = 18$ and individual spins $\chi_i \in [-0.85, 0.85]$ with an upgraded ansatz build on the phase derivative. It is the reference model of this work. Its formulation is given in detail in Chapter 5.

2.4 Numerical relativity models

Phenomenological models and `EOBNR` models rely on NR solutions of the Einstein field equations. As we have illustrated in the introduction, these form a set of 10 coupled, non-linear, second-order partial differential equations for the four-dimensional metric tensor $g_{\mu\nu}$ represented by (1.19). These equations are written in a fully covariant way thus making no clear distinction between time and spatial coordinates. While this is quite natural from the point of view of differential geometry we are intuitively accustomed to solve the dynamics of physical systems by taking time derivatives of our quantities to study its evolution in time. For instance, we could be interested in finding the future state of a BBH system given some physical configuration and initial data, tracking its orbit and dynamics. This inherently lead us to express the equations with time derivatives on the left hand side and some other arbitrary source terms on the right hand side thus labeling in a different way the *time* and *spatial* coordinates and which motivates the idea of the space-time foliation with three spatial and one time components (3+1). In this section, we briefly discuss the main points of *3+1* ADM decomposition and we will relate them with the BBH solutions. Here we outline the main derivations of [14, 76].

2.4.1 ADM 3+1 formalism

The study of the time evolution of a given physical system is commonly formulated as a Cauchy problem: given a system of dynamical equations and some adequate initial data, the fundamental equations must uniquely predict the past and future evolution of the system. Here, we first want to split (1.19) into a system of dynamical equations where the coordinates take the usual conception of space and time. Then, consider a four-dimensional manifold M, decomposed in three-dimensional Σ_t space-like surfaces (slices), being the parameter t an scalar field that connects two immediately consecutive space-like slices (see Figure 2.3). Notice that t does not necessarily coincides with the proper time of any particular observer but represents a general time function. The

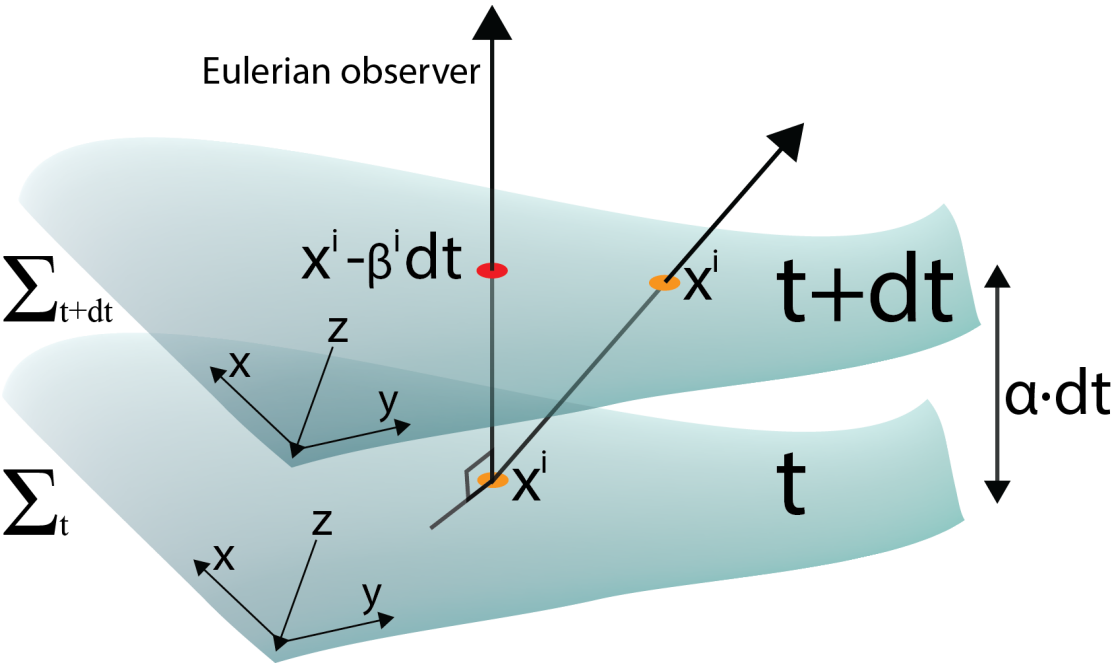

FIGURE 2.3: Example of space-time foliation of the space-like surfaces Σ given the time parameter t and the *lapse* and *shift* vector definitions.

geometry contained between two adjacent surfaces is described by the space-time metric which, in the most general form, can divided in the following components:

- **three-dimensional spatial metric** $\gamma_{ij}(t, x^i)$ with (i=1,2,3). It is the induced metric on a given space-like slice Σ and it defines the line element on the slice considered. It is used for raising and lowering indices on the slice,

$$dl^2 = \gamma_{ij} dx^i dx^j \tag{2.13}$$

- **Lapse function** $\alpha(t, x^i)$. It accounts for the time *elapsed* when one travels from Σ_t to Σ_{t+dt} for Eulerian observers (these moving along the normal vector $\vec{n}$ to the

surface). It directly relates the time coordinate t with the proper time τ.

$$d\tau^2 = \alpha(t, x^i)dt^2 \tag{2.14}$$

- **Shift vector** $\beta(t, x^i)$. It defines the relative velocity of the Eulerian observers with the lines of constant spatial coordinates. The particular case of $\beta(t, x^i) = 0$ defines the so called adapted coordinates (Eulerian observers).

$$x^i_{t+dt} = x^i_t - \beta^i(t, x^i)dt \tag{2.15}$$

The α and β functions can be specified freely. Different choices of these quantities will define different foliations of our space-time, thus fixing how different observers move on a given space-time. Indeed, since we are not restricted to any particular choice (it appears again the general covariance of GR), we have the freedom of defining a completely different representation of our space-time: they are just gauge dependent functions of our space-time. Then, combining the elements of Equations (2.13) to (2.15) it is possible to define a general four-dimensional space-time metric such that,

$$ds^2 = (-\alpha^2 + \beta_i\beta^i)dt^2 + 2\beta_i dt dx^i + \gamma_{ij}dx^i dx^j \,. \tag{2.16}$$

A natural way of describing the intrinsic geometry of a given hypersurface is through the gradient of its unit normal vector $\nabla\vec{n}$. Since our slicing is fixed by hypersufaces at t, the normal vector is given by the gradient $\nabla_\mu t$. It is easy to show that $\vec{n}$ takes the following form in these coordinates:

$$n_\mu = (-\alpha, 0) \qquad n^\mu = \left(1/\alpha, -\beta^i/\alpha\right) \,. \tag{2.17}$$

where n^μ has been normalised such $n^\mu n_\mu = -1$ while the sign convention is chosen such n^μ points to future. The variation of the normal vector $\vec{n}$ along a given surface Σ_t gives a sense of its three-dimensional shape and it is related to so called extrinsic curvature tensor $K_{\mu\nu}$. Mathematically, it is defined either by the projecting the $\nabla_\nu n_\mu$ or by means of the Lie derivative of the induced metric along the field of unit vectors $\vec{n}$:

$$K_{\mu\nu} = -P^\alpha_\mu \nabla_\alpha n_\nu \tag{2.18}$$

$$\pounds_{\vec{n}}(\gamma_{\mu\nu}) = \nabla_\mu n_\nu + n_\mu n^\alpha \nabla_\alpha n_\nu = -\frac{1}{2}K_{\mu\nu} \tag{2.19}$$

where $P^\mu_\nu := \delta^\mu_\nu + n^\mu n_\nu$ defines the projection operator onto spatial hypersurfaces and $n^\mu K_{\mu\nu} = 0$ ($K_{\mu\nu}$ is a purely spatial tensor). Notice that $K_{\mu\nu}$ only depends on how we move $\vec{n}$ within a given Σ_t thus being a geometrical property of the slice itself. Equation (2.18) is not only restricted to the propagation of observers along the normal vector $\vec{n}$

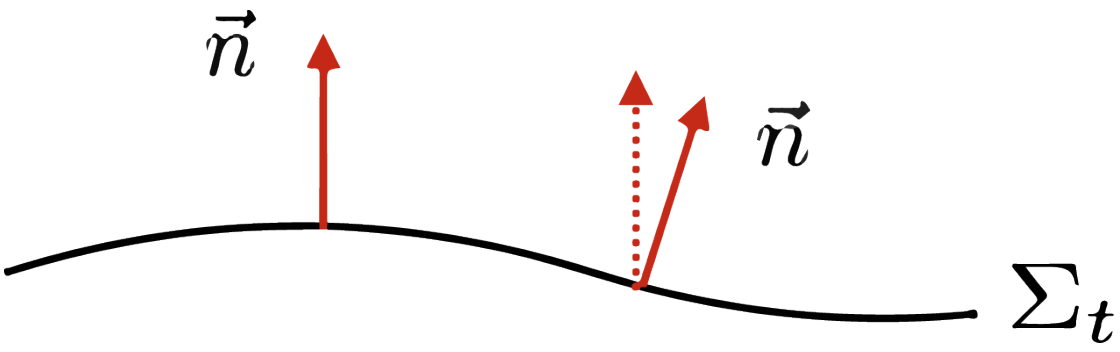

FIGURE 2.4: Representation of the normal vector $\vec{n}$ parallel transported into some specific Σ_t. Its variation draws intuitively the geometry of the slice considered.

(Eulerian observers). We can define any arbitrary time vector as

$$t^\mu \equiv \alpha n^\mu + \beta^\mu \,, \tag{2.20}$$

where t^μ defines the lines of constant spatial coordinates (see Figure 2.3). Since $\vec{n}$ is normal to Σ_t it satisfies for any scalar function,

$$\pounds_{\vec{n}}(\gamma_{\mu\nu}) = \frac{1}{\alpha}\pounds_{\alpha\vec{n}}(\gamma_{\mu\nu}) \,, \tag{2.21}$$

which implies,

$$\frac{1}{\alpha}\left(\partial_t - \pounds_{\vec{\beta}}\right)\gamma_{ij} = -2K_{ij} \tag{2.22}$$

and where we have used that in the adapted coordinates $\pounds_{\vec{t}} = \partial_t$.

2.4.2 Space-time 3+1 field equations

In the previous section we have obtained the evolution equation for the three-dimensional metric γ_{ij} from purely geometric concepts. To close the evolution system, we require the analogous equation for the extrinsic curvature K_{ij}. Although this is normally shown by considering the contractions of the normal vector $\vec{n}$ with the projector operator P^μ_ν, it can also be obtained by propagating the $3+1$ decomposition through the Einstein field equations (1.19). To do so and to illustrate the calculations, we use here the adapted coordinates, i.e., with $\beta^i = 0$ recalling that the essential modification with respect the general foliation of (2.16) concerns the time derivatives such,

$$\frac{1}{\alpha}\partial_t \to \frac{1}{\alpha}\left(\partial_t - \pounds_{\vec{\beta}}\right) \,, \tag{2.23}$$

as we have seen in (2.22). With this consideration and from the $3+1$ metric tensor defined in (2.16), it is possible to obtain the relations for the Christoffel symbols listed in Table 2.1.

$\Gamma^0_{00} = \partial_t \log \alpha$	$\Gamma^k_{00} = \alpha\gamma^{kj}\partial_j \alpha$
$\Gamma^0_{i0} = \partial_t \log \alpha$	$\Gamma^k_{i0} = -\alpha\gamma^{kj}K_{ij}$
$\Gamma^0_{ij} = -1/\alpha K_{ij}$	$\Gamma^k_{ij} = \hat{\Gamma}^k_{ij}$

TABLE 2.1: $3+1$ decomposition of the four-dimensional Christoffel symbols as in [14]. $\hat{\Gamma}^k_{ij}$ stands for the connection coefficients of the induced three-dimensional metric γ_{ij}.

Now, we apply an equivalent transformation to the energy-momentum tensor $T_{\mu\nu}$. Then, analogously to what we do in the special case of a flat space-time (special relativity), we identify three independent contributions:

- **The energy density**

$$\rho = T^{\mu\nu} n_\mu n_\mu \,, \tag{2.24}$$

- **The momentum density**

$$S_i = -T^\mu_i n_\mu \,, \tag{2.25}$$

- **The stress tensor**

$$S_{ij} = T_{ij} \,, \tag{2.26}$$

that correspond to the decomposition of $T_{\mu\nu}$ into parts that are either longitudinal with n_μ (ρ), tranverse (T_{ij}) or of mixed type ($T^\mu_i n_\mu$). Taking the relations obtained in Table 2.1 (see [14] for a detailed description) and inserting them in the Einstein field equations one finds the corresponding evolution equation for the extrinsic curvature K_{ij} that reads,

$$(\partial_t - \pounds_\beta)\,\gamma_{ij} = -2K_{ij} \,, \tag{2.27}$$

$$(\partial_t - \pounds_\beta)\,K_{ij} = \nabla_i\nabla_j\alpha + \alpha\left[R_{ij} + KK_{ij} - 2K_{ik}K^{kj}\right] \tag{2.28}$$

$$- 8\pi\alpha\left[S_{ij} - \frac{1}{2}\,(S-\rho)\,\gamma_{ij}\right] \,, \tag{2.29}$$

where we have rewritten (2.22) and we have applied (2.23). Doing the same with the mixed ($0i$) and (00) components we get the constraint equations,

$$\mathcal{H} \equiv \frac{1}{2}\left[R + K^2 - K_{ij}K^{ij}\right] - 8\pi\rho = 0 \,, \tag{2.30}$$

$$\mathcal{M}_i \equiv \nabla_j\left(K^j_i - K\delta^j_i\right) - 8\pi S_i = 0 \,. \tag{2.31}$$

The system of equations presented here gives all the ingredients to evolve any four-dimensional space-time given some *sane* initial conditions similarly to how the Maxwell equations are solved. However, Equations (2.27) to (2.31) do not form a well-posed evolution system, i.e., that the solution exists, it is unique and it changes continuosly with the initial conditions. One has to find a reformulation of the ADM equations to get

the well-posedness of the system of equations. For BBH hole evolutions this is addressed using two significantly different frameworks: based on the generalized harmonic gauge formulation [77–79] and on the BSSNOK conformal compactification [80–83]. Since the work of Pretorius [46], and based on these two strategies, several groups and codes around the world have succeeded in simulating gravitational waves from BBH mergers and that has resulted in the creation of several public waveform catalogues [6, 84, 85]. I review here the BSSNOK formulation since is the basis of the `BAM` code, used in this thesis for the performance of the nonprecessing, unequal-spin BBH simulations.

2.4.3 The BSSNOK formulation

In the late 80's and well into the 90's, first Nakamura, Oohara and Kojima [80, 81] and after Baumgarte, Shibata and Nakamura [82, 83] presented a novel formulation of the ADM equations based on two main modification of these equations: by a conformal transformation of the spatial metric and the introduction of a new evolution variable referred as $\tilde{\Gamma}^i$. The new reformulation exhibited far more stability than the old ADM equations [83]. Today, it is known as the BSSNOK formulation of the $3+1$ Einstein field equations. We show here some of the key points.

Consider the following conformal rescaling of the spatial metric:

$$\tilde{\gamma}_{ij} \equiv \psi^{-4}\gamma_{ij}, \tag{2.32}$$

where ψ is a positive scalar function called conformal factor. The conformal metric is chosen to has unit determinant $\tilde{\gamma} = 1$ not only on the initial slice, but also during the evolution. Although this choice is specially suitable in Cartesian coordinates some recent work by [86, 87] shows how to translate this condition to more general coordinate systems. This provides the following relation between the conformal factor ψ and the three-spatial metric determinant γ:

$$\psi = \gamma^{1/12}\,. \tag{2.33}$$

In addition, the extrinsic curvature is separated into its trace and its tracefree part thus defining:

$$A_{ij} = K_{ij} - \frac{1}{3}\gamma^{ij}K \quad , \quad \tilde{A}_{ij} = \psi^{-4}A_{ij}\,, \tag{2.34}$$

where one also rescales the traceless tensor A_{ij} with an appropriate power of ψ. As mentioned before, a crucial point on the BSSNOK formalism is the introduction of the

auxiliary conformal connection function defined by:

$$\tilde{\Gamma}^i := \tilde{\gamma}^{jk}\tilde{\Gamma}^i_{jk} = -\partial_j\tilde{\gamma}^{ij}, \tag{2.35}$$

where $\tilde{\Gamma}^i_{jk}$ are the Christoffel symbols of the conformal metric. This spatial gauge condition is specially suitable to eliminate the mixed second derivatives that would appear in the evolution equations in its absence. Since $\tilde{\Gamma}^i$ is evolved independently, (2.35) might be seen as an additional constraint equation. Then, we want to re-express now the set of ADM evolution Equations (2.27) to (2.29) in terms of the new conformal metric and the new connection gauge. Now, the system of equations takes the following form:

$$\partial_0\tilde{\gamma}_{ij} = -2\alpha\tilde{A}_{ij}, \tag{2.36}$$

$$\partial_0\phi = \frac{1}{6}\alpha K, \tag{2.37}$$

$$\partial_0\tilde{A}_{ij} = e^{-4\phi}\left(\alpha R_{ij} - D_iD_j\alpha\right)^{\mathrm{TF}} + \alpha\left(K\,\tilde{A}_{ij} - 2\tilde{A}_i{}^m\tilde{A}_{mj}\right), \tag{2.38}$$

$$\partial_t K = -D^iD_i\alpha + \alpha\left(\tilde{A}^{mn}\tilde{A}_{mn} + \frac{1}{3}K^2\right), \tag{2.39}$$

$$\begin{aligned}\partial_t\tilde{\Gamma}^i = {}& \tilde{\gamma}^{jk}\partial_j\partial_k\beta^i + \frac{1}{3}\gamma^{ij}\partial_j\partial_k\beta^k + \beta^j\partial_j\tilde{\Gamma}^i - \tilde{\Gamma}^j\partial_j\beta^j \\ & - 2\left(\alpha\partial_j\tilde{A^{ij}} + A^{ij}\tilde{\partial}_j\alpha\right),\end{aligned} \tag{2.40}$$

where $\partial_0 = \partial_t - \pounds_{\vec{\beta}}$, D_i is the covariant derivative associated to the spatial metric γ_{ij}, "TF" denotes the trace-free part and where we have defined $\phi = \log\psi = 1/12\,\log\gamma$. Now, instead of the 12 variables of the ADM evolution Equations (2.27) to (2.29), we count now in total 17: ϕ, K, $\tilde{\gamma}^{jk}$,$\tilde{A}_{ij}$ and $\tilde{\Gamma}_i$. Then, recalling that $\tilde{A} = 0$ and $\tilde{\gamma} = 1$, these variables get reduced to 15 independent ones. On the other hand, the Lie derivatives with respect to the shift vector are given by:

$$\pounds_{\vec{\beta}}\phi = \beta^k\partial_k\phi + \frac{1}{6}\partial_k\beta^k \tag{2.41}$$

$$\pounds_{\vec{\beta}}\tilde{\gamma_{ij}} = \beta^k\partial_k\tilde{\gamma_{ij}} + \tilde{\gamma_{ik}}\partial_j\beta^k + \tilde{\gamma_{jk}}\partial_i\beta^k - \frac{2}{3}\tilde{\gamma_{ik}}\partial_k\beta^k \tag{2.42}$$

$$\pounds_{\vec{\beta}}\tilde{A_{ij}} = \beta^k\partial_k\tilde{A_{ij}} + \tilde{A_{ik}}\partial_j\beta^k + \tilde{A_{jk}}\partial_i\beta^k - \frac{2}{3}\tilde{A_{ik}}\partial_k\beta^k \tag{2.43}$$

The conformal transformation and the splitting of the extrinsic curvature tensor in into its trace and trace-free components provide a better control over the slicing conditions α and β^i. However, the system of Equations (2.36) to (2.40) is still not stable by itself for long term simulations. We have to propagate the conformal transformation through the ADM constraint Equations (2.30) to (2.31). Indeed, (2.30) has already been considered in (2.39) to eliminate the Ricci scalar R. Now, we are left with the momentum constraint

(2.31) which takes the following form in the new variables:

$$\partial_j \tilde{A}^{ij} = -\tilde{\Gamma}^i_{jk}\tilde{A}^{jk} - 6\tilde{A}^{ij}\partial_j\phi + \frac{2}{3}\tilde{\gamma^{ij}}\partial_j K \tag{2.44}$$

Then, we replace the terms $\partial_j \tilde{A}^{ij}$ in (2.40) to get the following evolution equation for $\tilde{\Gamma}^i$:

$$\begin{aligned}\partial_t \tilde{\Gamma}^i = \quad & \beta^m\partial_m\tilde{\Gamma}^i - \tilde{\Gamma}^m\partial_m\beta^i + \frac{2}{3}\tilde{\Gamma}^i\partial_m\beta^m + 2\alpha\tilde{\Gamma}^i_{mn}\tilde{A}^{mn} + \frac{1}{3}\tilde{\gamma}^{im}\partial_m\partial_n\beta^n \\ & + \tilde{\gamma}^{mn}\partial_m\partial_n\beta^i - \frac{4}{3}\alpha\tilde{\gamma}^{im}\partial_m K + 2\tilde{A}^{im}\left(6\alpha\partial_m\phi - \partial_m\alpha\right) ,\end{aligned} \tag{2.45}$$

Finally, the complete system of evolution equations is given by Equations (2.36) to (2.45). However, it is worth to notice that the crucial piece in this formulation is the replacement of the momentum constraints directly in the evolution equations. The subsequent system of equations is known to be much more stable [83] than the original York-ADM equations. Indeed, Equations (2.36) to (2.45) are the most widely used representation of the Einstein 3+1 evolution equations of space-times with and without matter. In this work, the BBH data of three (`BAM`,`LAZEV`,`MAYA`) of the four NR codes used has been computed using the BSSNOK formulation.

Chapter 3

Simulations of BBH systems with the BAM code

In this chapter we present the numerical set up, evolution and final post-processing of a set of 23 NR simulations performed during the realization of this thesis project with the `BAM` code. These simulations have been selectively used for the formulation of new and enhanced fits for the final spin, energy radiated and peak luminosity paying special attention to the calibration of unequal-spin effects and the extreme mass-ratio limit (Chapter 4). These results are also expected to be a key ingredient for the ongoing upgrade of the PhenomD model [38, 39] to a three parameter model (Chapter 5) lead by the UIB group [88]. To this end, we have also complemented our data set with several public resources as the SXS [4, 89], GaTech [6, 90] and RIT [5, 85, 91, 92] public catalogues. Finally, an extra set of 38 extreme mass-ratio waveforms [93–95] have been used for the calibration of the extreme-mass-ratio limit in the peak luminosity fit.

3.1 The BAM code

The BAM code evolves the 3+1 decomposed Einstein field equations using the BSSNOK formulation introduced in the previous chapter and in the framework of the *moving puncture*. Then, the 2-black-hole initial data is modeled by adopting the Brill-Linquist wormhole topology [96] (see also Sec. 3.1) with 2+1 asymptotically flat ends for the initial geometry. The asymptotically flat ends are compactified and identified as r_i coordinate singularities which are referred to as the punctures (i labels the number of BHs on my initial data). This puncture view representation of the initial slice is particularly useful since it associates masses, momenta and spins with any number of black holes.

The BSSNOK variables (Sec. 2.4.3) are evolved as a partially constrained scheme, where the algebraic constraints $\det(g) = 1$ and $\mathrm{Tr}(A_{ij}) = 0$ are enforced at every intermediate time step to ensure the strong hyperbolicity of the evolution. Then, to close the system of evolution equations (Equations (2.36) to (2.45)), we are left to define the evolution equations for the gauge variables. In `BAM`, the lapse and shift are evolved though the *1+ log* [97] and *gamma-freezing* conditions [71] respectively thus,

$$\partial_0 \alpha = -2\alpha K \quad , \quad \partial_0 \beta^i = \frac{3}{4} B^i \quad , \quad \partial_0 B^i = \partial_t \tilde{\Gamma}^i - \eta B^i, \tag{3.1}$$

where $\partial_0 = \partial_t - \zeta \beta^m \partial_m$ and B^i is an auxiliary vector that has been shown particularly suitable to avoid having a perturbation in the constraints that persists at the initial location of the punctures [76].

There still remains some freedom in the choice of the conformal factor (Sec. 3.1). In `BAM`, it is usually chosen to evolve the variable $\chi = \psi^{-4}$ [98] (see (2.37)) instead of $\phi = \log \psi$ [99] (although some tests have been also performed with ϕ). This transformation involves that initially χ is $O(r^4)$ when ψ has the usual pole at the puncture $1/r$ thus replacing the singular structure of the black hole by a vanishing χ. Then, (2.37) takes the following [98],

$$\partial_0 \chi = \frac{2}{3} \chi (\alpha K - \partial_\alpha \beta^\alpha) + \beta^i \partial_i \chi, \tag{3.2}$$

This transformation allows to avoid excision and establishes a simple way of tracking the position of the punctures. Using the chain rule and recalling that $\chi = 0$ at the punctures one finds

$$\partial_t (\vec{x}_{punc}) = -\vec{\beta}(\vec{x}), \tag{3.3}$$

which gives name to the *moving puncture* framework.

Initial data and black hole parameters

To evolve the BSSNOK system of Equations ((2.30) to (2.45)) together with the gauge evolution Equations (3.1), we first need some initial conditions for all the set of equations. This means that we have to find a time-zero solution (initial data) for the 12 components of the spatial metric γ_{ij} and the extrinsic curvature K_{ij} together with some suitable initial values for the lapse α and the shift vector β^i.

In the `BAM` code the initial data is solved taking advantage of the York-Lichnerowicz conformal decomposition [100–102] that starts with a conformal transformation of the metric given by:

$$\gamma_{ij} = \psi^4 \bar{\gamma}_{ij} \,, \tag{3.4}$$

where to avoid any confusion with the BSSNOK conformal decomposition we represent the new metric with a *bar*. Initially, it is chosen a conformally flat three-dimensional metric with $\bar{\gamma}_{ij} = \delta_{ij}$ and a maximal slicing condition given $K = 0$. Then, it is possible to find an analytic expression for K_{ij} given by vectors with a relevant physical meaning (see Chapter 3 of [76]),

$$K^{ij} = \psi^2 \frac{3}{2r^2}\left[n_i P_j + n_j P_i + n_k P^k (n_i n_j - \delta_{ij})\right] - \frac{3}{r^3}(\epsilon_{ilk} n_j + \epsilon_{jlk} n_i) n^l S^k \,, \tag{3.5}$$

where n^i is the unit outward-pointing radial vector and where P^i and S^i can be indetified with the ADM linear momentum and the spin of the punctures. Equation (3.5) is known as the Bowen-York extrinsic curvature [103, 104].

Usually in BBH evolutions, the initial physical parameters of (3.5) are chosen by means of the quasi-circular 3.5PN and EOB predictions for the initial momenta and spins (Chapter 2). In particular, we freely select some spin configuration as well as some initial distance D_0 that defines the initial separation of the punctures. Then, the quasi-circular assumption involves that we can get $P_i = f(D_0, S^i)$ thus completing the definition of K^{ij}. Equation (3.5) is the usual definition of the initial extrinsic curvature for the puncture codes (`BAM`,`LAZEV`,`MAYA`) used in this thesis. It is also worth to notice that the ADM-TT coordinate gauge used to define the PN dynamics and the effective coordinates [22] used in EOB prescriptions is different although very close to the conformally flat gauge used for solving the initial data, getting this match better as the separation D_0 increases. Relatively small deviations of $\approx 1\%$ in the PN-EOB predictions result in the appearance of a residual eccentricity that we remove following the recipe described in Sec. 3.4.

Once the solution for K_{ij} is known, we are left to find a solution for the conformal factor ψ to finally obtain the physical three-dimensional metric γ_{ij}. This equation is given by the Hamiltonian constraint (2.30) that, after the conformal transformation of (3.4), reads:

$$8\bar{D}^2\psi - \bar{R}\psi + \psi^5\left(K_{ij}K^{ij} - K^2\right) = 0 \,, \tag{3.6}$$

where $\bar{D}^2$ and $\bar{R}$ are the Laplace operator and the Ricci scalar for the metric $\bar{\gamma}_{ij}$. Notice that by means of (3.5) we already have all the ingredients for solving (3.6). However, before attacking this solution let us try to pose the simplest case of a time-symmetric initial data problem with $\bar{R} = 0$. In this scenario we are left to solve a Laplace equation for a conformally flat metric, $D^2\psi = 0$. One of the possible solutions to this equation is given by $\psi = 1 + m/2r$ where m is the *bare* mass and that can be related to the mass of the puncture, i.e., recovering the Schwarzschild solution. Indeed, the Laplace equation

admits a solution given by a superposition of punctures, namely,

$$\psi = 1 + \sum_{i=1}^{N} \frac{m_i}{2|\vec{r} - \vec{r}_i|} = 1 + \psi_{BL} \,. \tag{3.7}$$

The latter is the so called Brill-Linquist initial data [96], and for binary black hole evolutions $N = 2$. The solution for a general case where the punctures have both linear momentum and spin is based on a Brill-Linquist solution but also accounting for the source terms and remnant interaction. This is synthesised by $\psi = \psi_{BL} + u$, presented in [105] and gives name to the so called *puncture* formalism. Then, the Hamiltonian constraint is solved for u and it reads,

$$\bar{D}^2 u + \frac{1}{8\psi_{BL}^7} \bar{A}_{ij} \bar{A}^{ij} = 0 \,, \tag{3.8}$$

where $\bar{A}_{ij} = \psi^2 K_{ij}$ and recalling that $\bar{\gamma}_{ij} = \delta_{ij}$ ($\bar{R} = 0$) and $K = 0$. The key feature of the puncture method concerns the fact that we do not need special boundary conditions close to the punctures. In this regime we find that $\psi_{BL} \sim 1/r$ while $\bar{A}_{ij}\bar{A}^{ij} \sim 1/r^6$ thus removing any divergence in (3.8).

To complete the definition of the initial conditions we need to specify some initial values for the gauge variables α and β^i. In `BAM`, it is chosen initially a pre-collapsed lapse $\alpha = \psi_{BL}^{-2}$ (that makes $\alpha = 0$ at the punctures) and $\beta^i = 0$.

An interesting consequence of BL initial data is that it represents a dynamical scenario that evolves towards the Kerr solution but being different from it initially. Moreover, it is known that the Kerr space-time can not be represented by Bowen-York initial data [106]. This incompatibility leads to an initial space-time that may be seen as the expected Kerr geometry plus a residual content on gravitational waves. Then, the extra energy content is radiated away in a short time, hence, taking energy out from the system. This ejection is the so called *junk radiation* and is a consequence of choosing conformally flat initial data (3.4) for a Kerr-based space-time and which restricts the values of the initial mass and spins to $0.812 \gtrsim M \leq 1$ and $\chi \lesssim 0.93$ [106–108]. This effect increases with the magnitude of the spin components while it decreases for larger D_0. Thus, since this ejection slightly perturbs the system, the initial masses and spins of the particles are usually readed after this ejection, i.e., when the system is relaxed. The superposed boosted Kerr-Schild data used by the SXS collaboration does not show this extra content of radiation and allow them to perform near extremal spin configurations [109, 110].

Then, in summary, this is how we solve the initial data for `BAM`:

1 - We solve either the PN or the EOB quasi-circular dynamics for a given $\left\{q, \vec{S}_1, \vec{S}_2\right\}$ configuration which yield the values for the momenta P^i of the punctures and defines the initial K_{ij}.

2 - The code solves (3.8) for the variable u which is directly related to the conformal factor given the following initial data choices: $\bar{\gamma}_{ij} = \delta_{ij}$, i.e., $\bar{R} = 0$ and $K = 0$. Then, we choose a pre-collapsed lapse and $\beta^i = 0$. At this point we already have all the ingredients to evolve our space-time.

3 - The analytic PN-EOB momenta will in general deviate from the quasi-circularity thus adding some residual eccentricity that in general is about $\sim 1\%$. This enforces to recalibrate the initial momenta following the results of Sec. 3.4 and then solve again the initial data equations.

Numerical setup

The computational domain is resolved by a set of L cubic hierarchically nested boxes that define L levels of mesh-refinement cubes indexed by $\ell = 0, ..., \ell_m, ..., L-1$. Here, $\ell = 0$ defines the outermost box while ℓ_m and $L-1$ the outermost and innermost moving boxes [72]. Each level of refinement ℓ is described by a Cartesian cube with a constant grid-spacing h_ℓ in the $x-y-z$ directions with N_ℓ^3 points on level ℓ. A refinement factor of two relates two consecutive nested refinements thus satisfying $h_\ell = h_0/2^\ell$. Then, each black hole is covered by a subset of moving nested $\ell \leq \ell_m$ boxes which track the position of the punctures by using (3.3) where a Berger-Oliger type adaptative-mesh-refinement (AMR) [111] is used for the time stepping. In addition, the finest boxes h_ℓ surrounding each particle must be sufficiently large to enclose both apparent horizons (AHs) (see Sec. 3.2.2). For unequal-mass systems where one tipically has $r_{AHl}/r_{AHs} \sim q > 1$ ($q = m_l/m_s \geq 1$) and where s/l label the *smallest* and *largest* particle respectively, some of individual the refinements $h_{\ell=L-1,L,...,0}$ surrounding the largest particle are eliminated to not overlap with its AH radius r_{AH}. Indeed, the sharped radial profile of some of the evolution variables around the punctures (e.g. the shift) enforces to setup a grid sufficiently large and resolved to capture them. In this line, it has been found empirically that this is achieved when the ratio between the finest box surrounding each particle and its apparent horizon satisfies,

$$\frac{L_{(s/l)}}{2r_{AH(s/l)}} \gtrsim \frac{3}{2}\,, \tag{3.9}$$

where $L_{s/l}$ represent the finest boxes surrounding each BH. This lower limit is not rigorously fixed, though a ratio of 1.5 is normally sufficient to resolve the mentioned profiles. Larger values for this ratio would even fit better the data though also increasing

the computational cost. Finally, the outermost boxes $\ell_m > \ell$ are kept unmoved and define the levels where the gravitational waveforms are extracted while $\ell = 0$ is chosen to be far enough to avoid inward reflections of our fields after reaching the boundaries of our computational domain. Close to merger, when the innermost boxes are close to meet each other, the domain is re-grided to enclose both the AH of the two individual black holes and the apparent horizon of the final object (from which we compute the final mass and final spin).

Finally, the evolution equations are usually evolved using sixth-order finite differencing in space combined with the method of lines with a fourth-order Runge-Kutta scheme for time integration. In addition, despite the robustness of the methods described, there always remain some numerical noise as a consequence of the discretization and rounding errors. This may lead to appearance of high frequency modes propagating through the numerical grid. Then, in order to minimise their effect, artificial dissipation is added trhough the standard Kreiss-Oliger dissipation operator (Q) of order $2r$,

$$Q = \frac{\sigma(-h)^{2r-1}(D_+)^r(D_-)^r}{2^{2r}}\,, \tag{3.10}$$

where h is the spatial stepping, $D_\pm$ first order derivative operators and with σ controlling the strength of the operator. Finally, the apparent horizons are tracked with the `AHmod` code [112].

BAM setup: summary

The BSSNOK and gauge evolution equations together with the initial data and the numerical setup form a closed system to evolve BBH simulations. However, we are still free to configure the initial setup by tuning some of the parameters, equations etc. In summary, this is all the freedom that we have in the initial configuration:

- The choice of the evolution variable for the conformal factor. In this thesis we have always used the χ method.
- The choice of the initial lapse function and shift condition. In our evolutions we set initially $\alpha = \psi_{BL}^{-2}$ and $\beta^i = 0$.
- The choice of η and ζ in the shift condition this being $\zeta = \eta = 1$ for all runs reported in this thesis.
- The Kreiss-Oliger dissipation factor and the order of spatial finite differencing on the evolution equations. In our case they have been set to $\sigma = 0.5$ and $2r = 6$ combined with a sixth-order finite differencing scheme in space.

- The Courant factor $C = \Delta t/\Delta x$; typically $\sim [0.25, 0.5]$. The upper limit $C = 0.5$ is normally sufficient for near equal-mass simulations while a more restrictive one $C = 0.25$ is needed for high mass-ratio cases to resolve the steeper profiles present in all the evolution variables caused by the asymmetry of these cases.
- The sampling of the spatial coordinates by using (3.9) or using a more relaxed version of it (with a factor larger than 1.5).
- The placement of the outer boundary defined through the outermost box $\ell = 0$.

3.2 Derived quantities

3.2.1 Gravitational waves

The simulation plan explained in Sec. 3.3 is targeted to recalibrate the existing spin-aligned phenomenological waveform models [38, 39] by adding subdominant effects as, in particular, the unequal-spin terms [7, 8]. Then, one of the main goals of this thesis has been the computation of the radiation resulting from 23 unequal-spin BBH mergers. In `BAM`, the gravitational wave signal is computed from the space-time metric using the 4th Newmann-Penrose scalar $\psi_4(t, r, \theta, \phi)$ [113]. (follow [114] for a detailed discussion about different alternatives of wave extraction methods). Then, the $\psi_4(t, r, \theta, \phi)$ is defined by:

$$\psi_4 = -R_{\alpha\beta\gamma\delta} n^\alpha \bar{m}^\beta n^\gamma \bar{m}^\delta, \tag{3.11}$$

where $R_{\alpha\beta\gamma\delta}$ is the four-dimensional Riemann tensor, and n and m form part of the null-tetrad $\{l, n, m, \bar{m}\}$ (see [72]), being $\bar{m}$ the complex conjugate of m. For many different purposes, it is usual to project the ψ_4 in a basis of spin-two spherical harmonics [115] ${}^{-2}Y_{lm}$ as:

$$\begin{aligned} \psi_{4,lm}(t, r) &= \int_0^{2\pi} \int_0^{\pi} \psi_4(t, r, \theta, \phi) {}^{-2}\bar{Y}_{lm}(\theta, \phi) d\Omega \\ \psi_4(t, r, \theta, \phi) &= \sum_{l=2}^{\infty} \sum_{m=-l}^{l} \psi_{4,lm}(t, r) Y_{lm}(\theta, \phi) \end{aligned} \tag{3.12}$$

where the $l = 2, m = \pm 2$ modes are the well known quadrupolar modes. Thus, (3.11) allows to split the emission in terms of even/odd contributions (higher modes) that are weighted by its corresponding spherical harmonics and superposed as individual contributions. This is particularly useful for current waveform modelling purposes where,

historically, only the quadrupolar terms has been calibrated (see the overview of waveform models of Chapter 2) and motivated by the fact that they carry with the majority of the power of the signal for comparable mass and nonprecessing systems[1].

The ψ_4, as well as other quantities in NR, is only well defined at null infinity where all the gauge effects are expected to vanish. However, the finiteness of our computational domain obligates to compute the GWs signal ψ_4 at a finite distance over spheres located at finite radius r_f according to (3.12). Far from the source, the peeling theorem [116–118] states that $\psi_4 \sim r^{-1}$ thus being more natural to define the quantity $r_f\psi_4(t, r_f)$. This rescaling partially removes the amplitude decay and also reduces the gauge dependency on the radial coordinate[2]. In fact, $r_f\psi_4(t, r_f)$ is the natural magnitude provided by NR codes (`BAM`,`LAZEV`,`MAYA`, `SpEC`) and analytic (EOB, PN) and semi-analytic (SEOBNR, Phenom) models for waveform-derived analysis. To minimise this finite radius effects, there exist a few strategies to extrapolate $\psi_4(t, r)$ to null-infinity through polynomial extrapolation [60, 119] and by using results of perturbation theory [120]. We address this issue in Sec. 3.6 and Chapter 4. Then, for the sake of clarity,

$$r\psi_4(t, r, \theta, \phi) = \sum_{l=2}^{\infty} \sum_{m=-l}^{l} r\psi_{4,lm}(t, r)Y_{lm}(\theta, \phi) \tag{3.13}$$

A three-dimensional intuition of (3.13) is given in Figure 3.1. This figure illustrates a snapshot of the three-dimensional ψ_4 into its AMR box of length $100M$[3] corresponding to a `BAM` run with physical parameters consistent with GW150914. The red and blue colors determine the maximums and minimums of the radiation at merger times traveling out from the source. The waves in the outer regions (green and yellow) correspond to the late inspiral regime where the strength is not as strong as in the merger. They represent the solution at a retarded time $\tau \sim t - r$, i.e, when the two BHs are still further apart.

Equation (3.13) is the standard representation of the ψ_4 on the context of gravitational wave detectors and waveform modelling. However, the detectors measure the change on the proper length of the arms produced by a passing gravitational wave, being proportional to the strain $h(t)$. These two quantities are related through a second time

[1] There is an ongoing effort for including higher than quadrupolar corrections using the EOB formalism and the phenomenological framework carried out by the LIGO waveform group.

[2] Recall that in the Newman-Penrose decomposition [113] there still remain higher order terms in r^{-a} with $a \geq 2$ that are not contemplated in the (3.13). This gives sense to the *far-from-source* restriction that it is normally considered for the wave extraction and that helps to reduce the gauge effects on the ψ_4.

[3] For BBH evolutions the total mass is factored out from the system of equations. These equations are usually formulated in geometrical units where $M = 1$. In `BAM` units this would correspond to $200r_S$, where $r_S = 2GM/c^2$ is the Schwarzschild radius for a system of total mass M.

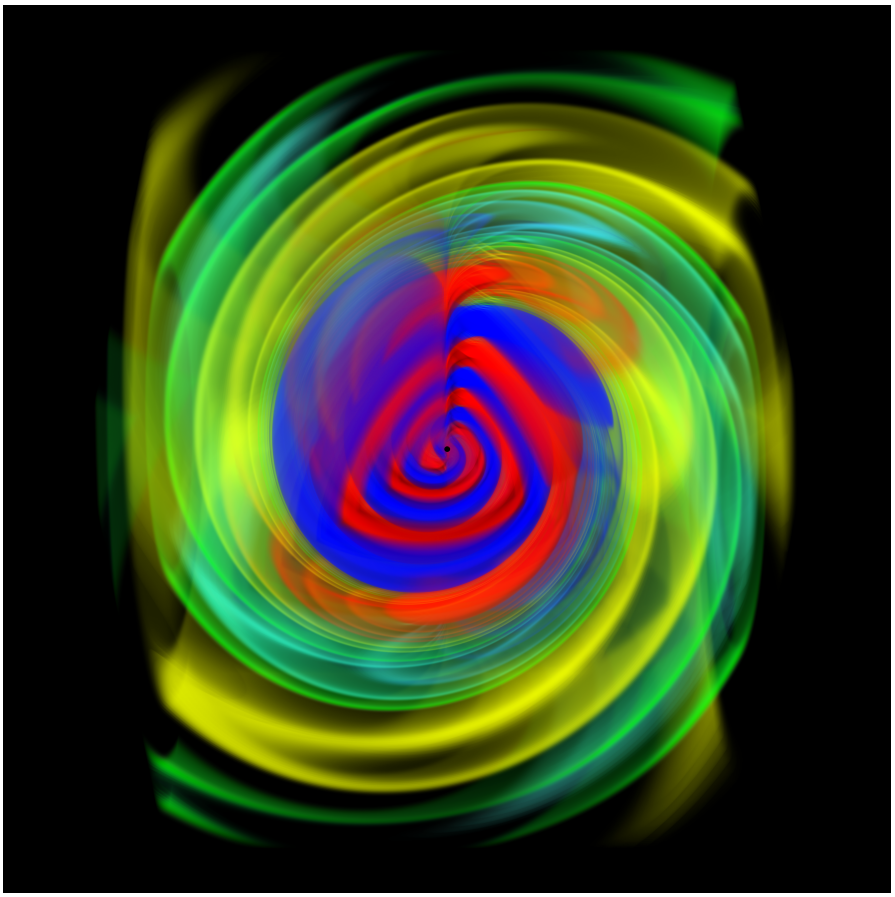

FIGURE 3.1: Snapshot of of the three-dimensional ψ_4 for a run with parameters compatible with GW150914 as seen in a Cartesian box about $\sim 100M$ times larger than the apparent horizon $\sim 1M$ (the small sphere at the center of the grid). The color gradient reveal the peaks (red) and valleys (blue) of the emission as seen when averaging over orientations (see Figure 3.2). The system was evolved with the BAM code by Sascha Husa while the visualization was performed by Rafel Jaume [88].

derivative, as:

$$h(t,\theta,\phi) = \frac{d^2\psi_4(t,\theta,\phi)}{dt^2} = \sum_{l=2}^{\infty}\sum_{m=-l}^{l} h_{lm}(t)Y_{lm}(\theta,\phi)\,, \tag{3.14}$$

where we have dropped the radial coordinate to simplify the notation.

Current time-domain [63, 64] and frequency-domain [38, 39] waveform models used in the template banks of the detectors calibrate the $l=2, m=\pm 2$ contributions of (3.14). An example is illustrated in Figure 3.2, where we show the real part of the time evolution of the $l=2, m=\pm 2$ term for the same physical case that in Figure 3.1 and for the $\psi_{4,22}(t)$ (left) and $h_{22}(t)$ (right) modes. In these figures, we show the last $\sim$ 20 GW cycles for a nonprecessing simulation performed with the `BAM` code (black) with parameters $\{q=1.2, \chi_1=-0.5, \chi_2=0.5\}$ overlapped with its equivalent `SEOBNRv4` signal [66] (red) and where it is clear the agreement between the NR waveform and the semi-analytic approximant. The minimal spike located at the beginning of the simulation is the so

called junk radiation (Sec. 3.1) and it is usually cut off for any waveform-derived analysis.

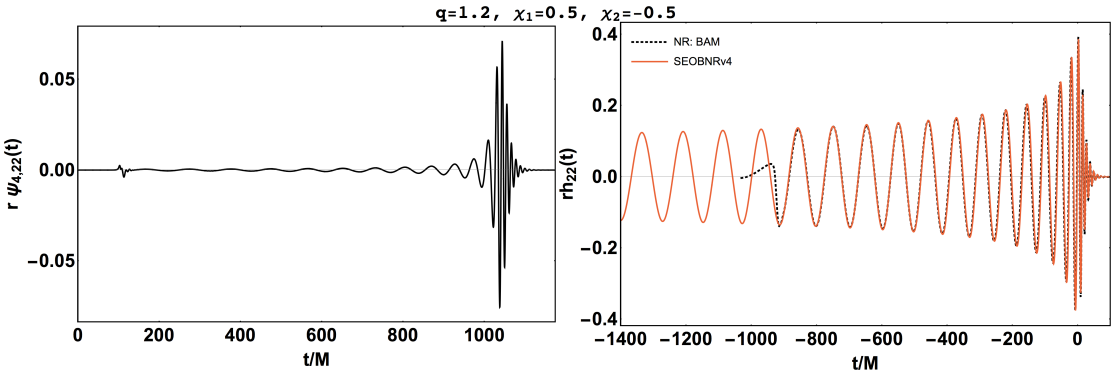

FIGURE 3.2: Illustration of the 22 mode $r\psi_{4,22}(t)$ (left panel) and its corresponding strain $rh_{22}(t)$ (right panel). The simulation was performed with the `BAM` code and used for the calibration of the new final state and luminosity fits [7, 8] as well as in the new calibration of the phenom model (Sec. 5).

3.2.2 Apparent horizons

Multiple physical quantities might be computed directly from the geometry of the BHs at each time step. For instance, spin and mass are well defined horizon quantities that come out naturally from the event horizon (EH) . An event horizon defines the boundary surface where light cannot escape from the black hole. They are invariant properties of our space-time. However, in NR simulations, where we evolve our three-dimensional slices, EHs are only well defined at the future of each slice, i.e., after the full performance of the simulation. This makes AHs the right quantity to followup [121].

An apparent horizon defines the limiting boundary of a succession of trapped null surfaces, where the light rays does not propagate away from the BH[4]. They are always contained into an EH being also dependent on the choice of the gauge variables. NR codes include different strategies to track and monitor their shape during the full evolution. In particular, AHs provide a very good approximation to EHs when the final object has finally settled down and the space-time is stationary (see Sec. 3.3.3). Then, final mass and final spin can be computed from surface integrals over the final AH by means of the Isolated Horizon (IH) and Dynamical Horizon (DH) approaches [123, 124]. The `BAM` code finds the horizons through the `AHmod` code [112] (see [125, 126] for a detailed description of different strategies to find AHs).

Final mass and final spin computed from the AH are generally expected to be more accurate than those based on the evaluation of radiative and asymptotic quantities such as the Bondi mass or the ADM angular momentum. These are computed through the

[4]Mathematically it is defined by a vanishing expansion Θ of the null geodesics [122].

waves evaluated at finite radius, where errors may arise due to finite radius truncation, insufficient extrapolation to infinity or numerical inaccuracies in propagating the wave content to large distances at sufficient numerical resolution. We briefly discuss below (Sections 3.2.3 and 3.2.4) the different approaches for computation the final spin and final mass (radiated energy).

3.2.3 Final spin

The final spin of a BBH system is nothing more than the remnant total angular momentum J saved in final object that has not been ejected through gravitational wave radiation and where, for low mass-ratio cases, the major contribution comes from the orbital angular momenta L. It can be computed from surface integrals over the AH using the IH [123, 124, 127], from surface integrals over spheres at large or infinite radius (as in [72]), or from the energy or angular momentum balance computed from initial and radiated quantities (see Equations 3.16 and 3.19 below). Moreover, it is also obtained from fits to the ringdown [128]. Then, once the AH surface S_{AH} is known the final spin is calculated through,

$$J = -\frac{1}{8\pi} \oint_{S_{AH}} K_{\mu\nu}\phi^{\nu} dS^{\mu} \,, \tag{3.15}$$

where $K_{\mu\nu}$ is the extrinsic curvature, ϕ^{ν} a killing vector reflecting an axial symmetry on S and dS the area element. While the situation is simple for nonprecessing cases where the axial symmetry is quite well preserved so ϕ^{ν} is naturally defined, it may become complicated when there is strong precession [129].

Alternatively, the angular momentum loss is also formulated in terms of radiation-based quantities as,

$$\frac{dJ_z}{dt} = -\lim_{r\to\infty}\left\{\frac{r^2}{16\pi}\mathrm{Re}\left[\int_{\Omega}\left(\partial_{\phi}\int_{-\infty}^{t} r\Psi_4 d\tilde{t}\right)\left(\int_{-\infty}^{t}\int_{-\infty}^{\hat{t}} r\overline{\Psi}_4 d\tilde{t}d\hat{t}\right)d\Omega\right]\right\}, \tag{3.16}$$

where $d\Omega = \sin\theta d\theta d\phi$. Thus, the final J_z may be computed by integrating (3.16) once the radiation $r\Psi_4$ has been computed. However, as stated in Sec. 3.2.2, (3.16) may suffer from truncation, extrapolation and from the different levels of resolution accounted for. Then, (3.16) is normally only used as a cross-check of the horizon value whenever it is available.

3.2.4 Final mass

In asymptotically flat space-times the usual definitions of the mass are through the ADM mass and the Bondi mass. Both definitions assume an asymptotic behavior of the

space-time, being both quantities defined at spatial infinity and null infinity respectively. One of the problems underlying the ADM mass and Bondi mass is that the eventual extra radiation living in our space-time is also included in its definition thus merging the isolated BH mass with the eventual gravitational wave radiation. This ambiguity is disentangled by means of the second law of black hole thermodynamics or the area theorem of black holes [130] which fixes a nice relation between the area of the EH and the lowest possible BH mass namely,

$$M_{irr}^2 = \frac{A_{EH}}{16\pi}\,, \tag{3.17}$$

where M_{irr} is the so called the *irreducible mass*, and A_{EH} never decreases. Then, given the irreducible mass, the final Kerr mass is defined trhough the so called Christodoulou formula [131],

$$M^2 = M_{irr}^2 + \frac{S^2}{4M_{irr}^2}\,, \tag{3.18}$$

where S is the dimensionful spin of the BH. Equation (3.17) is the usual definition of the BH mass in BBH evolutions. It is important to notice here that the area that appears in (3.17) is the EH area. However, as we suggest in Sec. 3.3.3, the apparent horizon AH is found to be an excellent approximation to the EH for stationary space-times, i.e., when the final BH has settled down [126] and the gauge effects tend to vanish.

On the other hand, the energy radiated may be also computed from the waves through,

$$\frac{dE}{dt} = \lim_{r\to\infty}\left[\frac{r^2}{16\pi}\int_\Omega \left|\int_{-\infty}^{t}\Psi_4(t,r,\theta,\phi)d\tilde{t}\right|^2 d\Omega\right]\,. \tag{3.19}$$

Likewise for the final spin and for the same reasons, the mass computed from the radiation is in general less accurate than the horizon one. In all our computations it is used as cross-check of the horizon related values and as an estimator of the error on its magnitude. This is extended in Chapter 4.

3.2.5 Luminosity and peak luminosity

The gravitational wave luminosity is defined as the total power emitted through gravitational waves. It is a purely radiative magnitude related to the waves through equation (3.19). Then, taking into account (3.13), (3.19) and the orthonormality of the spin-two spherical harmonics, the luminosity can be expressed as a linear superposition of the quadratic amplitudes of the (lm) modes $|\dot{h}_{lm}(t)|^2$ namely,

$$\frac{dE}{dt} = L \approx \frac{1}{16\,\pi} \sum_{l=2}^{l_{max}} \sum_{m=-l}^{+l} \left| \dot{h}_{lm}(t) \right|^2 , \tag{3.20}$$

where the equality is only satisfied in the limit $l_{max} \to \infty$ and where $l_{max} \sim 6$ is in general sufficient to collect all the physical content (see [8] and Chapter 4).

For an accurate computation of $L(t)$ through (3.20) we have to find an appropriate numerical setting for resolving not only the (22) and (2-2) modes but also the lm modes up to l_{max}. This is not always easy due to the large differences in the frequency evolution of the different modes (see Sec. 3.3 for clarification). These difficulties are evident in Figure 3.3 where we have plotted the indidual contributions to the total luminosity for the set of dominant modes: $\{22, 21, 33, 32, 44, 43\}$ for a `BAM` simulation with physical parameters $q = 1.75$, $\chi_1 = -0.85$ and $\chi_2 = 0.85$. Notice that the accuracy of some of the modes is not optimal in the early stages of the evolution. In particular, the subdominant modes $\{21, 32, 43\}$ are shown to be very noisy. Also notice that the effect of the junk radiation seems to be larger than in Figure 3.2 since in this case the spins are closer to the BL limit. In this work we give priority to the peaks, being the quantities used for the luminosity peak fit [8]. Then, we do not expect that the loss observed in the inspiral regime affects too much the peak values.

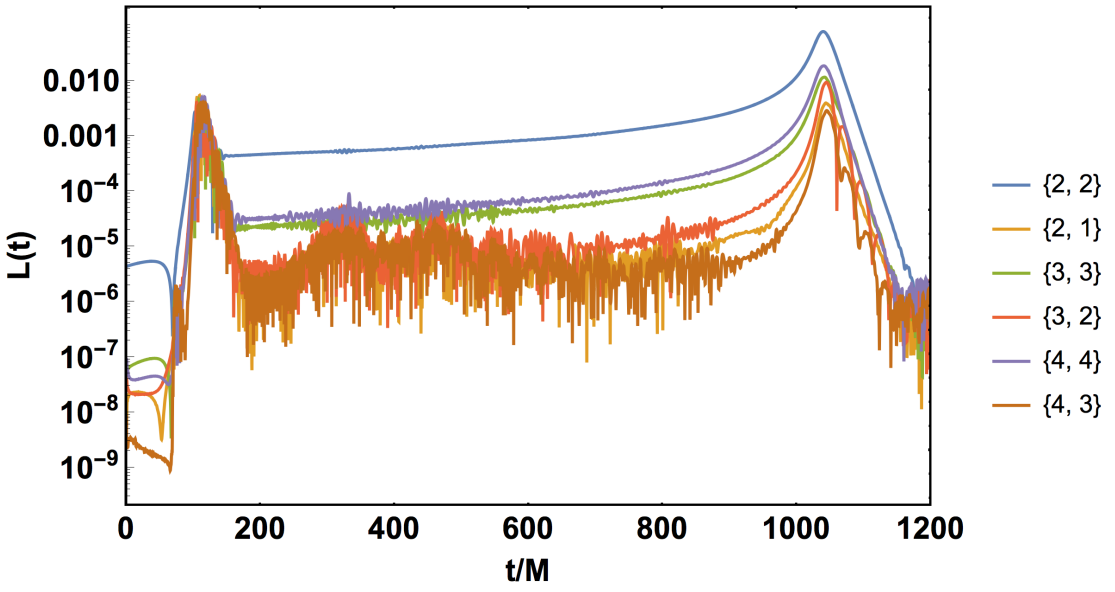

FIGURE 3.3: Luminosity per mode for a `BAM` $q = 1.75$, $\chi_1 = -0.85$ and $\chi_2 = 0.85$ case. Notice that the noise affects dominantly the subdominant modes being comparable with their amplitudes. In this case, the junk radiation seems be more important although still far from corrupting the evolution.

The hierarchical fitting procedure developed in this work has been tested on the related quantity L_{peak}, this corresponding to the maximum amplitude (3.20). In Chapter 4 we extend some of the numerical issues that may affect its value.

3.3 Unequal-spin simulations with BAM

Before going into much detail about the coverage of the parameter space, we must emphasize that the evolution of the 3+1 Einstein field equations introduced in Chapter 2 require an extremely large amount of computational resources. This is not a particularity of the `BAM` code or the BSSNOK framework but a common feature in any of the existing formulations that evolve BBH systems. The amount of resources needed for simulating each point of the parameter space is enormous, typically ranging from 10^5 to 10^6 CPU hours. Thus, to optimize the use of the resources it is essential a previous and careful analysis of the parameter space we want to cover. Although during the working plan we have produced several nonprecessing equal-spin configurations [38, 39], the main contribution has been the production a set of 23 nonprecessing unequal-spin configurations used in the calibration of [7, 8]. We detail below some aspects of the parameter space coverage.

3.3.1 Unequal spin simulations

With unequal-spin simulations, we aim to add to any waveform-related quantity an additional dependence on the physical parameter $\Delta\chi = \chi_1 - \chi_2$. As we detail in Chapter 4, the choice of this parameter is influenced by the form of the PN expressions following a similar strategy than for the choice of the dominant spin term S_{eff}. Ideally, one would like to populate the parameter space with as many different $\Delta\chi$ cases as possible. However, the limitedness of the computational resources motivates a previous devising of the parameter space that we want to fill. Then, in our case, the parameter space chosen is basically motivated by the astrophysical predictions, which anticipate that the mass-ratio distributions will peak on $q \approx 1$ (this is being confirmed by the current LIGO GWs observations [3, 45]) though they do not place strict constraints[5] on the spin configuration beyond the well known Kerr limit $\chi_{iz} \leq 1$. Thus, based on these expectations we have drawn the edges of our parameter space at $q = [1, 4]$ with the spins χ_{iz} contained $\in [-0.85, 0.85]$. Notice we could not achieve higher spins due to the limitations imposed by the Bowen-York limit which restricts the initial spins to be $\chi \lesssim 0.93$ [106–108]. Indeed, the `BAM` code shows some instabilities after the first few orbits of the evolution for $\chi_{iz} = 0.9$ and in the simplest $q = 1$.

The simulation plan is shown in Figure 3.4. The corners of our parameter space coincide with the regions where $\Delta\chi$ is expected to be larger (an extended revision of this effect can

[5]The different formation chanels also predict different spin distributions (see [132, 133]). However, based on the current observations, it is still not possible to say much about any preferred channel thus making plausible any spin configuration.

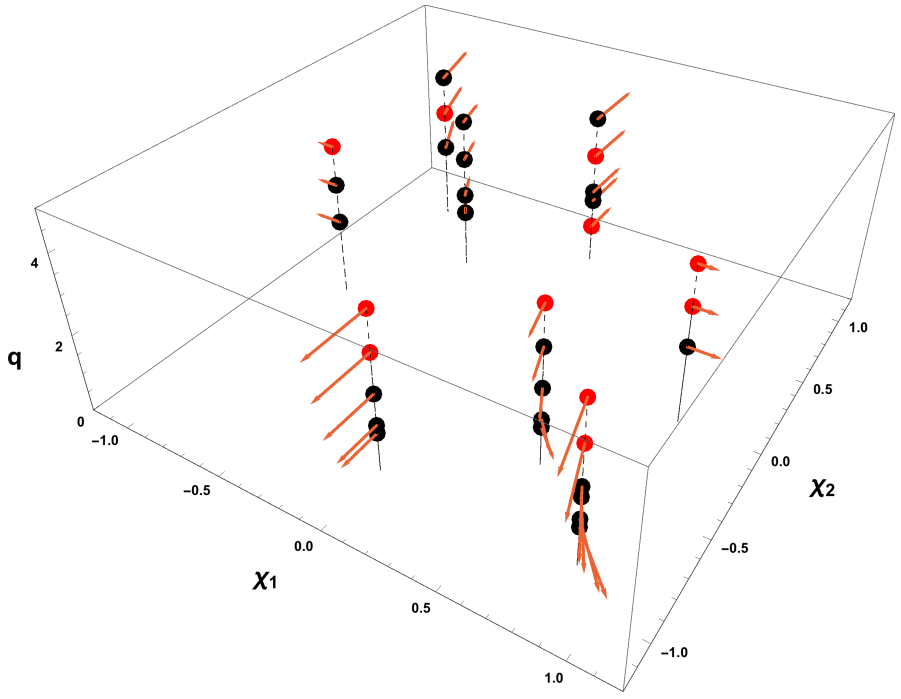

FIGURE 3.4: Simulation plan for the 34 original unequal-spin configurations. In black we plot the 23 simulations performed, postprocessed and included in this work while in red we show the planned but not simulated. The arrows in orange are related with the effective $\chi_{eff} = m_1\chi_1 + m_2\chi_2$ (see Chapter 4). Notice that the arrows point dominantly to χ_2 as the mass-ratio increases (recall that $m_2 > m_1$ in BAM).

be found in Chapter 4). We have also populated the intermediate regions with $\chi_{iz} = \pm 0.5$ to favor the interpolation of the points placed within the boundaries and reducing the possible extrapolation artifacts in any of the waveform magnitudes. The arrows represent the $\chi_{eff} = m_1\chi_1 + m_2\chi_2$ effective spin used in some of the phenomenological models. Since the convention used in BAM sets $q = m_2/m_1 > 1$ most of them point in the χ_2 direction In addition, we have added in red a subset of simulations originally planned but not finally performed by the time of the thesis writing. The physical parameters of the configurations are listed in Table 3.1.

3.3.2 Grid configuration

In this work, the waveforms have been extracted at finite radii and as far as possible to minimise some well-known gauge effects [72] of finite extraction. This involves that we have to deal with very different scales from the numerical point of view; one centered in the punctures and its evolution ($\mathcal{O} \sim 10M$) and the other at the wave zone ($\mathcal{O} \sim 100M$) making unpractical to build a uniform and sufficiently resolved grid covering the whole space-time for obvious reasons. If we would have to propagate the resolution of the finest levels to the wave extraction zone the computational cost would increase by a factor of $(L_{coarsest}/L_{finest})^3$. This issue is solved by setting up a hierachy of nested Berger-Oliger

q	χ_1	χ_2	ω_0	e $[\times 10^{-3}]$	$E_{\rm rad}$	$\chi_{\rm f}$	L_{peak} $[\times 10^{-3}]$
1.00	0.00	-0.85	0.022	2.25	0.0392	0.5514	0.856
1.00	0.85	-0.85	0.023	2.61	0.0491	0.6854	1.048
1.00	0.50	-0.50	0.023	1.59	0.0485	0.6858	1.018
1.20	0.00	-0.85	0.020	0.74	0.0401	0.5747	0.868
1.20	0.50	-0.50	0.028	1.76	0.0503	0.7142	1.058
1.20	0.85	-0.85	0.028	2.16	0.0527	0.7359	1.110
1.50	-0.50	0.50	0.024	1.80	0.0408	0.5865	0.844
1.75	-0.85	0.85	0.021	2.66	0.0343	0.4607	0.710
1.75	0.85	0.00	0.021	1.00	0.0682	0.8724	1.313
2.00	0.50	-0.50	0.024	1.76	0.0464	0.7510	0.916
2.00	0.00	-0.85	0.023	2.85	0.0347	0.5693	0.722
2.00	0.00	0.85	0.024	2.52	0.0436	0.6732	0.834
2.00	0.85	-0.85	0.024	1.78	0.0556	0.8344	0.609
2.00	-0.85	0.85	0.022	3.07	0.0310	0.4002	0.620
2.00	-0.50	0.50	0.023	2.60	0.0336	0.4925	0.666
2.00	-0.85	0.00	0.022	2.70	0.0292	0.3425	0.580
2.00	0.85	0.00	0.023	2.02	0.0646	0.8782	0.864
3.00	-0.50	0.50	0.024	1.69	0.0237	0.3339	0.424
3.00	0.50	-0.50	0.025	1.41	0.0373	0.7410	0.410
3.00	-0.85	0.00	0.023	3.25	0.0201	0.1562	0.371
4.00	0.00	0.85	0.026	1.79	0.0230	0.4900	0.372
4.00	-0.85	0.85	0.023	2.04	0.0158	0.0323	0.263
4.00	-0.50	0.50	0.024	1.68	0.0177	0.2152	0.293

TABLE 3.1: New BAM simulations used in this work. We have put a special focus on highly unequal spins; For each simulation, we list mass ratio $q = m_1/m_2$, initial spins χ_1 and χ_2, reference orbital frequency Ω_0, initial separation D_0 (after junk radiation), eccentricity e, radiated energy $E_{\rm rad}$ (scaled to unit initial mass) and dimensionless final spin $\chi_{\rm f}$.

Cartesian grids [72, 111], where the innermost and most resolved $l \geq l_m$ grids surround and track the individual positions of each puncture while the coarsest ones are static and far beyond the typical orbital scales as illustrated in Figure 3.5. In addition, recall that the resolution decreases by factor of 2 per level. This scaling captures the $1/r$ fall-off of the metric for a single puncture [72]. Then, if a certain level l at a distance r_l is sufficiently well resolved by h_l, the next one $2r_l$ should also be well resolved by $2h_l$.

A typical grid setup for the `BAM` code is shown in Table 3.2. This configuration corresponds to the same GW150914-type system illustrated in Figures 3.1 and 3.2. Then, we proceed as follows:

- We first set the size of the innermost/finest moving boxes. These must resolve the a priori *unknown* AHs (see Sec. 3.3.3) thus forming two separate sets of nested boxes that resolve each BH. The outer boxes are just gridded at $h_l = h_0 2^l$.

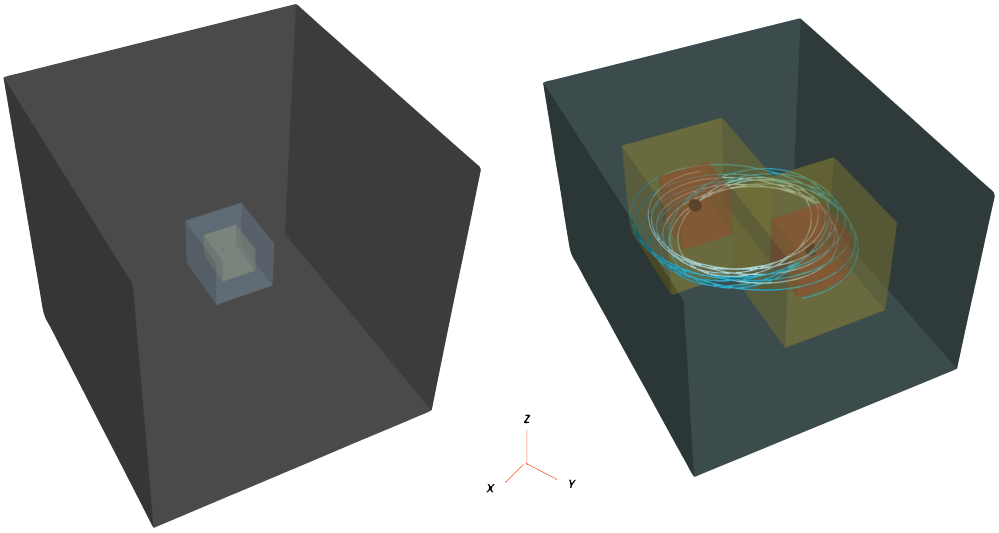

FIGURE 3.5: Illustration of the BAM l boxes. The ones surrounding the AHs evolve according to the evolution of the *shift* vector (3.3) while the outermost boxes are static. The extraction of the gravitational waves is normally performed in the outermost boxes where the resolution is also increased with respect other levels.

l	h_l	dt_l	N_l	$\frac{h_l N_l}{2}$	extraction level wave R_{ex}
0	29.696	0.1856	144	2138.11	{}
1	14.848	0.1856	144	1069.05	{}
2	7.424	0.1856	144	534.53	{}
3	3.712	0.1856	144	267.26	{}
4	1.856	0.1856	192	178.18	{}
5	0.928	0.1856	360	167.04	{120, 140, 160}
6	0.464	0.1856	480	111.36	{60, 70, 75, 85, 90, 100}
7	0.232	0.0928	96	11.14	{}
8	0.116	0.0464	96	5.57	{}
9	0.058	0.0232	96	2.78	{}
10	0.029	0.0116	96	1.39	{}
11	0.0145	0.0058	96	0.69	{}

TABLE 3.2: Configuration of the initial adapted grid for the evolution of the system GW150914. We provide the following information in this order: level of refinement l, spacial resolution h_l, time resolution dt_l, number of points of the box N_l, size of the boxes $0.5h_lN_l$ and waveform extraction levels R_{ex}. The blue line delineates the separation between *moving boxes* $l > 6$ and the static ones $l \leq 6$. The size of the box with the finest grid is highlighted in red.

- The outermost box (or the boundary of our space-time) must be placed far enough to not have reflections of the radiation back to the computational domain which involves that $L_{R_{ex}} > 2t_{coal}$ where t_{coal} is the coalescense time (for this purpose is sufficient a 1PN estimate).

- The time step must be chosen in order to satisfy the Courant factor condition. For the `BAM` numerical scheme it has been shown to be sufficient $\Delta t/\Delta x \lesssim 0.5$ although the optimal value may slightly depend on the physical parameters. In the example illustrated in Figure 3.2 this factor is set to 0.4. For high mass-ratio cases $q \gtrsim 4$ the time stepping has to be in general reduced to capture the field dynamics around the small particle thus being more indicated a value of $\Delta t/\Delta x \sim 0.25$.

- It is also required to maintain an appropriate resolution on the levels where the waveforms are extracted. These are located as far as possible to minimise the gauge effects in the wave zone. We consider a sufficiently far away extraction radii when $R_{ex} \sim 100$. The required resolution is normally $h_{R_{ex}\sim 100} \lesssim 0.8$. In terms of points per wavelength we normally require at least about 16 per oscillation (see Figure 3.6).

Of particular note is the resolution at the wave zone $R_{ex} \sim 100M$ since we obtain the main product of our simulations there: the gravitational waves. During the evolution the frequency of the orbit changes in about one order of magnitude from the inspiral regime to the merger. Indeed, the typical wavelength at the starting of the simulation of the dominant mode is $\lambda_{22} \sim 100M$ whereas at merger times it gets reduced to $\lambda_{22} \sim 10M$. This effect is even magnified when one considers higher modes, broadening the frequency range by a factor up to $[1/2, m_{max}]$ where m_{max} normally coincides with l_{max}. This makes difficult properly to resolve with a unique grid not only the different modes but also the different frequencies regimes. This issue is illustrated in Figure 3.6, where we have plotted two sine waves traveling along the x direction in a spatial grid with $h_{R_{ex}} = 1M$. To visualize the discretization effects on the waves, we have fixed the frequencies according to the typical BBH (22) mode inspiral and merger frequencies (orange and blue) and the (32) merger frequency (green). Then, in this example, it is clear that whereas the inspiral regime is sufficiently resolved by our grid, the merger remains unresolved. This is even more evident in the case of the (33) mode where the frequency satisfies that $f_{33} \sim 1.5 f_{22}$. Although in general we will adapt our grid to the get an accurate (22) mode by a grid configuration adapted to the merger, where the frequency is higher, the situation may be more complicated when considering the higher modes.

The accuracy of our waveforms is not only limited by resolution-dependent numerical errors but also by the finiteness of our numerical computational domain. Recall that the

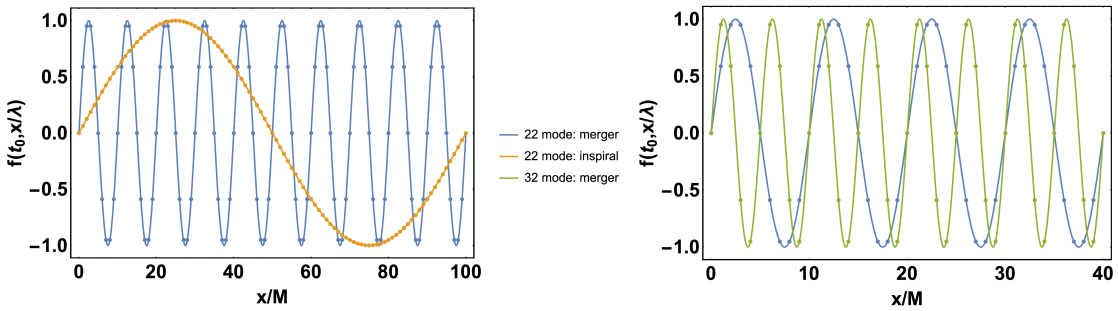

FIGURE 3.6: Snapshot of different sine waves $f(t_0, x/\lambda)$ traveling along a discretized spacial coordinate x with the typical wavelengths that characterize the gravitational wave emission in different regimes. Left panel: Representation of the sine waves with the typical (22) mode frequencies for the inspiral phase (orange) and merger (blue). Right panel: Comparison of the (22) (blue) and (32) (green) mode frequencies in the merger phase. Due to the broad frequency band of our systems, the same grid may not resolve sufficiently all the regimes and perturbations.

GW signal is only unambiguosly defined for an observer at null infinity. However, most of the codes (`SpEC`, `BAM`,`LAZEV`, `MAYA`) extract the waveforms at finite radii and follow different strategies for extrapolating the waveforms [60, 120]. For example, if we expand the Newman-Penrose scalar ψ_4 in terms of the radial distance and far from the source we see that (see the detailed review of [76]):

$$\psi_4 \sim \frac{1}{r} + \mathcal{O}(\frac{1}{r^2}) \tag{3.21}$$

The same qualitative behavior is obtained from perturbation theory through the Regge-Wheeler-Zerilli odd-parity equations [114, 134, 135]. In this scenario, one considers the propagation of tensor fields in a perturbed asymptotic Schwarzschild/Kerr background space-time that, at the same time, resembles our BBH space-time with GWs propagating far from the source. Then, the importance of the $\mathcal{O}(1/r^2)$ correction is tightly related to the frequency of the oscillatory tensor field (see equation 10 of [120]) which in our study correspond to gravitational waves propagating through the perturbed space-time. In particular, these corrections take the following form for the evolution of the gravitational wave phase:

$$\phi_{lm} \sim \frac{l(l+1)}{4\pi(r/\lambda_{lm})} \tag{3.22}$$

where (lm) tags the mode considered, λ_{lm} the wavelength and r the radial distance from the source in isotropic coordinates.

Equation (3.22) fixes a quantitative relation to estimate the importance of neglected $O(r^{-2})$ terms by relating them to the frequency (or wavelength) of the waveforms. Coming back to our (22) example shown in Figure 3.2 we see that for $r \sim 100M$ the relation given in (3.22) gives a correction $\mathcal{O}(1)$ for the phase which might be relevant for the inspiral and not so much for the merger, where we have $\mathcal{O}(0.1)$. Again, this effect is

also augmented for some of the higher modes. In this case, configurations with $m > 2$ and given that in the inspiral phase it is satisfied $\lambda_{lm} = m/2\lambda_{22}$, will tend to increase the r/λ_{lm} ratio thus being the neglected $1/r^2$ corrections more relevant. For NR waveforms, the higher-order $1/r^2$ terms are also accounted for from two main approaches: using analytic extrapolation by means of the Regge-Wheeler-Zerilli equations [120] or by polynomial extrapolation. Analytic extrapolation [120] follows the procedure sketched in this section. It also includes higher than $\mathcal{O}(1/r)$ factors to account for the effect of the spin. Although it provides a physically motivated expansion in $\mathcal{O}(1/r^n)$ powers, it may conflicts with the gauge effects, which are also known to be on the same order. On the other hand, the polynomial extrapolation is purely driven by looking at the data at different extraction radii and adjust its behavior by higher order polynomials. In Sec. 3.6 we address this issue for `BAM` and `SpEC` waveforms.

3.3.3 Apparent horizon fits for the BAM code

In Sec. 3.2.2 we have justified that AHs are the proper quantities to followup in NR simulations given their similarities to EHs in local quasi-stationary space-times. Although they are shown to depend on the gauge choice, for the `BAM` code it has been found and longer used a standardized setup[6] of the gauge variables which allow us to relate the AHs for different BBH physical configurations. Then, any predictability about the AHs would also make possible an estimate of the size of the boxes that define our computational domain.

The construction of the respective finest grids enclosing each of the horizons involves a previous knowledge of their sizes. However, the AHs are not steady gauge dependent quantities but they grow along the evolution until they get stabilized. The growth and stabilization of the apparent horizon is controlled by the choice of the shift condition and, implicitly, through an appropriate choice of the damping term η of (3.1).

To illustrate its qualitative effect in our evolution let us assume $\eta \to \infty$. Then, from (3.1) and in this extreme limit it is easy to show that $B^i \sim \exp^{-\eta t}$ and $\beta^i \sim \exp^{-\eta t}/\eta$ that goes to zero as $\eta \to \infty$. After a time $t \sim 4/\eta M$ our space-time will satisfy $\beta^i \approx 0$ thus defining a slicing characterized by Eulerian observers with $n^\nu = \{-\alpha, 0\}$. In this situation, the black hole horizon grows rapidly in the coordinate space to eventually cover the whole computational domain and breaking the evolution. This is clear if one computes the outgoing null geodesics from the ADM equations in the $\beta^i = 0$ case. In

[6] We call the *standard setup* as the optimal setup of gauge variables and values that has been historically fine tuned to perform the recent BBH simulations. Needless to say that this *standardized/optimal* setup may vary across the parameter space but, even in this case, there would exist one optimal configuration per each case.

this case, the coordinate speed of the outgoing null rays is $v \sim \alpha > 0$ thus making self-evident this unstoppable growth. Then, following the same deduction and using the ADM 3+1 metric results we see that the shift vector acts as a *brake* of the coordinate speed that helps to stabilize this growth. Indeed, any finite value of η will increasingly constrain the coordinate speed as $\eta \to 0$ thus fixing the apparent horizon size. This is shown in Figure 3.7 where I illustrate the time evolution of the AH for three different choices of η for the GW150914-type simulation. We see that the coordinate size of the AH decreases as $\eta \to 0$. On the contrary, the masses associated to the horizon do not show any gauge dependence as expected, being a consequence of the area invariance.

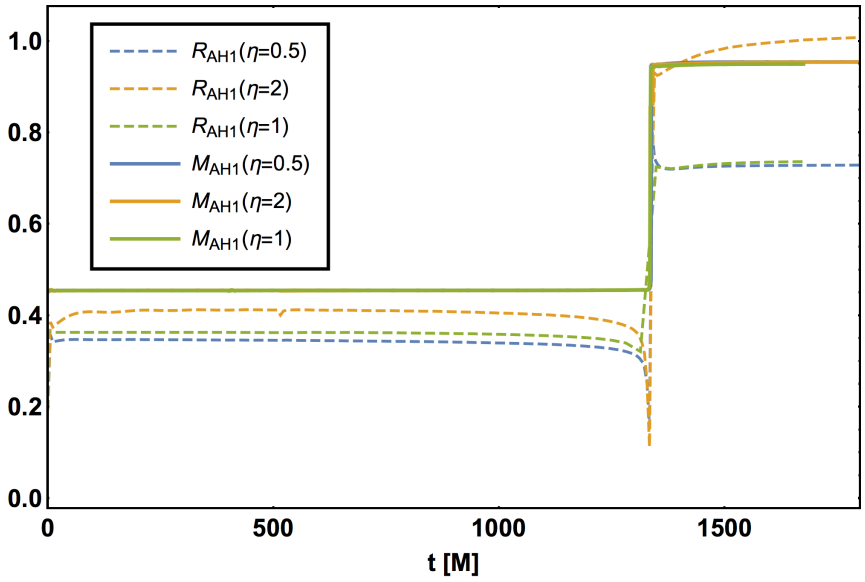

FIGURE 3.7: The simulation corresponds to the same system consistent with GW150914 with $q = 1.2$ and $\vec{\chi}_1 = -\vec{\chi}_2 = \{0, 0, 0.5\}$. The dashed lines represent the evolution of the apparent horizons and where it is evident the dependence on η. On the other hand, the horizon masses are equivalent for the three choices as expected. The sharped jump occurs at merger-ringdown times, where the final object is formed.

The control of the coordinate speed (and the slicing) through the η value is important not only for controlling the size of the AH but for the global good performance of the simulations. For the `BAM` code it has been found empirically that fixing $\eta = 1$ results in having more sane evolutions [72] and where the gauge effects on the waveforms get quickly dissipated. We have also observed that for lower values of η the initial fluctuations originated by the junk radiation are also quickly radiated away. However, it takes some time to achieve the quasi-stationay solution. The coordinates evolve rapidly initially and this stage of the evolution is driven by NR. Thus, the initial ignorance of the AHs sizes makes unclear the definition of our finest boxes and grids. To solve this, one could define a "sufficiently" large and well resolved finest box based on some previous empirical studies across the parameter space with the risk of not matching the (3.9) condition. On the other hand, a *reasonable* grid configuration that leads to a

stable evolution until the final formation of the AHs would allow us to compute their size. Then, we could restart the simulation again now exactly satisfying (3.9). This was exactly the strategy followed in all the old `BAM` runs [38] adding an extra computational cost of $\sim$ 10000 CPU hours per case.

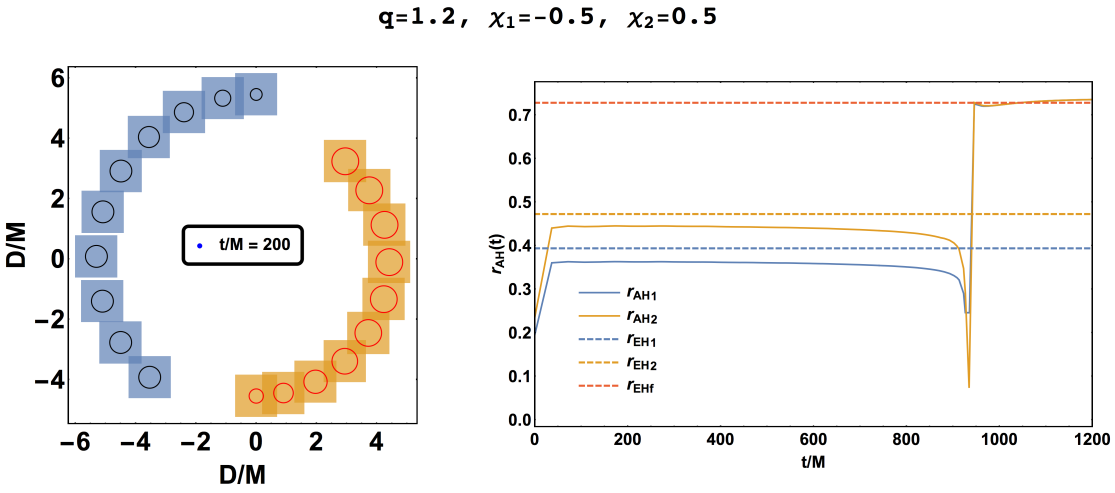

FIGURE 3.8: Time evolution of the apparent horizons of the two particles (small BH in blue and large BH in orange). Left panel: Orbital motion of the two horizons resolved by the respective finest boxes. The system has evolved $200M$, time enough to reach the domain in which the horizons are formed and get stabilized. Right panel: Time evolution of the horizons up to the ringdown and posterior relaxation of the system. Notice that the horizons take about $\sim 100M$ to be formed and stabilized although their steady value might depend on the choice of the η. The simulation corresponds to the same GW150914 system of Figure 3.7.

Figure 3.8 illustrates the evolution of the horizons and their relation to the finest boxes for a GW150914-type configuration. The system takes about $100M$ to get stabilized and follow an almost steady evolution until the merger, where the high NR-dynamics arises and the two AH horizons result in a single AH. Notice the closeness of the AH values to the EHs predictions (dashed lines) after the stabilization of the gauge variables ($\sim 100M$). At this stage the space-time is locally quasi-stationary in the regions surrounding each black hole and where η has been tuned to satisfy this. After the formation final object (r_{EHf} in the plot), AH and EH values are almost the same up to numerical accuracy since at this stage the space-time is stationary.

To avoid the extra step of computing numerically the AHs and save computational cost we studied its dependence on the physical parameters for a given gauge setup. Then we collected a set of NR evolutions with $\eta = 1$, ranging from $q\,[1.,4.]$ and $|S_i| \in [0.,0.85]$ that resulted in the calibration of two different fits for each AH. Both fits depend on the mass ratio q and the norm of the spin S_i and their prescription have been shown to be quite similar to the Kerr EH for isolated BHs in isotropic coordinates,

$$r_{EH,i} = m_i\sqrt{1-\chi_i^2}\,, \tag{3.23}$$

where m_i labels the mass of each BH and χ_i the magnitude of the dimensionless spin. Ideally, this would describe the situation where the two BHs were infinitely apart from each other or increasingly *isolated*. However, as they get closer this description deviates from the physical reality due to the space-time deformation caused by the other BH. Then to account for this interaction, we have proposed a modified form of (3.23) by inserting some extra free coefficients namely,

$$r_{EH,small} = \frac{0.899767\sqrt{1-0.852345\chi^2_{\text{small}}} - 0.0100553q\sqrt{1-0.852345\chi^2_{\text{small}}}}{q+1}, \quad (3.24)$$

$$r_{EH,large} = \frac{q\left(0.84086\sqrt{1-0.852345\chi^2_{\text{large}}} + 0.0488517q\sqrt{1-0.852345\chi^2_{\text{large}}}\right)}{q+1}, \quad (3.25)$$

where q is the mass-ratio, $m_{small} = 1/(1+q)$ and $m_{large} = q/(1+q)$. The first factor of (3.24) is the dominant one. Indeed it resembles the Kerr prescription for the EH (3.23) except that the m_i and χ_i coefficients are different to one as a consequence of the mentioned interaction. The second term is less dominant and it helps to reduce the errors even in the extrapolation regions. Moreover, both formulas are well behaved on the extreme spin limit $\chi = 1$. In Figure 3.9 we show the results for the AH fits in relation to the calibration points and some extra test points that have not been used in the calibration. We have obtained a maximum deviation $\sim 5\%$ for the non calibrated $q = 8$ which is consistent with the accuracy required for our initial grid setup and being this point far beyond the calibration region. Recall that the main purpose of these fits is to get closer to the empirical relation imposed by (3.9), which is well satisfied given the accuracy reached with (3.24). In addition, notice that we have constrained the fits to satisfy $r_{EH,small}(1,\chi) = r_{EH,large}$.

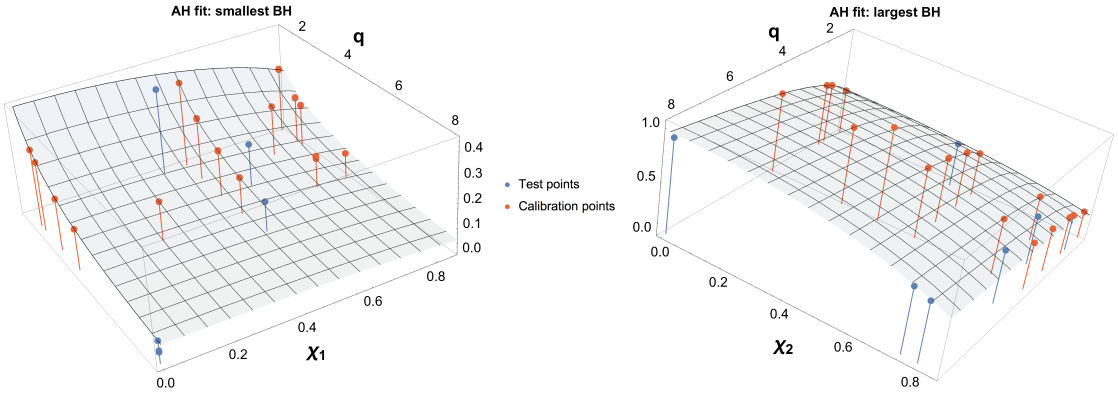

FIGURE 3.9: Apparent horizons fits for the smallest BH (left) and for the biggest one (right) compared to calibration points (red) and the test points (blue). We see a good agreement between data and fits even for the points out of the calibration region.

3.4 Eccentricity reduction

Most of stellar mass compact objects are expected to have zero eccentricity when entering in the LIGO band [49]. At these frequencies all the eccentricity is diluted through the emission of gravitational waves thus circularizing the orbit. For instance, the Hulse-Taylor pulsar [25] has today an eccentricity of $e \approx 0.617$ while it is orbiting at a frequency of 4×10^{-5} Hz, still far away from the initial ~ 10 Hz of the ground based detectors. By the time that the two objects reach a separation compatible with the ~ 10 Hz the eccentricity of this system is estimated to be about $e \sim 10^{-4}$. These values, besides being residual compared to the $e \approx 0.617$ of the Hulse-Taylor pulsar and other astrophysical binaries [136], are currently undetectable by the parameter estimation pipelines and search algorithms [137, 138] given the actual SNR expectations of the past and future GW detections. This historically led the *waveform modellers* to develop zero-eccentric models thus reducing the dimension of the parameter space by one unit (see the overview of the PhenomD [38, 39] waveform model in Sec. 5). In addition, recent but not sufficiently tested formulations of eccentric waveforms are being developed [138–140] with the hope of constraining the eccentricity in future and more powerful GWs observations. These models are expected to be clearly more relevant for space-based missions as LISA, where the frequency band is estimated to be centered about the 0.001 Hz thus making possible the observation of inspiraling objects with noticeable values of eccentricity.

3.4.1 Eccentricity in the Keplerian two body problem

To illustrate the problem let us start with the simple Keplerian two body formulation and assuming zero gravitational wave emission. In this context, the solution of the orbit is given by equation (3.26):

$$r = \frac{p}{1 + e\cos\theta}\,, \tag{3.26}$$

where $r = |\vec{r}_1 - \vec{r}_2|$, $e \in [0, 1]$ is the eccentricity, p the so called semi-latus rectum of the curve and θ the phase of the orbit. It is also useful to describe the orbital motion in terms of its radial and tangential velocities, namely:

$$V_r = \dot{r} = \sqrt{\frac{\mu}{p}} e \sin\theta\,, \tag{3.27}$$

$$V_t = r\dot{\theta} = \sqrt{\frac{\mu}{p}}(1 + e\cos\theta)\,, \tag{3.28}$$

where V_t and V_r are the tangential and radial velocities respectively, $\mu = G(m_1 + m_2)$ and where the *dots* represent first time derivatives. Combining (3.26) and (3.28) we can

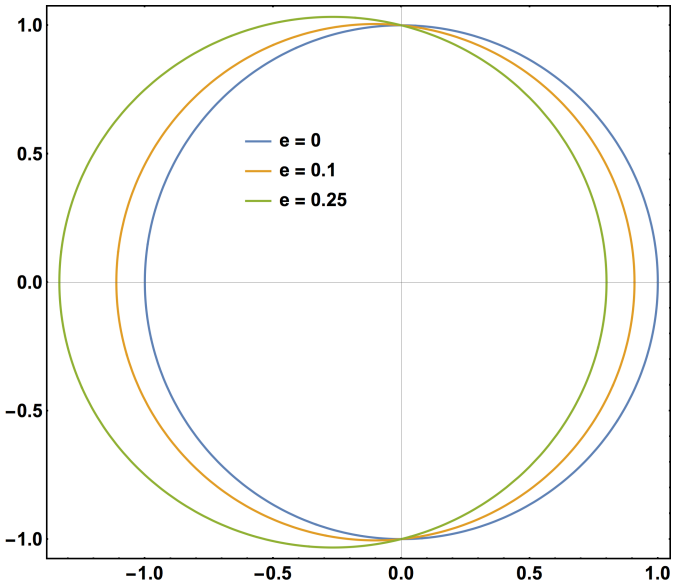

FIGURE 3.10: Keplerian representation of three orbits with three different values of the eccentricity.

relate the orbital frequency $\dot{\theta}$ with the radial separation r and the eccentricity e:

$$\dot{\theta} = \sqrt{\frac{\mu}{p^3}}(1 + e\cos\theta)^2 \tag{3.29}$$

Equations (3.26) to (3.31) encode a series of properties that are also satisfied when we consider the gravitational waves emission. First, notice that $V_t \gg V_r$, i.e, that the tangential velocity is always larger than the radial one. This property is well maintained during the evolution getting only important deviations during the very last orbits (~ 4) where the merger takes place. Then, for small values of e, the orbital distance r and the orbital frequency $\dot{\theta}$ may be expressed as:

$$r \approx p(1 - e\cos\theta + \mathcal{O}(e^2)) \tag{3.30}$$

$$\dot{\theta} \approx \sqrt{\frac{\mu}{p^3}}(1 + 2e\cos\theta + \mathcal{O}(e^2)) \tag{3.31}$$

This situation represents the most common frame in the context of the BBH simulations. However, despite the quasi-circular assumptions of our equations, different agents may insert a residual eccentricity in the orbital motion. These agents are dominantly caused by either taking inaccurate initial parameters from the known analytic solutions (PN, EOB models) or by the coordinate mismatch between NR codes and these approximants. The usual eccentricity estimated from our NR simulations is typically small $e \lesssim 0.01$ and we aim to remove it not only to better match the astrophysical predictions but also for simplifying the process of building our hybrids (see Chapter 5).

Figure 3.11 illustrates the effect of the eccentricity in the Keplerian two body problem.

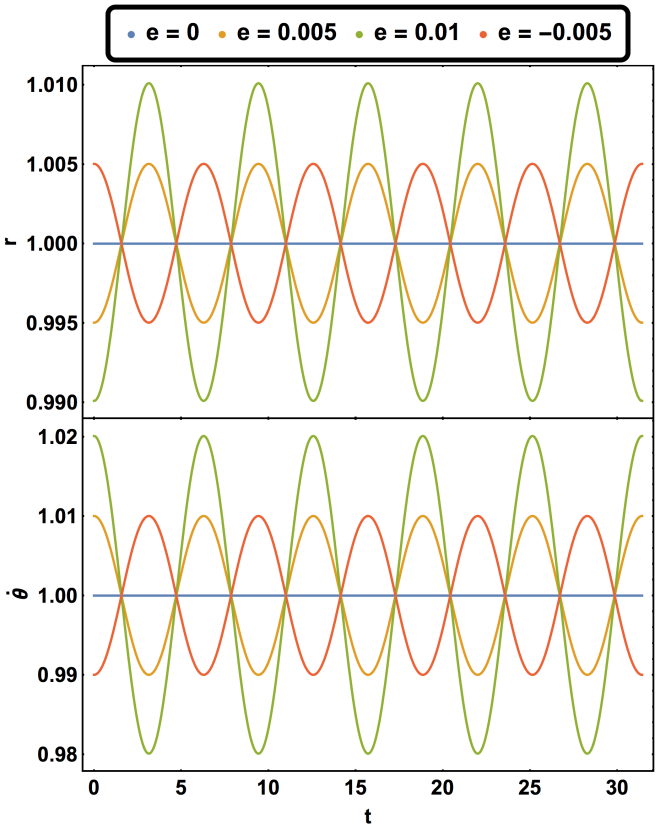

FIGURE 3.11: Illustration of the effect of perturbing the initial state for a Keplerian orbit by e. Top panel: Radial coordinate r (or distance between the two particles) for three different initial parameter configurations: one non-eccentric (blue), and two with residual eccentricities (orange and green). Bottom panel: Orbital frequency $\dot{\theta}$ for the same initial configuration.

We see that whenever the eccentricity is small, it provokes an oscillation with the same period of the orbit and with amplitude $\lambda = e$ for the radial separation and $\lambda = 2e$ for the orbital frequency. In addition, the maximums and minimums of the oscillations are correlated with the sign of the perturbation. Then, an estimate of the amplitude of these oscillations in the orbital quantities is directly related to the correction factor λ, thus quantifying the correction needed to get a circular motion. This procedure may be iterated in many steps to get increasingly lower values of e. In Sec. 3.4.2 we extend this method to the gravitational wave emission case, showing no significant differences to what we see in the Keplerian case.

3.4.2 NR eccentric waveforms

The initial conditions of our NR simulations are given by the analytic solutions of the PN and EOB models. Likewise in the Keplerian two body problem, given the physical

parameters of our system (mass-ratio and spins) and the initial positions and momenta, the orbital evolution may be described by the analytic models although they are not accurate enough to reproduce the late inspiral and merger-ringdown regimes. Then, once defined an initial orbital frequency Ω_0 (or distance D_0) as the starting value of the NR simulation, the quasi-circular values of the momenta are univocally defined from the PN/EOB evolutuion equations. With this, we have all the ingredients to define the initial extrinsic curvature and then for solving the Bowen-York initial data (see Sec. 3.1).

We aim to model the evolution of quasi-circular/non-eccentric orbits according to the current astrophysical models and LIGO expectations. Hence, we must solve the quasi-circular formulation of the analytic models for a system described by $\left\{q, \vec{S_1}, \vec{S_2}\right\}$ that evolves from Ω_0 to merger. Each Ω_0 will correspond to a different initial momenta configuration that we could continuously vary resulting in a longer/shorter evolution. However, we must keep in mind two major points:

- Analytic models are known to deviate from the physical solution in the late inspiral of the evolution. This involves that all the physical magnitudes leading the evolution differ from the *real*[7] physical solution. The location of the late inspiral is quite compatible with the typical Ω_0's chosen by the NR codes, hence, the values of the initial momenta might also get deviated from the quasi-circularity, thus inserting a residual eccentricity in the evolution.

- The solution to the previous item would be trivial if we would have infinite computational resources: let us locate the initial distance D_0 far enough in order to get negligible PN deviations and, consequently, a non-eccentric representation of the Bowen-York initial data. However, this is rather unpractical since the computational cost for simulating a single orbit increases as we get further and further from the merger, being quite different across the parameter space.

Then, we must define an intermediate criterion which optimizes the combination of the two listed items. For waveform modeling purposes we typically demand to have about 20 NR cycles, which may be roughly converted to typical initial distances within $D_0 \in [12, 8]M$ (which will vary across the parameter space) and being these numbers still affordable in terms of the CPU hours. To illustrate this, see Figure 3.13 where we have plotted the time elapsed per orbit for a low mass-ratio (i.e. computationally not very demanding) system. Notice the pronounced increasing of the computational cost

[7] It is widely assumed by the gravitational wave community that, in general, the NR solutions represent the most faithful representation of the physical waveforms. In each LIGO detection the observed waveform have been matched to the closest NR representation to study possible GR deviations.

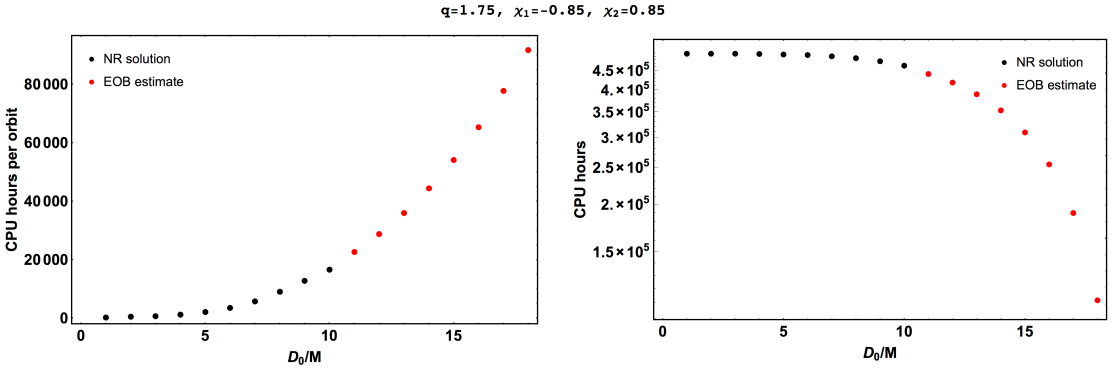

FIGURE 3.12: CPU hours per orbit (left panel) and cumulative CPU hours (right panel) for the simulation of BBH system with parameters $q = 1.75$ and $\{\vec{\chi}_1 = -0.85, \vec{\chi}_2 = 0.85\}$. In red we show the EOB estimate for the time elapsed per orbit while in black we represent the same quantity but for the NR simulation. It is clear the steep increase of the computational cost when reaching initial distances $D_0 > 12M$.

per orbit when moving the system further than $D_0 \sim 12$. At this stage, we do not still detect strong deviations from the analytic models: the PN and NR evolutions seem to agree. However, this match is not perfect and for some cases it creates the residual eccentricity shown in Figure 3.13.

3.4.3 Reducing the eccentricity in a real case

In Sec. 3.4.1 we have given the ingredients for reducing the eccentricity in the simplified case of a Keplerian orbit. As a first analysis, we apply the Newtonian corrections to the initial parameters as described in Sec. 3.4.1. Due to the high computational cost of these runs, I have chosen one highly eccentric case with $e = 0.013$ to show the full process. Thus, Figure 3.13 illustrates the evolution of three equal-parameter systems with three different degrees of eccentricity for a given separation $D = 11$. In this plot, the evolution with $e = 0.013$ represents the original eccentric data while the others result from applying the $1 \pm 2e$ corrections to the tangential momenta.

To reduce the eccentricity of this case to a more reasonable value $e_f \sim 10^{-3}$ (where the the subscript refers to the *final* eccentricity after the iteration) we apply a similar and simplified version of the iterative procedure described in [141]. Thus, we first aim to estimate the λ correction from the formulas shown in Sec. 3.4.1. Once the amplitude of the correction has been estimated, we must look at the position of the maximums and minimums to find out the direction of the correction (larger or lower than one) and then correct the tangential momenta by $p_t^1 = p_t^0(1 + \lambda) = p_t^0(1 + 2e)$ (superscripts denote the number of iterations performed) and where e can take positive and negative values. Thus, we are left to solve again the initial data for this new configuration and let the system evolve with a lower value of the eccentricity. Note that other agents as an ill

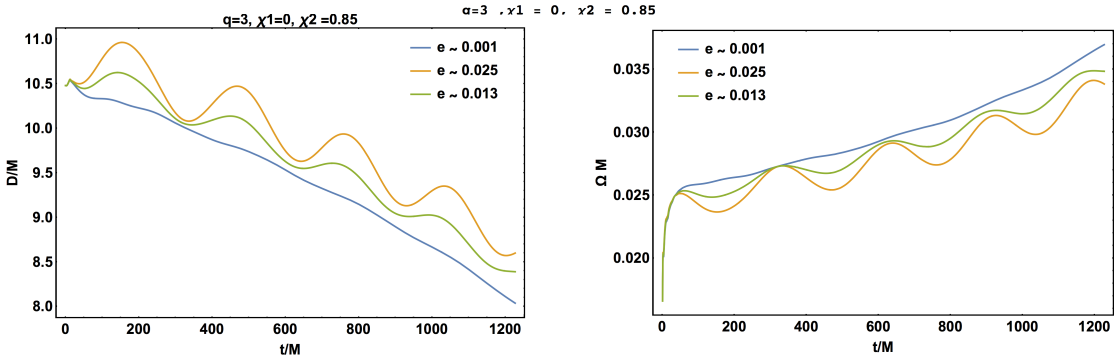

FIGURE 3.13: Shrinking of the orbital distance and frequency rising of a non-precessing BBH simulation with parameters $q = 3$ and $\{\vec{\chi}_1 = 0, \vec{\chi}_2 = 0.85\}$. The effects of the eccentricity not only makes the system fluctuate around the quasi-circular evolution but also shifts (delays or speeds up) the evolution. The primary run in this case is represented by the orange line while the others result after a first iteration for correcting e.

gauge choice may induce the system to oscillate although it normally does not last as long as the orbital eccentricity. In addition, in the optimal scenario, where all the gauge quantities have been calibrated carefully to minimise these effects, we have found that the mismatch in the initial momenta values is the most dominant agent in creating these oscillations.

The eccentricity is clearly related to the amplitude of the oscillations by (3.26) and (3.31). Then, we have worked out two different methods to estimate the amplitude of these oscillations: by fitting a lower order, time-dependent polynomial $p(t) \sim \mathcal{O}(t^{2-4})$ that fits the data neglecting the oscillations and, alternatively, using the well known results of the PN models. For the latter, we may need to correct the secular deviations that appear at late inspiral caused by the inaccuracy of the PN models. This is addressed by a cutting the PN expansions at low order and then complement them by adding a polynomial ansatz that is fitted to the data. Both methods share the same virtues and inconveniences; while the polynomial is PN independent so it does not propagate the possible mismatch of the PN evolution at the inspiral, it lacks at the same time of the physical PN intuition. Indeed, both arguments may be turned around to justify one or the other approach. In this work we have tested both algorithms obtaining a very good agreement between the two approaches.

The polynomial ansatz is chosen capture the smooth quasi-circular evolution (non-oscillatory) but taking care of not overfitting the data to not capture the oscillations. This typically involves to constrain the degree of the polynomial ansatz to $\mathcal{O}(t^{2-4})$:

$$p(t) = \sum_{n=0}^{2-4} b_n t^n \,, \tag{3.32}$$

On the other hand the 1PN terms of the evolution have been shown to be sufficiently accurate in order to capture the quasi-circular trend of the evolution. Then, the expanded 1PN $r(t)$ and $\Omega(t)$ read:

$$\theta = \left(\eta \frac{t_0 - t}{5}\right)^{-1/8} ,$$

$$\Omega(t) = (a\theta^3/(16\pi))(1 + b\theta^2 + c\theta^3 + d\theta^5) , \tag{3.33}$$

$$r(t) = D_0 \frac{(t_0 - t)}{t_0}^{1/4} \left(a + bt + ct^2\right) , \tag{3.34}$$

where η is the symmetric mass-ratio, D_0 the initial distance of the simulation[8], t_0 the 1PN estimate of the coalescense time and $\{a, b, c, d\}$ a set of free coefficients that capture the deviations from the 1PN term. Then, through (3.32) and (3.33) we capture the non-eccentric trend of the $r(t)$ and $\Omega(t)$ evolutions. Now, we are left to adjust the sinusoidal oscillations. To do so, we use the same functionality observed for the Keplerian problem (Sec. 3.4.1):

$$1 - f_{non-ecc}/f_{ecc}(t) \approx A \sin(\Omega(t)t + \phi_0) , \tag{3.35}$$

where $f_{non-ecc}$ is our non-eccentric fit (either the polynomial fit or the 1PN one), $f_{ecc}(t)$ is our eccentric function (r or Ω), $\Omega(t)$ the non-eccentric angular velocity (in this notation it is satisfied that $\Omega(t) = f_{non-ecc}$ if the orbital frequency is the quantity chosen to correct e) and $\{A, \phi_0\}$ the remaining two coefficients that adjust the amplitude and the time-shift of the oscillations. Then, we fit the sinusoidal ansatz to the first 4-5 cycles of the evolution to get an estimate of the eccentricity and that is related to the amplitude of the oscillation by $e = A$. However, these cycles can not be taken from $t = 0$ since the system is not yet relaxed until it overtakes the junk radiation emission which typically occurs at $t \sim 150$. Thus, for the sanity of the fit, we select the data after the junk emission which increases even more the computational cost of each iteration.

In Figure 3.14 and Figure 3.15 we show the results of the eccentricity estimate for the highly eccentric case shown in Figure 3.13 (green line) using the two mentioned methods: polynomial fitting and through a PN fit, repeating the analysis for the radial separation $r(t)$ and orbital frequency $\Omega(t)$. On the left panel of the figure, we illustrate the strength of the oscillation in relation to the non-eccenctric motion (3.35) with respect to the polynomial and PN fits. We see good agreement between the two predictions where we have obtained that $e = 0.012 \pm 0.001$ and where the error has been computed from the averaged differences between the fit and data amplitudes. The right panel shows the normal evolution of the oscillatory fits in relation to the non-oscillating ones and

[8]The initial distance is given in terms of the ADMTT coordinates. In the case of the `BAM` code there exist a good agreement between the code coordinates and the ADMTT ones. However, we have also found an agreement within the $\sim 1\%$ of match between this coordinates choice with alternative formulations as the SpEC code [84] for such far-merger regions.

the data. Both plots show a good match between the data and the oscillating fits thus ensuring an accurate estimate of e. There also exists a minimal offset between the PN-based fits and the polynomial-based ones. However, in this case this does not affect the estimate of the eccentricity since we are computing the amplitude of the oscillations with respect the non-eccentric fit, i.e., if there is any trend in the non-oscillating fit $f_{non-ecc}(t)$, it is immediately propagated to $f_{ecc}(t)$ (see (3.35)) thus keeping the relative amplitudes almost constant (within numerical accuracy). For the radial separation $r(t)$ the PN fit has not worked so well in this case likely caused by the step slope observed in the first stages of the evolution.

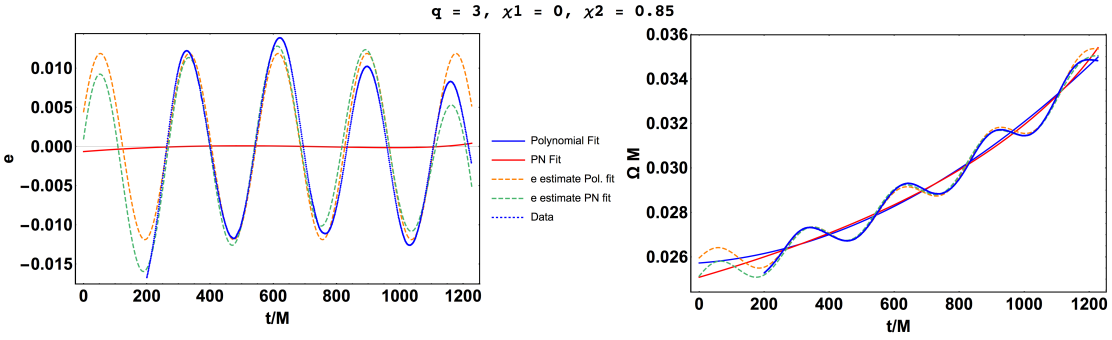

FIGURE 3.14: Eccentricity estimate of a BBH simulation with parameters $q = 3$ and $\{\vec{\chi}_1 = 0, \vec{\chi}_2 = 0.85\}$ using as an estimator the orbital frequency Ω. On the left panel we show the relative difference of the eccentric and non-eccentric evolutions with respect to the polynomial fit. On the right sided panel we show in blue and red the non-eccentric fits using polynomial and PN ansatze respectively while the dashed curves represent the eccentricity estimates by fitting a sinusoidal ansatze (3.35) to capture the oscillations.

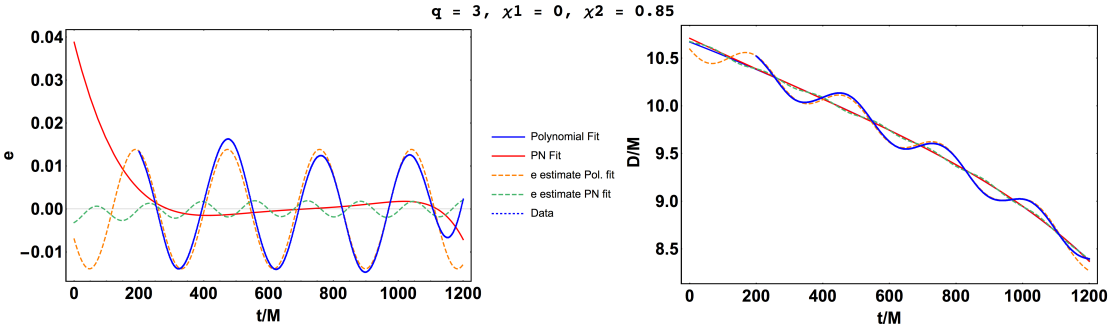

FIGURE 3.15: Eccentricity estimate of a BBH simulation with parameters $q = 3$ and $\{\vec{\chi}_1 = 0, \vec{\chi}_2 = 0.85\}$ using as an estimator radial coordinate separation r. We repeat the same analysis as in figure 3.14. Here we see that the PN fit does not work so well as for Ω.

Finally, in Figure 3.16 we show the results after applying the methods proposed in this section for the subset of the waveforms listed in Table 3.1. The points in red represent the original eccentricity computed in the first iteration for the cases with highest eccentricity. The points in black show the eccentricity after applying the λ corrections outlined in this section. Notice that for most of the cases the eccentricity is sufficiently reduced

after one single iteration, being reduced on average a factor of ~ 5. To avoid extra computational cost the eccentricity tests are performed in a low resolved grid where the moving boxes are resolved by 64 points (we use about 96 in highly resolved evolutions). This may create some extra noise in the orbital quantities that may be propagated to the eccentricity estimate (3.35). In these set of runs this effect has been shown to be negligible in relation to the errors originated by fitting only a reduced number oscillations (about 3-4). In this line, notice that the λ corrections needed are $\mathcal{O}(10^{-3)})$, i.e., very compatible with the fit errors. For this reason, it is sometimes difficult to reach lower values than $e \sim (10^{-3)})$.

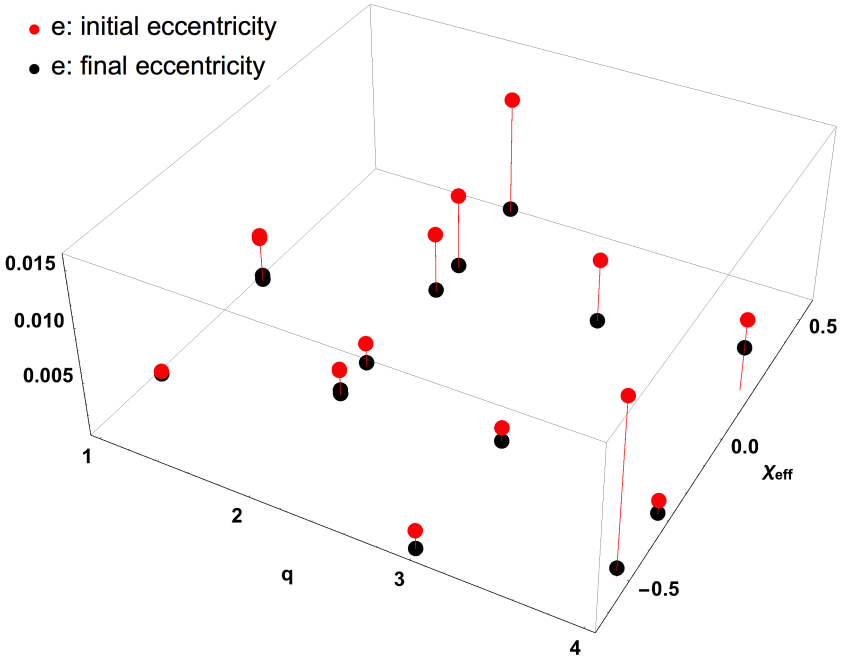

FIGURE 3.16: Eccentricity reduction for 15 of the 23 runs performed in this thesis. Here q is the mass-ratio and $\chi_{eff} = m_1\chi_1 + m_2\chi_2$. With the simplistic iterative method proposed in this chapter the eccentricity has been reduced about a factor ~ 5 for almost all the cases. We observe a minimal increasing in the initial e for positive χ_{eff} that might indicate some more lack of accuracy of the PN-EOB models in these regimes. The values labeled in black are low enough to avoid further iterations.

3.5 Time and frequency integration of the psi4

The frequency-domain gravitational wave models [38, 39] are calibrated through the so called *hybrid* waveforms [54, 119], built from the match of the inspiral part of the analytic models and the corresponding NR waveform. However, the natural waveform-related quantity obtained from the simulations is the ψ_4, which is related to the strain $h(t)$ through (3.14). This involves a double time integration of the $\psi_4(t)$ to get $h(t)$ and

a single time integration to get the luminosity $dE/dt = L(t)$, i.e.:

$$h(t) = \psi_4(t)|_{(t\to-\infty)} + \frac{d\psi_4(t)}{dt}|_{(t\to-\infty)} + \int^t \int^{t'} \psi_4(t')dt'dt\,, \tag{3.36}$$

$$L(t) = \frac{d\psi_4(t)}{dt}|_{(t\to-\infty)} + \int^t \psi_4(t')dt'\,, \tag{3.37}$$

A direct time integration of the data usually leads to non-secular drifts that can not be explained through the two unknown constants resulting from the time integration [142] and arise as numerical artifacts originated from noisy, finite and discrete data segments. While there exist different strategies to perform the $\psi_4(t)$ to $h(t)/L(t)$ conversion, in this thesis we will briefly describe two integrators defined in the Fourier domain: the fixed-frequency-integration (FFI) algorithm described in [142] and a modification of the FFI driven by the low frequency patterns observed in the Fourier domain 22 mode $\tilde{h}_{22}(f)$ and which are repeated across the parameter space [8].

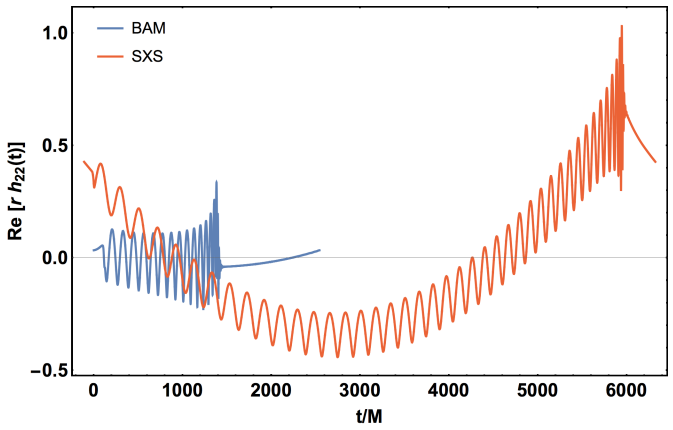

FIGURE 3.17: Time domain h_{22} mode strain computed from the 22 mode ψ_4 for a BAM (blue) and SXS (red) simulations with parameters $q = 1.5$, $\chi_1 = -0.5$ and $\chi_1 = 0.5$. The linear drifts are fairly evident in both cases. Both waveforms have been shifted to be centered at $h(t) \sim 0$.

FFI algorithm

The FFI algorithm [142] is a frequency-based integrator which eliminates the low frequency noise originated when operating in finite segments of the data by down-weighting the noisiest part by a factor f_0. It relies on the idea that all the frequency content must be contained in $[f_{0,orb}, f_{QNM}]$, where $f_{0,orb} \sim f_0$ is the first physical orbital frequency of the system, f_0 a tunable parameter similar to $f_{0,orb}$ and f_{QNM} the highest pole of the quasi-normal mode frequencies. Then, the algorithm is defined as:

$$\widetilde{h}\,(f) = \begin{cases} -\frac{\widetilde{\psi_4}(f)}{f^2}, & \text{if} \quad f \geq f_0\,, \\ -\frac{\widetilde{\psi_4}(f)}{f_0^2}, & \text{if} \quad f < f_0\,. \end{cases} \tag{3.38}$$

Although f_0 ideally should correspond to the first physical frequency, the noisy character of the numerical data, normally force us to tune it around an "optimal" value. Then, f_0 must be chosen such:

- Sufficiently large to not capture the increasing low frequency contribution.
- Sufficiently small to not apply a too restrictive factor that reduces too much the amplitude of the waveform in the inspiral regime.

Exponential Fit (EF)

The exponential-fit (EF) relies on the same idea proposed for the FFI algorithm: the application of a down-weighting function that reduces to the minimum the low-frequency noise artifacts. However, in this case we avoid the tuning of the f_0 parameter by fitting a restrictive exponential ansatz to the data contained between the first "clean" frequency (see Figure 3.18) and the minimum of the parabola formed at low frequencies. This pattern is repeated on the data across codes, and the parameter space and it has been shown to work for BAM, SXS, and GaTech waveforms.

The performance of the different methods is shown in Figure 3.18 where we show the effect of a straightforward Fourier transform (`BAM` and `SpEC` $\tilde{h}_{22}(f)$ waveforms in blue and red) and how the two algorithms smoothly drive the amplitude of the low frequency regime to zero.

Both methods described has been proven to be consistent with each other [8] as long as the f_0 is selected properly and the data used for the exponential fit is sufficiently well sampled. We have tested this method across the parameter space not finding any significant deviations between both approaches.

3.6 Extrapolation

The gauge independence of the waveforms is only strictly satisfied at null infinity $\mathcal{J}^+$ where a natural inertial coordinate system can be defined. However, most of NR codes resolve a finite domain thus restricting the computation of any quantity at a finite time/spatial coordinates. This may insert some well known distortion as the $1/r$ corrections considered in Sec. 3.3.2. There exist different strategies for taking the waveform quantities to null infinity; by polynomial extrapolation [60], by means of the Cauchy-characteristic extraction [143, 144] or by combining the results of the perturbation theory with the zero order $r\psi_4(r,t)$ solution [120].

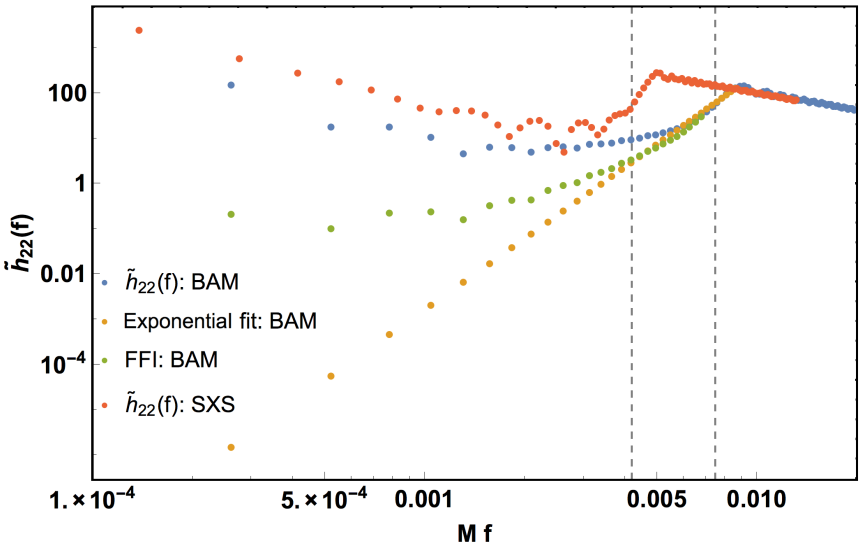

FIGURE 3.18: Frequency domain 22 mode strain computed from the 22 mode ψ_4 from BAM (blue) and SXS (red) simulations with parameters $q = 1.5$, $\chi_1 = -0.5$ and $\chi_1 = 0.5$. In the plot we show the low frequency behavior for both simulations and how the FFI (green) and Exponential Fit (orange) algorithms down-weight the artificial frequency increasing when approaching to $f \sim 0$. The two gridlines lines fix an optimal f_0's choice for the two respective runs.

In this work we have computed final spin and radiated mass from both radiative and horizon quantities, being the radiative ones used as an estimator of the NR error. Moreover, the peak luminosity is uniquely defined from the waves thus forcing us to analyse the extrapolation effects not only on `BAM` waveforms but also on waveforms from other codes (see for instance Sec. 4.3.10.2). Here, we have followed a prescription similar to [60] to take the quantities to null infinity J^+. Far from the source, the waves travel along outgoing null geodesics described in a Schwarzschild space-time,

$$u = T - r_*(R) \quad , \quad r_*(R) = R + 2M_{ADM} \log \frac{R}{2M_{ADM}} - 1 \,, \tag{3.39}$$

where u is the retarded time, R and T are the Schwarzschild radial and time coordinates and where all the NR codes considered in this work satisfy,

$$\lim_{r\to\infty} r = R \,, \qquad \lim_{r\to\infty} t = T \,. \tag{3.40}$$

Then, the polynomial extrapolation works as follows: fix several retarded times u_i and then study the dependence of some quantity $f(u_i, r)$ on the radius r_i. Then, fit the finite radii data with a polynomial as,

$$f(u_i, r) = \sum_0^p \frac{a_n}{r^n} \,. \tag{3.41}$$

In our case, $f(u_i, r)$ is chosen to be the amplitude of the wave and where we fix $u_i = t_{max}$,

being t_{max} the time of the maximum amplitude and p the extrapolation order. In Figure 3.19 we show the results of polynomial extrapolation on a BAM case with $q = 18$, $\chi_1 = 0$, $\chi_2 = -0.4$ (left panel) and on a SXS (right panel) case with $q = 1$, $\chi_1 = 0.97$, $\chi_2 = 0.97$. The quantity $f(u_i, r)$ studied here is the maximum amplitude $\psi_4(t_{max}, r)$ and plotted in terms of $1/r$. As expected, in both cases we have a good agreement between the r^{-1} and r^{-2} fits which validates the $1/r^n$ expansion of (3.41) and motivated in Sec. 3.3.2 from perturbation theory. The shadowed regions represent the 90% credible intervals for each fit and that can be used as an estimate of the extrapolation error.

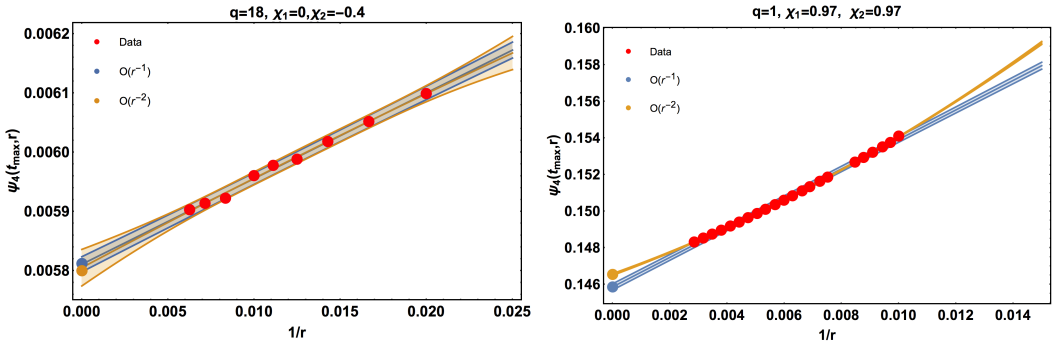

FIGURE 3.19: Extrapolation of the maximum amplitude $\psi_4(t_{max}, r)$ for an `BAM` $q = 18$, $\chi_1 = 0$, $\chi_2 = -0.4$ case (left panel) and a `SpEC` $q = 1$, $\chi_1 = 0.97$, $\chi_2 = -0.97$ (right panel). In red we plot the data at $\psi_4(t_{max}, r_i)$ whereas the blue points represent the $\mathcal{O}(r^{-1})$ and $\mathcal{O}(r^{-2})$ extrapolated values. The shadowed regions give us the 0.9 credible intervals for each fit. Notice that we are plotting here $1/r$.

The polynomial expansion described in this section and shown in Figure 3.19 have been relevant for the computation of the peak luminosity as well as the final mass and final spin from the radiation. In Chapter 4 we explain these effects on a more general data set where several codes fill our parameter space. In this line, we have seen that the different tetrad convention used in the `SpEC` code may induce substantial differences in the finite radii ψ_4. By comparing cases with equal physical parameters with other codes (Chapter 4) we have observed steeper slopes on finite radii data thus making the extrapolation to infinity essential. Finally, SXS and BAM waveforms used in this work have been extrapolated with the method outlined in this section.

Chapter 4

Hierarchical data-driven fitting of BBH mergers

Numerical relativity is an essential tool in studying the coalescence of binary black hole systems (BBHs). It is still computationally prohibitive to cover the BBH parameter space exhaustively, making phenomenological fitting formulas for BBH waveforms and final-state properties important for practical applications. In this chapter, we describe a general hierarchical bottom-up fitting methodology to design and calibrate fits to numerical relativity simulations for the three-dimensional parameter space of quasicircular nonprecessing BBHs, spanned by mass ratio and the individual spin components following the novel results presented in [7, 8]. Particular attention is paid to incorporating the extreme-mass-ratio limit and the subdominant unequal-spin effects. As an illustration of the method, we provide three different applications: a fit to the final spin and final mass (or equivalently, radiated energy) of the remnant black hole (Sec. 4.2) and to the peak luminosity (Sec. 4.3). Then, using a total of 427 numerical relativity simulations for the final mass and final spin fits and 457 for the peak luminosity (including the Teukolsky and RWZ waveforms mentioned in Sec. 4.1.5), we obtain results broadly consistent with previously published fits, but improving in overall accuracy and particularly in the approach to the extreme limit and for unequal-spin configurations. We also discuss the importance of data quality studies when combining simulations from diverse sources, how detailed error budgets will be necessary for further improvements of these already highly accurate fits, and how this first detailed study of unequal-spin effects helps in choosing the most informative parameters for future numerical relativity runs.

4.1 Hierarchical data-driven approach

4.1.1 Motivation

Phenomenological waveform models [38, 39, 53, 54, 68, 69], as well as other NR data-based models (final spin, final mass etc.) complement the information known from the analytic prescriptions by fitting different ansätze to NR data. In particular, nonprecessing, quadrupolar models provide a really accurate prescription of the strong GR regime, where the analytic representation of the waveforms can not be longer trusted. Then, the physical reliability of these fits will depend on different factors that may range from the match of the ansätze to the actual physics, the number of data points used in the calibration, how these points are spanned across the parameter space and the quality of the NR data. Not all of these considerations were totally satisfied in the old phenomenological waveform models, where the ansätze coefficients (see Chapter 5) used to be mapped to the physical parameter space by means of of two parameter polynomials as,

$$\Lambda^i = \sum_{m,n} (\lambda^i_{mn} \eta^m) S^n_{eff} \,, \tag{4.1}$$

being again S_{eff} a given parametrization of the spin and where all the inspiral merger and ringdown coefficients were fitted through the same ansatz. In this line, a similar ansatz was also used for the calibration of the old final mass and final spin fits [38] where the match to the NR data was more than satisfactory in the low mass-ratio regime but observing larger deviations in the high-spin and high mass-ratio regime. This inaccuracy was not only explained by the lack of data but also helped by the rigidity in the choice of the ansätze. Some of the considered weak points were:

- The known analytic results as the extreme mass-ratio limit were not satisfactorily incorporated. The proper accounting of this limit helps to calibrate the fits also in the intermediate regions by smoothing out the interpolation to the extreme regime.
- The prescription of the coefficients through two parameters has been sufficient but not optimal for parameter estimation purposes. Although they are known to dominate the dynamics of BBH mergers, other subdominant effects as the unequal spin terms may become relevant for a better estimate of the physical parameters and in particular, of the individual spin components.
- The root mean square errors were the only quantity used to assess the quality of the fits and to rank them. While they provide a useful measure of how the pair fit-data is related, they do not account for the possible overfitting carried by (4.1).

In this work, we have addressed the last points by replacing (4.1) by a list of ansätze based on rational functions (more suitable for the fitting of the extreme mass-ratio limit), ranked by information criteria magnitudes and where the extreme mass-ratio and the unequal spin effects have been also accounted for. Then, we build up the fits from lower to higher dimensions in order of importance (hierarchically), where the most populated regions of the parameter space are used to constrain the fits. All of this has been synthesised in a workflow that has been tested in the calibration of the final spin, radiated energy and peak luminosity and which will replace (4.1) in the new calibration of PhenomD model (Chapter 5).

4.1.2 Flowchart

We develop our hierarchical approach with the aim to ensure an accurate modelling of the subdominant spin-difference effects and the extreme regions, along the lines illustrated as a flowchart in Figure 4.1. First we study the one-dimensional subspaces of nonspinning and of equal-mass-equal-spin black holes, being the regions where more NR data is accumulated. Then, we combine and generalize these subspace fits by adding additional degrees of freedom to cover the entire two-dimensional space of equal-spin black holes but also constraining the generalized ansatz with information from the extreme-mass-ratio limit. The approach to this limit is performed either in form of analytic expressions or by directly including low mass-ratio data (see Sec. 4.1.5). In a third step, we investigate the leading subdominant terms, which are dominantly linear in the spin difference $\Delta\chi$. We finally produce a three-dimensional fit to the complete data set from this new hierarchical ansatz. Doing so, we can construct a full ansatz with a relatively low number of free fit coefficients and avoid the overfitting of spurious effects caused by small sample sizes, while still capturing the essential physical effects.

At each step, we evaluate the performance of different fit choices by several quantitative measures: by the overall residuals, by the Akaike and Bayesian information criteria (AICc, BIC, [145, 146]), and by how well determined are the individual fit coefficients. The information criteria are model selection tools to choose between fits with comparable goodness of fit but different degrees of complexity, i.e. they penalize high numbers of free coefficients. See Section 4.1.6 for details on these statistical methods.

4.1.3 NR data as a driver of the phenomenological fits

Since the 2005 breakthrough [46] the different NR groups have concentrated their efforts in covering the physical parameter space with several BBH simulations to obtain increasingly faithful descriptions of the gravitational waves emitted. However, given the

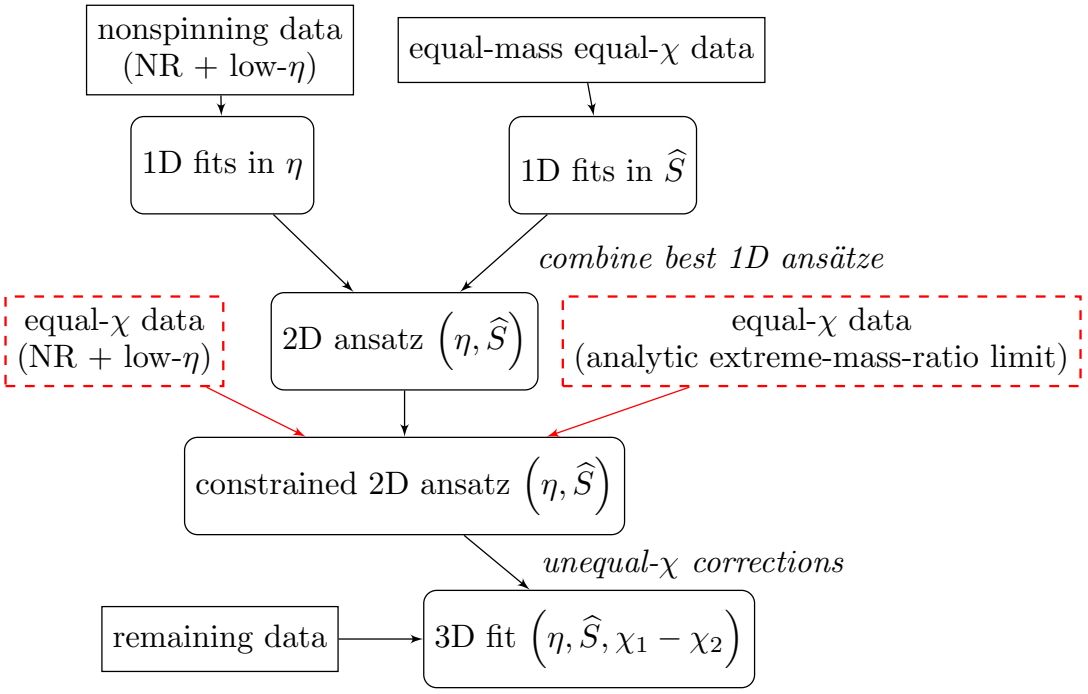

FIGURE 4.1: Flowchart of the hierarchical step-by-step construction leading to a three-dimensional ansatz and fit for the quantity of interest over the $(\eta, \chi_1, \chi_2) \equiv \left(\eta, \widehat{S}, \Delta\chi\right)$ space. The only variation between the final state fits and the peak luminosity fit is how we process the extreme mass ratio limit (see 4.1.5).

technical difficulties and computational cost of the runs, the coverage of the physical space has continued to grow rather asymmetrically not only motivated by technical considerations but also supported by the astrophysical expectations. I list below some of these considerations:

1. Old astrophysical event rate estimates [26, 147] (previous to the first GW detection) predicted mass distributions very peaked at equal-mass systems. Indeed, these predictions are quite consistent with the actual GW observations [24] which seem to favor the formation of systems with $m_1 \approx m_2$.

2. Equal-mass, nonprecessing, and slowly-spinning systems require less "technical complexity" from the NR point of view. The symmetries of the system allow to speed up of the performance of the simulations by reducing the complexity of the grids that resolve the system.

3. Although there is not much astrophysical information constraining the spin orientation, the systems with equal spin and parallel to the total angular momentum ($\vec{S}_i\vec{L} = +|S||L|$) are predicted to be the most powerful GW emitters. This led both GW and NR community to focus the calibration of the models to the spin-aligned region, putting some more emphasis in the positive alignment.

4. Special attention has been also payed to non-spinning systems since they represent a natural guideline for going sequentially to higher mass-ratios while monitoring the level of difficulty in the way to the high mass-ratio region.

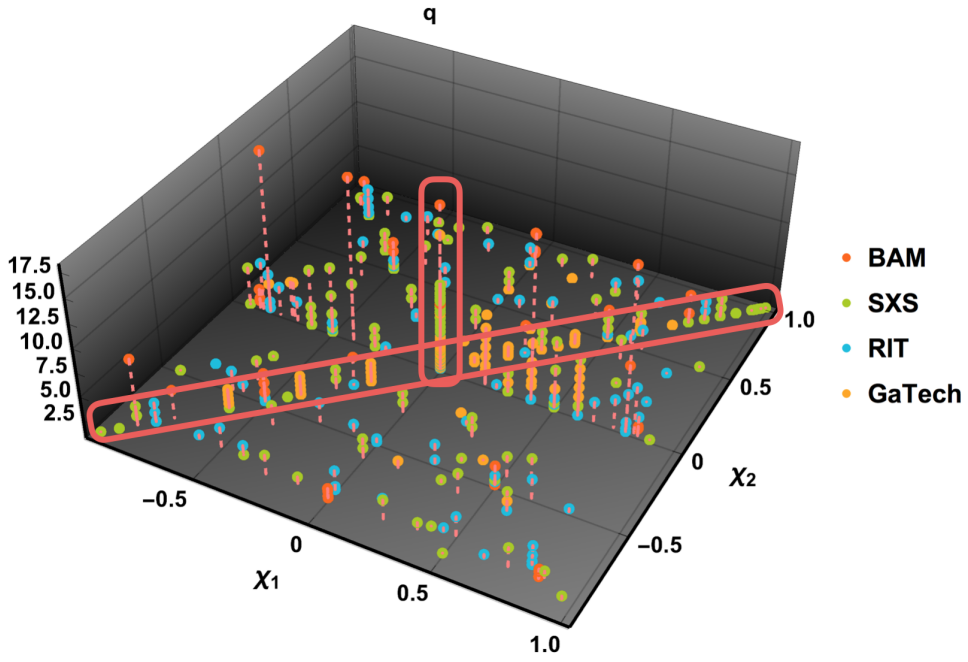

FIGURE 4.2: NR data used for the final mass and radiated energy fits spanned by mass-ratio $q = m_1/m_2$ and the two dimensionless spin components χ_1, χ_2, where the color indicates the source catalog. The two perpendicular red regions determine the equal-spin $\chi_1 = \chi_2$ (vertical frame) and the non-spinning $\chi_1 = \chi_2 = 0$ configurations (horizontal) where it is clear the overdensity of points.

All these considerations have given way to the generation of the parameter space illustrated in Figure 4.2, where we have collected NR data from four different codes: `BAM` [72], `SpEC` [84], `LAZEV` [85] and `MAYA` [6]. This data set has been the basis to calibrate the final spin, energy radiated and peak luminosity fits and where the hierarchical build-up of the model is sustained by the clear overdensity of points in the low mass-ratio and non-spinning zones.

4.1.4 Spin parametrization and unequal-spin motivation

From PN theory, one can read off that the leading-order spin effect on the binary's inspiral phase [39, 148–150] is proportional to:

$$S_{eff} = \chi_{PN} = \frac{\chi_1 m_1 + \chi_2 m_2}{M} - \frac{38\eta}{113}(\chi_1 + \chi_2) \tag{4.2}$$

where M is the total mass of the system (that is set to 1), m_i the mass of the BHs, η the symmetric mass-ratio, χ_i the dimensionless spin and S_{eff} labels one possible spin parametrization. Such PN-based effective spin parametrization comes out from the dominant spin-orbit terms and is shown to be valid not only during the inspiral phase (where PN theory is still reliable) but also for the calibration of the merger-ringdown regime. The situation described is similar for the current final state fits [7, 8, 151] where the spin dependence is parametrized following a similar PN-based intuition but without restricting ourselves to a unique definition of S_{eff}. In this work and for the final spin, radiated energy and peak luminosity fits we have tested three different definitions of S_{eff}:

$$\widehat{S} = \frac{S}{m_1^2 + m_2^2} \qquad S = \frac{m_1^2\,\chi_1 + m_2^2\,\chi_2}{M^2} \qquad \chi_{\rm eff} = \frac{m_1\chi_1 + m_2\chi_2}{M} \tag{4.3}$$

where all of them satisfy that $S_{eff} \in [-1, 1]$ and that $\widehat{S} = S = \chi_{\rm eff}$ in the extreme mass-ratio limit ($m_1 \gg m_2$).

Then, we follow a similar PN-based argument for the definition of the unequal spin parameter by looking at the leading order $\Delta\chi = \chi_1 - \chi_2$ terms, which come out as (see the appendix of [39]):

$$f(\eta)\Delta\chi + \mathcal{O}(g(\eta)S_{eff}\Delta\chi + h(\eta)\Delta\chi^2) \tag{4.4}$$

where $f(\eta)$, $g(\eta)$ and $h(\eta)$ are functions that only depend on the symmetric mass-ratio η and that we adjust to model the full 3D-unequal spin dependence (see Section 4.2).

Although the PN expressions reveal the presence of the unequal spin terms, there are also some evidences from the point of view of the phenomenological fitting. A study of the residuals of two-dimensional (η, S_{eff}) fits [38] for the final spin and energy radiated with respect to unequal spin data (Section 4.2.1) reveal the subdominant deviations predicted by these terms. For final spin, we find that 90% of relative errors are below 3% which suggests that unequal-spin effects make a large contribution to these small errors, as shown by four times smaller 90% quantiles when restricting to equal-spin cases only. See also Figure 4.3 for histograms of these distributions. For radiated energy, 90% of relative errors are below 2%, with a reduction of that quantile by 1.4 for equal-spin cases only, indicating that spin-difference effects are even smaller for this quantity, which we will also see confirmed in our final results.

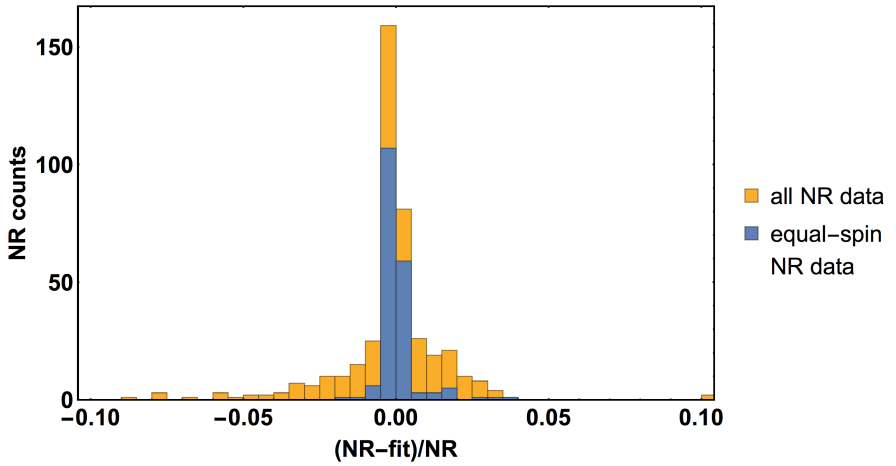

FIGURE 4.3: Relative errors in final spin of the combined NR data set for this paper under the two-dimensional PhenomD fit [38].

4.1.5 Extreme-mass-ratio limit

The computational cost of numerical simulations of BH binaries in full general relativity diverges in the extreme-mass-ratio limit $\eta \to 0$[1]. However, in this extreme zone, the evolution is equivalent to the much simpler case of a test particle orbiting a Kerr black hole where many quantities are known analytically (see [152] and for final spin and final mass and [153, 154] for the peak luminosity). Then, we have adapted the various ansätze to this well known limit either by constraining directly the fit coefficients (final spin and energy radiated) or through a direct calibration to high mass-ratio data (peak luminosity). With this, we reduce the possible extrapolation artifacts originated by the sparsity of the data in this region. In this section, we describe both approaches.

Extreme-mass-ratio limit: final spin and radiated energy

The energy and orbital angular momentum in the extreme mass-ratio limit have long been known analytically for the final mass and final spin [152]: inserting the radius of the innermost stable circular orbit (ISCO) from Eq. (2.21) of [152] into Eqs. (2.12) and (2.13) of the same reference yields the test-particle energy (equivalent to the radiated energy) and orbital angular momentum at ISCO:

$$E_{\rm ISCO}(\eta,\chi) = \eta\left(1-\sqrt{1-\frac{2}{3\,\rho_{\rm ISCO}(\chi_{\rm f})}}\right), \tag{4.5a}$$

$$L_{\rm orb,ISCO}(\eta,\chi) = \frac{2\eta\left(3\sqrt{\rho_{\rm ISCO}(\chi)}-2\chi\right)}{\sqrt{3\,\rho_{\rm ISCO}(\chi)}}, \tag{4.5b}$$

[1]Using the `TaylorT2` approximant we get a time estimate of $T \sim f_0^{-8/3}/\eta$ where f_0 is the innermost stable circular frequency.

with

$$\rho_{\rm ISCO}(\chi) = 3 + Z_2 - {\rm sgn}(\chi)\sqrt{(3-Z_1)(3+Z_1+2\,Z_2)}, \tag{4.6a}$$

$$Z_1(\chi) = 1 + (1-\chi^2)^{1/3}\left[(1+\chi)^{1/3} + (1-\chi)^{1/3}\right], \tag{4.6b}$$

$$Z_2(\chi) = \sqrt{3\chi^2 + Z_1^2}\,. \tag{4.6c}$$

Note that both $E_{\rm ISCO}$ and $L_{\rm orb,ISCO}$ depend linearly on η.

In the test-particle limit, the small BH plunges after reaching the ISCO, and further mass loss scales with η^2 [155]. Similar to previous work [91, 151, 156, 157], we will exploit this fact to compute the final spin and radiated energy to linear order in η from the analytical expressions, (4.5), holding at the ISCO. To linear order in η, we thus simply have $E_{\rm rad} = E_{\rm ISCO}$ or $M_{\rm f} = 1 - E_{\rm ISCO}$ for the final mass, and for the final spin $\chi_{\rm f}$ we obtain the implicit equation

$$\chi_{\rm f}\, M_{\rm f}(\eta, \chi_{\rm f})^2 = L_{\rm orb,ISCO}(\eta, \chi_{\rm f}) + S_1 + S_2\,, \tag{4.7}$$

being $L_{\rm orb}$ the quantity we chose to fit in order to eliminate the trivial dependence in $S_1 + S_2$ (see Section 4.2.2). The individual BH spins can be written in terms of our effective spin as

$$S_1 + S_2 = (1 - 2\eta)\,\widehat{S}\,. \tag{4.8}$$

Equation (4.7) can then be solved numerically for the final spin $\chi_{\rm f}$ as a function of η and of the effective spin $\widehat{S}$. Since this result holds to linear order in η, and assuming that the final spin and mass are regular functions of η, we have thus essentially computed the derivatives $\partial E_{\rm rad}/\partial\eta$ and $\partial\chi_{\rm f}/\partial\eta$ at $\eta = 0$, in addition to the values at $\eta = 0$, which are $E_{\rm rad}(0) = 0$ and $\chi_{\rm f}(0) = S_1/M^2$.

Additionally, assuming that the final state is indeed a Kerr BH, its final spin has to satisfy $\chi_{\rm f} \leq 1$. One would also expect the final spin for maximal effective spin, $\widehat{S} = 1$, to decrease monotonically with increasing η. To construct an accurate fit in a neighborhood of $\widehat{S} \to 1$ that satisfies these expectations – in particular the Kerr limit – we will constrain our ansatz with the analytically computed value of $\chi'_{\rm f} = \partial\chi_{\rm f}/\partial\eta$ at $(\eta = 0, \widehat{S} = 1)$. By perturbing (4.7) around $\{\eta \to 0, \chi_{\rm f} \to 1\}$ to linear order before taking the derivative in η at the same point, we find

$$\chi'_{\rm f}\left(\eta \to 0, \widehat{S} \to 1\right) = 0\,. \tag{4.9}$$

Several variations of this procedure have been used for previous final-spin fits, and differences are due to previous works neglecting the radiated energy in (4.7) [91, 157], or not enforcing the derivative for satisfying the Kerr limit [151].

Extreme-mass-ratio limit: peak luminosity

For the peak luminosity, it is known [153, 154] that the leading-order term as $\eta \to 0$ must be $L_{\rm peak} \propto \eta^2$, with the symmetric mass ratio $\eta = (m_1 m_2)/(m_1+m_2)^2 = q/(1+q)^2$. However, no fully analytical results for the spin dependence in the extreme-mass-ratio limit exist. Instead, here we constrain our fit by numerical results for finite, but very large mass ratios produced by Refs. [158] and [95] which evolve BBH mergers in the test-mass (large-mass-ratio) limit by combining a semi-analytical description of the dynamics with a time-domain numerical approach for computing the multipolar waveform based on BH perturbation theory. Waveforms are calculated by solving either the Regge-Wheeler-Zerilli (RWZ) 1+1 equations (nonspinning case) or the Teukolsky 2+1 equation (spinning case). Follow Refs. [8, 93–95] for a detailed description of this method.

In this work we use only the Teukolsky results at $q = 10^3$ (31 data points) and the RWZ results at $q = 10^4$ and $q = 10^5$ (7 data points each), as the RWZ at $q = 10^3$ are expected to be less accurate, and indeed their luminosities deviate at negative χ_1.

4.1.6 Model selection criteria and ranking statistics

One of the major novelties of this work regarding the phenomenological modelling and ansätze selection is the ranking of ansätze by several model selection tools (not used in the previous phenom models [38, 39, 53, 54] and final state fits [92, 151, 159]) and the usual residuals-based definitions. Thus, we rank fits by several standard statistical quantities which are briefly summarized here for the benefit of the reader.

A basic figure of merit is the root-mean-square-error,

$$\mathrm{RMSE} = \sqrt{\frac{1}{N_{\rm data}} \sum_{n=1}^{N_{\rm data}} \left[X_{\rm NR}(\eta_n, \chi_{1,n}, \chi_{2,n}) - \mathrm{fit}(\eta_n, \chi_{1,n}, \chi_{2,n})\right]^2}\,, \tag{4.10}$$

which just checks the overall goodness of fit. One caveat here is that down-weighted NR cases are fully counted in the RMSE, so that a generalized variance estimator using weights can be more useful.

Furthermore, it is important in model selection to penalize models with too many free coefficients, as in principle the RMSE can be made arbitrarily small when the number of coefficients approaches the number of data points. A popular figure of merit for model selection considering the number of coefficients is the Akaike information criterion [145],

$$\mathrm{AIC} = -2 \ln \mathcal{L}_{\rm max} + 2 N_{\rm coeffs}\,, \tag{4.11}$$

which intuitively can be understood as weighing up goodness of fit (measured by the maximum log-likelihood $\mathcal{L}_{\max}$) against parsimony. Standard implementations, as the one from Wolfram Mathematica, assume Gaussian likelihoods.

A generalization that corrects the AIC for low numbers of observations and reproduces it for large data sets is the AICc:

$$\mathrm{AICc} = \mathrm{AIC} + \frac{2N_{\mathrm{coeffs}}(N_{\mathrm{coeffs}}+1)}{N_{\mathrm{data}} - N_{\mathrm{coeffs}} - 1}\,. \tag{4.12}$$

In this work, we always use AICc instead of AIC.

A related quantity, similar in form but with a completely different theoretical justification and with subtle differences in practice, is the Bayesian information criterion or Schwarz information criterion [146]:

$$\mathrm{BIC} = -2\ln\mathcal{L}_{\max} + N_{\mathrm{coeffs}}\ln(N_{\mathrm{data}})\,. \tag{4.13}$$

Though based on an approximation to full Bayesian model selection (while the AIC is derived from information theory), the BIC in general cannot be interpreted as a direct measure of Bayesian evidence between models.

For all of AIC, AICc and BIC, the model with the *lowest* value is preferred. Higher than unit differences between two models are generally required to count as significant evidence; [160] quotes ± 5 as "strong" and ± 10 as "decisive" evidence. In addition, to augment our model selection criteria we also demand the well-constrainedness of each individual fit coefficient, allowing for picking a fit with slightly worse summary statistics (though requiring a goodness compatible with the previous values) if it has better-constrained coefficients; or we drop individual coefficients from a high-order ansatz and reassess the quantitative criteria for that reduced model.

As an example of how e.g. the BIC can guide model selection, we show in Figure 4.4 the BIC ranking for the one-dimensional $L'_{\mathrm{orb}}\left(\eta, \widehat{S}=0\right)$ fits from Section 4.2.3. A plateau of almost constant BIC is made up of several fits with $N_{\mathrm{coeffs}} \geq 3$, with the more complex fits yielding no additional improvement, so that we choose the simplest fit among this group. Still, even if it had not come up actually top-ranked, as in this case, choosing a low-N_{coeffs} fit from within the high-ranked group would be preferable over some slightly higher-ranked, but less-well-constrained fit.

Then, this ranking procedure is applied at each step in the build-up of the three-dimensional fit to obtain the most statistically faithful fit form the zoo of ansätze proposed. The selection process is applied for the final spin, radiated energy, peak luminosity and also for the new calibration of the fit coefficients described in Chapter 5.

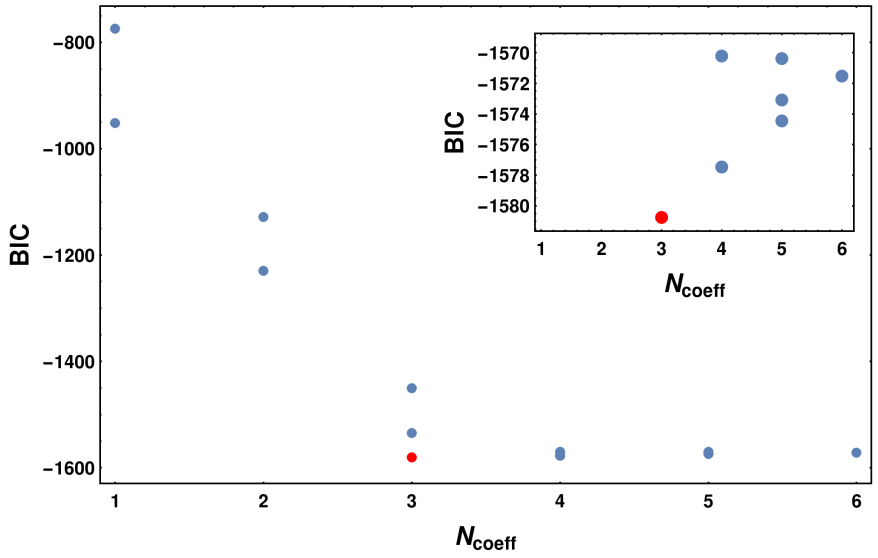

FIGURE 4.4: BIC example for the one-dimensional final spin $L'_{\text{orb}}\left(\eta, \widehat{S}=0\right)$ fits from Section 4.2.3. The inset panel is a zoom-up of the top-ranked fits. The tested set of ansätze includes all polynomials from second to seventh order in η and all rational functions of order (i, j), $j \leq i$, up to $i + j = 6$. The preferred ansatz, a rational function of order (3,1) with three free coefficients, is highlighted.

4.1.7 Fit uncertainties

The uncertainty of evaluating a fitted quantity Q at a point (η, χ_1, χ_2) can be expressed through *prediction intervals* [161]

$$Q\left(\eta, \chi_1, \chi_2\right) \pm q_t\left(x, N_{\text{data}} - N_{\text{coeffs}}\right) \sqrt{\widehat{\sigma}^2 + \sigma_{\text{fit}}^2}\,, \tag{4.14}$$

where q_t is the student-t quantile for a confidence level x, $\widehat{\sigma}^2$ is the error variance estimator from the (weighted) mean-square error of the calibration data under the fit, and σ_{fit}^2 is the standard error estimate of the fitted model, which for a single-stage fit is

$$\sigma_{\text{fit}}^2 = \text{grad}^t\left(\eta, \chi_1, \chi_2\right) \cdot \mathcal{C}_{\text{fit}} \cdot \text{grad}\left(\eta, \chi_1, \chi_2\right) \tag{4.15}$$

with the gradient vector $\text{grad}\left(\eta, \chi_1, \chi_2\right)$ of the fit ansatz in the coefficients, evaluated at this point, and the covariance matrix $\mathcal{C}_{\text{fit}}$ of the fit. Note that (4.14) gives the uncertainty for a single additional observation, as opposed to the narrower *confidence interval* of the mean prediction, which lacks the $\widehat{\sigma}^2$ term.

In our hierarchical fitting approach, to propagate the uncertainties from the nonspinning, equal-mass and extreme-mass-ratio limits, we have to assume that the uncertainties in these regimes and that of the final fit are independent, so that we can take the full covariance matrix as a block-diagonal composition of these four contributions. The half

width of a prediction interval at confidence x is then

$$q_t\left(x, N_{\rm data} - N_{\rm coeffs}\right) \sqrt{\widehat{\sigma}^2 + \sigma^2_{\rm final} + \sigma^2_{\eta} + \sigma^2_{\widehat{S}} + \sigma^2_{\eta=0}}\,. \tag{4.16}$$

As these three particular regimes are significantly better constrained than the bulk of the parameter space (which is the main motivation for the hierarchical approach, in the first place), their uncertainty contribution is small, so that the accuracy of this approximation is not critical.

4.2 Hierarchical data-driven fitting: Application to final spin and energy radiated

We first apply the hierarchical method to the final spin and final mass (energy radiated) of the remnant black hole. Both quantities are crucial to obtain the frequencies of the quasinormal-mode ringdown [162–165] for the calibration of the ringdown regime in full inspiral-merger-ringdown waveforms [38, 39, 53, 63, 64, 69, 166, 167]. Although final mass and final spin are actually known to a level of accuracy still unreachable by the LIGO parameter estimation pipelines they can also be obtained from bayesian analysis to the full waveforms with an accuracy similar to other BBH parameters [13, 24]. Then, these phenomenological fits provide a parallel, accurate and fast shortcut to final state values avoiding a full waveform analysis and that might be relevant in future observations of stronger GW signals.

Apart from GW observations, the final state of a BBH merger is astrophysically interesting in itself, e.g. for the computation of merger trees [168–175]. The mass and spin of BHs surrounded by matter, e.g. accretion disks, may also be inferred from electromagnetic observations (see [176, 177] for stellar-mass BHs and [178–180] for supermassive BHs).

In this work, we concentrate on nonprecessing quasicircular BBHs, where the black hole spins are parallel or antiparallel to the total orbital angular momentum of the binary. These configurations are fully described in a three-dimensional parameter space: given the masses $m_{1,2}$ and physical spins $S_{1,2}$, we use the two component spins $\chi_1 = S_1/m_1^2$ and $\chi_2 = S_2/m_2^2$ and the mass ratio, given either as $q = m_1/m_2$ with the convention $m_1 > m_2$, or as the symmetric mass ratio $\eta = (m_1 m_2)/(m_1 + m_2)^2 = q/(1+q)^2$. The total mass is only a scaling factor, and here we work in units of $m_1 + m_2 = 1$. Then, here we exploit and investigate this structure by parametrizing spin effects in terms of an effective spin $\widehat{S}$ and a spin-difference parameter $\Delta\chi = \chi_1 - \chi_2$. As the effective spin we choose $\widehat{S}$ described in (4.3).

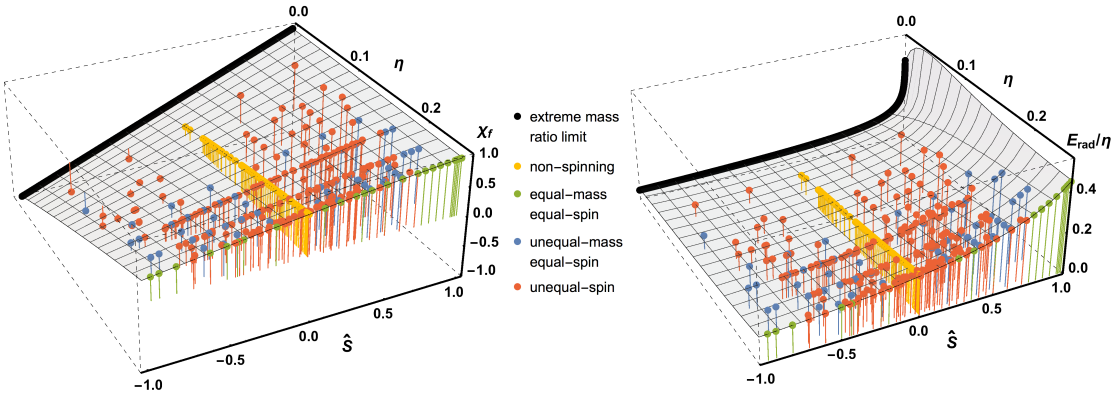

FIGURE 4.5: Input data plotted against symmetric mass ratio η and effective spin $\widehat{S}$. Data consist of the combined set of NR simulations (colored points) and the analytically known [152] extreme-mass-ratio behavior (black line). Left panel: final spin; right panel: radiated energy rescaled by η. Both $\chi_{\rm f}$ and $E_{\rm rad}/\eta$ follow a smooth surface in this space, and the well-constrained 1D subspaces together already give a good indication of its curvature.

4.2.1 NR data selection

We combine four data sets of nonprecessing, aligned-spin numerical relativity BBH simulations from independent codes and sources: the public SXS [4, 89], RIT [91, 92] and GaTech [6, 90] catalogs as well as a set of simulations performed with the `BAM` code [38, 72, 181], including 27 new cases for which initial configurations and results are listed in Table 3.1. Then, we collected 161 cases from the SXS catalog, 107 from RIT, 114 from GaTech and 45 from `BAM`; for a total of 427 cases. The sampling of our three-dimensional parameter space by the four data sets is shown in Figure 4.2.

To obtain a qualitative understanding of the hierarchical structure in the two-dimensional parameter space of mass ratio and effective spin, in Figure 4.5 we show the NR data set over the $(\eta, \widehat{S})$ plane together with the analytical extreme-mass-ratio results, discussed in Sec. 4.1.5. For both final spin and radiated energy, we find a reasonably smooth surface spanned by the NR data points. In this work, these data surfaces are built from Wolfram Mathematica standard Hermite interpolation. These plots already suggests that – together with the known extreme-mass-ratio results to compensate the sparsity of NR simulations at increasingly unequal masses – good one-dimensional fits in the two best-sampled one-dimensional subsets (equal-mass-equal-spin and nonspinning BHs) will significantly constrain any two-dimensional fits.

For details about extraction of final-state quantities, NR data quality and weight assignment, see Section 4.2.10. As explained there, we do not have a full set of NR error estimates available, so we assign heuristic fit weights to each case based on the expected accuracy of the respective NR code in that particular parameter space region. For example, high-mass-ratio cases are down-weighted more for puncture codes.

4.2.2 Choice of fit quantity

We first need to decide which quantity exactly we want to fit. It appears natural to fit a quantity related to the "final" orbital angular momentum $L_{\rm orb}$ near merger, i.e. separating out the known initial spins S_i. This is particularly useful in connection with the extreme-mass-ratio limit, since with (4.5b), $L_{\rm orb}$ is linear in η to leading order. We can use the relation from (4.7) between $L_{\rm orb}$ and the dimensionless Kerr parameter $\chi_{\rm f}$ of the remnant BH, $M_{\rm f}^2\,\chi_{\rm f} = L_{\rm orb} + S_1 + S_2 = L_{\rm orb} + S$, also outside the extreme-mass-ratio limit. Here $M_{\rm f}$ is the final mass of the remnant BH.

Instead of the actual angular momentum $L_{\rm orb}$, we take the liberty of fitting the quantity $L'_{\rm orb} = M^2\,\chi_{\rm f} - S$, where (as throughout the paper) M is set to unity. This way, all fit results are easily converted to the final Kerr parameter $\chi_{\rm f}$ by adding the total initial spin S, and no correction for radiated energy has to be applied.

For the energy radiated we directly fit the quantity $E_{\rm rad}$ to the data set described in Section 4.2.1.

4.2.3 One-dimensional subspace fits

As the methodology is strictly equivalent for both quantities for every step shown in the flowchart 4.1, we provide in the next subsections the separated results for final spin and energy radiated. The peak luminosity is treated separately in Section 4.3.

4.2.3.1 1D fits: Final Spin

Motivated by the the unequal sampling of the parameter space by NR simulations, as visualized in Figure 4.5, we start our hierarchical fit development with the simplest and best-sampled subspaces of the NR data set, constructing one-dimensional fits $L'_{\rm orb}\left(\eta, \widehat{S}=0\right)$ and $L'_{\rm orb}\left(\eta=0.25, \widehat{S}\right)$ over 92 nonspinning and 37 equal-mass-equal-spin cases. We do not restrict ourselves to polynomial fits, and also include ansätze in the form of rational functions. We have also found good fits for more general functions, but we omit these here since we have not explored that option systematically.

Thus, we obtain the $L'_{\rm orb}\left(\eta, \widehat{S}=0\right)$ and $L'_{\rm orb}\left(\eta=0.25, \widehat{S}\right)$ fits for a large set of polynomial and rational functions. Several of them produce competitive goodness of fit, as measured by the root-mean-square-error (RMSE) or the full distribution of residuals. However, we do not want to overfit the data, which could induce spurious oscillations in the region of very unequal BH masses that is not covered by NR data. Hence, we rank the fits by information criteria penalizing superfluous free coefficients.

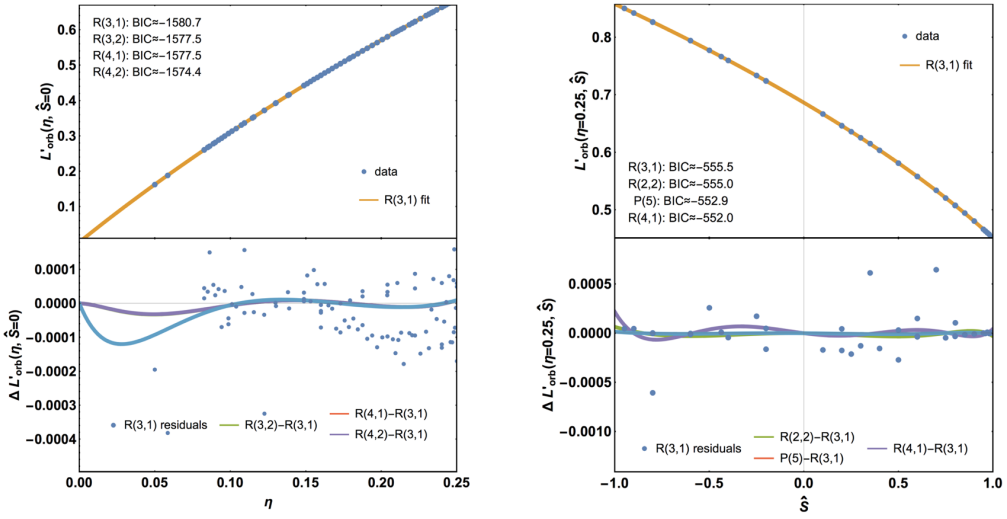

FIGURE 4.6: 1D-fits for the two constrained regions: nonspinning (left panel) and equal-mass-equal-spin (right panel). Top panels: best fits in terms of the Bayesian information criterion (BIC). Lower panels: residuals ($\Delta L'_{\rm orb}$ = data−fit) of this fit (points) and differences from the three next-best-ranking fits in terms of BIC (lines). See also Figure 4.4 in Sec. 4.1.6 for an illustration of BIC ranking for this example.

	Estimate	Standard error	Relative error [%]
a_2	3.833	0.085	2.2
a_3	−9.49	0.24	2.5
a_5	2.513	0.046	1.8
b_1	1.00096	0.00068	0.1
b_2	0.788	0.042	5.3
b_3	0.654	0.074	11.4
b_5	0.840	0.030	3.6

TABLE 4.1: Fit coefficients for the one-dimensional nonspinning $L'_{\rm orb}\left(\eta, \widehat{S}=0\right)$ and equal-mass-equal-spin $L'_{\rm orb}\left(\eta=0.25, \widehat{S}\right)$ fits over the 92 nonspinning and 37 equal-mass-equal-spin NR cases, along with their uncertainties (standard errors) and relative errors (Std.err./estimate).

Figure 4.6 shows the top-ranked fits for $L'_{\rm orb}\left(\eta, \widehat{S}=0\right)$ and $L'_{\rm orb}\left(\eta=0.25, \widehat{S}\right)$ in terms of Schwarz's Bayesian information criterion (BIC), which are both rational functions of order (3,1):

$$L'_{\rm orb}\left(\eta, \widehat{S}=0\right) = \frac{1.3a_3\eta^3 + 5.24a_2\eta^2 + 2\sqrt{3}\eta}{2.88a_5\eta + 1}\,. \tag{4.17}$$

$$L'_{\rm orb}\left(\eta=0.25, \widehat{S}\right) = \frac{0.00954b_3\widehat{S}^3 + 0.0851b_2\widehat{S}^2 - 0.194b_1\widehat{S}}{1 - 0.579b_5\widehat{S}} + 0.68637\,, \tag{4.18}$$

The fit coefficients a_i and b_i along with their uncertainties are given in Table 4.1; all are well determined. For $L'_{\rm orb}\left(\eta, \widehat{S}=0\right)$ we find that (4.17) is top-ranked by both BIC and AICc. While only ranked 6th by RMSE, none of the considered fits is better than (4.17) by more than 6% in that metric either. For $L'_{\rm orb}\left(\eta=0.25, \widehat{S}\right)$, we first must

constrain this fit to get $L'_{\rm orb}(\eta = 0.25, \widehat{S} = 0)$ according to the nonspinning constraint (4.17). This condition fixes an extra constraint for the constant term of the 1D ansatz in $\widehat{S}$ to reproduce the $\eta = 0.25$ nonspinning result, i.e. $L'_{\rm orb}(\eta = 0.25, \widehat{S} = 0)$ must be identical for both 1D fits resulting in (4.18). Then, we fit the $L'_{\rm orb}\left(\eta = 0.25, \widehat{S}\right)$ data to the $L'_{\rm orb}\left(\eta = 0.25, \widehat{S}\right)$ ansatz finding that the best choice is represented by (4.18), this being ranked 8th by RMSE, but with only 3% difference from the lowest RMSE, which is attained by a P(5) fit with one more coefficients, marginally disfavored by about +1.7 AICc and +2.6 in BIC.

The exact ranking of fits can depend on the choice of fit weights (see section 4.2.10) and on the ranking criterion, but we find that both (4.17) and (4.18) are top-ranked by both BIC and AICc. Then, as long as the weights are the same, these are the fits among the top-ranked group – by all three criteria – with the lowest number of fitting coefficients, indicating they both represent a robust choice.

The lower panels of Figure 4.6 also compare the preferred fit both to the NR data and to the three next-best ranking fits by BIC. For the η fit (left panel), we find that the residuals are centered around zero with no major trends, while the differences among high-ranked fits are much smaller than the scatter of residuals for the well-covered high-η range, and that the "systematic uncertainty", as indicated by the difference of high-ranked fits, is still at the same level even in the extrapolatory low-η region. For the equal-mass-equal-spin (right panel) we also find no major trends in the residuals distribution, these being also centered around zero and with similar deviations than for the nonspinning fit.

4.2.3.2 1D fits: Radiated energy

For the nonspinning 1D fit in symmetric mass ratio η, a simple fourth-order polynomial

$$E_{\rm rad}\left(\eta, \widehat{S} = 0\right) = a_4\eta^4 + a_3\eta^3 + a_2\eta^2 + \left(1 - \frac{2\sqrt{2}}{3}\right)\eta \tag{4.19}$$

with three free coefficients, listed in Table 4.2, is marginally preferred by both AICc and BIC. More complicated rational functions are not able to yield any significant change in residuals (only up to 1% in RMSE), while the differences between (4.19) and the next-ranked fits are again much smaller than the remaining residuals, as shown in Figure 4.7.

For the effective-spin dependence, again the value at $\left(\eta = 0.25,\ \widehat{S} = 0\right)$ is fixed from the η fit which it is again conditioned to the choice of the form of the ansatz, now being constructed as a product of nonspinning $E_{\rm rad}\left(\eta, \widehat{S} = 0\right)$ with the equal-mass-equal-spin

$E_{\rm rad}\left(\eta = 0.25, \widehat{S}\right)$ (see Sec. 4.2.4). A rational function of order (3,1) is top-ranked by AICc, BIC and RMSE and thus unambiguously selected as the preferred ansatz:

$$E_{\rm rad}\left(\eta = 0.25, \widehat{S}\right) = \frac{0.0484161\left(0.128 b_3 \widehat{S}^3 + 0.211 b_2 \widehat{S}^2 + 0.346 b_1 \widehat{S} + 1\right)}{1 - 0.212 b_5 \widehat{S}} \tag{4.20}$$

with four free coefficients listed in Table 4.2, and well-behaved residuals as seen in Figure 4.7.

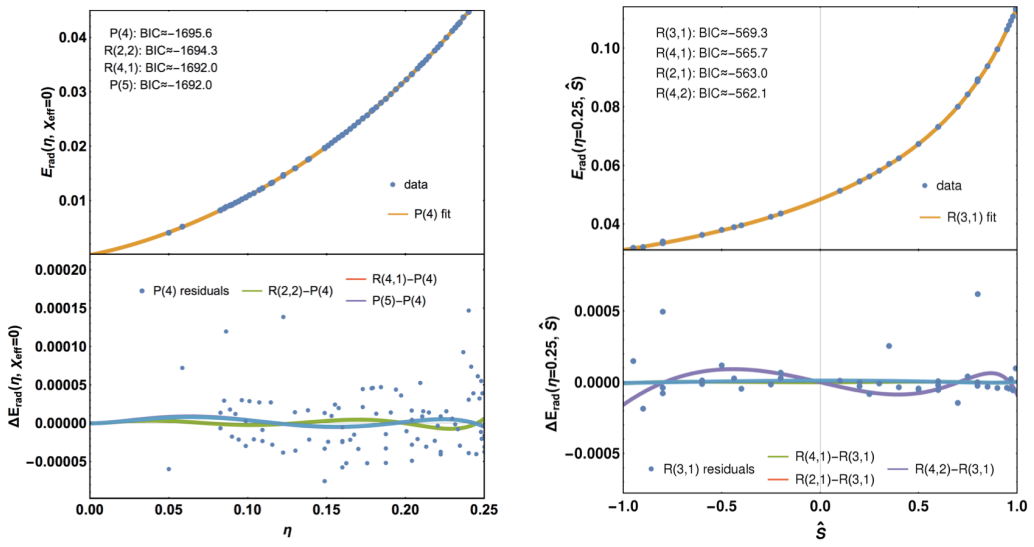

FIGURE 4.7: 1D-fits for the two constrained regions: nonspinning (left panels) and equal-mass-equal-spin (right panels). Top panels: selected fit, a fourth-order polynomial P(4) for the nonspinning fit (4.19) and a rational R(3,1) function for the equal-mass-equal-spin one (4.20). Lower panels: residuals of the fits (points) and differences from the three next-best-ranking in terms of BIC (lines).

	Estimate	Standard error	Relative error [%]
a_2	0.561	0.003	0.5
a_3	−0.847	0.027	3.2
a_4	3.145	0.069	2.2
b_1	−0.209	0.016	7.6
b_2	−0.197	0.026	13.2
b_3	−0.159	0.049	31.1
b_5	2.985	0.034	1.1

TABLE 4.2: Fit coefficients for the one-dimensional nonspinning $E_{\rm rad}\left(\eta, \widehat{S} = 0\right)$ and equal-mass-equal-spin $E_{\rm rad}\left(\eta = 0.25, \widehat{S}\right)$ fits over the 92 nonspinning and 37 equal-mass-equal-spin NR cases.

4.2.4 Two-dimensional fits

Next, we want to construct a two-dimensional fit covering the $(\eta, \widehat{S})$ space, as it was illustrated in Figure 4.5, by combining both the 1D subspace fits and the extreme-mass-ratio limit. As discussed above, for the final spin we take the sum of (4.17) and the spin-dependent terms of (4.18) while for the energy radiated we take the product of (4.19) and (4.20). In principle, the fitting procedure is robust enough to use either a sum or product ansatz for either final-state quantity. However, we have found that for the energy radiated the sum ansatz tends to produce suspicious curvature in the S = 1, low-η region, which cannot be suppressed by the extreme-mass-ratio information due to the lack of data in this region.

Then, we introduce the necessary flexibility to describe 2D curvature and the extreme-mass-ratio limit by generalizing the $\widehat{S}$-dependent terms, inserting a polynomial of order J in η for each b_i through the substitution

$$b_i \to b_i \sum_{j=0}^{j=J} f_{ij}\, \eta^j \,. \tag{4.21}$$

We describe below the 2D build up of the final spin and radiated energy ansätze.

4.2.4.1 Two-dimensional fits: final spin

The general 2D ansatz is thus

$$L'_{\rm orb}\left(\eta, \widehat{S}\right) = L'_{\rm orb}\left(\eta, 0\right) \,+\, L'_{\rm orb}\left(0.25, \widehat{S}, f_{ij}\right) \,-\, L'_{\rm orb}\left(0.25, 0\right) \,. \tag{4.22}$$

Here we choose to expand to third order in η ($J = 3$), which is the lowest order leaving enough freedom to incorporate all available constraints from the 1D fits and the extreme-mass-ratio limit, and, as evidenced by the residuals we find below, also high enough to adequately model this data set. Of the resulting 16 coefficients, the three f_{i0} in the numerator must vanish to preserve the $L'_{\rm orb}\left(\eta = 0, \widehat{S}\right) = 0$ limit, while consistency with the equal-mass fit from (4.18) provides four constraints which we use to fix the f_{i3} terms:

$$f_{i3} = 64 - 64 f_{i0} - 16 f_{i1} - 4 f_{i2} \,. \tag{4.23}$$

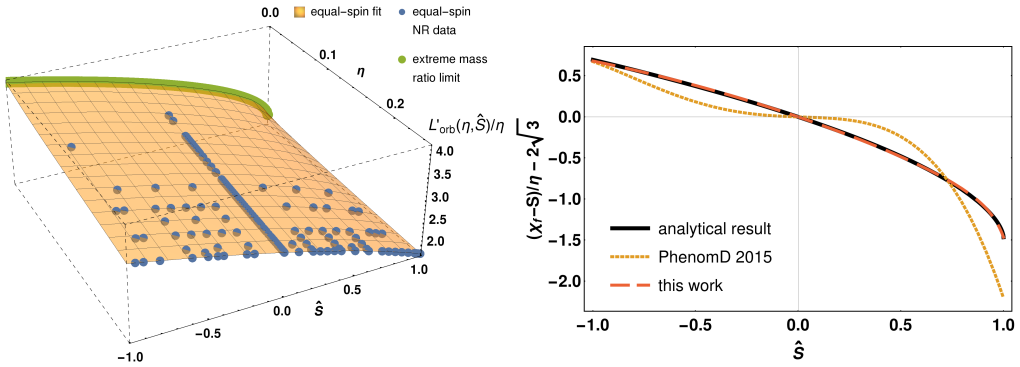

FIGURE 4.8: Left panel: Two-dimensional $L'_{\rm orb}\left(\eta,\widehat{S}\right)$ fit, visualized as $L'_{\rm orb}\left(\eta,\widehat{S}\right)/\eta$. Right panel: Extreme-mass-ratio comparison of the rescaled final spin: analytical results from solving (4.7), the previous PhenomD final-spin fit of [38], and this work.

	Estimate	Standard error	Relative error [%]
f_{21}	8.774	0.019	0.2
f_{31}	22.83	0.27	1.2
f_{50}	1.8805	0.0025	0.1
f_{11}	4.4092	0.0047	0.1

TABLE 4.3: Fit coefficients for the extreme-mass-ratio limit of the final spin, fitted to discretized analytical results. The fourth coefficient, f_{11}, is fixed by the derivative constraint in (4.25) and its estimate and error computed from the others.

Four more coefficients are fixed by the extreme-mass-ratio information discussed in Sec. 4.1.5: we re-express (4.7) in terms of $L'_{\rm orb}/\eta$ and fit the discretized quantity

$$\lim_{\eta\to 0}\frac{L'_{\rm orb}\left(\eta,\widehat{S}\right)}{\eta}-2\sqrt{3}=\lim_{\eta\to 0}\frac{\chi_{\rm f}\ (\eta,S)-S}{\eta}-2\sqrt{3} \tag{4.24}$$

where $2\sqrt{3}$ is the linear contribution from the nonspinning part (cf. (4.17)) and the $\chi_{\rm f}\ (\eta\to 0,S)$ values are obtained by solving (4.7) numerically for small η. Before fitting, we apply the derivative constraint from (4.9), which for the sum ansatz (4.22) implies a coefficient constraint

$$f_{11}\to 0.345225 f_{21}+0.0321306 f_{31}-3.66556 f_{50}+7.5397. \tag{4.25}$$

We find this extra physical constraint to be essential in avoiding superextremal $\chi_{\rm f}$ results due to fitting artifacts. The extreme-mass-ratio limit fit coefficients are listed in Table 4.3, and the improved agreement between analytical results and this new fit, as compared with the previous fit of [38], is illustrated at the right panel of Figure 4.8.

In summary, after constraining to the well-covered one-dimensional NR data subsets and the analytically known extreme-mass-ratio limit, the 2D ansatz from (4.22) has reduced from 16 to 5 free coefficients: $\{f_{12},f_{22},f_{32},f_{5,1},f_{52}\}$.

4.2.4.2 Two-dimensional fits: energy radiated

We now apply exactly the same to the energy radiated. For the 2D ansatz, we combine the two 1D fits from Eqs. (4.19) and (4.20), expanding each $\widehat{S}$-dependent term with a polynomial in η, according to (4.44):

$$E_{\rm rad}\left(\eta,\widehat{S}\right) = E_{\rm rad}\left(\eta,0\right)\frac{E_{\rm rad}\left(0.25,\widehat{S},f_{ij}\right)}{E_{\rm rad}\left(0.25,0\right)}\,. \tag{4.26}$$

Contrary to the sum ansatz for $\chi_{\rm f}$ in (4.22), we do not need to set the η-independent coefficients f_{i0} of the $\widehat{S}$ terms to zero, as the $E_{\rm rad}\left(\eta,\widehat{S}\right) = E_{\rm rad}\left(\eta,0\right)(1+\dots)$ form of (4.26) already guarantees the correct $\eta = 0$ limit. Hence an expansion up to third order in η of each $\widehat{S}$ term, as we chose for the $\chi_{\rm f}$ fit, would yield too many free coefficients, and instead we only expand up to second order. The four f_{i2} coefficients are again fixed by the equal-mass boundary conditions:

$$f_{i2} = 16 - 16f_{i0} - 4f_{i1}\,. \tag{4.27}$$

Similar to the procedure for $\chi_{\rm f}$, we can use the extreme-mass-ratio limit to fix the four coefficients f_{i0} of the linear-in-η terms. Using the analytic result from (4.5a), we force the fit to satisfy the equality

$$E_{\rm rad}(\eta\to 0,\widehat{S}) = 1 - E_{\rm ISCO}(\widehat{S}) \tag{4.28}$$

and fit the corresponding leading-order η dependence of our 2D ansatz to discretized values of this quantity. Again we fix one of the four free coefficients of $E_{\rm rad}\left(\eta\to 0,\widehat{S}\right)$ by a constraint fixing the value at $\widehat{S} = 1$, which is necessary to capture the very steep rise of (4.28) as $\widehat{S}\to+1$:

$$f_{10} \to -0.574752 f_{20} - 0.280958 f_{30} + 64.6408 f_{50} - 88.3165\,. \tag{4.29}$$

The agreement between discretized analytical result and fit is shown in Figure 4.9 (right plot), and fit coefficients are listed in Table 4.4.

We thus have $12 - 4 - 4 = 4$ free coefficients f_{i1} $\{f_{11}, f_{21}, f_{31}, f_{51}\}$, of which f_{21} turns out to be extremely poorly constrained, so that we set it to zero before refitting. Results of the 2D fit, calibrated to equal-spin simulations only, are shown in Figure 4.9, which shows that the steep shape of the extreme-mass-ratio limit at high $\widehat{S}$ is smoothly attained by the extrapolated fit. For the curvature at low η and extremal $\widehat{S} = 1$, where there is

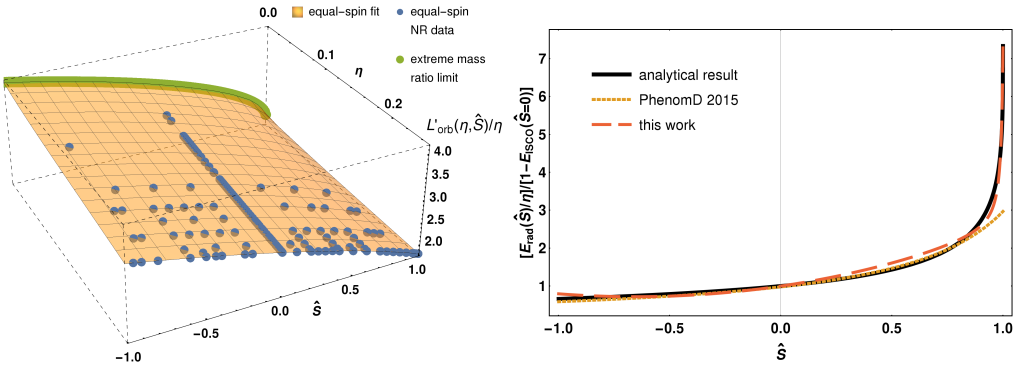

FIGURE 4.9: Left panel: Two-dimensional $E_{\rm rad}\left(\eta, \widehat{S}\right)$ fit, visualized as $E_{\rm rad}\left(\eta, \widehat{S}\right)/\eta$. Application of the extreme-mass-ratio limit helps in avoiding extrapolation artifacts which would otherwise appear at low-η, high-$|\widehat{S}|$ regions that are uncovered by NR simulations. Right panel: extreme-mass-ratio comparison of analytical results, the previous PhenomD radiated-energy fit of [38], and this work.

	Estimate	Standard error	Relative error [%]
f_{20}	4.27	0.38	8.9
f_{30}	31.09	0.71	2.3
f_{50}	1.56735	0.00032	0.02
f_{10}	1.81	0.15	8.2

TABLE 4.4: Fit coefficients for the extreme-mass-ratio limit of the radiated energy, fitted to discretized analytical results. The fourth coefficient, f_{10}, is fixed by the constraint at $\widehat{S} = 1$, cf. (4.29), and its estimate and error are computed from the others.

no NR data, there might be also a contribution from the small remaining fit issues in the extreme-mass-ratio limit (cf. Figure 4.9). The residuals again have larger RMSE than the 1D fits in η and $\widehat{S}$, by factors of 6.5 and 1.8 respectively, but show no clear apparent trends, allowing us to use this 2D fit as the basis for an unequal-spin residuals study in the next step.

4.2.5 Unequal-spin contributions and 3D fit

In the previous section we have attacked the fourth level of Figure 4.1, which concerns the fitting of the best possible $f_{2D}(\eta, \widehat{S})$ ansatz. This is possible due to the dominance of the primary physical parameters compared to the unequal-spin effects which allow us to split the final ansatz in a sum of $f_{2D}(\eta, \widehat{S}) + \mathcal{O}(\Delta\chi)$. Now the final step in the hierarchical procedure is to explore the subdominant effects of unequal spins, parametrized by the spin difference $\Delta\chi = \chi_1 - \chi_2$. Thus, following the same structure as in the previous section, we show separately the results for the calibration of the final spin and the energy radiated.

4.2.5.1 Unequal-spin contributions and 3D fit: final spin

We first study the residuals of the 238 unequal-spin NR cases under the equal-spin 2D fit:

$$\Delta L'_{\rm orb}\left(\eta, \widehat{S}, \Delta\chi\right) := L'_{\rm orb,NR}\left(\eta, \widehat{S}, \Delta\chi\right) - L'_{\rm orb}|_{\rm eqSpinFit}\left(\eta, \widehat{S}\right) . \tag{4.30}$$

We do this at fixed steps in mass ratio, having sufficient numbers of NR cases for this analysis at mass ratios $q = \{1, 1.33, 1.5, 1.75, 2, 3, 4, 5, 6, 7, 8\}$. This per-mass-ratio analysis is only used to guide the construction of the full 3D ansatz and as a consistency check, while the final full 3D fit will consist of fitting the constrained 2D ansatz plus spin-difference terms directly to the full data set.

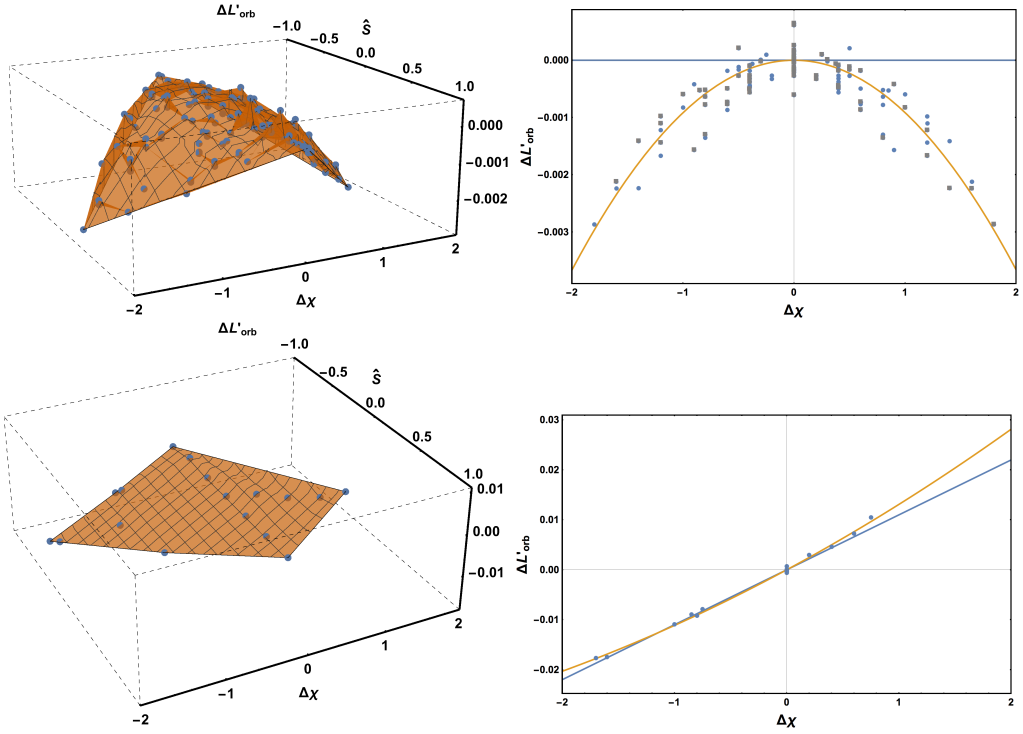

FIGURE 4.10: Examples of spin-difference behavior at fixed mass ratios, for residuals $\Delta L'_{\rm orb}$ after subtracting the two-dimensional $L'_{\rm orb}\left(\eta, \widehat{S}\right)$ fit, as defined in (4.30). Top row: $q = 1$; lower row: $q = 4$; left column: surfaces in $\left(\widehat{S}, \Delta\chi, \Delta L'_{\rm orb}\right)$ space; right column: projections onto the $\Delta\chi$ axis with linear and quadratic fits. At equal mass, the surface is parabolic, with the linear term (blue line) and mixture term (not shown) vanishing, but a clear quadratic dependence (orange line). At $q = 4$ and other intermediate mass ratios, the surface is very close to flat and the linear term dominates.

At each mass ratio, we visually inspect the residuals, which span 2D surfaces in $(\chi_1, \chi_2, L'_{\rm orb})$ or, equivalently, $\left(\widehat{S}, \Delta\chi, L'_{\rm orb}\right)$ space. As illustrated in Figure 4.31, we find surfaces close to a plane, indicating a dominant linear dependence on $\Delta\chi$ and possibly a mixture term $\widehat{S}\,\Delta\chi$. The exception is at equal masses, where quadratic curvature in the $\Delta\chi$ dimension dominates. In this case, exchange of χ_1 and χ_2 yields an identical binary configuration, so that terms linear in $\Delta\chi$ indeed have to vanish for symmetry reasons. We have also

exploited this fact in the $q = 1$ analysis by adding mirror duplicates of each NR data point. Motivated by these empirical findings and symmetry argument, we introduce up to three spin-difference terms,

$$\Delta L'_{\rm orb}\left(\eta, \widehat{S}, \Delta\chi\right) = A_1(\eta)\,\Delta\chi + A_2(\eta)\,\Delta\chi^2 + A_3(\eta)\,\widehat{S}\Delta\chi\,. \tag{4.31}$$

The full 3D ansatz is then simply the sum of Eqs. (4.22) and (4.31):

$$L'_{\rm orb}\left(\eta, \widehat{S}, \Delta\chi\right) = L'_{\rm orb}\left(\eta, \widehat{S}\right) + \Delta L'_{\rm orb}\left(\eta, \widehat{S}, \Delta\chi\right)\,. \tag{4.32}$$

Adding higher orders in the effective spin or spin difference is not supported by visual inspection. At each mass ratio, we now perform four fits in $\Delta\chi$ for the values of the A_i: linear, linear+quadratic, linear+mixed, or the sum of all three terms. Examples are also shown in Figure 4.31.

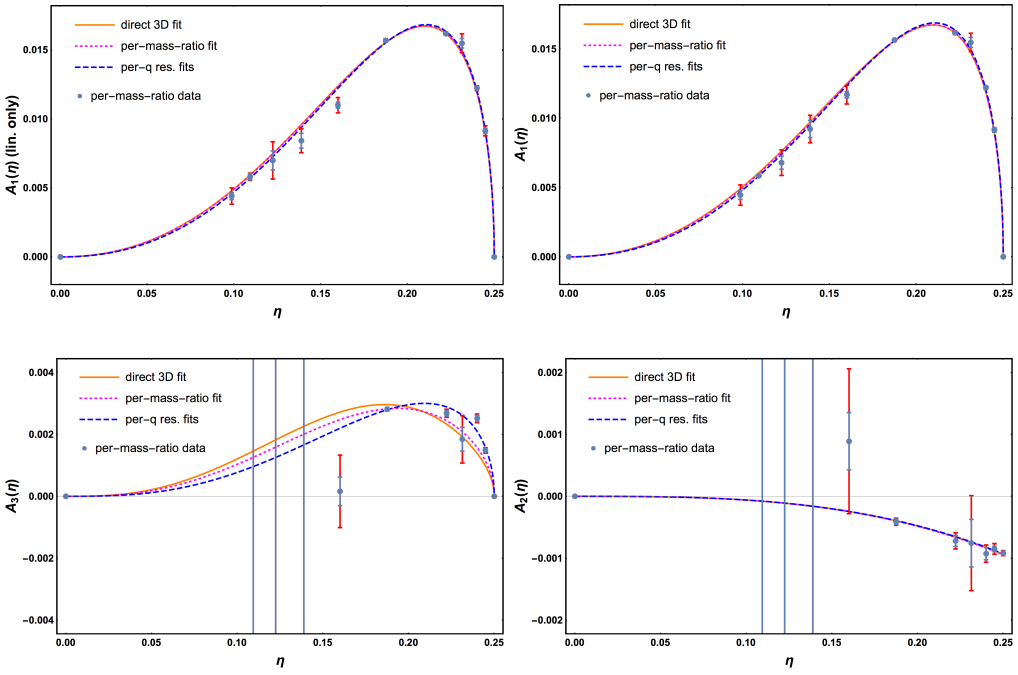

FIGURE 4.11: Spin-difference behavior of final-spin data after subtraction of the two-dimensional $L'_{\rm orb}\left(\eta, \widehat{S}\right)$ fit, showing the results of fits as in Figure 4.31 at η steps corresponding to $q = \{1, 1.33, 1.5, 1.75, 2, 3, 4, 5, 6, 7, 8\}$ and three estimates for the three ansatz functions $A_i(\eta)$ from Eqs. 4.31 and 4.35: (i) unequal-spin part of the final 3D fit from (4.32) ("direct 3D fit"), (ii) fit of the unequal-spin terms from (4.35) ("fit to residuals") to the residuals of the 2D fit from (4.22) over all mass ratios, (iii) fits of (4.35) to the per-mass-ratio results. Top-left panel: linear term A_1 only. The remaining panels are for the combined linear+quadratic+mixture fit, in clockwise order: linear term A_1, quadratic term A_2 and mixture term A_3. The A_1 results from the combined fit are very similar to those from the linear-only fit, demonstrating the robustness of extracting leading-order spin-difference effects. For the two lower panels, data points for low η are outside the displayed range, but the error bars are huge and hence this region does not contribute significantly to the weighted per-mass-ratio fits. In the direct 3D fit to the full data set, however, low-η information can be better incorporated, leading to the somewhat different shape of the mixture-term fit.

We then collect the coefficients of each of these fits and use them as data $A_i(\eta)$ to be fitted as functions of mass ratio (see the 'per-mass-ratio data' in Figure 4.11), using as weights the fit uncertainty from each mass ratio rescaled by the average data weight for that mass ratio. We also apply what we know about the extreme-mass-ratio and equal-mass limits: all three $A_i(\eta)$ have to vanish in the limit $\eta = 0$, and the A_1, A_3 linear in $\Delta\chi$ have to vanish for $\eta = 0.25$. We thus choose ansätze of the form

$$A_i = d_{i0}\,\eta^{p_i}\left(\sqrt{1-4\eta}\right)^{q_i}(1 + d_{i1}\eta) \tag{4.33}$$

for $A_{i=1,3}$ linear in $\Delta\chi$, where the factor $\left(\sqrt{1-4\eta}\right)^{q_i}$ is motivated from post-Newtonian (PN) results [20, 52], and

$$A_2 = d_{20}\,\eta^{p_2}\left(1 + d_{21}\left(\sqrt{1-4\eta}\right)^{q_2}\right) \tag{4.34}$$

for the term quadratic in $\Delta\chi$. We find that the data can be well fit without any higher-order terms and by reducing some of the freedom of these three terms exploratory fits keeping all coefficients free give results close to integer numbers for the p_i, $q_i = 1$ and $d_{21} = 0$. Hence we choose the three parsimonious ansätze

$$A_1(\eta) = d_{10}(1-4\eta)^{0.5}\eta^2\,(d_{11}\eta + 1) \tag{4.35a}$$

$$A_2(\eta) = d_{20}\eta^3 \tag{4.35b}$$

$$A_3(\eta) = d_{30}(1-4\eta)^{0.5}\eta^3\,(d_{31}\eta + 1)\ . \tag{4.35c}$$

The blue points and lines in Figure 4.11 show these per-mass-ratio results. The shape and numerical results of the dominant linear term A_1 are quite stable under adding one or two of the other terms. Fitting two terms, either linear+quadratic or linear+mixture, yields quadratic/mixture effects of very similar magnitude, with the quadratic term following the same basic shape (an intermediate-mass-ratio bulge) as the other two. However, combining all three terms, the results match better with the expectations from symmetry detailed before, with the bulge shape limited to the linear and mixture terms while the quadratic term provides a correction mostly at similar masses.

Using again the $q = 1$, $\widehat{S} = 0$ and $\eta \to 0$ constraints on the general ansatz from (4.32), we end up with a total of nine free coefficients in this final step. We now fit to 298 cases with arbitrary spins not yet used in the 1D fits, with results given in Table 4.5. Together with the coefficients from Tables 4.1–4.3, these fully determine the fit. To convert back from our fit quantity $L'_{\rm orb}$ to the actual dimensionless final spin $\chi_{\rm f}$, just add the total initial spin $S = m_1^2\,\chi_1 + m_2^2\,\chi_2$.

	Estimate	Standard error	Relative error [%]
d_{10}	0.322	0.020	6.2
d_{11}	9.33	0.87	9.3
d_{20}	−0.0598	0.0021	3.5
d_{30}	2.32	0.28	12.1
d_{31}	−3.26	0.20	6.1
f_{12}	0.512	0.085	16.7
f_{22}	−32.1	3.6	11.3
f_{32}	−154	10	6.5
f_{51}	−4.77	0.34	7.1

TABLE 4.5: Fit coefficients for the final 3D step of the $L'_{\rm orb}$ fit to 298 cases not yet used in the 1D fits of 4.2.3.

We find that the data set is sufficiently large and clean, and the equal-spin part modeled well enough from the 2D step, to confidently extract the linear spin-difference term and its η-dependence, which is stable when adding the other terms; and to find some evidence for the combined mixture and quadratic terms, whose shape however is not fully constrained yet.

4.2.5.2 Unequal-spin contributions and 3D fit: energy radiated

The spin-difference dependence of unequal-spin residuals is less clear here than for the final spin: As seen in the examples of Figure 4.12, the general trend is the same with a quadratic dependence on $\Delta\chi$ at equal masses and more dominant linear effects as η decreases, but the distributions are generally noisier and the second-order terms (quadratic and mixture $\propto \widehat{S}\Delta\chi$) cannot be as cleanly separated.

For both the per-mass-ratio-step analysis and the direct 3D fit, we use the same general functional forms for possible linear, quadratic and mixture terms as in Eqs. (4.31), (4.33) and (4.34). After fixing ill-constrained coefficients to integer values, these reduce to

$$A_1(\eta) = d_{10}(1-4\eta)^{0.5}\eta^2\,(d_{11}\eta+1) \tag{4.36a}$$

$$A_2(\eta) = d_{20}\eta^3 \tag{4.36b}$$

$$A_3(\eta) = d_{30}(1-4\eta)^{0.5}\eta\,(d_{31}\eta+1)\ . \tag{4.36c}$$

Figure 4.13 shows that the linear term is again robustly determined and does not change shape much when adding the two additional terms, but already the per-mass-ratio and direct-3D fits for this term do not agree quite as closely as in the $\chi_{\rm f}$ fit. The quadratic term is more noisy, and for the mixture term the results are rather uncertain, with an apparent sign change in the effect over η, but the stepwise cross-checks at least agreeing

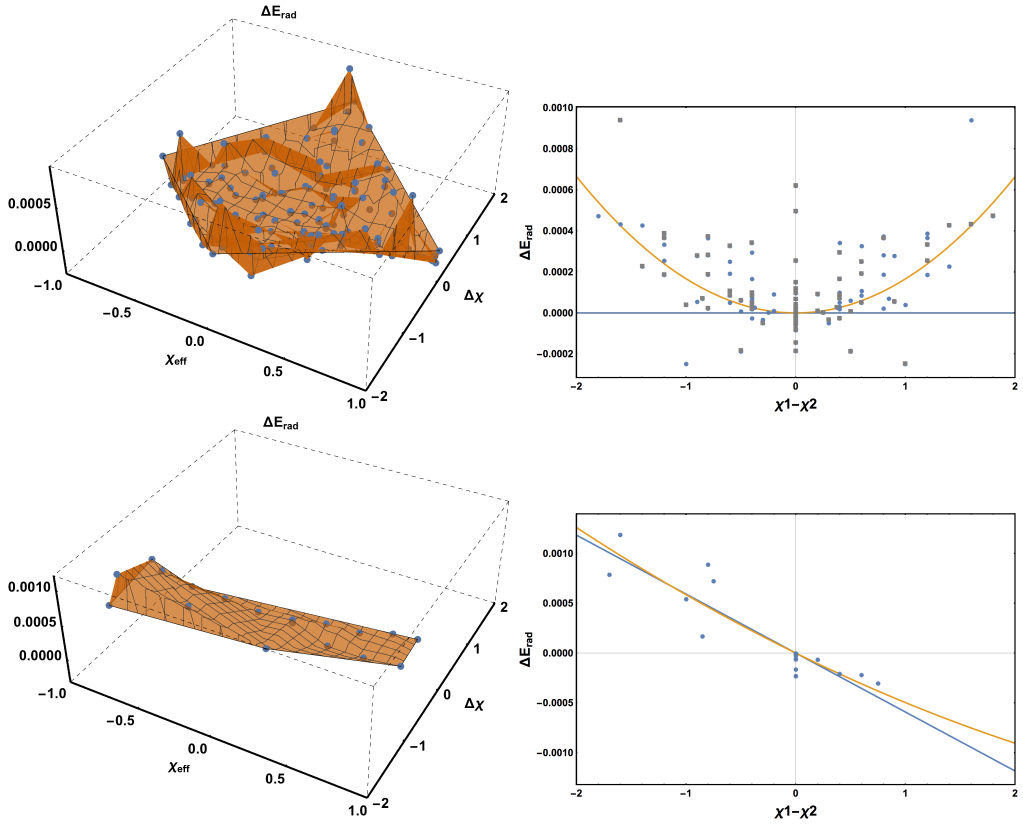

FIGURE 4.12: Examples of spin-difference behavior of the radiated energy at fixed mass ratios, for residuals $\Delta E_{\rm rad}$ after subtracting the two-dimensional $E_{\rm rad}\left(\eta, \widehat{S}\right)$ fit. Top row: $q = 1$ (mirror-duplicated data points shown in gray); lower row: $q = 4$; left column: surfaces in $\left(\widehat{S}, \Delta\chi, \Delta E_{\rm rad}\right)$ space; right column: projections unto the $\Delta\chi$ axis with linear and quadratic fits. At equal mass, the linear term and mixture term vanish, but the expected quadratic dependence (parabolic surface) is less clearly pulled out from rather noisy residuals than for the final spin (cf. Figure 4.31). At $q = 4$ and other intermediate mass ratios, the surface is not as close to flat as in the final-spin case, and the noisy data still shows some quadratic dependence.d

on the overall shape. Still, we will see below that inclusion of both these effects is statistically justified.

The full 3D ansatz for $E_{\rm rad}\left(\eta, \widehat{S}, \Delta\chi\right)$ is then built up as

$$E_{\rm rad}\left(\eta, \widehat{S}, \Delta\chi\right) = E_{\rm rad}\left(\eta, \widehat{S}\right) + \Delta E_{\rm rad}\left(\eta, \widehat{S}, \Delta\chi\right), \tag{4.37}$$

and this time has eight free coefficients (three from the 2D ansatz and five from the spin-difference terms). Results for the fit to 298 NR cases not previously used in the 1D fits are listed in Table 4.6.

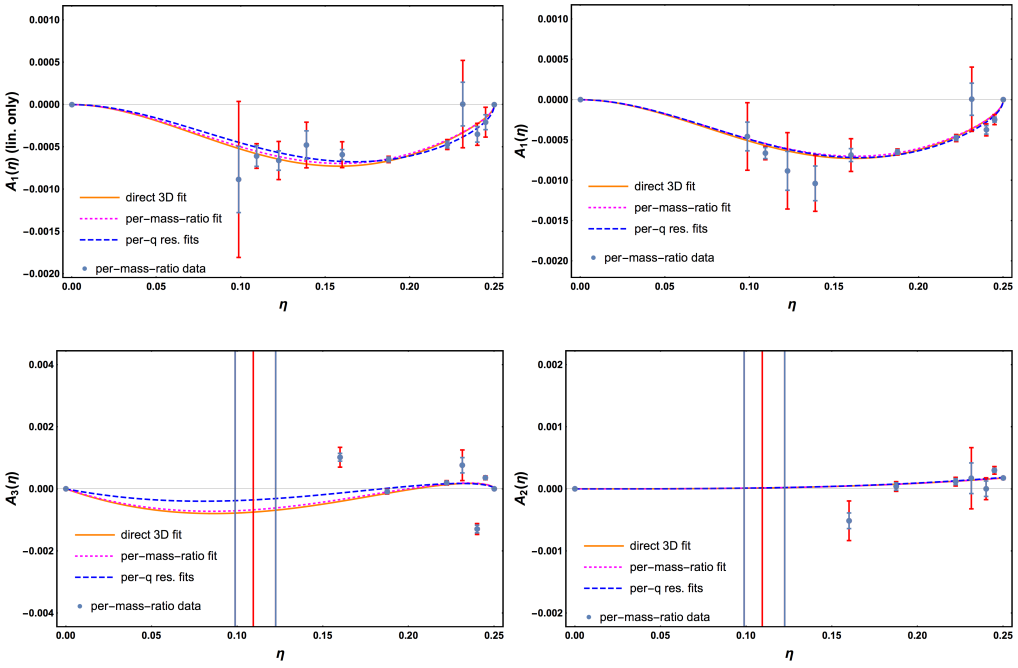

FIGURE 4.13: Spin-difference behavior of radiated-energy data after subtraction of the two-dimensional $E_{\rm rad}\left(\eta, \widehat{S}\right)$ fit, for the three ansatz functions $A_i(\eta)$ from (4.36), with the same mass-ratio steps and fits as in Figure 4.11. Top-left panel: linear term A_1 only. The remaining panels are for the combined linear+quadratic+mixture fit, in clockwise order: linear term A_1, quadratic term A_2 and mixture term A_3. The A_1 results from the combined fit are very similar to those from the linear-only fit, demonstrating the robustness of extracting leading-order spin-difference effects. For the two lower panels, results are much more uncertain, and the error bars for low η go far outside the displayed range, so that this region does not contribute significantly to the weighted per-mass-ratio fits.

	Estimate	Standard error	Relative error [%]
d_{10}	-0.098	0.011	11.3
d_{11}	-3.23	0.18	5.6
d_{20}	0.0112	0.0012	10.5
d_{30}	-0.0198	0.0036	18.4
d_{31}	-4.92	0.19	3.9
f_{11}	15.7	1.2	7.9
f_{31}	-243.6	8.0	3.3
f_{51}	-0.58	0.13	21.6

TABLE 4.6: $E_{\rm rad}$ fit coefficients for the final 3D step, using 298 cases.

4.2.6 Fit assessment

In Figures 4.11 and 4.13 we compare the spin-difference terms for the final spin and radiated energy from the final "direct 3D" fit to those obtained from the per-mass-ratio residuals analysis. In both cases, the linear term is fully consistent, confirming that it is well determined by the data, while for the quadratic and mixture terms both approaches agree on the qualitative shape, but do not match as closely. Under the chosen ansätze, the 3D fit coefficients even for those terms are tightly determined (see Tables 4.5 and 4.6). However, we have explicitly chosen the spin-difference terms in (4.35) to achieve this goal, while several other ansatz choices (changing the fixed exponents of the multiplicative η or $\sqrt{1-4\eta}$ terms, or adding more terms with free coefficients in the η polynomials) can produce fits that are indistinguishable by summary statistics (AICc, BIC, RMSE). Still, most of these have some strongly degenerate and underconstrained coefficients, while the reported fit has the desirable property of sufficient complexity to be within the plateau region of summary statistics while not having any degenerate coefficients.

Yet, the shape of the functions $A_2(\eta)$ and $A_3(\eta)$ for the mixture and quadratic terms is not actually as closely constrained from the current data set as the coefficient uncertainties alone seem to imply, due to this ambiguity in ansatz selection. This becomes clear from the comparison of direct 3D fit and per-mass-ratio analysis in Figure 4.11 and Figure 4.13. The per-mass-ratio analysis also demonstrates that the data at mass ratios $\eta < 0.16$ are not yet constraining enough to help characterize these terms. (The error bars are so large, and hence the weights so low, that they effectively do not contribute to the fit.) It also becomes clear that additional unequal-spin data at intermediate mass ratios would be very useful in constraining the $A_{2,3}(\eta)$ functions. Meanwhile, it is important to note again that the leading linear spin-difference term is already determined much more narrowly and robustly with the current data set.

We can further assess the success of the hierarchical 3D fitting procedure by comparing

- a 2D fit (equal-spin physics only) to equal-spin NR cases only (same as in Figure 4.8 and Figure 4.9),
- a 2D fit (equal-spin physics only) to all NR data,
- and the 2D part of the full 3D fit.

As shown in Figure 4.14 and Figure 4.14, fitting the 2D equal-spin ansatz to the full data set induces strong curvature in the $(\eta, \widehat{S})$ plane, which the full 3D fit is able to correct by the additional degrees of freedom in the spin-difference dimension. This is how it was possible to pull out the subdominant spin-difference effects with this enlarged

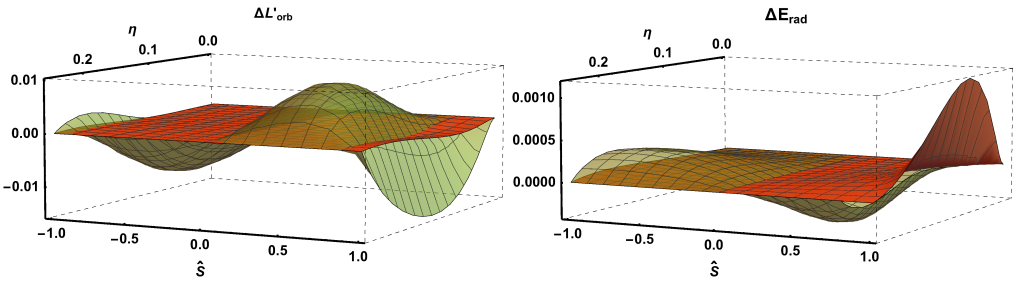

FIGURE 4.14: Green: Difference $\Delta L'_{\rm orb}$ (left panel) and $\Delta E_{\rm rad}$ (right panel) of a 2D fit (equal-spin physics only) to the full data set minus the 2D fit to equal-spin cases only, both including extreme-mass-ratio constraints. The strong curvature at intermediate mass ratios and nonzero spins is due to the equal-spin-physics-only fit trying to compensate for the addition of unequal-spin NR cases.
Orange: Difference $\Delta L'_{\rm orb}$ (left panel) and $\Delta E_{\rm rad}$ (right panel) of the 2D part of the 3D fit to the full data set minus the 2D-only fit to equal-spin data. The bulk of the parameter space is no longer distorted, and only at high effective-spin magnitudes a small opposite effect to the η-dependent behavior of the spin-difference terms (cf. Figure 4.11) can be seen.

	$N_{\rm data}$	$N_{\rm coeff}$	RMSE	AICc	BIC
1D η	92	3 : 3	$(9.41 : 4.14) \times 10^{-5}$	−(1590.8 : 1705.7)	−(1580.7 : 1695.6)
1D $\hat{S}$	37	4 : 4	$(2.05 : 1.51) \times 10^{-4}$	− (563.6 : 577.3)	− (555.5 : 569.3)
2D ($\chi_1 = \chi_2$)	60	4 : 3	$(3.90 : 2.67) \times 10^{-4}$	− (880.5 : 875.3)	− (870.8 : 867.4)
2D all	298	4 : 3	$(8.05 : 0.43) \times 10^{-3}$	−(2247.4 : 4070.9)	−(2229.0 : 4070.9)
3D lin	298	6 : 5	$(9.20 : 3.24) \times 10^{-4}$	−(3628.4 : 4282.9)	−(3602.9 : 4282.9)
3D lin+quad	298	7 : 6	$(8.28 : 2.72) \times 10^{-4}$	−(3765.0 : 4391.9)	−(3735.8 : 4391.9)
3D lin+mix	298	8 : 7	$(8.11 : 2.91) \times 10^{-4}$	−(3693.4 : 4339.3)	−(3660.6 : 4339.3)
3D lin+quad+mix	298	9 : 8	$(6.10 : 2.62) \times 10^{-4}$	−(4087.3 : 4417.8)	−(4050.9 : 4417.8)

TABLE 4.7: Summary statistics for the various steps of the hierarchical final-spin fit. Note that it is not meaningful to compare AICc and BIC between data subsets of different sizes. For each column, the left value is for the final spin while the right one is for the energy radiated. Thus, for both quantities, there is statistical preference for the 3D fit including all three linear+mixture+quadratic terms, although many different choices of the $A_i(\eta)$ ansatz functions yield similar results with just $\pm$ a few percent in RMSE and $\pm$ a few in AICc/BIC, so that the shape of the mixture and quadratic terms is not yet fully constrained.

data set. The same conclusion is supported by the comparison of summary statistics between the various steps and 2D/3D fit variants in Table 4.7, showing that the RMSE only increases by 50% from the 2D equal-spin case to the full 3D fit using all data.

The distribution of fit residuals with other previously published fits, over the calibration data set of the current work, is shown as histograms in Figure 4.15 and Figure 4.16 and summarized in Table 4.8 and Table 4.9 along with AICc and BIC metrics. The shape of the distributions is consistent, and for all fits the means are much smaller than the standard deviations, showing no evidence for any systematic bias. Our new fit improves significantly over the previous fit [38] used in the calibration of the IMRPhenomD waveform model [39], and also yields some improvement over recent fits from other groups [92, 151], even when those ansätze are refit to our present NR data set.

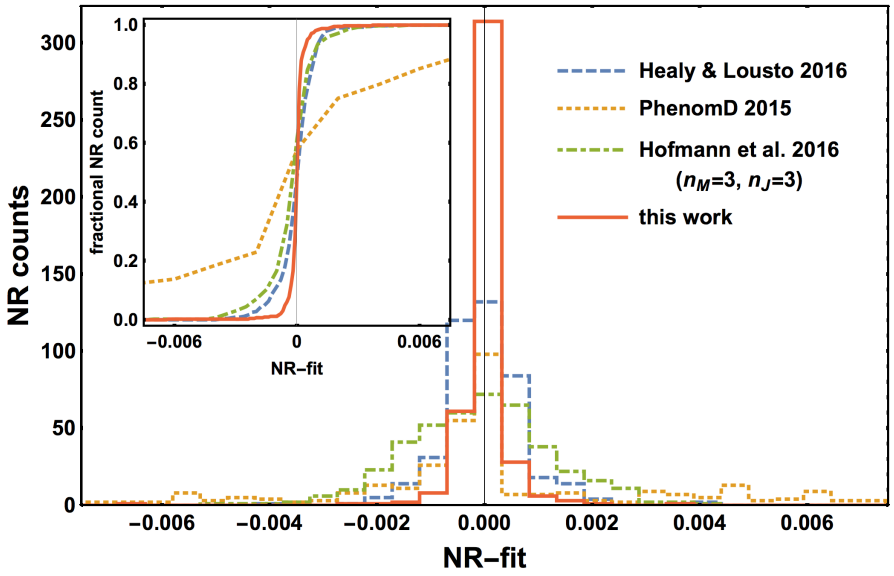

FIGURE 4.15: Fit residuals of the final spin $\chi_{\rm f}$, for this work and for previously published fits [38, 92, 151], evaluated over the set of 427 NR simulations shown in Figure 4.5. Main panel: histograms, with 102 outliers for PhenomD with $|\mathrm{NR}-\mathrm{fit}|>0.0075$ outside of the plot range. Inset: cumulative distributions over the same range.

	$N_{\rm coef}$	mean	stdev	AICc	BIC
HLZ2014 [91]	19	-4.8×10^{-5}	8.9×10^{-4}	−5141.0	−5061.7
HL2016 [92]	19	8.1×10^{-7}	7.9×10^{-4}	−5358.1	−5278.9
PhenomD [38]	11	-4.7×10^{-5}	7.2×10^{-3}	−3309.0	−3260.9
(refit)	11	-1.7×10^{-4}	7.0×10^{-3}	−3334.5	−3286.5
HBR2016 [151]	6	-1.2×10^{-4}	1.4×10^{-3}	−4717.2	−4689.0
(refit)	6	-1.4×10^{-4}	1.3×10^{-3}	−4791.4	−4763.2
HBR2016 [151]	16	-2.8×10^{-4}	1.2×10^{-3}	−4877.3	−4809.7
(refit)	16	-1.4×10^{-5}	1.0×10^{-3}	−4975.8	−4908.2
This work	16	-2.3×10^{-5}	5.2×10^{-4}	−5991.5	−5923.9
(refit)	16	-2.1×10^{-5}	5.1×10^{-4}	−6011.3	−5943.6
(uniform)	16	-1.2×10^{-5}	5.0×10^{-4}	−5240.1	−5172.5
(uniform refit)	16	-6.9×10^{-6}	4.9×10^{-4}	−5256.8	−5189.2

TABLE 4.8: Summary statistics for the new final-spin fit compared with previous fits [38, 91, 92, 151], evaluated over the 427 NR simulations. For Hofmann *et al.* [151], both the $(n_M=1, n_J=2)$ fit (6 coefficients) and the $(n_M=3, n_J=3)$ version (16 coefficients) are listed. We also show results for refitting previous ansätze to the present NR data set, for a refit of our hierarchically obtained ansatz directly using the full data set, and for the same fitting procedure, but using uniform weights.

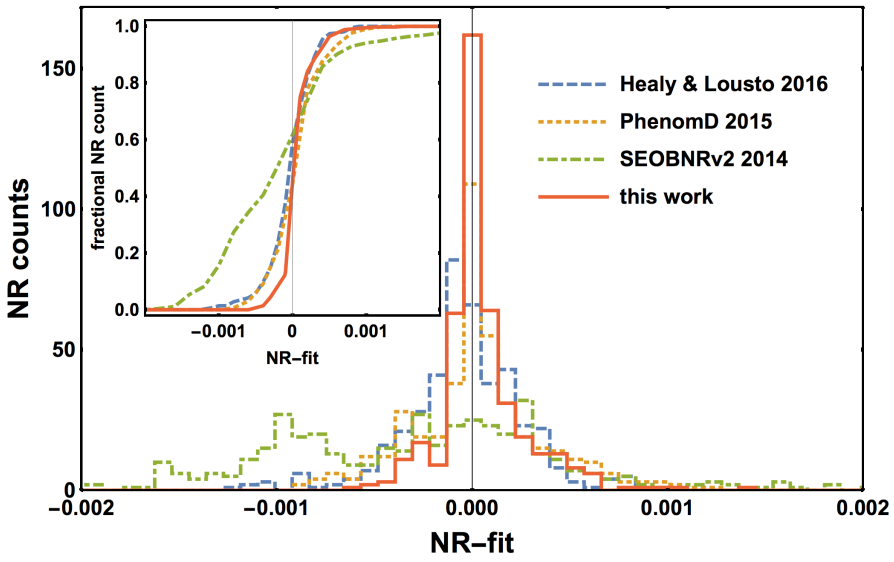

FIGURE 4.16: Fit residuals of the radiated energy $E_{\rm rad}$, for this work (cf. Table 4.6) and for previously published fits (SEOBNRv2 2014 [63], Healy & Lousto 2016 [92], PhenomD 2015 [38]), evaluated over the set of 427 NR simulations shown in Figure 4.5. Main panel: histograms, with 10 outliers for SEOBNRv2 (a recalibration of the fit from [159]) with $|\mathrm{NR}-\mathrm{fit}|>0.002$ outside of the plot range. Inset: cumulative distributions over the same range.

	$N_{\rm coef}$	mean	stdev	AICc	BIC
HLZ2014 [91]	19	-5.4×10^{-5}	3.4×10^{-4}	−5802.5	−5723.2
HL2016 [92]	19	-4.4×10^{-5}	3.0×10^{-4}	−5909.8	−5830.5
PhenomD	10	2.5×10^{-5}	3.4×10^{-4}	−5914.9	−5870.8
(refit)	10	6.1×10^{-5}	3.3×10^{-4}	−5947.7	−5899.6
SEOBNRv2 [63]	2	-1.7×10^{-4}	1.0×10^{-3}	−5036.1	−5023.9
This work	15	4.7×10^{-5}	2.2×10^{-4}	−6454.8	−6391.0
(refit)	15	6.3×10^{-5}	2.1×10^{-4}	−6482.8	−6419.0
(uniform	15	-4.0×10^{-6}	2.1×10^{-4}	−5987.3	−5923.5
(uniform refit)	15	1.4×10^{-6}	2.0×10^{-4}	−6034.2	−5970.4

TABLE 4.9: Summary statistics for the new radiated-energy fit compared with previously published fits [38, 63, 91, 92], evaluated over the full set of 427 NR simulations shown in Figure 4.5. Also listed are a refit of the PhenomD [38] ansatz to the present NR data set, a refit of our hierarchically obtained ansatz directly to the full data set, and results with the same fitting procedure, but using uniform weights.

Refitting our final hierarchically obtained ansatz directly to the full data set produces slightly better summary statistics, but also allows uncertainties from the less well-controlled unequal-spin set to influence the other parts of the fit, while the stepwise fit gives better control over the extreme-mass-ratio behavior and better-determined coefficients for the well-constrained subspaces.

As a further test of robustness, we have repeated the hierarchical fitting procedure with uniform weights instead of the weights used so far and discussed in Sec. 4.2.10. This yields a fit consistent with our main result, though slightly less well constrained, but

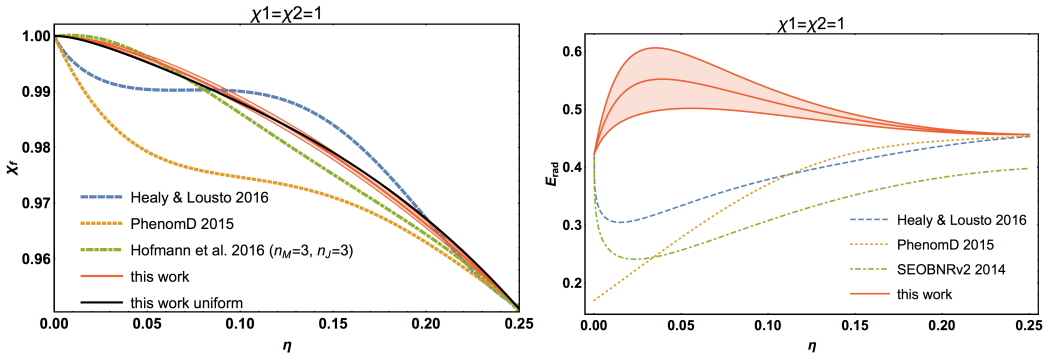

FIGURE 4.17: Comparison of this work with previously published fits [38, 92, 151, 159] in the limit of extremal aligned spins, $\chi_1 = \chi_2 = 1$ for final spin (left) and radiated energy (right). The shaded region shows our fit's 90% confidence interval, which is narrow enough (do not overlap with the other fits) to indicate that discrepancies with the referenced fits are significant and due to the different ansatz constructions, especially in the extreme-mass-ratio limit, and not just a consequence of insufficient data.

still improving over previous fits, thus demonstrating the robustness of the hierarchical fit construction under weighting choice.

We have also verified that our new fit does not violate the $\chi_{\rm f} \leq 1$ Kerr bound, particularly in the extreme-spin limit ($\widehat{S} = 1$) and at low η, see Figure 4.17.

4.2.7 Precessing binaries

Precession effects are in general relevant in the computation of remnant quantities. The final mass and final spin are used to compute the QNM frequencies that model the ringdown regime and where precession also causes a modulation of these frequencies. Then, we can turn the argument around: the modulation in the ringdown frequencies must be also related to the remnant properties of the BBH merger. Indeed, whereas precession effects are normally neglected for the final mass, they appear to be more dominant for the final spin.

Precessing systems have been long accounted in final-spin fits [151, 182, 183] by either calibrating the model directly to precessing cases or using a simple "augmentation" procedure [184] (see also [156]) for aligned-spin-only calibrations by adding the contribution of in-plane spins in quadrature to the aligned-spin fit result:

$$\chi_{\rm f}^{\rm aug} = \sqrt{\left(\chi_{\rm f}^{\rm aligned}\right)^2 + \left(S^{\rm in\text{-}plane}/M^2\right)^2}\,. \tag{4.38}$$

This procedure is known to significantly improve accuracy and reduce bias for precessing binaries. For example, it has been applied to the aligned-spin PhenomD fit [38] for the precessing PhenomPv2 model [166, 167], and to the RIT fit [91] in recent parameter

estimation work of the LIGO-Virgo collaboration [24, 185, 186] (including spin evolution according to [148]).

We have tested (4.38) to our aligned-spin fit, finding a small overshooting of the $|\chi_{\rm f}| \leq 1$ Kerr bound for mass ratios $q \gtrsim 24$, when the spin magnitude of the heavier BH is very close to extremal, and for certain orientation angles θ_i of the black holes' spins to the angular momentum. The worst cases give an excess in $\chi_{\rm f}$ of about 0.12% at $q \sim 60$ and intermediate opening angles, comparable to the aligned-spin fit residuals. No overshooting occurs if only the linear-in-η term in the final spin is used. Such a small inaccuracy when extending the aligned-spin fit to precessing cases is in principle not surprising, as this parameter-space region is not covered with NR simulations and hence the fit slope in this region is purely determined by extrapolation between the NR data and the extreme-mass-ratio limit, which we have ensured to be smooth with a flat approach to $\chi_{\rm f} = 1$ at $(\eta = 0,\, \chi_1 = 1)$ (see Sec. 4.1.5 and Figure 4.17). Very small inaccuracies in the intermediate-η extrapolation region can thus lead to a minimal Kerr violation when adding the in-plane spins according to (4.38). A clean solution to this issue would require more calibration NR simulations in the critical region and a study of precessing spin contributions in the extreme-mass-ratio limit.

Here, we opt for truncating the augmentation from (4.38) at unity: $\chi_{\rm f} = \min\left(\chi_{\rm f}^{\rm aug}, 1.0\right)$. This is justified as the overshooting is very small, on the order of the fit residuals, and limited to an extremal parameter-space region. The need for this *ad hoc* truncation will reduce or become obsolete when low-η-high-spin NR simulations and/or precessing extreme-mass-ratio information become available. A detailed comparison of fit accuracies over a representative set of precessing NR runs is left to future work.

4.2.8 Spin parameter selection

The results of the main text are given in terms of the spin parameter $\widehat{S}$. However, we have also tested the robustness of our hierarchical approach for two additional spin parameters: S and $\chi_{\rm eff}$ (Section 4.1.4).

We have redone the hierarchical ansatz construction and fitting for S and $\chi_{\rm eff}$, making the same ansatz choices for $\chi_{\rm eff}$ as we did for $\widehat{S}$ in the main text, but changing the 1D spin ansatz to a polynomial P(7) for S (instead of R(3,1) for $\widehat{S}$ and $\chi_{\rm eff}$) because rational functions in S tend to yield singularities. Checking other possible choices, we have not found any ansatz combination that makes these alternatives match or exceed the performance of the $\widehat{S}$-based fits presented in the main part of this paper. Results in terms of the RMSE, AICc and BIC are listed in Table 4.10, and residual histograms

shown in Figure 4.18. We still obtain better results than most previous fits (see Tables 4.8 and 4.9) with any parametrization, thus demonstrating the robustness of our method.

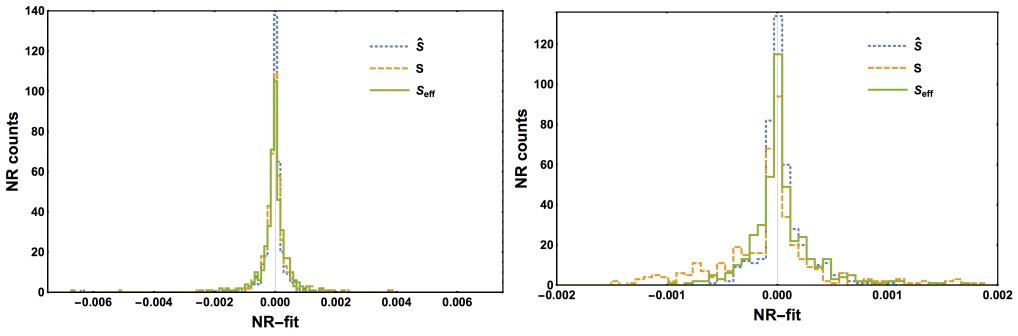

FIGURE 4.18: Fit residuals for three different choices of effective spin parameter. Right panel: final spin; left panel: radiated energy.

	RMSE	AICc	BIC
$\hat{S}$	$(5.15 : 2.24) \times 10^{-4}$	$-(5991.5 : 6454.8)$	$-(5923.9 : 6391.0)$
S	$(5.24 : 6.45) \times 10^{-4}$	$-(5930.9 : 5526.1)$	$-(5863.3 : 5439.1)$
$\chi_{\rm eff}$	$(5.97 : 4.23) \times 10^{-4}$	$-(5799.6 : 5962.7)$	$-(5731.9 : 5898.8)$

TABLE 4.10: Summary statistics for fits with three different choices of effective spin parameter and ansatz choices as discussed below, evaluated over the full 427 point NR data set. Values at left column: Final spin, Values at right column: radiated energy.

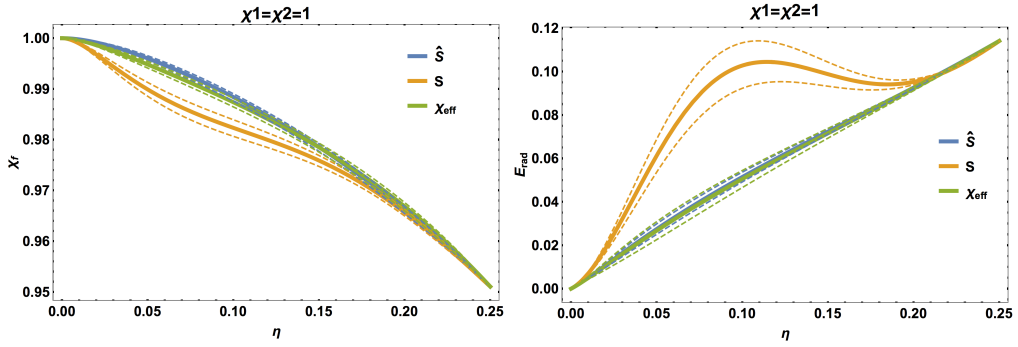

FIGURE 4.19: Final-state quantities in the extremal $\chi_1 = \chi_2 = 1$ limit for three different choices of effective spin parameter. Left panel: final spin, right panel: radiated energy.

Again, we have also analyzed the fit in the extrapolation regions to detect any artifacts not reflected by the statistical criteria (which are meaningful only in the calibrated region). In Figure 4.19 we check the extrapolation behavior of fits with the alternative parametrizations in the notoriously difficult $\chi_1 = \chi_2 = 1$ limit. The approach to this limit is smoother for the fits using $\widehat{S}$ and $\chi_{\rm eff}$ than for that using S, which shows some certainly nonphysical oscillations.

The conclusion is that the hierarchical fitting method is quite robust under a change of effective-spin parametrization, and indeed we would expect full equivalence in the limit of a huge data set with small, completely known NR errors (using appropriately adapted ansätze for each parametrization). With the current data set, $\widehat{S}$ and $\chi_{\rm eff}$ perform

similarly, while when using S additional high-spin data would be even more important to ensure smooth extrapolation.

4.2.9 Apparent horizon and area theorem

In Chapter 3 we justified why the mass of a BH is defined through the area theorem and where the area of the apparent horizon can be computed once the mass and the spin of the BHs are known. Thus, using the new expressions obtained for the final mass and final spin, it is also possible to compute the area of the final object and test whether this area satisfies the area theorem $A_1 + A_2 \leq A_f$ across the parameter space. Then, taking (3.18) it is possible to get,

$$A_j = 16\pi M_{irr,j}^2 = 8\pi M_j^2 \left(1 + \sqrt{1 - \chi_j^2}\right) , \tag{4.39}$$

where $j = 1, 2, f$, and tagging f the final object.

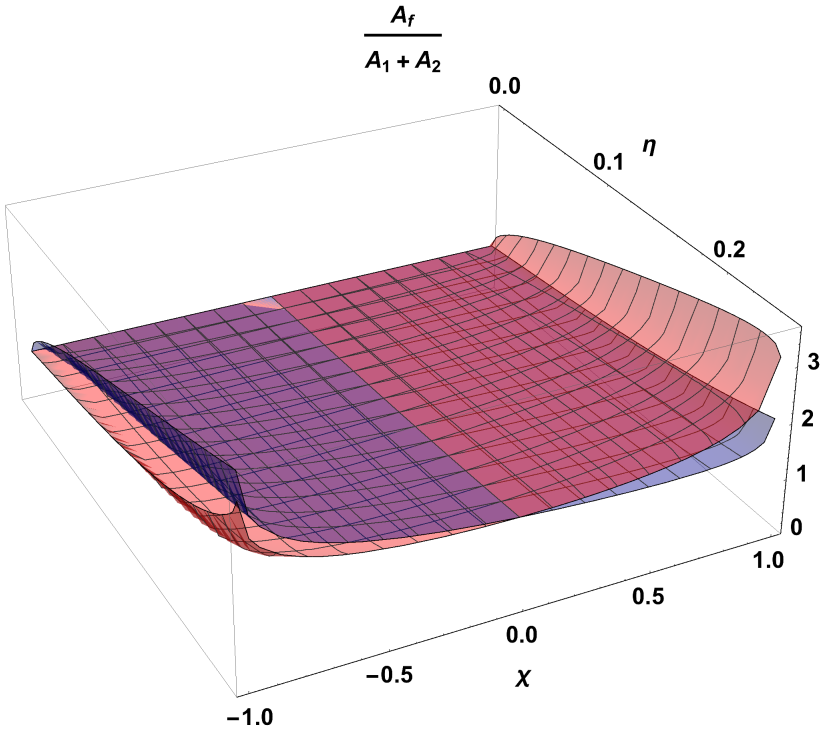

FIGURE 4.20: Test of the area theorem on the final state fits. The blue surface shows the equal-spin configurations while for the red one we are plotting the unequal spin ones $\chi_1 = -\chi_2$. Notice that is everywhere satisfied $A_f \geq (A_1 + A_2)$.

Figure 4.20 shows the profile of the ratio $A_f/(A_1 + A_2)$ across the two-dimensional parameter space for the equal-spin configurations $\chi_1 = \chi_2$ (blue) and the unequal-spin configurations $\chi_1 = -\chi_2$ (red). It is clear that both configurations satisfy everywhere $A_1 + A_2 \leq A_f$ only being equal when the $\eta = 0$. The latter can be trivially obtained analytically taking into account that $E_{rad}(0, \pm\chi, \chi) = 0$ and $\chi_f(0, \pm\chi, \chi) = \pm\chi$. Then,

from (4.39) we see that $A_f(\eta = 0, \pm\chi) = A_1(\eta = 0, \pm\chi)$ and where we have fixed $A_1 \geq A_2$.

4.2.10 Data sets and NR uncertainties

In our calibration of final state quantities we have used data from four different codes: `BAM`, SXS, RIT and GaTech. This has been done both to increase robustness against code inaccuracies and errors in the preparation of data products (such as incorrect metadata) and to benefit from the combined computational resources of different groups. However, though we are almost using all the publicly available BBH data, this data set is not sufficiently large to to make the possible outliers contributions irrelevant in the final results. Then, we need to carefully design procedures to eliminate data points of poor quality, to assign fit weights, and to check consistency between assumed error bars and our fit results.

We expect two main avenues to significantly improve over the fits we have presented in this paper: (a) providing more data points with high spins and unequal masses, in order to improve the accuracy of the fit near the boundaries of the fitting region and to reduce the need for extrapolation; and (b) determining more accurate and robust error bars for NR data, which would allow one to isolate small subdominant effects. In this chapter we address the latter point.

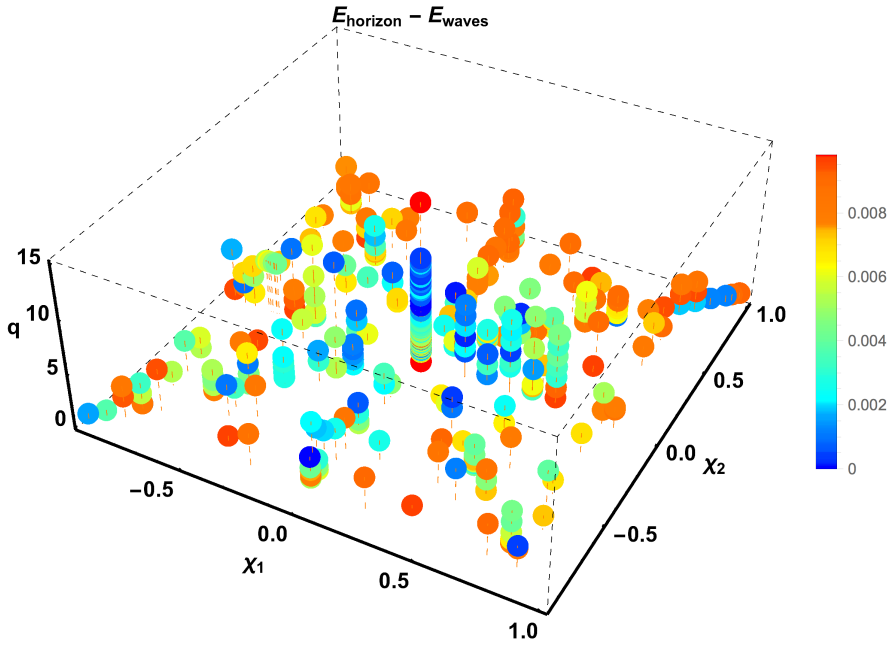

FIGURE 4.21: Differences between radiated energy computed from either horizon or waveform data, across the parameter space. The color scale quantifies the differences between the two computations. Differences are largest for high-mass-ratio and high-spin cases, where high NR accuracy is more demanding.

Final spin and final mass are usually computed as surface integrals over the apparent horizon using the isolated-horizon formalism although they can also be computed from the Weyl scalar as explained in (3.19). Then we can consider the differences between radiated energy values from the horizon and from the integrated waveforms, shown in Figure 4.21, as an estimate of NR errors. However, this will typically be a *pessimistic* estimate because horizon quantities are in general more reliable and thus big differences are typically caused by inaccuracies in the integrated emission. Thus, for SXS, RIT and GaTech results, we take the horizon values provided in the catalogs [4, 6, 89–91] whereas for `BAM` we take the horizon values when they are available and we use data computed from the waves when the AH finder fails[2]. This reduces our data set to 414 cases where we have both the waveform and AH estimate available. In Figure 4.22 we show that the distribution of this pessimistic estimate is similar to, but much wider-tailed than, the residuals from our radiated-energy fit.

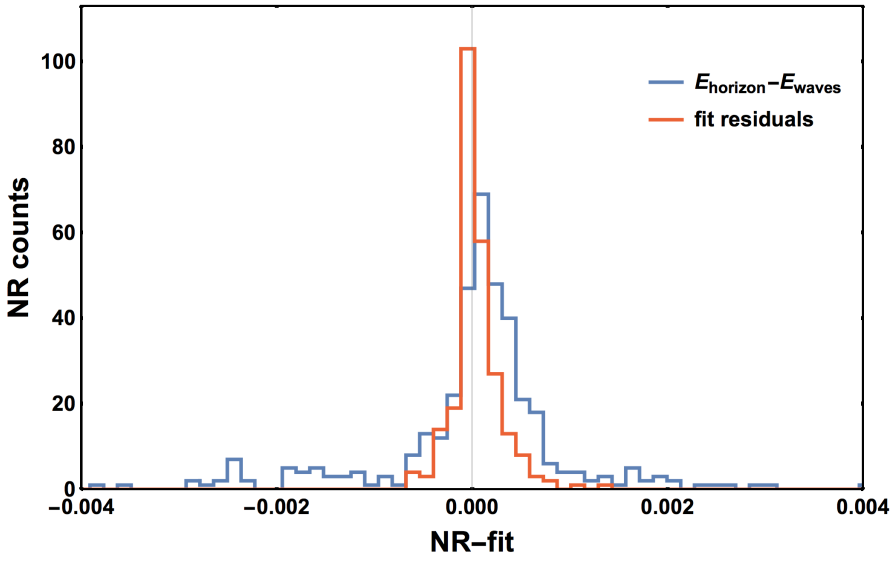

FIGURE 4.22: Histograms of the differences between radiated energy computed from either horizon or waveform data (as in Figure 4.21), compared with the residuals of the new radiated-energy fit (as in Figure 4.16).

A more realistic measure of NR errors is the difference between results from different codes for equal initial parameters. With a strict tolerance requiring equal initial parameters to within numerical accuracy,

$$|\lambda_i - \lambda_j| \leq \epsilon = 0.0002 \text{ with } \lambda_i = \{\eta_i,\, \chi_{1i},\, \chi_{2i}\}\ , \tag{4.40}$$

[2]For the `BAM` code, for some large-mass-ratio cases the AH finder fails due to the unfortunate choice of a shift condition, which results in a coordinate growth in the horizon which is roughly linear in time during the evolution. After several orbits the horizon of the larger BH is then no longer contained within the fine grid of the mesh refinement, which may trigger a failure of the horizon finder code. Due to the high computational cost of the simulations, we have not rerun these cases with improved parameters for the apparent horizon finder code. But rather, we compute the final angular momentum from the angular momentum surface integral at large radius, and the energy from the radiated GWs.

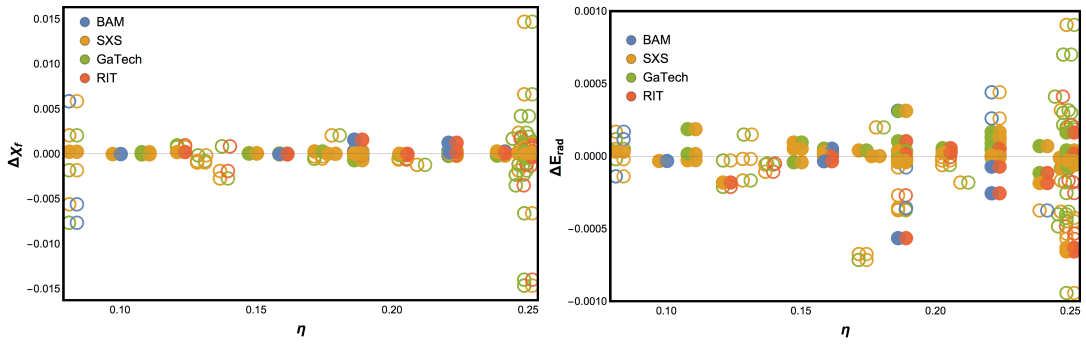

FIGURE 4.23: Differences in final spin χ_f (right panel) and radiated energy E_{rad} (left panel) for equal-parameter configurations but different NR codes. Solid circles: configurations with parameters equal to within numerical accuracy (narrow tolerance). Open circles: similar configurations but with some deviation in the parameters (wider tolerance, e.g. up to $\Delta\eta \approx 0.001$). Pairs of simulations are shown with a small horizontal offset for ease of visual identification.

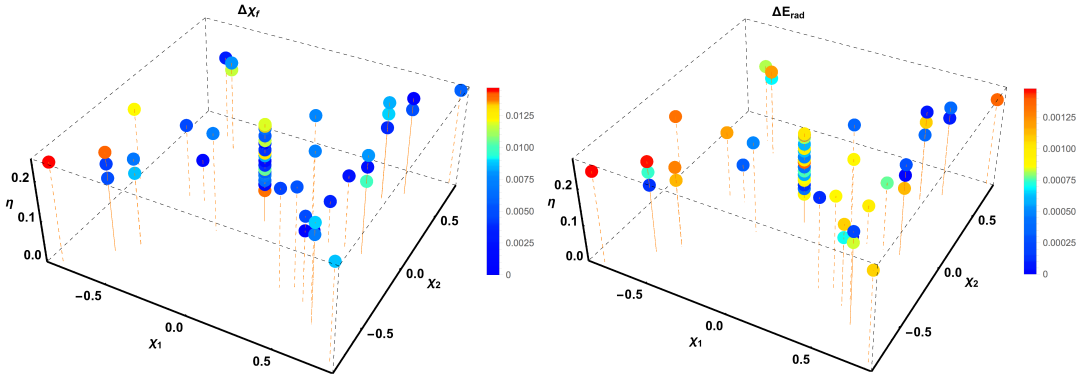

FIGURE 4.24: Differences in the final-state quantities for equal-parameter configurations and different NR codes. right panel: final spin χ_f, left panel: radiated energy E_{rad}. Points here correspond to both open and solid circles from Figure 4.23 (wider tolerance).

we find 41 such duplicate configurations out of the total of 427 cases.[3] We evaluate differences between these equal-parameter cases for final spin and radiated energy. Figure 4.23 shows that, with strict tolerance, these error estimates (standard deviations of 3.1×10^{-4} for χ_f and 1.6×10^{-4} for E_{rad})[4] are still on the same order but smaller than the respective fit residuals (RMSE of 5.2×10^{-4} for χ_f and 2.2×10^{-4} for E_{rad}). However, the set of true duplicates is small and mostly concentrated in equal-spin-similar-mass regions of the parameter space (cf. Figure 4.24), preventing us from naively extrapolating this error estimate to the full parameter space. Hence we consider it as a somewhat *optimistic* estimate of final-state NR errors.

We therefore have a rough expectation for the range of possible NR errors bracketed by these pessimistic and optimistic estimates, but no detailed information for each case

[3] With a more relaxed tolerance, $\epsilon = 0.001$ in (4.50), we find 33 duplicates and 19 sets of two or more configurations with reasonably similar parameters, corresponding to a total of 131 cases (30% of the total data set), compatible with the 71 "twins" out of a data set of 248 reported in [151]. The wider-tolerance tuples are shown as open circles in Figure 4.23.

[4] For the relaxed tolerance, the values are 2.8×10^{-3} for χ_f and 3.5×10^{-4} for E_{rad}, compatible with the 2×10^{-3} given in [151] for χ_f.

over the whole parameter space. Instead, we use simple heuristic fit weights. The overall scale of the NR error is not relevant for determining fit weights, so we only need to assign relative weights between the cases, emulating the usual quadratic scaling with data errors which can also be deduced from Figure 4.21. For SXS data we down-weight cases with $\eta < 0.1$ by a factor of 2^2; while for the puncture codes (`BAM`, GaTech, RIT) we expect larger inaccuracies especially at low η, and so we down-weight by a factor of 2^2 above $\eta = 0.223$ and 3^2 below that mass ratio, and a factor of 5^2 below $\eta = 0.05$ (including the computationally challenging $q = 18$ cases). As mentioned before, a more detailed NR error study, leading to better-determined weights, would be a clear avenue to further improve fit results.

Outliers

From the original set of NR simulations we have removed 16 cases as outliers, which are listed in Table 4.17. For this decision, we have considered three main sources of outliers: cases whose NR setup is not appropriate for the purpose of this study, duplicated configurations for which the variations in the final quantities are much larger than the RMSE, and cases that are found to be drastically off the trend of otherwise smooth data sets in any of the one-dimensional plots in our hierarchical fitting procedure. Outliers 1,2,5,16 have rather short orbital evolutions, so that they can be used for ringdown-only studies, but not for our purpose of predicting the final state from initial parameters. For outliers 10–12 and 15–16 we have found large variations in the final-state values for different codes (see Figure 4.23). Here we have used only the equivalent SXS configuration, in each case corresponding to longer and presumably more accurate evolutions. The remaining seven outliers have been identified after performing the step-by-step one-dimensional analysis of the data, each deviating so clearly that there must be an underlying systematic problem and not just a statistical fluctuation (in which case they could not be excised from the data set). As an example, we highlight in Figure 4.25 three clear GaTech outliers found in the unequal-spin calibration step; however, it was recently confirmed [187] that these three cases should have a negative sign of their final spin, and with this change they are fully consistent with our fits. We note that the overall data quality of the omitted cases may be perfectly adequate for other studies; while for this final-state study, due to good data coverage in the corresponding parameter-space regions and clear global trends in the full data set, the consistency requirements are quite narrow.

id	q	χ_1	χ_2	ω_0	D_0	$E_{\rm rad}$	$\Delta E_{\rm rad}$	$\chi_{\rm f}$	$\Delta\chi_{\rm f}$	tag	code
1	1.00	-0.80	-0.80	0.060	5.88	0.0325	-0.0010	0.4122	-0.0146	D6.2_q1_a-0.8_m100	GaTech
2	1.00	-0.60	-0.60	0.058	5.93	0.0349	-0.0013	0.4876	-0.0066	D6.2_q1_a-0.6_m100	GaTech
3	1.00	0.80	-0.80	0.025	10.92	0.0491	0.0002	0.6839	-0.0000	D11_a0.8_q1.00_m103_As	GaTech
4	1.00	0.80	0.80	0.024	11.07	0.0883	-0.0005	0.9086	0.0010	D11_q1.00_a0.8_m200	GaTech
5	2.50	0.60	0.60	0.051	6.27	0.0528	0.0002	0.8255	0.0004	Lq_D6.2_q2.50_a0.6_th000_m140	GaTech
6	3.50	0.00	0.00	0.015	15.90	0.0258	0.0007	0.5046	0.0005	BBH_CFMS_d15.9_q3.50_sA_0_0_0_sB_0_0_0	SXS
7	5.00	-0.73	0.00	0.030	9.53	0.0129	0.0004	0.0222	0.0460	D10_q5.00_a-0.73_0.00_m240	GaTech
8	5.00	-0.72	0.00	0.030	9.54	0.0129	0.0004	0.0164	0.0340	D10_q5.00_a-0.72_0.00_m240	GaTech
9	5.00	-0.71	0.00	0.029	9.55	0.0130	0.0005	0.0105	0.0220	D10_q5.00_a-0.71_0.00_m240	GaTech
10	5.00	0.00	0.00	0.027	10.07	0.0176	-0.0001	0.4175	0.0009	D10_q5.00_a0.0_0.0_m240	GaTech
11	5.50	0.00	0.00	0.031	9.16	0.0161	0.0001	0.3932	-0.0002	D9_q5.5_a0.0_Q20	GaTech
12	6.00	0.00	0.00	0.027	10.13	0.0145	-0.0001	0.3732	0.0007	D10_q6.00_a0.00_0.00_m280	GaTech
13	6.00	0.40	0.00	0.026	10.35	0.0195	0.0000	0.6257	-0.0000	D10_q6.00_a0.40_0.00_m280	GaTech
14	8.00	0.85	0.85	0.048	6.50	0.0248	-0.0027	0.8948	-0.0012	q8++0.85_T_80_200_-4pc	BAM
15	10.00	0.00	0.00	0.035	8.39	0.0082	-0.0000	0.2588	-0.0019	D8.4_q10.00_a0.0_m400	GaTech
16	10.00	0.00	0.00	0.035	8.39	0.0081	-0.0001	0.2665	0.0058	q10c25e_T_112_448	BAM

TABLE 4.11: NR cases from the source catalogs not included in the fit calibration, for reasons detailed below.

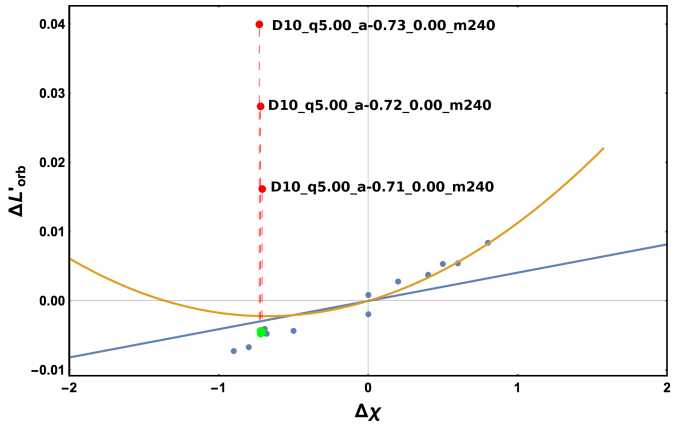

FIGURE 4.25: Unequal-spin effects for final spin $\chi_{\rm f}$ at $q = 5$, shown as residuals against the 2D equal-spin fit (cf. Figure 4.31). The three points highlighted in red are similar configurations from the GaTech catalog, for which it has since been confirmed [187] that the sign of $\chi_{\rm f}$ should be negative instead, making $L'_{\rm orb}$ fit with the trend – corrected values are shown in green.

4.3 Hierarchical data-driven fitting: Application to peak luminosity

The successful implementation of the hierarchical data-driven fitting on the final spin and radiated energy motivates the testing of this methodology on other waveform-related quantities were a calibration to NR data is also needed. The intuition and the relevant improvements obtained with the extreme-mass-ratio limit and unequal-spin calibration may be transferred to any other physical quantity related to the BBH mergers. In this case we study a merger-related quantity as the peak luminosity described in Chapter 3.

The peak luminosities for the first BBH observations (GW150914, LVT151012, GW151226) were inferred using a preliminar version of the fit methodology described in this thesis but without considering the extreme-mass-ratio constraints [188]. Thus, we show here an improved version of the old model but now including more unequal-spin cases and

the calibration to the extreme-mass-ratio limit following the hierarchical data-driven approach described in this chapter. Then, we develop a three-dimensional ansatz and fit to 378 simulations from four separate NR codes, including more subdominant modes than before, and to independent numerical results for large mass ratios obtained with the perturbative scheme of Refs. [93, 95, 158]. Still, we concentrate on cases where the spin of each BH is aligned with the system's total angular momentum, using the dimensionless components $\chi_i = S_i/m_i^2 = \frac{\vec{S}_i}{m_i^2} \cdot \frac{\vec{L}}{|\vec{L}|}$ of the spins $\vec{S}_i$ projected onto the orbital angular momentum $\vec{L}$.

The results described below refer to the ones published in [8].

4.3.1 Astrophysical implications of the peak luminosity

The peak rate at which BBHs radiate GW energy makes them the most luminous known phenomena in the universe. The source of the first GW detection GW150914 has been inferred to be consistent with two BHs of $29^{+4}_{-4}\,M_\odot$ and $36^{+5}_{-4}\,M_\odot$ inspiralling, merging and ringing down as described by GR. Its emission of GW energy reached, for a small fraction of a second, a peak rate of $3.6^{+0.5}_{-0.4} \times 10^{56}$ erg/s, equivalent to $200^{+30}_{-20}\,M_\odot\,c^2$/s [3, 13, 189]. Though this *peak luminosity*, $L_{\rm peak}$, is not electromagnetic, but gravitational, we can compare its numerical value to the photon luminosity of other astrophysical sources to illustrate its scale: GW150914 at its peak emitted as much power as $\sim 10^{23}$ suns, $\gtrsim 10^{11}$ times more than all stars in the Milky Way, and still 60–90 times more than the ultra-luminous gamma-ray burst GRB 110918A [190].[5]

Beyond using $L_{\rm peak}$ to compare the energetics of GWs and other astrophysical events, one can also consider its relevance for the effect of BBH coalescences on their immediate surroundings. The influence of super-massive black hole (SMBH) mergers on circumbinary accretion disks (see Ref. [191] and references therein) is determined mostly by the integrated radiated energy of the late-inspiral and merger phase, though Refs. [192, 193] suggested weak prompt EM counterparts sensitive to $L_{\rm peak}$ and $L_{\rm GW}(t)$. For stellar-mass BBHs, any significant interaction with surrounding material or fields is highly speculative – see e.g. the references in Sec. 4 of Ref. [194]. Still it is conceivable that an accurate $L_{\rm peak}$ model could be useful in constraining exotic models. Furthermore, the GW peak luminosity $L_{\rm peak}$ does not depend on the total mass of a BBH system: Luminosity generally scales with emitted energy over emission timescale, $L \sim E_{\rm rad}/\Delta t$. But for a BBH, both the total radiated energy $E_{\rm rad}$ and the characteristic merger timescale Δt are proportional to the total mass, so that $L_{\rm peak}$ is independent of it. Hence, the GW peak luminosities even of SMBH binaries, observable by eLISA-like missions [175, 195, 196]

[5] Assuming $L_\odot = 3.8 \times 10^{33}$erg/s, $L_{\rm MW} = 2 \times 10^{11} L_\odot$ and the GRB's estimated peak isotropic equivalent luminosity of $(4.7 \pm 0.2) \times 10^{54}$ erg/s [190].

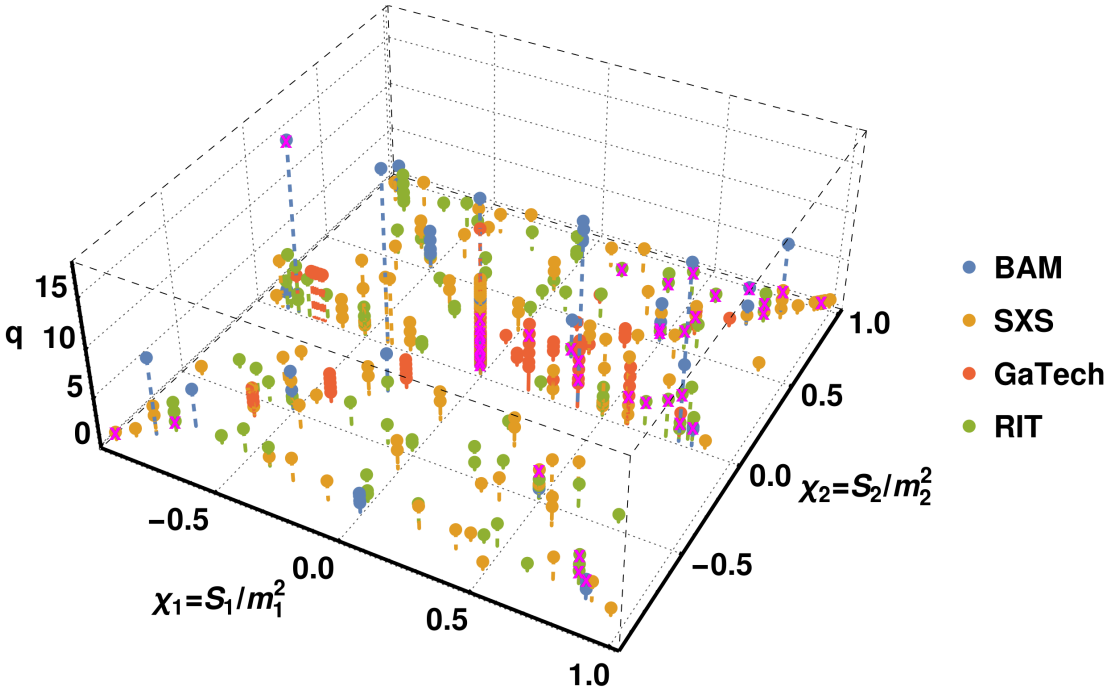

FIGURE 4.26: Parameter-space coverage of the combined NR data set from BAM, SXS, GaTech, RIT, shown against the individual BH spins and the mass ratio $q = m_1/m_2$ of the system. Simulations not used in the fit (see the outliers Table 4.17) are marked with magenta crosses.

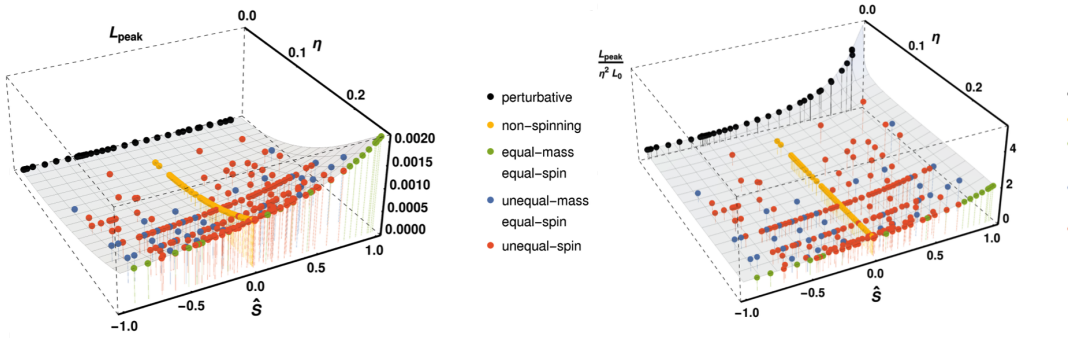

FIGURE 4.27: Combined data set over the two-dimensional space spanned by symmetric mass ratio η and effective spin $\widehat{S}$, defined in (4.3). Left panel: peak luminosity $L_{\rm peak}$, right panel: rescaled as $L_{\rm peak}/\eta^2 L_0$. Subsets used in the various steps of Figure 4.1 are highlighted by colors. The shaded surface is added here to guide the eye, but is in fact the 2D projection of the new fit developed in this paper.

or by pulsar timing arrays (PTAs, [197–199]), are similar to those of stellar-mass BBHs. The results of this work will be applicable to such systems as well.

4.3.2 NR data

We begin by considering the same 427 non-precessing NR simulations from the four sources used for the final spin and final mass calibration (section 4.2), covering the

parameter space illustrated in Figs. 4.26 and 4.27 and distributed:

- 45 simulations performed by the authors with the `BAM` code [72, 181], including those first used in Refs. [7, 38];
- 161 simulations from the public SXS catalog [4, 89] performed with the Spectral Einstein Code [84];
- 114 simulations from the public GaTech catalog [6, 90], performed with the `MAYA` code [200–203];
- 107 simulations [5, 85, 91, 92] with the `LAZEV` code [204], labeled "RIT" in the following.

We use mass and spin parameters of the component BHs after equilibration and the initial burst of 'junk' radiation. To compute the luminosity for `BAM`, SXS and GaTech simulations, we begin with the Weyl scalar ψ_4 decomposed into its spin-two spherical harmonic multipoles following (3.19). From these spherical harmonic multipoles, we calculate the GW strain-rate multipoles $\dot{h}_{\ell m}(t)$ via the FFI method described in 3 and in Ref. [142]. We then compute the peak luminosity according to (3.20) and truncating the sum over ℓ at $\ell_{\rm max} = 6$. For RIT simulations, we use directly the peak luminosity values as given in Ref. [92], which again include all modes up to $\ell_{\rm max} = 6$.

We remove 41 cases from the initial catalog for reasons as discussed in Section 4.2, e.g. because they are inconsistent with equivalent or nearby configurations from the same or other codes. Thus, we perform our fit with a final set of 427 NR results.

4.3.3 Constructing the phenomenological fit

We apply the hierarchical modeling scheme for the three-dimensional non-precessing BBH parameter space that introduced in this chapter and is summarized in Figure 4.1. The general idea, as before, is to construct a fit ansatz that matches the structure actually seen in the data set, and to model effects in order of their importance: first fit well-constrained subspaces as functions of the dominant parameters, then add subdominant effects only to the degree that they are supported by the data. In this case the extreme-mass-ratio limit is included by calibrating the fit to the Teukolsky and the RWZ results (see Section 4.1.5). The parameter-space dimensionality is the same for peak luminosity as for final spin or radiated energy. Hence, for non-precessing quasi-circular BBHs, this leaves a three-dimensional parameter space: mass ratio and two spin parameters χ_1 and χ_2 or, in terms of the *effective* physical parameters, mass-ratio, S_{eff} and

$\Delta\chi$. Just like the final state fits, we use $\widehat{S}$ as the optimal choice for the spin parameter. Akaike and Bayesian information criteria (Section 4.1.6), help to choose between fits based not only on the overall goodness of fit, as measured e.g. by the root-mean-square error (RMSE), but also penalize excessively high numbers of free coefficients.

4.3.4 One-dimensional subspace fits

4.3.4.1 One-dimensional non-spinning fit

First, we analyse 84 non-spinning cases, including 81 NR simulations as well as the non-spinning large-mass-ratio data points. As we do in Sec. 4.2.3.1 and Sec. 4.2.3.2, we consider several ansatz choices for the one-dimensional function $L'_{\rm peak}(\eta)$: polynomials up to seventh order, denoted as $\mathrm{P}(m)$, as well as rational functions, denoted as $\mathrm{R}(m,k)$ for polynomial orders m and k in the numerator and denominator, respectively. We construct the latter as Padé approximants from an initial polynomial fit to simplify the handling of initial values in the fitting algorithm.

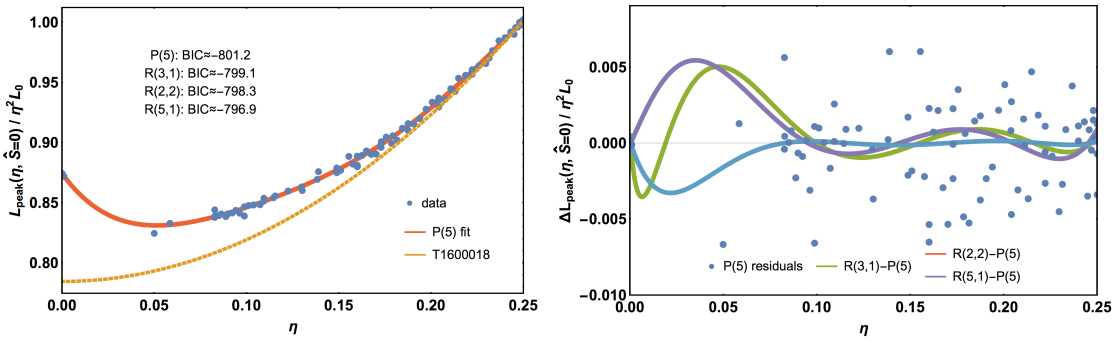

FIGURE 4.28: One-dimensional fits of the rescaled non-spinning peak luminosity $L'_{\rm peak}\left(\eta, \widehat{S}=0\right)$. Left panel: the preferred fifth-order polynomial, see (4.41), and comparison with the previous fit from Ref. [188]. Right panel: residuals of this fit (points) and differences from the three next-highest-ranking fits in terms of BIC (lines).

	Estimate	Standard error	Relative error [%]
a_0	0.8742	0.0010	0.1
a_1	−2.11	0.28	13.3
a_2	35.2	7.0	19.9
a_3	−245	64	26.0
a_4	877	248	28.3
a_5	−1173	354	30.2

TABLE 4.12: Fit coefficients for the one-dimensional non-spinning $L'_{\rm peak}\left(\eta, \widehat{S}=0\right)$ fit over 84 data points, along with their uncertainties (standard errors) and relative errors (std.err./estimate).

With the dominant η^2-dependence already scaled out, fitting the higher-order corrections allows us to achieve sub-percent accuracy, though the additional fit coefficients are not

very tightly constrained. The top-ranked fit both by BIC and AICc (with marginally significant differences) is a fifth-order polynomial

$$L'_{\rm peak}\left(\eta, \widehat{S}=0\right) = a_5\eta^5 + a_4\eta^4 + a_3\eta^3 + a_2\eta^2 + a_1\eta + a_0 \tag{4.41}$$

with its fit coefficients and their uncertainties given in Table 4.12.

Figure 4.28 shows this fit, its residuals and comparisons with both the previous fit from Ref. [188] ("T1600018") and the next-highest-ranked alternatives. These next-best alternatives are all rational functions, with the next-simpler polynomial P(4) disfavored by 7 in BIC and 20% in RMSE and the next-higher-order P(6) marginally disfavored by 4 in BIC with almost identical RMSE. We find a clear upwards correction over the T1600018 result at low η, and differences between highly-ranking fits that are much smaller than this correction or the typical residuals. In the data-less region between the lowest-η NR case ($q = 18$) and the perturbative results, differences between the highest-ranking fits are larger, but still at most at the same level as the typical fit residuals at higher η, corresponding to relative errors below 0.6%. As another comparison, refitting the simple $L_{\rm peak}(\eta) = a_2\eta^2 + a_4\eta^4$ ansatz that we used in Ref. [188] (which in $L'_{\rm peak}$ corresponds to just const. $+\,\eta^2$) is disfavored by over 280 in BIC over this data set, and has a four times higher RMSE.

All highly-ranked fits agree that the NR data cannot be connected to the large-mass-ratio regime with a simple monotonic function. This behavior might seem surprising, but can be explained by studying the individual modes: the observed behavior of the total peak luminosity results from competing trends of modes that either fall or rise towards $\eta \to 0$. (See Figure 4.40 for details, and Refs. [128, 205–208] for previous studies of higher-mode amplitudes.) Also we recall that the full $L_{\rm peak}\left(\eta, \widehat{S}=0\right)$ is of course monotonic after the dominant η^2 term has been factored back in.

4.3.4.2 One-dimensional equal-mass-equal-spin fit

Next, we consider 32 equal-mass and equal-spin NR simulations, i.e. configurations with $\eta = 0.25$ and $\chi_1 = \chi_2 \neq 0$, fitting the one-dimensional function $L'_{\rm peak}\left(\eta = 0.25, \widehat{S}\right)$. We use a similar set of polynomial and rational ansätze, with the intercept fixed by requiring consistency with the η fit in the non-spinning case, $L'_{\rm peak}\left(\eta = 0.25,\ \widehat{S}=0\right)$. The curvature of this spin dependence at equal masses is relatively mild and can be best fit by a three-coefficient rational function ansatz

$$L'_{\rm peak}\left(\eta = 0.25, \widehat{S}\right) = \frac{0.107 b_2 \widehat{S}^2 + 0.465 b_1 \widehat{S}}{1 - 0.328 b_4 \widehat{S}} + 1.00095\,, \tag{4.42}$$

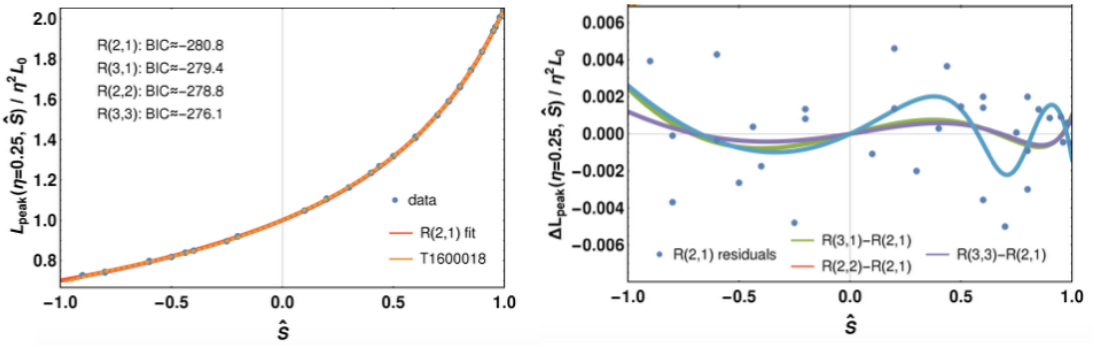

FIGURE 4.29: One-dimensional fits of the rescaled equal-mass-equal-spin peak luminosity $L'_{\rm peak}\left(\eta = 0.25, \widehat{S}\right)$. Left panel: best fit in terms of BIC, a rational function R(2,1), see (4.42), and the almost indistinguishable P(5) from Ref. [188]. Right panel: residuals of this fit (points) and differences from three next-best-ranked fits by BIC (lines).

	Estimate	Standard error	Relative error [%]
b_1	0.9800	0.0023	0.2
b_2	−0.178	0.028	15.5
b_4	1.786	0.014	0.6

TABLE 4.13: Fit coefficients for the one-dimensional equal-mass-equal-spin $L'_{\rm peak}\left(\eta = 0.25, \widehat{S}\right)$ fit over 32 data points.

with the numerical prefactors due to constructing the ansatz as a Padé approximant to simplify handling of initial values in the fitting code. This fit is marginally top-ranked by both AICc and BIC; it is shown in Figure 4.29 and the coefficients b_i are given in Table 4.13. Low-order rational functions are clearly preferred over polynomials, with the P(5) we used in Ref. [188] disfavored by +14 in BIC and having 12% higher RMSE, and the simple R(2,1) ansatz is fully sufficient to describe the data to similar sub-percent accuracy as the non-spinning set. Adding another term in either the numerator or denominator is possible, but does not improve the statistics; while adding too many terms tends to induce unconstrained coefficients or singularities within the fitting region.

4.3.5 Two-dimensional fits

In proceeding with the hierarchical modeling approach, we can now make a two-dimensional equal-spin ansatz informed and constrained by the previous 1D steps and the large-mass-ratio information. In Ref. [7], we constructed 2D final-state ansätze by first simply adding the two one-dimensional fits and then generalizing each spin coefficient by a polynomial in η. This time, we find that we need to introduce additional η-dependent higher-order terms in $\widehat{S}$, as the curvature of $L'_{\rm peak}$ along the spin dimension increases from equal masses towards the largest mass ratios.

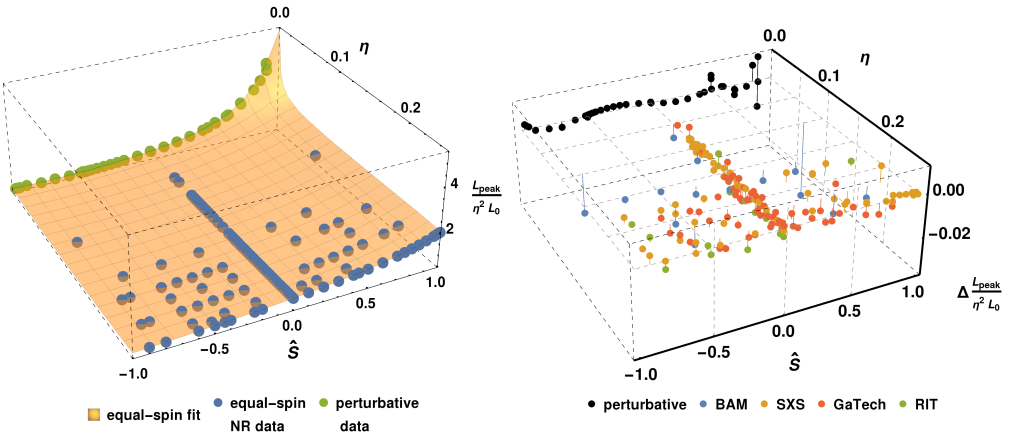

FIGURE 4.30: Results of the two-dimensional equal-spin $L'_{\rm peak}\left(\eta, \widehat{S}\right)$ fit. First panel: comparison of the smooth fit surface with the equal-spin NR data and perturbative results; second panel: residuals over the parameter space, color-coded by data provenance.

We thus consider a 2D ansatz of the general form

$$L'_{\rm peak}\left(\eta, \widehat{S}\right) = L'_{\rm peak}\left(\eta, \widehat{S}=0\right) + \mathrm{R}(m,k)\left(\eta, \widehat{S}\right) \tag{4.43}$$

with the η fit from (4.41) and the rational function $\mathrm{R}(m,k)$ in $\widehat{S}$ inheriting the coefficients b_i from Table 4.13 and filled up with $b_i = 1.0$ for orders not present in $L'_{\rm peak}\left(\eta = 0.25, \widehat{S}\right)$ from (4.42). We then introduce the required freedom to change the curvature along the η dimension through the substitution

$$b_i \to b_i \sum_{j=0}^{j=J} f_{ij}\,\eta^j\,, \tag{4.44}$$

with a maximum expansion order J.

On the other hand, the number of free coefficients is reduced again by consistency constraints with the 1D fits:

$$f_{i2} = 16 - 16 f_{i0} - 4 f_{i1} \quad \text{for } b_i \text{ from } \eta = 0.25 \text{ fit}\,, \tag{4.45a}$$

$$f_{i2} = -16 f_{i0} - 4 f_{i1} \quad \text{for other } b_i\,. \tag{4.45b}$$

In practice, we use R(4,2) to match the $q = 10^3$ result, thus introducing one extra power of $\widehat{S}$ in both numerator and denominator compared to $L'_{\rm peak}\left(\eta = 0.25, \widehat{S}\right)$ in (4.42).

With 92 equal-spin data points not yet used in the two one-dimensional subspace fits (including 50 NR simulations and the single-spin large-mass-ratio results, which as discussed above can be considered as effectively equal-spin), we can easily expand the

polynomials in η from (4.44) to order $J = 2$, $b_i \to b_i \left(f_{i0} + f_{i1}\eta + f_{i2}\eta^2\right)$, and still obtain a well-constrained fit. The only further constraint is that we set the remaining highest-order coefficient in the denominator, f_{71}, to zero to avoid a singularity within the physical $\left(\eta, \widehat{S}\right)$ region, leaving 11 free coefficients.

The resulting fit and its residuals over the equal-spin data set are plotted in Figure 4.30. We again find sub-percent relative errors over most of the calibration set, with an RMSE of ≈ 0.0057 and only two cases over 1% relative error (both $q = 8$ from `BAM`). There is no apparent curvature or oscillatory feature except for the large-mass-ratio region, where the $L'_{\rm peak}$ quantity plotted in Figure 4.30 over-emphasizes any remaining features and the corresponding relative errors are below 0.5%. This accuracy is similar to that of the large-mass-ratio-only fits, thus proving that the combined two-dimensional fit successfully captures both the shallow spin slope at similar masses and the steep slope in the perturbative regime. Several outliers have been removed before the fit; the 2D fit still matches all equal-spin outliers to below 4% relative error.

As this equal-spin part of the full $L'_{\rm peak}\left(\eta, \widehat{S}, \Delta\chi\right)$ will be refitted, together with unequal-spin corrections, in the next and final step of the hierarchical procedure, we do not tabulate its best-fit coefficients at this point.

4.3.6 Unequal-spin contributions and 3D fit

Simply extending the 2D fit to the full 3D parameter space either by evaluating fit errors of the equal-spin-only calibrated fit over the whole data set, or by refitting the 2D ansatz from (4.43), more than doubles the RMSE and induces oscillations at high $\left|\widehat{S}\right|$. But even for such a naive approach, relative errors are still limited to below 10%, so that the effects of unequal spins can evidently be treated as subdominant corrections. We follow here the same approach as in Ref. [7] to model spin-difference effects, constructing a 3D ansatz as

$$L'_{\rm peak}\left(\eta, \widehat{S}, \Delta\chi\right) = L'_{\rm peak}\left(\eta, \widehat{S}\right) + \Delta L'_{\rm peak}(\eta, \widehat{S}, \Delta\chi)\,. \tag{4.46}$$

We choose the correction terms $\Delta L'_{\rm peak}$ with guidance from (i) Post-Newtonian (PN) analytical results and (ii) an analysis of the residuals of unequal-spin NR simulations under the 2D equal-spin fit.

Though PN cannot be expected to be quantitatively accurate for the late-inspiral and merger stages of BBH coalescence – where the peak luminosity emanates – it can still give some intuition on the qualitative shape of spin and spin-difference effects. The PN spin-orbit flux terms as given in Eq. (3.13) of Ref. [20] and Eq. (4.9) of Ref. [52] include

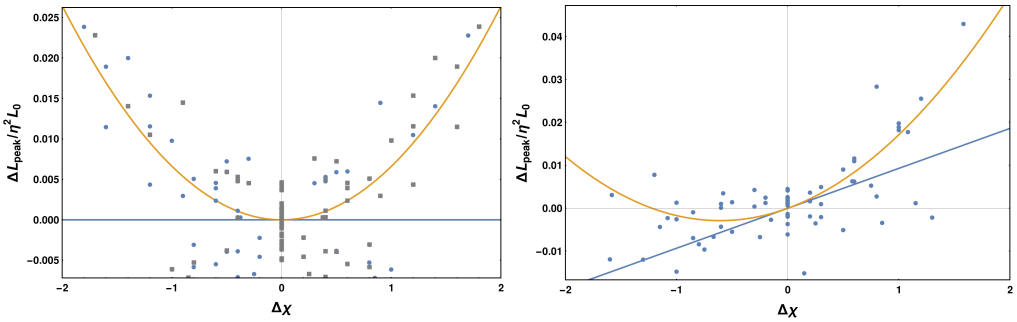

FIGURE 4.31: Examples of spin-difference behavior at fixed mass ratios, for scaled NR data $L'_{\rm peak}$ after subtraction of the 2D $\left(\eta, \widehat{S}\right)$ fit. Right panel: $q = 1$ with linear term vanishing due to symmetry and mainly quadratic dependence; points in gray are mirror duplicates exploiting the $\chi_1 \leftrightarrow \chi_2$ symmetry at equal masses. There is residual scatter in the $|\Delta\chi| \lesssim 1$ range not captured by the quadratic fit, which is however not much larger than the scatter in equal-spin residuals, and hence probably related to the general uncertainties in NR data quality for $L_{\rm peak}$. Left panel: $q = 3$ where the linear term dominates and the apparent quadratic dependence likely is noise-dominated.

linear terms in $\Delta\chi$ with an η-dependent prefactor that can be expressed as $\mathrm{P}(\eta)\sqrt{1-4\eta}$ with a polynomial $\mathrm{P}(\eta)$. The next-to-leading-order contributions would be quadratic in $\Delta\chi$ and a mixed term proportional to $\widehat{S}\Delta\chi$.

At equal masses ($\eta = 0.25$) BBH configurations are symmetric under relabeling of the component BHs, so that terms linear in $\Delta\chi$ must vanish; this is ensured by the $\sqrt{1-4\eta}$ factor, which we therefore expect both in the linear and the mixture term, but not in the quadratic term. Hence, we make the general spin-difference ansatz

$$\Delta L'_{\rm peak}\left(\eta, \widehat{S}, \Delta\chi\right) = A_1(\eta)\,\Delta\chi + A_2(\eta)\,\Delta\chi^2 + A_3(\eta)\,\widehat{S}\Delta\chi \tag{4.47}$$

with a simple polynomial for $A_2(\eta)$ and $A_1(\eta)$, $A_3(\eta)$ both being a polynomial multiplied by the symmetry factor.

To check that these up to three terms accurately describe our available set of 238 unequal-spin NR cases, and to get a handle on the functions $A_i(\eta)$, we visually inspect the data in steps of fixed mass ratio with sufficient numbers of data points. Examples for $q = 1$ and $q = 3$ are shown in Figure 4.31. The unequal-spin data set appears more noisy for luminosity than for the final-state quantities studied in Ref. [7], yet can still be analyzed following the same procedure. For each mass ratio step, $q = \{1, 1.33, 1.5, 1.75, 2, 3, 4, 5, 6, 8\}$, we compute the residuals under the non-spinning fit from (4.43), then perform four fits in $\Delta\chi$: linear, linear+quadratic, linear+mixed, or the sum of all three terms. Fits of the collected coefficients, as functions of η, give estimates of the functions $A_i(\eta)$, as displayed with the "per-mass-ratio data" points and "per-mass-ratio fit" lines in Figure 4.32.

The scatter of fit coefficients at individual mass-ratio steps is again larger than found for final spin and radiated energy in Ref. [7], but this procedure still yields sufficient evidence for the existence and shape of a linear spin-difference term and some preference for including both second-order terms, though the data is too noisy to constrain their η-dependent shape very well. For example, there is an apparent sign switch in the linear term at mass ratio $q = 4$ ($\eta = 0.16$), which is most likely due to a combination of the 2D fit being relatively weakly constrained in this region and non-negligible errors in some of the unequal-spin data points, which however cannot easily be discarded as outliers.

The overall fits in η are reasonably robust against such problems, and in the next step we will use not this step-by-step analysis, but a more robust fit of the full 3D ansatz to the full data set, to judge the overall significance of spin-difference terms. A full model selection of $A_i(\eta)$ is clearly not feasible at this point without a more detailed understanding of the point-by-point data quality. Hence, we make very simple choices for the $A_i(\eta)$ with just one power of η each:

$$A_1(\eta) = d_{10}\eta^3\sqrt{1-4\eta} \tag{4.48a}$$

$$A_2(\eta) = d_{20}\eta^3 \tag{4.48b}$$

$$A_3(\eta) = d_{30}\eta^3\sqrt{1-4\eta}\,, \tag{4.48c}$$

and investigate how much improvement this can yield over the 2D fit.

We now use the full data set except for the 1D subspaces (307 data points, including 265 NR simulations) to fit the full 3D ansatz from (4.46), with the equal-spin and spin-difference contributions from Eqs. 4.43 and 4.47+4.48, respectively. The sets of coefficients a_i, b_i and f_{i2} are already fixed from the 1D fits and consistency constraints (see Tables 4.12, 4.13 and Equation (4.45)), leaving between 11 and 14 free coefficients in this final 3D stage. When including all three spin-difference terms, the full ansatz (with the constraints from (4.45) for the f_{i2} still to be applied) is:

$$\begin{aligned} L'_{\text{peak}}\left(\eta,\widehat{S},\Delta\chi\right) &= a_5\eta^5 + a_4\eta^4 + a_3\eta^3 + a_2\eta^2 + a_1\eta + a_0 \\ &+ \frac{0.107b_2\widehat{S}^2\left(f_{22}\eta^2+f_{21}\eta+f_{20}\right) + 0.465b_1\widehat{S}\left(f_{12}\eta^2+f_{11}\eta+f_{10}\right) + \widehat{S}^4\left(f_{42}\eta^2+f_{41}\eta+f_{40}\right) + \widehat{S}^3\left(f_{32}\eta^2+f_{31}\eta+f_{30}\right)}{-0.328b_4\widehat{S}\left(f_{62}\eta^2+f_{61}\eta+f_{60}\right) + \widehat{S}^2\left(f_{72}\eta^2+f_{70}\right) + 1.0} \\ &+ d_{20}\,\eta^3\left(\chi_1-\chi_2\right)^2 + d_{10}\sqrt{1-4\eta}\,\eta^3\left(\chi_1-\chi_2\right) + d_{30}\sqrt{1-4\eta}\,\eta^3\,\widehat{S}\left(\chi_1-\chi_2\right)\,. \end{aligned} \tag{4.49}$$

We consider residuals and information criteria, summarized in Table 4.14, to check which spin-difference terms are actually supported by the data. These rankings depend on the specific choice of $A_i(\eta)$, but with the current parameter-space coverage and understanding of NR data quality, the main goal is to find general evidence for spin-difference effects and a general idea of their shape, not to exactly characterize them. With the choices made in (4.48), we find a 14-coefficient fit with linear+quadratic+mixture corrections

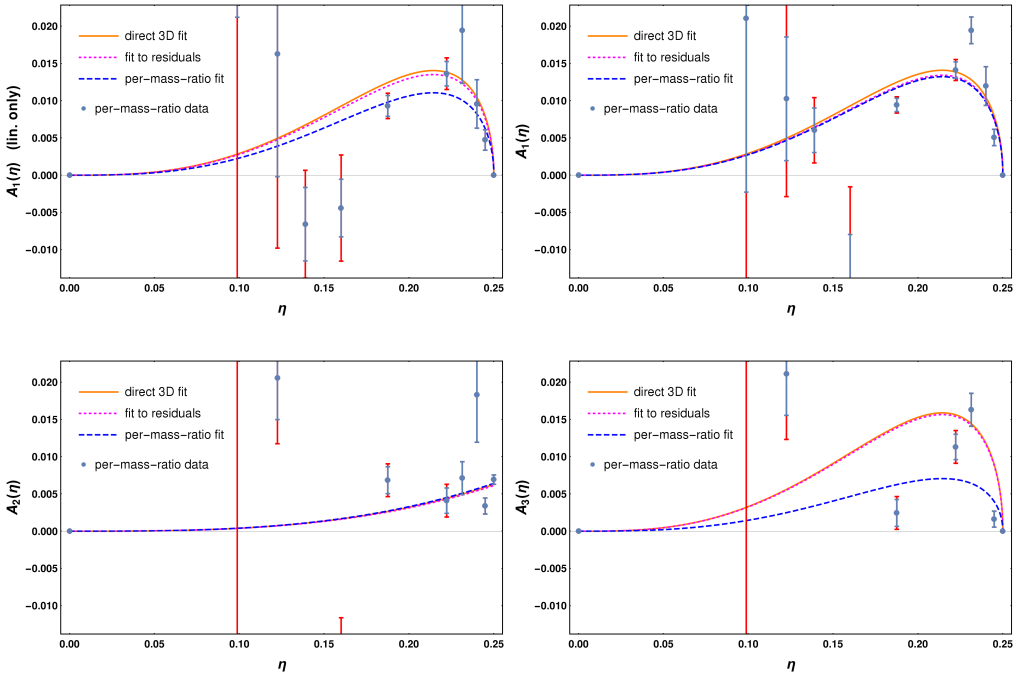

FIGURE 4.32: Spin-difference behavior of the scaled NR luminosities $L'_{\rm peak}$ after subtraction of the 2D $\left(\eta, \widehat{S}\right)$ fit over mass ratio η, showing the results of fits as in Figure 4.31 at η steps corresponding to $q = \{1, 1.33, 1.5, 1.75, 2, 3, 4, 5, 6, 8\}$ and three estimates for the ansatz functions $A_i(\eta)$ from (4.48): (i) unequal-spin part of the final 3D fit from (4.49) ("direct 3D fit"), (ii) fit of the unequal-spin terms from (4.48) ("fit to residuals") to the residuals of the 2D fit from (4.43) over all mass ratios, (iii) fits of (4.48) to the per-mass-ratio results. Top-left panel: linear term A_1 only. The remaining panels are for the combined linear+quadratic+mixture fit, in clock-wise order: linear term A_1, quadratic term A_2 and mixture term A_3. $A_1(\eta)$ from the combined ansatz is very similar to the linear-only fit, demonstrating its robustness. Error bars for the per-mass-ratio points include components from the fit uncertainty at that ratio (blue) and the average data weight of the contributing NR cases (red). At the lowest η, some points lie outside the plot range, but are so uncertain that they do not contribute significantly to the total fit. The direct-3D and residuals-only results are consistent, while the per-mass-ratio analysis only matches them qualitatively, which is however sufficient since it was only used to investigate the possible shapes of $A_i(\eta)$.

that has well-constrained coefficients (see Table 4.15), is evidently preferred in terms of AICc and BIC, and reduces overall residuals by about 20% in RMSE. Different choices for the powers of η in (4.48) yield compatible results, while polynomials in η with several free coefficients tend to produce under-constrained fits.

4.3.7 Fit assessment

In this section, we assess in some detail the properties and statistical quality of the new three-dimensional peak luminosity fit, with the actual non-rescaled luminosity (in geometric units of $G = c = M = 1$) obtained as $\eta^2\, L_0\, L'_{\rm peak}\left(\eta, \widehat{S}, \Delta\chi\right)$.

	$N_{\rm data}$	$N_{\rm coeff}$	RMSE	AICc	BIC
1D η	84	6	2.81×10^{-3}	-817.1	-801.2
1D $\hat{S}$	32	3	2.42×10^{-3}	-285.8	-280.8
2D ($\chi_1 = \chi_2$)	92	11	5.65×10^{-3}	-751.7	-724.8
2D all	307	11	1.67×10^{-2}	-1914.2	-1870.4
3D lin	307	12	1.51×10^{-2}	-2008.0	-1960.6
3D lin+quad	307	13	1.39×10^{-2}	-2134.2	-2083.3
3D lin+mix	307	13	1.41×10^{-2}	-2082.6	-2031.7
3D lin+quad+mix	307	14	1.36×10^{-2}	-2157.8	-2103.3

TABLE 4.14: Summary statistics for the various steps of the hierarchical fit. Note that it is not meaningful to compare AICc and BIC between datasets of different sizes. There is preference for the 3D fit including all three linear+mixture+quadratic terms, although many different choices of the $A_i(\eta)$ ansatz functions yield similar results with just $\pm$ a few percent in RMSE and $\pm$ a few in AICc/BIC, so that the shape of these terms is not yet strongly constrained.

	Estimate	Standard error	Relative error [%]
d_{10}	3.79	0.28	7.5
d_{20}	0.402	0.044	10.9
d_{30}	4.27	0.84	19.7
f_{10}	1.628	0.012	0.7
f_{11}	-3.63	0.23	6.3
f_{20}	31.7	1.3	4.2
f_{21}	-274	29	10.4
f_{30}	-0.235	0.011	4.7
f_{31}	6.96	0.44	6.3
f_{40}	0.211	0.022	10.6
f_{41}	1.53	0.45	29.6
f_{60}	3.090	0.044	1.4
f_{61}	-16.7	1.7	10.0
f_{70}	0.836	0.023	2.8

TABLE 4.15: Fit coefficients for the final 3D fit stage, cf. (4.49).

We compare with our previous fit [188] used for LIGO parameter estimation during O1 [3, 13, 24, 45, 186], which used a much smaller calibration set of 89 `BAM` and SXS simulations, only modes up to $\ell_{\rm max} = 4$ and no extreme-mass-ratio constraints; and with the recent Healy&Lousto fit [92] based on 107 RIT simulations, using modes up to $\ell_{\rm max} = 6$. We attempt to present a fair comparison by analyzing NR and perturbative large-mass-ratio results separately, and also consider the improvement from refitting the unmodified ansätze of Refs. [92, 188] to the present NR data set.

4.3.8 Residuals and information criteria

In Figure 4.30 we show the distribution of residuals for the 3D fit in $L'_{\rm peak}$ projected to the $\left(\eta, \widehat{S}\right)$ parameter space. The strongest visible outliers in this scaling are at low η

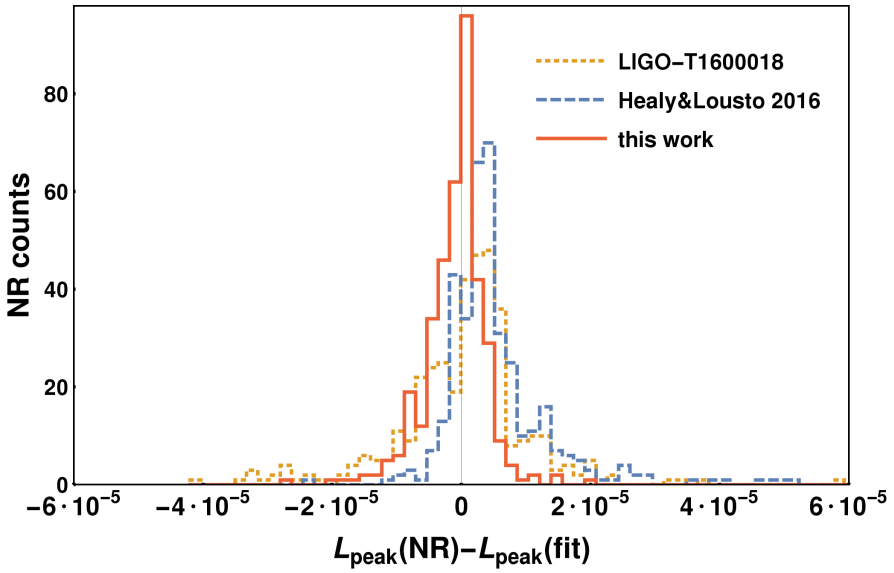

FIGURE 4.33: Fit residuals of the final 3D peak luminosity fit compared with the previous fits of LIGO-T160018 [188] and Healy&Lousto2016 [92], evaluated over the set of 427 NR simulations shown in Figure 4.26. 6 outliers for Healy&Lousto with $|\mathrm{NR} - \mathrm{fit}| > 0.00006$ are outside of the plot range.

	N_{coef}	mean	stdev	AICc	BIC
T1600018	11	3.0×10^{-7}	1.0×10^{-5}	−7732.1	−7685.6
(refit)	11	-1.8×10^{-6}	4.0×10^{-5}	−6706.0	−6659.5
HL2016	19	6.9×10^{-6}	1.5×10^{-5}	−7225.5	−7148.9
(refit)	19	-4.9×10^{-7}	1.0×10^{-5}	−7708.3	−7631.7
this work	23	-9.8×10^{-7}	4.8×10^{-6}	−8298.1	−8206.7
(refit)	23	-5.5×10^{-7}	4.8×10^{-6}	−8323.6	−8232.3

TABLE 4.16: Summary statistics for the final 3D peak luminosity fit compared with previous fits with the previous fits of LIGO-T160018 [188] and Healy&Lousto2016 [92], evaluated over the 427 NR simulations shown in Figure 4.26. The new fit has a total of 23 free coefficients, corresponding to Tables 4.12, 4.13 and 4.15. We also show results for re-fitting the three ansätze to the full NR + large-mass-ratio data set, again evaluating the statistics over NR only.

and correspond to mild actual deviations; of at most a 7% relative error at $q = 18$, with 417 of the 423 data points below 3% relative error.

For a comparison with the two previous fits, we first concentrate on the 378 NR simulations only and revisit large mass ratios in subsection 4.3.9. In Figure 4.33 we show histograms of the residuals in L_{peak} for the three fits over this data set, demonstrating that the new fit achieves a narrower distribution. As listed in Table 4.16, the standard deviation of residuals is only half of that for our previous fit and three times lower than for the RIT fit. With a mean offset by only a ninth of a standard deviation, there is no evidence for bias, though that notion is notoriously ambiguous for a data set that samples the parameter space non-uniformly.

The same table contains AICc and BIC values evaluated over the same NR-only data

set, which both find a very significant preference for the new fit. Note that, being computed over a different data selection and for $L_{\rm peak}$ instead of $L'_{\rm peak}$, these values are not directly comparable with the previous Table 4.14. Since we have removed 41 cases from the full available data set (see Sec. 4.3.10.4), it is advisable to check that the statistical preference still holds when including these in the evaluation set. Indeed, the reduction in standard deviations of residuals is then less against the T1600018 and RIT fits, but still roughly 20% and 30%, and there is still a preference of several hundreds in both information criteria.

We also show results for re-fitting the T1600018 and RIT ansätze to the present NR + perturbative data set, with the statistics then again evaluated over NR data only. Our old ansatz with only 11 coefficients is not well suited to matching the large-mass-ratio region and the large unequal-spin population in the NR data set, and the refitted version of this 11 coefficient ansatz performs worse than the original. On the other hand, the RIT ansatz with 19 coefficients was only weakly constrained in the original version [92] fitted to 107 simulations, with large errors on several fit coefficients, but improves now significantly through the refit. Yet, it does not achieve the same level of accuracy as the new ansatz and fit developed in this paper.

As a test of robustness, we also perform a refit of our final hierarchically-obtained ansatz directly using the full data set, instead of using the constraints from the 1D subsets. This produces somewhat better summary statistics, but it also allows uncertainties from less well-controlled unequal-spin data to influence the non-spinning part of the fit. The more conservative approach is to calibrate the non-spinning part of the fit only to the corresponding data subset. Hence we recommend the stepwise fit, with coefficients as reported in Tables 4.12, 4.13 and 4.15, for further applications.

4.3.9 Large-mass-ratio and extremal-spin limits

In Figure 4.34, we compare our full 3D fit with the perturbative large-mass-ratio data and find that it correctly reproduces the behavior it is meant to be constrained to. The T1600018 fit did not predict the steep rise for positive spins, and while at negative spins it matches the shape roughly, it is still off by about 10% in that region. The RIT fit disagrees with the perturbative data at high spin magnitudes, either negative or positive, and does not reproduce the increasing steepness for even higher mass ratios.

The clearest difference between this fit and the previous ones in the NR-dominated region is for high aligned spins, which is shown in Figure 4.35 for the extremal spin limit, $\chi_1 = \chi_2 = \widehat{S} = 1$. The RIT fit estimates a lower luminosity at equal masses, but higher values at $\eta < 0.16$ before approaching the $\eta \to 0$ limit rather flatly, as discussed

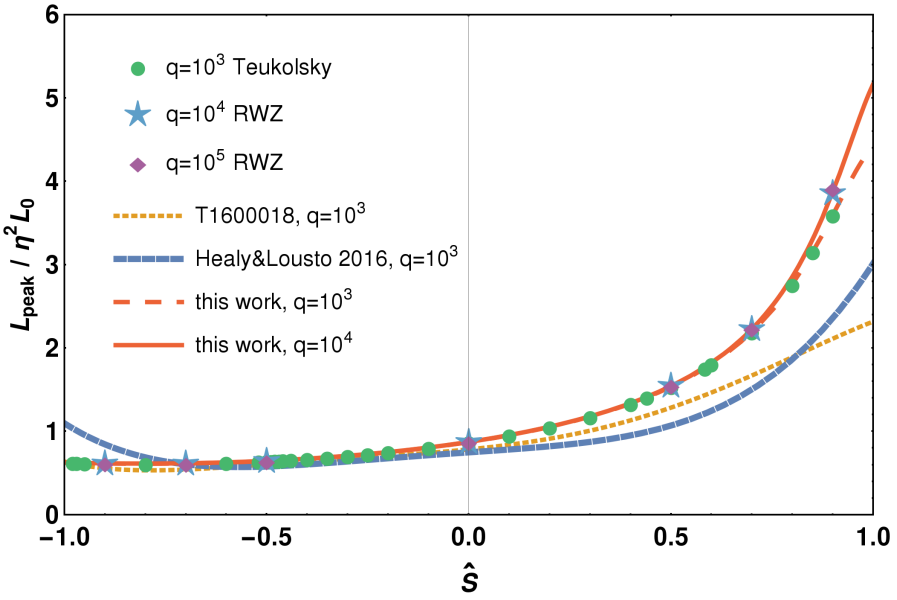

FIGURE 4.34: Full NR-calibrated fits from this work and from Refs. [92, 188] evaluated at large mass ratios, compared with the same perturbative data (circles, stars and diamonds for mass ratios $q = \{10^3, 10^4, 10^5\}$). The T160018 and RIT fits are essentially converged at $q = 10^3$ (e.g. 0.4% change at $S = 1.0$ for the RIT fit going to $q = 10^4$), and the visually identical lines for higher q are not shown; our new fit still matches the data at higher q.

before. Our older fit and the new one roughly agree at similar masses, but in the lower panel with the rescaled $L'_{\rm peak}$ it is obvious that the previous fit did not anticipate the steep $\eta \to 0$ limit that we are now implementing through fitting the perturbative data.

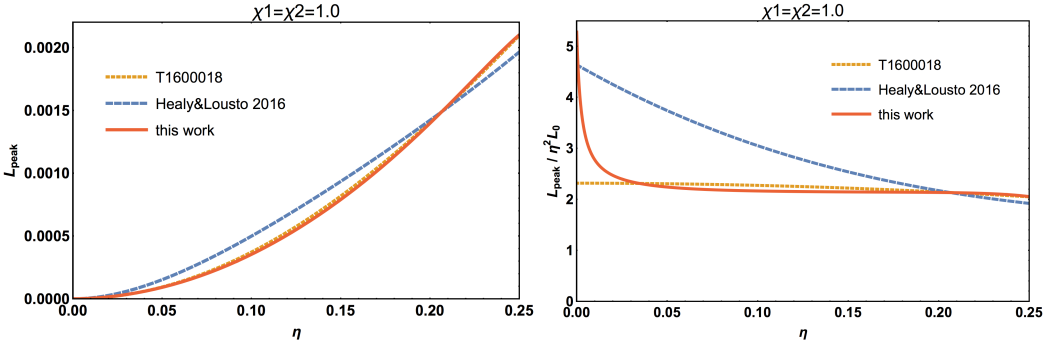

FIGURE 4.35: Behavior of the full 3D fit (4.46) in the extremal-spin limit, $\chi_1 = \chi_2 = \widehat{S} = 1$, where there is no data available. Both panels give functions of mass ratio η, and we again compare with the fits from Refs. [92, 188]. Left panel: in terms of physical peak luminosity $L_{\rm peak}$, right panel: in terms of rescaled $L'_{\rm peak} = L_{\rm peak}/\eta^2 L_0$.

4.3.10 NR data investigations

As a first estimate of the *overall* accuracy of the peak luminosity data set, we study the differences between results from different codes for equal initial parameters. We

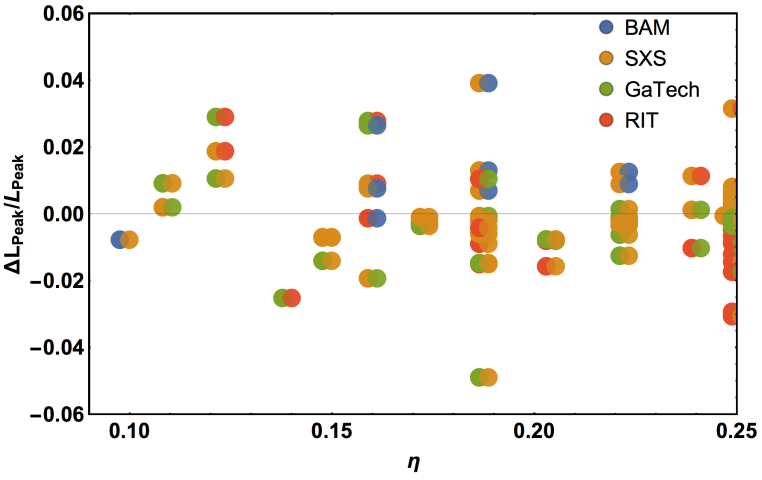

FIGURE 4.36: Relative differences in the peak luminosity for equal-parameter configurations from different NR codes, shown against symmetric mass ratio η. Pairs of simulations are shown with a small horizontal offset for ease of visual identification.

then give additional details on the possible error sources listed in Sec. 4.3.2 and on the properties of higher modes, and discuss the 41 cases not used in the calibration set.

4.3.10.1 Comparison between different codes

To analyze typical deviations between results from different NR codes, we identify simulations with initial BH parameters equal to within numerical accuracy, with a tolerance criterion

$$|\lambda_i - \lambda_j| \leq \epsilon = 0.0002 \text{ for } \lambda_i = \{\eta_i,\, \chi_{1i},\, \chi_{2i}\}\ , \tag{4.50}$$

as we do in Sec. 4.2.10. In Figure 4.36 we show the relative difference in $L_{\rm peak}$ between such matching cases, including the non-spinning $q = 4$ case where we have results from all four codes and a few triple coincidences. The set of these tuples is too sparse for clear conclusions on the parameter-space dependence of discrepancies between codes, though there might be some indication of increasing differences at large positive spins, which are particularly challenging to simulate due to increased resolution requirements for capturing the larger metric gradients in the near-horizon zone. We find many pairs with differences below 1%, but also several up to a few % even at not particularly challenging configurations.

This study gives a useful overall estimate of the possible error magnitude on the NR data set: while certainly many simulations are accurate to more than the few-% level, in general for any given simulation that does not have a paired case from another code, or at least nearby neighbors in parameter space, we cannot confidently assume that the errors will be low. This affects in particular the unequal-spin cases, where due to

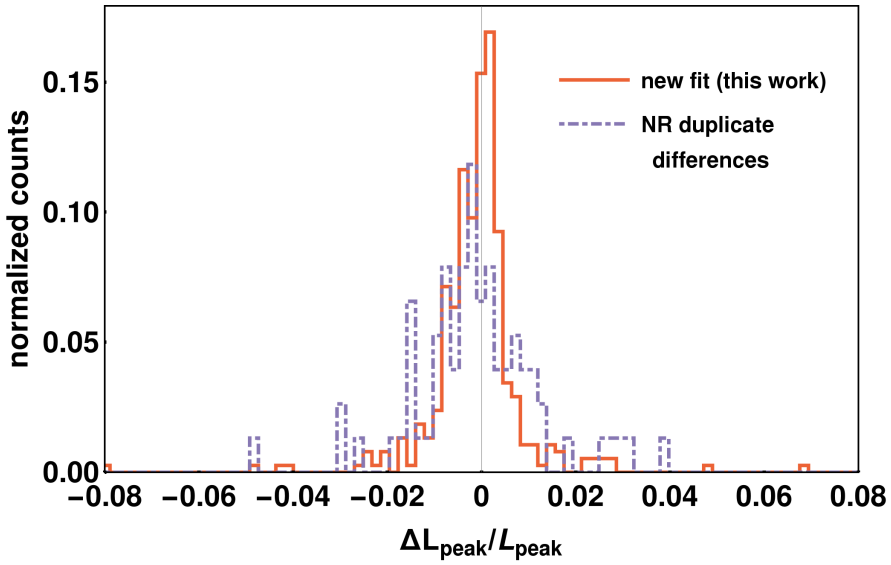

FIGURE 4.37: Comparison of the distribution of relative fit errors (NR only, same set as in Figure 4.33) and of differences between NR codes for equivalent parameters.

the much larger 3D parameter space very few duplicates exist. On the other hand, for equal spins – and particularly for the densely covered non-spinning or equal-mass subsets – we can use the duplicates analysis to make a very strict selection of calibration points, allowing the sub-percent calibration demonstrated in Secs. 4.3.4.1 and 4.3.4.2. The specific decisions are detailed below in Sec. 4.3.10.4.

As shown in the histograms of Figure 4.37, the overall distribution of (relative) differences between equivalent configurations is of a similar width than that of the fit residuals. This demonstrates that we are indeed not overfitting the data, but also that one would need to characterize the accuracy of all NR cases to a significantly lower level to extract more information on subdominant effects.

4.3.10.2 Extrapolation

The NR waveforms used in this paper are extracted at finite radii, which implies ambiguities, in particular due to gauge effects. We therefore extrapolate all waveforms to null infinity, where unambiguous waveforms can be defined. This allows us to assemble a consistent set of peak luminosity values for different codes, and to estimate the errors due to finite radius effects.

However, the extraction properties of the codes are not equal, and thus we have extrapolated the available waveforms following the following prescriptions:

- `BAM`: We have calculated $L_{\rm peak}$ at each finite radius and then performed a linear-in-$1/R$ extrapolation using only the well-resolved extraction radii. The maximum

used for any case is $R \leq 180M$, but for some cases significantly fewer radii can be used for a robust extrapolation, depending on simulation grid resolutions.

- GaTech: $L_{\rm peak}$ is again calculated at finite radii and then extrapolated with a fit quadratic in $1/R$, only using up to $R \leq 100M$ because the slope generally changes for higher radii; this choice of extrapolation order and radius cut yields the most consistent results with other codes in the analysis of equivalent configurations.

- SXS: These waveforms are already provided at 2nd, 3rd and 4th order polynomial extrapolation, and we compute $L_{\rm peak}$ from these data products, after a correction [209–211] for center-of-mass drift, using the 2nd order extrapolation as the preferred value following Refs. [60, 119]. We use waveforms based on the Weyl scalar ψ_4, but also compare with waveforms based on a computation of the strain. The SXS ψ_4 data use a definition of null-tetrad which is different from their Regge-Wheeler-Zerilli strain data [134, 212–214], and from the definition used in other codes. For the luminosity this difference corresponds to an overall scaling factor of the lapse function to the fourth power as a consequence of the difference between Eqs. (30-33) in Ref. [72] and Eqs. (11-12) in Ref. [60]. A rough correction for the different tetrad scaling used to compute the Weyl scalar ψ_4 is to multiply it by α^4 with $\alpha = 1 - 2M_{\rm f}/R$, where $M_{\rm f}$ is the final mass and R is an approximation to the luminosity distance using the standard relation with the isotropic radial coordinate for the Schwarzschild spacetime. (Compare also with the analysis in Ref. [120].) Comparisons of SXS luminosities computed from ψ_4, strain, and heuristically rescaled ψ_4 with data from other codes are included in Figs. 4.38 and 4.39.

- RIT: The luminosity data provided in Ref. [92] uses the extrapolation method of Ref. [120].

In Figure 4.38 we show the only configuration, the non-spinning $q = 4$ case, for which we have data from all four codes. This includes peak luminosities computed from the finite-radius strain data available as additional data products from SXS to cross-check the pre-extrapolated value. We see that extrapolation for $R \to \infty$ reduces discrepancies in $L_{\rm peak}$ between the different codes, but cannot completely alleviate it in this case. Another similar example is shown in Figure 4.39 for a $q = 2.5$ non-spinning configuration where we have three simulations from SXS, GaTech and RIT, with the GaTech and RIT values more consistent with each other than with SXS in this case.

The uncertainties of extrapolation fis for `BAM`, SXS and GaTech can be estimated by the standard deviation on the intersection parameter (equivalent to the confidence interval on the extrapolation to $1/R = 0$). For the plotted non-spinning $q = 4$ case, these are

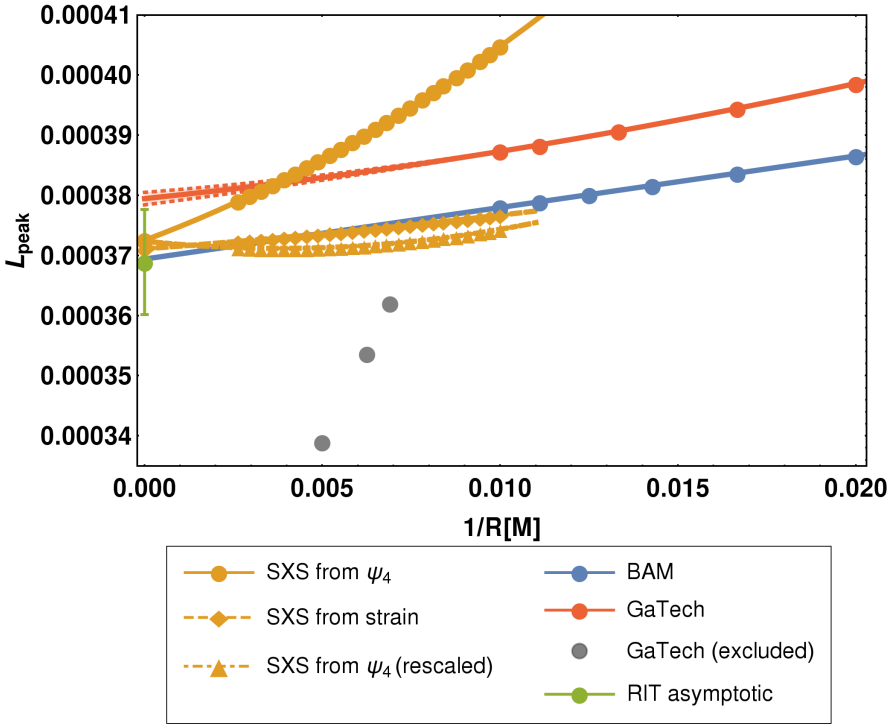

FIGURE 4.38: $q = 4$ non-spinning example of extrapolation from finite radii for BAM, SXS and GaTech, with second-order fits for SXS and GaTech and linear for BAM; as well as the RIT value extrapolated with the method of Ref. [120] and its error bar also containing a finite-resolution estimate. In this case we find consistent values from BAM, SXS and RIT, with the GaTech case an outlier. The $R > 100$M GaTech data would make the trend more inconsistent, and are excluded from extrapolation. SXS luminosities computed from strain, or from ψ_4 but with the α^4 rescaling discussed in the text, show a flatter finite-R behavior more similar to the other codes, and extrapolated values consistent with the luminosity from ψ_4.

smaller than the remaining largest difference between the results from GaTech and other codes, while for the $q = 2.5$ the uncertainties are almost wide enough to make the results marginally consistent. For some other cases, these uncertainties can reach up to a few %, especially when we want to be conservative and take the maximum of (i) the statistical uncertainty for the standard extrapolation-order choice and (ii) the difference between this and the closest alternative order. In general, such an uncertainty estimate cannot provide information about any systematics present in the data from different codes, and indeed for example we find that for BAM the purely statistical extrapolation uncertainties are much smaller in some high-q cases than for low-q cases which are generally considered more reliable.

Hence, a study of the extrapolation uncertainties over the whole parameter space is useful in gaining an understanding of the properties of the different codes, but cannot directly be used as a measure of total NR uncertainties.

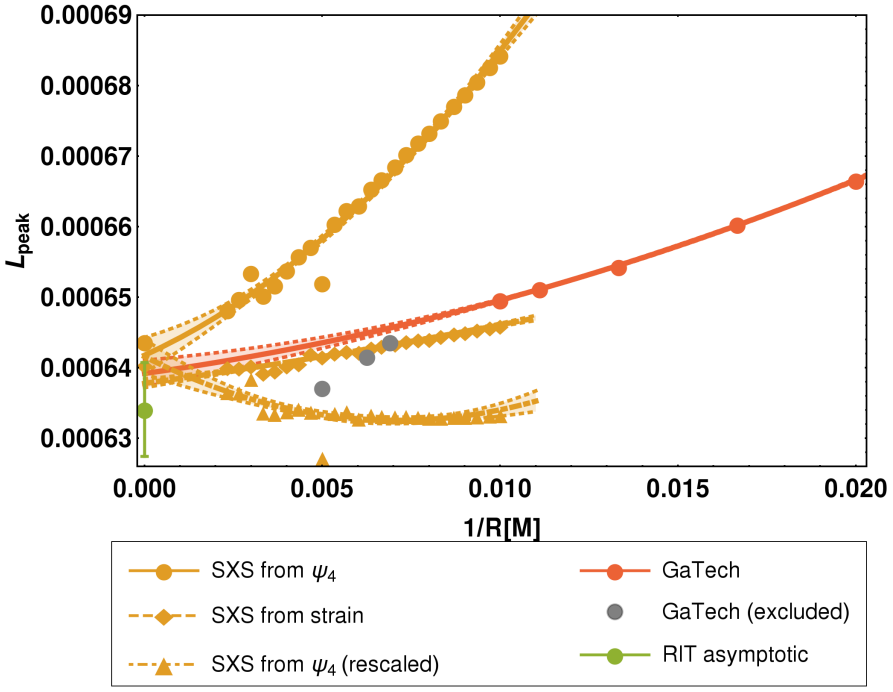

FIGURE 4.39: $q = 2.5$ non-spinning example of extrapolation behavior for SXS and GaTech, compared with the extrapolated RIT value. In this case we find consistent GaTech and RIT values, with the asymptotic SXS computed from ψ_4 a marginal outlier. Extrapolating the finite-radius peak luminosities computed from ψ_4 with rescaling, or from strain, seems to improve consistency in this example, which however needs further study before applying it to the whole data set.

4.3.10.3 Mode selection

As introduced in (3.20), we compute NR peak luminosities for `BAM`, SXS and GaTech waveforms as sums over all modes up to $\ell_{\rm max} = 6$. The RIT luminosities from Refs. [91, 92] use the same cut-off. For the perturbative data from Refs. [93, 95, 158] at large mass ratios, we use $\ell_{\rm max} = 8$. These choices are based on studying the individual contribution of each mode to the total luminosity, finding that $\ell > 6$ contributions are sufficiently small to be discarded for the NR data in comparison with other sources of uncertainty.

As an illustrative example, we show in the top panel of Figure 4.40 the cumulative peak luminosity when adding modes ℓ by ℓ (including all $|m| \leq \ell$ at each step) for the $q = 10$ non-spinning SXS waveform, and the per-ℓ contributions in the lower panel. The fall-off of the higher-ℓ contributions to the global peak is expected to be exponential, which is indeed found in this case.

To quantify and extrapolate the loss generally expected for non-spinning configurations, we have estimated the relative loss in $L_{\rm peak}$ from not including the $\ell = 7, 8$ modes for non-spinning SXS waveforms up to mass-ratio $q = 10$ (maximum loss of 0.6%) and the

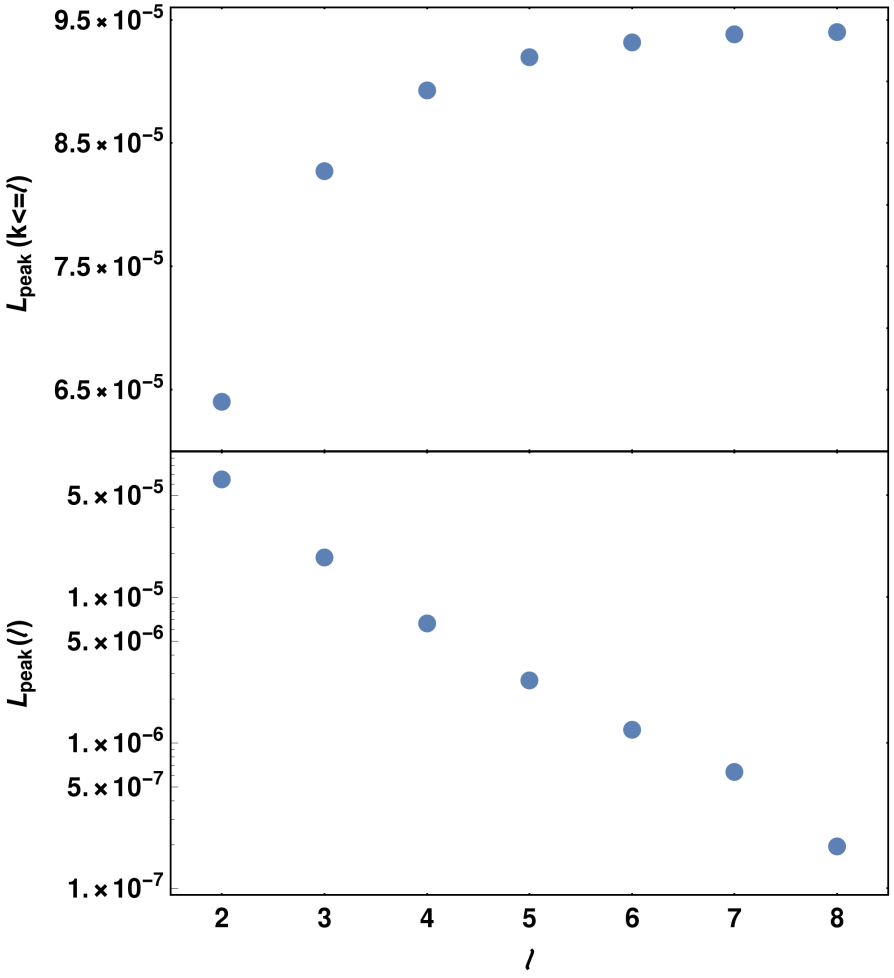

FIGURE 4.40: Per-mode contributions to the total peak luminosity for the same SXS case. Top panel: cumulative sum up to ℓ. Lower panel: Natural logarithm of the luminosity contribution per ℓ. Each point contains all m for the given ℓ. Similar behavior for large mass ratios was found in Ref. [215].

non-spinning `BAM` simulation at $q = 18$ (loss of 1%), and fit a quadratic function in η:

$$\frac{\Delta L_{\rm peak}}{L_{\rm peak}} = 0.017611 - 0.153760\eta + 0.334803\eta^2 \,. \tag{4.51}$$

This result is illustrated in Figure 4.41, together with a marginally consistent fit when including the $q = 10^3$ Teukolsky result (loss of 2%). The $\ell > 6$ contributions are smaller for negative spins and larger for positive spins, as illustrated in the same figure with $\chi_1 = \pm 0.8$ results at $q = 10^3$ and from `BAM` at $q = 18$. The largest loss for any NR case investigated is $\lesssim 2\%$ for the $q = 18$, $\chi_1 = +0.8$ `BAM` case, which is a significant contribution to the overall error budget but still on the level of other error sources. For the perturbative large-mass-ratio results, with a worst-case $\ell > 6$ of $\approx 5\%$, we use $\ell_{\rm max} = 8$ instead, so that the loss from $\ell > 8$ is limited to $< 1\%$.

Another useful investigation is to consider the η dependence, and especially the $\eta \to 0$ behavior, for individual modes.

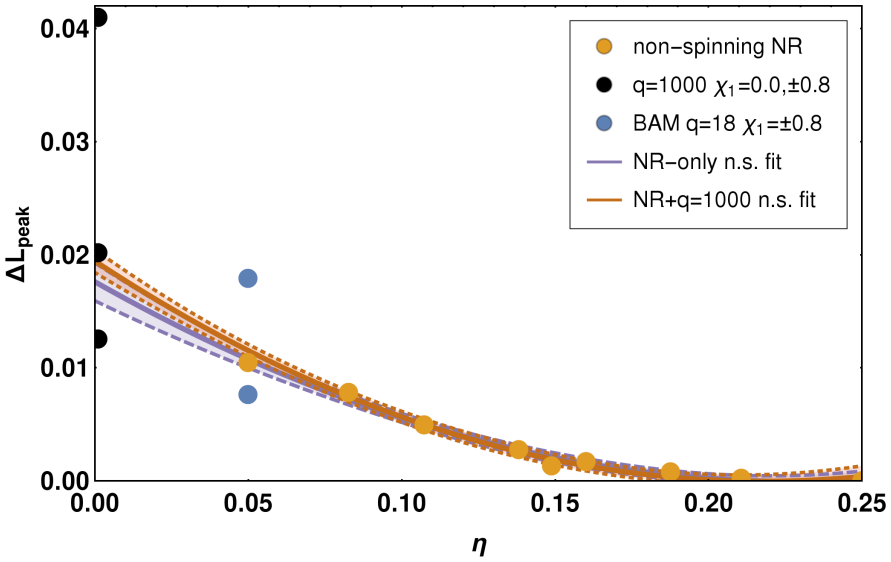

FIGURE 4.41: Relative loss in the peak luminosity including modes up to $\ell_{\rm max} = 6$ against $\ell_{\rm max} = 8$, for non-spinning SXS cases up to $q = 10$, a non-spinning `BAM` case with $q = 18$ and the $q = 10^3$ Teukolsky result. Also shown are $q = 18$ and $q = 10^3$ results for $\chi_1 = +0.8$ (above the non-spinning line) and for $\chi_1 = -0.8$ (below), as well as the quadratic non-spinning fit from (4.51) to NR data points only and a fit of the same order including the $q = 10^3$ point, with 90% confidence intervals for both fits.

Fitting $L'_{\rm peak}\left(\eta, \widehat{S} = 0\right)$ in Sec. 4.3.4.1 we found, as illustrated in Figure 4.28, that the peak luminosity of all modes summed up to $\ell_{\rm max} = 6$, after scaling out the dominant η^2 dependence, is not a monotonic function towards low η. The increasing relative amplitudes of higher-order modes at low η have been studied with NR results previously [128, 205–208], but with our large peak luminosity data set we can now investigate the slope more closely.

Repeating the same comparison as in Figure 4.28 of rescaled non-spinning peak luminosities between NR (SXS+`BAM` non-spinning) and perturbative large-mass-ratio data, but for individual modes, we find – as shown in Figure 4.42 for a subset of modes – that these are all monotonic as $\eta \to 0$; however, the slopes are very different, with the dominant 22 mode falling off faster than η^2 and the subdominant and higher modes falling off much slower, consistent with the general expectation of stronger contributions at low η. This finding of monotonicity in each mode increases our trust in the combination of NR and perturbative results, and the non-monotonicity of the rescaled peak luminosities after summing the modes can thus be explained as a superposition of these counteracting trends in the individual modes.

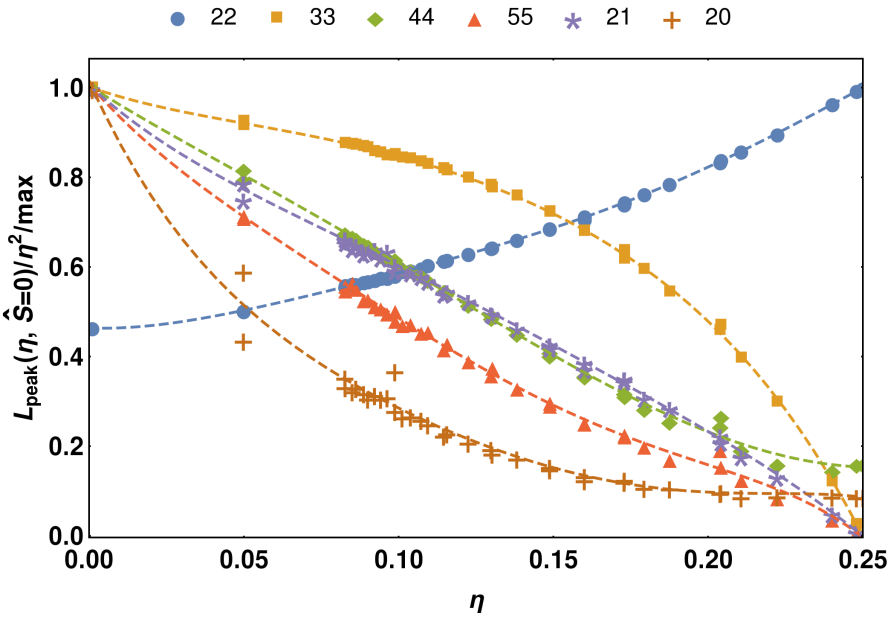

FIGURE 4.42: Comparison of rescaled peak luminosities for non-spinning SXS and BAM and perturbative large-mass-ratio data, for a small selection of modes. The points for each mode have been scaled by the maximum for that mode, which is at $\eta = 0.25$ for the 22 mode and at $\eta \to 0$ for the other modes. The connecting lines are fifth-order polynomial fits, which were not statistically optimized and just added to guide the reader's eye. This can be compared with the sum over modes in Figure 4.28. As a guide to the overall strength of the individual modes, we list the non-rescaled maxima $\max_\eta L^{\ell m}_{\rm peak}(\widehat{S} = 0)$ of each of the displayed modes $(\ell m) = \{22, 33, 44, 55, 21, 20\}$: $\{1.0 \times 10^{-3}, 5.9 \times 10^{-5}, 1.5 \times 10^{-5}, 5.3 \times 10^{-6}, 9.8 \times 10^{-6}, 6.3 \times 10^{-7}\}$.

4.3.10.4 Outliers

Of the full catalog of 419 NR simulations from four codes, we have only used 378 to calibrate our new fit. 22 of the 41 removed cases are non-spinning or equal-spin configurations. Of these, 17 belong to one of the pairs or groups of equivalent initial parameters identified in Sec. 4.3.10.1, with differences between the paired results inconsistent at a level higher than the fit residuals we can otherwise achieve in the corresponding subspace fit; or are individual points inconsistent with an otherwise consistent set of direct neighbors. In these cases we removed from each tuple the case most discrepant with the others and with the global trend. This includes for example the GaTech $q = 4$ and SXS $q = 2.5$ non-spinning cases shown in the extrapolation comparisons of Figs. 4.38 and 4.39, or the SXS $\left(q = 1, \widehat{S} = 0.97\right)$ point whose luminosity seems inconsistent with other $q = 1$, high-spin SXS results.

We emphasize that in the one-dimensional fits for non-spinning and equal-mass-equal-spin BBHs we calibrate the fits to sub-percent accuracies, so that this is a very strict criterion for removing cases, which mainly serves to guarantee a very clean calibration of the well-covered subspaces and dominant effects so that in the later steps we have

a better chance of isolating and extracting subdominant effects from the general, more noisy data set. In terms of total absolute or relative errors compared with the whole NR data set, several of these cases are not overly inaccurate, and we do not imply that necessarily there are data quality issues with the waveforms from which the luminosities are calculated.

	q	χ_1	χ_2	$L_{\rm peak}$	$\Delta L_{\rm peak}$	$\Delta L_{\rm peak}/L_{\rm peak}$	tag	code
1	1.00	0.20	0.80	0.00133540	−0.00001456	−0.011	Q1.00_0.20_0.80	RIT
2	1.00	0.25	0.25	0.00114910	−0.00001078	−0.009	Q1.0000_0.2500_0.2500	RIT
3	1.00	0.40	0.80	0.00143030	−0.00001617	−0.011	Q1.00_0.40_0.80	RIT
4	1.00	0.50	0.50	0.00132610	−0.00002155	−0.016	Q1.0000_0.5000_0.5000	RIT
5	1.00	0.80	0.80	0.00165190	−0.00005163	−0.031	Q1.0000_0.8000_0.8000	RIT
6	1.00	0.97	0.97	0.00185963	−0.00017055	−0.092	d15_q1_sA_0_0_0.97_sB_0_0_0.97_ecc6e-4	SXS
7	1.00	−0.80	−0.80	0.00075683	−0.00000522	−0.007	d15_q1_sA_0_0_-0.8_sB_0_0_-0.8	SXS
8	1.00	−0.95	−0.95	0.00071785	−0.00001083	−0.015	d15_q1_sA_0_0_-0.95_sB_0_0_-0.95	SXS
9	1.10	0.00	0.00	0.00102562	0.00000646	0.006	D9_q1.1_a0.0_m160	GaT
10	1.33	0.50	0.50	0.00127610	−0.00001496	−0.012	Q0.7500_0.5000_0.5000	RIT
11	1.33	0.80	−0.80	0.00113510	0.00001336	0.012	Q0.7500_-0.8000_0.8000	RIT
12	1.33	0.60	0.80	0.00144390	−0.00002266	−0.016	Q1.33_0.80_0.60	RIT
13	1.50	0.00	0.00	0.00092086	−0.00000929	−0.010	Q0.6667_0.0000_0.0000	RIT
14	1.67	0.00	0.00	0.00089059	0.00001118	0.013	Q0.6000_0.0000_0.0000	RIT
15	2.00	0.85	−0.85	0.00104805	−0.00005372	−0.051	q2_-85_85_0.2833_it2_T_96_468	BAM
16	2.00	0.60	0.60	0.00113005	−0.00001154	−0.010	D11_q2.00_a0.60_m200	GaT
17	2.00	0.85	0.00	0.00119969	−0.00004465	−0.037	q2_0_85_0.566667_T_80_360	BAM
18	2.00	0.80	0.80	0.00133220	−0.00004371	−0.033	Q2.00_0.80_0.80	RIT
19	2.00	0.60	0.50	0.00109870	−0.00002568	−0.023	Q0.5000_0.5000_0.6000	RIT
20	2.00	0.80	0.00	0.00115110	−0.00004828	−0.042	Q0.5000_0.0000_0.8000	RIT
21	2.50	0.00	0.00	0.00064369	0.00000637	0.010	BBH_CFMS_d16.9_q2.50_sA_0_0_0_sB_0_0_0	SXS
22	3.00	0.50	−0.50	0.00067168	−0.00002270	−0.034	q3_-50_50_0.25_T_80_400	BAM
23	3.00	0.00	0.00	0.00051866	−0.00000761	−0.015	D10_q3.00_a0.0_0.0_m240	GaT
24	3.00	0.40	0.00	0.00065030	−0.00001591	−0.024	D10_q3.00_a0.4_0.0_m240	GaT
25	3.00	0.50	0.80	0.00074376	−0.00001267	−0.017	Q0.3333_0.8000_0.5000	RIT
26	3.00	0.60	0.00	0.00074392	−0.00003003	−0.040	D10_q3.00_a0.6_0.0_m240	GaT
27	3.00	0.67	0.00	0.00078909	−0.00002904	−0.037	Q3.00_0.00_0.67	RIT
28	3.00	0.80	−0.80	0.00084159	−0.00002278	−0.027	Q3.00_-0.80_0.80	RIT
29	3.00	0.85	0.85	0.00107685	0.00003335	0.031	BBH_SKS_d13.9_q3_sA_0_0_0.850_sB_0_0_0.850	SXS
30	4.00	0.75	0.75	0.00069840	0.00001188	0.017	q4a075_T_112_448	BAM
31	4.00	0.75	0.00	0.00063280	−0.00002841	−0.045	Q4.00_0.00_0.75	RIT
32	4.00	0.00	0.00	0.00037948	0.00000782	0.021	D10_q4.00_a0.0_0.0_m240	GaT
33	4.30	0.00	0.00	0.00034217	0.00000421	0.012	D9_q4.3_a0.0_m160	GaT
34	4.50	0.00	0.00	0.00031462	−0.00000329	−0.010	D9_q4.5_a0.0_m160	GaT
35	5.00	0.80	0.00	0.00052483	−0.00000926	−0.018	Q5.00_0.00_0.80	RIT
36	5.00	0.00	0.00	0.00026999	−0.00000480	−0.018	D10_q5.00_a0.0_0.0_m240	GaT
37	5.00	0.40	0.00	0.00034792	−0.00001784	−0.051	D10_q5.00_a0.4_0.0_m240	GaT
38	6.00	0.00	0.00	0.00020707	−0.00000395	−0.019	Q0.1667_0.0000_0.0000	RIT
39	6.00	0.00	0.00	0.00021325	0.00000234	0.011	D10_q6.00_a0.00_0.00_m280	GaT
40	6.00	0.20	0.00	0.00023419	−0.00000829	−0.035	D10_q6.00_a0.20_0.00_m280	GaT
41	18.00	−0.80	0.00	0.00006179	0.00003868	0.626	q18a0aM08c025_96_fine	BAM

TABLE 4.17: NR cases from the source catalogs not included in the fit calibration, for reasons detailed below.

The remaining cases were identified as strong outliers outside of the main distribution in visual inspection of the two-dimensional equal-spin fit (4.3.5) and the per-mass-ratio analysis of residuals of unequal-spin cases against the 2D fit (4.3.6). For these simulations, there are no equivalent or nearby comparison cases, so that it cannot be said with certainty if they would still be outliers in a more densely covered future data set; and at the same time a small residual for any given point is no guarantee for its absolute accuracy when there are no equivalent comparison points. Hence, we have made much less strict exclusions in the sparsely covered unequal-spin range, which limits the accuracy to which we can extract the subdominant spin-difference effects (which are of a similar

scale as the remaining scatter in the data set), but also reduces the risk of overfitting to spurious trends in a more strongly-trimmed data set.

Chapter 5

A phenomenological frequency-domain model: PhenomD

In this thesis, the major part of the research has been orientated towards the calibration and upgrading of the phenomenological inspiral-merger-ringdown waveform models [38, 39, 53, 54, 69, 70, 148, 166, 167] by:

1. Setting up and running nonprecessing BBH NR simulations with a special emphasis in unequal-spin configurations.
2. Performing detailed NR data studies in order to calibrate the quality of the NR runs.
3. Developing an optimised fitting strategy to better match the extreme-mass-ratio limit and that facilitates the inclusion and calibration of subdominant terms as the unequal-spin effects.

The forthcoming LIGO and Virgo upgrades will make them more sensitive to the last orbits and merger-ringdown phases of BBH mergers. This will help to better constrain the physical parameters of future GW observations, which at the same time motivates the continuous improvement of our waveform models. In this work I have contributed to the development of the last phenomenological model PhenomD [38, 39, 70] and, based on the hierarchical data-driven studies, to its upgrade by treating in a similar way the unequal-spin terms and the extreme-mass-ratio limit than for the final state and peak luminosity models. Then, in this last chapter of the thesis I give a general overview of the so called PhenomD model [38, 39, 70], with a particular interest in the sections

that I contributed to, while adding some preliminary results based on the hierarchical data-driven fitting methodology that will result in a future upgraded version of the model.

5.1 Overview of the phenom-based models

In Chapter 2 I have briefly summarised the progress on the phenomenological waveform modelling since its first version PhenomA [68] to the most recent updated PhenomD model [38, 39, 70]. The evolution of the models has been sustained on the optimization of the analytic and pseudo-analytic models and the growth of the NR field. I here summarise some of the key points on the construction of the last phenomenological model.

5.1.1 Some notes on the PhenomD construction.

The goal is to formulate a model of the quadrupolar radiation in the frequency domain, which can be used for LIGO and Virgo data analysis pipelines, and covers the complete coalescence, from inspiral to merger-ringdown regimes. To do so, the frequency domain signal is split into its amplitude and phase, sectioned in three regimes morphologically different: *Region I*, capturing the inspiral and part of the merger, *Region IIa*, formed by an incomplete merger and finally *Region IIb* composed by the late merger and the ringdown, being the different sections fitted by different ansaetze. This morphology is illustrated in Figure 5.1, which shows the amplitude and phase evolution of a SXS $q = 1$, $\chi_1 = \chi_2 = -0.95$ case sectioned as it is shown in [39]. Both amplitude and phase are obviously defined by a different profile. Though they are split in a similar way, the frequency range of each section varies, with the intermediate region of the phase being broader than for the amplitude.

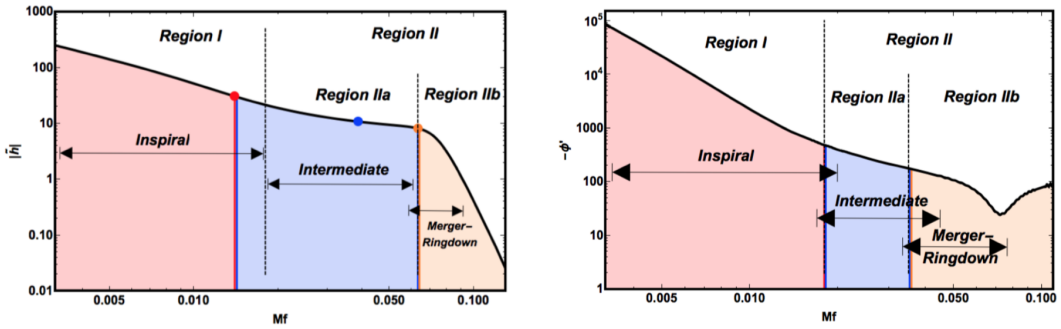

FIGURE 5.1: PhenomD amplitude and phase derivative as shown in [39] for a SXS case with $q = 1$, $\chi_1 = \chi_2 = -0.95$.

Phase

The phase of *Region I* is modelled considering the `TaylorF2` approximant where the late regimes (purple Figure 5.1) are calibrated through `SEOBv2`-NR hybrids (see Sec. 5.2) which correct the higher order secular deviations of the approximant.

Region I, *IIa* and *IIb* fit the phase derivative $\phi'(f)$ instead of the phase $\phi(f)$. This is done for two main reasons: to eliminate the propagation of any phase shift when going to the Fourier domain but mainly motivated by the properties of the dip observed in *Region IIb* of Figure 5.1. This region is particularly well fitted by a Lorentzian-based ansatz where the position of the minimum and the width are consistent (within numerical accuracy) with the values of the ringdown $f_{\rm RD}$ and damping $f_{\rm damp}$ frequencies. These are computed from ringdown fits [128] once the final mass and final spin are known and allow to reduce the number of parameters used in the calibration while at the same time includes more physical insight to the waveform anatomy. Equation (5.1) shows the ansatz chosen for *Region IIb*.

$$\eta\,\phi'_{\rm MR} = \alpha_1 + \alpha_2 f^{-2} + \alpha_3 f^{-1/4} + \frac{\alpha_4 f_{\rm damp}}{f_{\rm damp}^2 + (f - \alpha_5 f_{\rm RD})^2}. \tag{5.1}$$

The explicit expressions for *Region I* and *Region IIa* are given in Equations (28) and (15) of [39].

Amplitude

The strategy for the amplitude is similar. *Region I* is modelled also using a reduced form of the `TaylorF2` expressions and calibrating the higher order parameters to NR data (see equation 4.8 of [38]) through hybrid waveforms. *Region IIa* is modelled by an $\mathcal{O}(f^4)$ polynomial where the free parameters are constrained to satisfy the differentiability in the boundaries with *Region I* and *Region IIb*. Finally, *Region IIb* is represented by Lorentzian function coupled to an exponatinally decaying function (Equation 4.5 of [38]).

Mapping the parameters to the physical space

Then, the simplified idea behind a phenomenological model relies on inspecting the morphology of a given waveform, split it in different domains considering the patterns observed in its evolution and then, assume some ansätze and fit the region considered. If one extends this analysis across the parameter space it becomes evident that the morphology is quite well preserved. This means that the ansätze proposed are also valid

for other physical configurations although, obviously, the values obtained for the free parameters will be different in each case, i.e., we can express the coefficients of (5.1) as $\alpha(\eta, S_{eff})$. Here, S_{eff} takes again the role of an effective spin parameter that results from the linear combination of the two spins (see Chapter 2 and Chapter 4). In the old PhenomD the physical dependence of the ansätze coefficients was fitted through:

$$\Lambda^i = \sum_{m,n}^{n=3,m=2} (\lambda^i_{mn}\eta^m)\widehat{S}^n\,, \tag{5.2}$$

where the Λ^i terms represent each one of the coefficients used for both amplitude and phase fits. While this has been shown to be sufficient in the calibration region when compared to NR data [39], the unequal-spin effects, the approach to the extreme-mass-ratio limit and all the other considerations studied in Chapter 4 are not included in (5.2). Then, the intuition gained through the final state and peak luminosity studies has been also propagated to the re-calibration of the PhenomD coefficients. In Sec. 5.4 we show some of the preliminary results of this upgrading.

5.2 Hybrids

The model presented in the last section has been calibrated by matching the *reliable* part of the PN-EOB evolution to the corresponding NR waveforms, building the so called IMR hybrid waveforms. This is motivated by the impossibility of covering the low LIGO frequency band with NR simulations. The potential increasing of the time to simulate one orbit in the inspiral phase (Chapter 3) added to the global computational cost of the NR runs lead sometimes to high values of the initial GW frequency f_0. For instance, the first GW frequency for the $q = 10$ non-spinning SXS waveform (SXS:BBH:0303 from [4]) is $f_0 \sim 0.048Mf$ which implies that for $M = 100M_\odot$, $f_0 \approx 100$Hz thus loosing a significant part of the waveform.

Here we briefly illustrate the key points of the hybrid construction. For a more detailed description see [57, 216].

Construction of a hybrid

Let me represent a general GW strain by $h^X(t) = A^X(t)e^{i\phi^X(t)}$ where $A(t)$ and $\phi(t)$ refer to the amplitude and phase respectively and both defined in $[0, t^X]$, where X =PN/NR denotes the PN/NR versions of a given physical case. We also need to define the gravitational wave frequency as $\omega^X = d\phi^X/dt$ which for quasi-circular orbits is a monotonically

increasing function of t. Then, ideally we can find a time interval where both representations satisfy that:

$$h^{NR}(t) = e^{\phi_0} e^{h^{PN}(t+\tau)} \qquad \omega^{NR}(t) = \omega^{PN}(t+\tau)\,, \tag{5.3}$$

$$\psi_0 = \frac{h^N R(\omega_0)}{h^P N(\omega_0)}\,, \tag{5.4}$$

where $\tau = t^P N(\omega_0) - t^{NR}(\omega_0)$, ω_0 is some matching frequency, ψ_0 is a constant phase offset between the two representations and $t^X(\omega_0) = t_0^X$. Then the procedure would be the following:

a) Select a matching frequency ω_0 and align the waveform through (5.3).

b) Correct the phase offset through (5.4).

c) Build a waveform such that $h = h^{PN}(t)$ for $t \leq \tau$ and $h = h^{NR}(t)$ for $t \geq \tau$.

However, in a real case both representations may be affected by errors and (5.3) may be never fulfilled over any interval. For instance, a $h^{NR}(t)$ with a residual eccentricity e that makes the frequency oscillate it would make difficult to fix a unique correspondence $t^{NR}(\omega_0) = t_0^{NR}$. To resolve this issue $\omega_0(\tau)$ is chosen to minimise the following expression:

$$\Delta(\tau, t_0^{PN}, \Delta t) := \int_{t_0^{PN}}^{t_0^{PN}+\Delta t} \left(\omega^{PN}(t) - \omega^{NR}(t-\tau)\right)^2 dt \tag{5.5}$$

where t_0^{PN} denotes a chosen PN matching time and Δt a certain time interval that defines a window where we compare the two representations. Then:

$$h(t) = \begin{cases} e^{i\varphi_0} h^{PN}(t+\tau) & \text{if } t < t_0 - \tau \\ w^-(t) e^{i\varphi_0} h^{PN}(t+\tau) + w^+(t) h^{NR}(t) & \text{if } t_0 - \tau < t < t_0 - \tau + \Delta t \\ h^{NR}(t) & \text{if } t_0 - \tau + \Delta t < t \end{cases} \tag{5.6}$$

where $w^{\pm}$ are blending functions that connect the two regimes. In Figure 5.2 we show an example of the resulting hybrid for a SEOBNRv4/BAM hybrid with parameters $q = 1$ and $\chi_1 = -\chi_2 = 0.50$. In this work we had to automatize the process of the hybrid construction for the new set of `BAM` waveforms and the nonprecessing `SpEC` used for the calibration. Thus, the same algorithm have been applied to a set of 362 waveforms collected from the `BAM` and `SpEC` codes, extreme mass-ratio data and purely `SEOBNRv4` data. The choice of t_0 (ω_0) and Δt ($\Delta\omega$) will vary across the parameter space, thus being also essential a proper estimate of the first clean frequency ω_0. This value is usually defined about two cycles after the emission of the junk radiation, where its effect has been normally dissipated. In Figure 5.3 where we illustrate the physical parameter

space in terms of η, S_{eff} and $\Delta\chi$. To cover the regions with lower density of points, we have also used non-hybrid `SEOBNRv4` data.

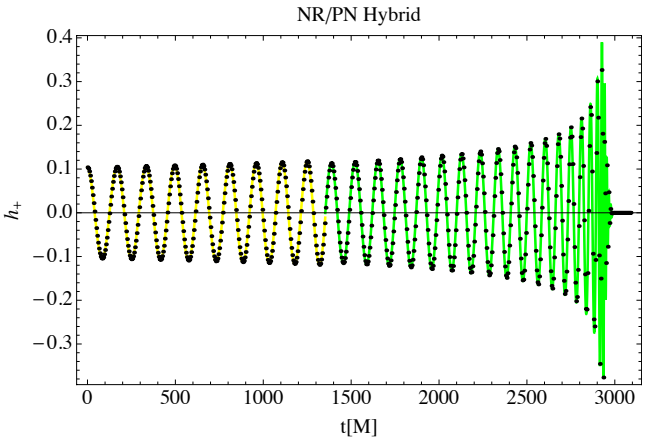

FIGURE 5.2: h_+ polarization of a 22 mode hybrid with $q = 1$ and $\chi_1 = -\chi_2 = 0.50$. In yellow we show the shifted TaylorT1 approximant that is matched to the NR representation (in green). The dotted line is a down-sampled version of the resulting hybrid. The NR waveform was computed with the `BAM` code [72].

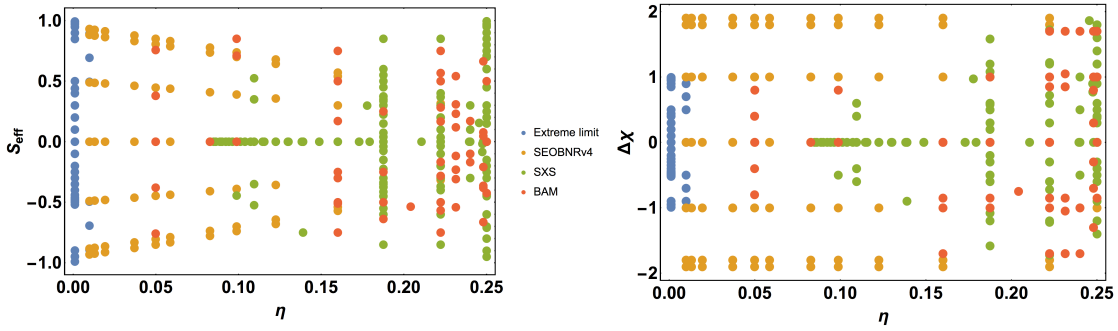

FIGURE 5.3: Left panel: Parameter space covered for the new PhenomD upgrade in terms of η and the effective spin S_{eff}. Right panel: Same parameter space but now in terms of η and the spin difference $\Delta\chi$. The points denote a hybrid waveform of the given legend with the `SEOBNRv4` approximant and build with the procedure outlined in this chapter. `SEOBNRv4` legend refers to full `SEOBNRv4` waveforms.

5.3 Inspection of the PN approximants

The goodness of the model also depends on the PN-EOB approximants used for building the hybrids. It is well known that some of them present secular deviations at frequencies compatible with the initial frequency of the NR runs which may also variate across the parameter space. Typically, the analytic models are more satisfactory for low mass-ratio and low and equal-spin configurations than for more demanding configurations. This may affect not only the model itself but also the hybridization process by matching the two evolutions (PN-EOB and NR) when the analytic models are no longer valid. Thus,

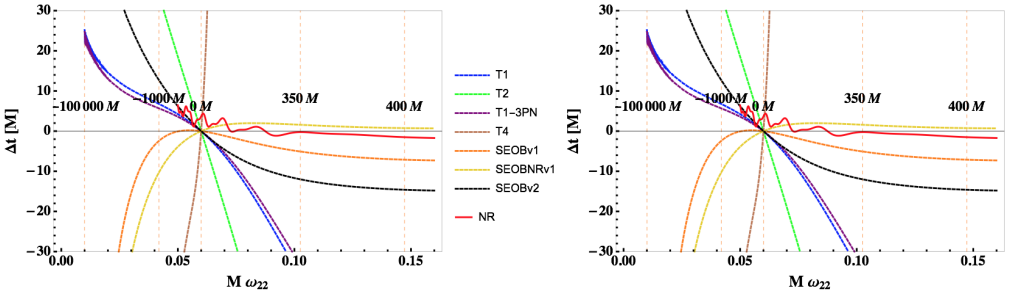

FIGURE 5.4: Left panel: time shift according to (5.7) as a function of ω for the case of mass ratio 18 with spins $\{0.4, 0\}$ where SEOBNRv2 is chosen as the reference waveform. Right panel: Same analysis for $q = 1$ with equal spins $= 0.98$. The NR waveform is SXS:BBH:0172 from the SXS catalogue [4]. SEOBNRv1/SEOBv1 are not shown for this case, since the model is not valid for high spins parallel to the orbital angular momentum.

we have tested the quality of the analytic approximants by first aligning them at an early enough time-frequency point in order to get diminished any possible drift in relatio to NR data. This is, we compute the hybridization time shift as a function of the matching frequency by inverting the functions $t(\omega^{PN})$ and $t(\omega^{NR})$ so

$$\Delta t = t^{PN}(\omega) - t^{NR}(\omega)\,. \tag{5.7}$$

We have repeated this analysis for several configurations trying to get the best analytic approximant. The approximants considered are the ones referenced in Chapter 2: `TaylorT1`, `TaylorT2`, `TaylorT3` (the 3PN and 3.5PN versions), `TaylorT4`, and the two uncalibrated EOB models `SEOBv1` and `SEOBv2` which are nothing more than different versions of [56] with no calibration to NR waveforms. The results are displayed in Figure 5.4. In this figure we see that EOB approximants match better the NR data profile by showing in general a diminished secular trend in relation to PN approximants. In particular, `SEOBv2` agrees surprisingly well with the NR data. Notice that these cases represent rather extreme parameter configurations (one with $q = 18$ and the other with $\chi = 0.98$) where the calibration to NR effects should be more dominant. This motivated the choice of `SEOBv2` for building the hybrids in the PhenomD model, allowing to perform a clean calibration of the *Region I* and avoiding any interaction with an early calibration of the approximant. For the high-spin case (right panel), the `SEOBv1` approximation and its calibrated version `SEOBv1` are not shown since they are not valid for high-spin configurations.

5.4 Unequal-spin effects on the PhenomD coefficients

One key motivation of the phenomenological fits to final state quantities and peak luminosity has been to extend the calibration of the PhenomD coefficients to an unequal-spin model. In forthcoming work with the UIB group, we will apply the same hierarchical machinery explained in Chapter 4 to PhenomD waveforms, that is; we will build up a fit from the one-dimensional regions to the full three-dimensional fits in a hierarchical way, we will use rational functions to capture the steep slope of the positive spins, we will allow for different ansätze choices ranking them in terms of the BIC and AICc values and we will use the extreme mass-ratio waveforms for calibrating the extreme-mass-ratio limit. The first results obtained evince the effect of the unequal-spin terms in some of the coefficients λ_i listed in (5.2) in all the three regimes considered for the previous PhenomD model.

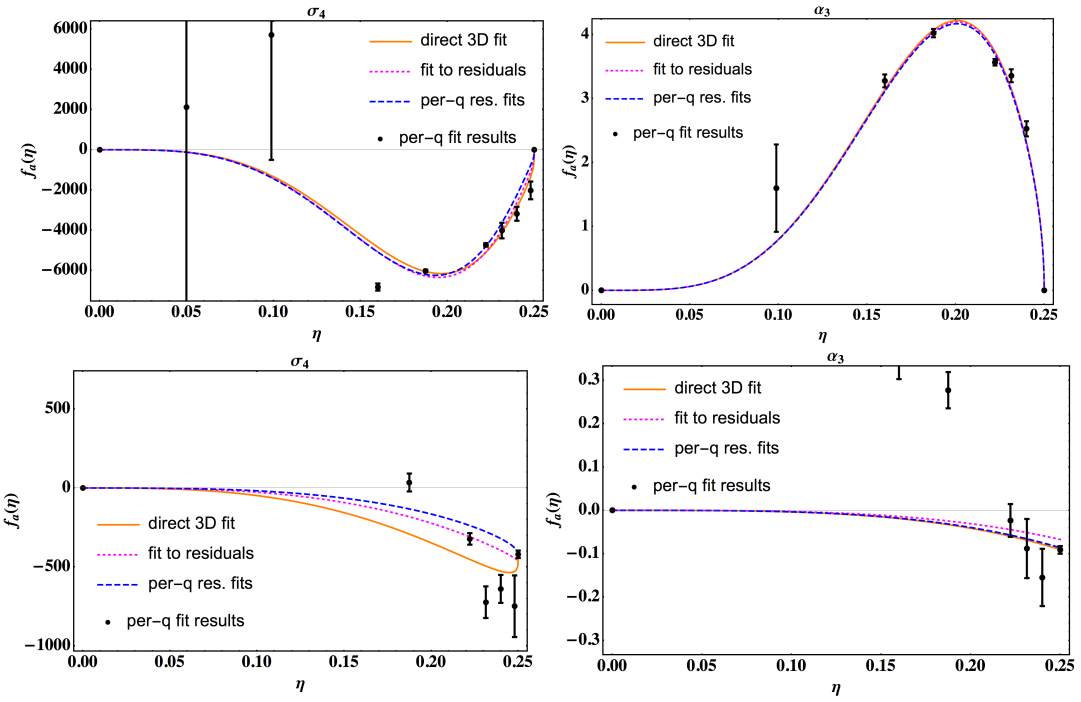

FIGURE 5.5: Top panel: unequal-spin linear terms on two of the PhenomD phase coefficients . We show the inspiral σ_4 coefficient on the left panel and the ringdown related ones α_3 on the right panel (equations (14) and (28) of [39]). Bottom panel: unequal-spin quadratic terms on the same two PhenomD phase coefficients.

In Figure 5.5, we show the unequal-spin effects on two different phase coefficients, split all over the three regimes considered in Sec. 5.1. In particular, here we show σ_4 and α_3 of equations (14) and (28) of [39] which are related to the inspiral (region I) and ringdown (region IIb) regimes. Then, it is clear that the consideration of these terms as a linear plus higher order perturbations of the main $f_{2D}(\eta, S_{eff})$ ansätze is still valid here. The linear terms are adjusted as well with the same sort of ansatz $A_1(\eta) =$

$d_{10}(1-4\eta)^{0.5}\eta^2\,(d_{11}\eta+1)$ used in Sec. 4.2.5.2 and 4.3.4, providing a similar match between the per-mass-ratio analysis (blue) and the direct three-dimensional results (red). Moreover, we see the same profile along the different frequency points of the waveform (different coefficients) thus giving some more credibility to this effect. Regarding the quadratic terms, we have to deal with the same problem as in the final state and peak luminosity fits. These terms are again shown to be subdominant in relation to the linear corrections but also compatible with the NR inaccuracy of the waveforms. Then, as in the previous fits, the statistical support for the higher order terms is very weak. This is also consistent with Figure 5.5 where despite we find some weak but similar profile as for the quadratic terms shown in Chapter 4, the noise uncertainty is still too high to consider a proper calibration of these terms. With increasingly more and more accurate NR cases we expect to capture these quadratic effects with more statistical support.

Chapter 6

Conclusions and outlook

In this thesis I have treated several topics related with BBH waveform modelling, from the NR perspective by devising and performing a novel set of BBH simulations to the phenomenological modelling by prescribing a general hierarchical fitting procedure tested in final state quantities and peak luminosity. The same methodology is also intended to be a pillar for further upgrades of the waveform models. To this end, I have simulated the dynamics of nonprecessing BBH systems by means of the `BAM` code. This needed the appropriate calibration of the gauge quantities across the parameter space, dealing with a proper choice of the PN-EOB initial parameters, solving the initial data, the evolution and eccentricity reduction, the extraction of the radiation, the computation of final state quantities, the extrapolation of the waveforms and the conversion from ψ_4 to strain and luminosity. All this way right to the final product needed a careful postprocessing of the data to not affect its final quality. This becomes more relevant when aiming to incorporate subdominant effects as the unequal-spin effects. All these issues have been addressed in Chapter 3 with a particular interest on questions related to NR data quality studies. Then, in Chapter 3 I show all the way up from the initial setup of a BBH system to the final product for a set of 23 BBH simulations performed with `BAM`. In Chapter 4 I use this data to define a new fitting strategy based on a hierarchical inclusion of the physical effects which has been successfully tested for the fitting of the final mass, final spin and peak luminosity and that looks promising for the further upgrading of the PhenomD model. Finally in Chapter 5 I illustrate the procedure to build 22 mode hybrids, I show some tests performed on the PN-EOB approximants in order to assess its correspondence with NR waveforms [38] and I add some preliminary but promising results on the hierarchical fitting methodology applied to the phenomenological coefficients. In this conclusion, I divide the results in two main blocks: NR results and phenomenological modelling results.

NR results

I have performed a set of 23 unequal-mass unequal-spin nonprecessing simulations with the `BAM` code that I had to devise, evolve and postprocess. I detail below some of the most important aspects studied in Chapter 3.

- I have obtained a fitting formula for estimating the apparent horizon radius r_{AH} for the pair of BHs simulated. An estimator of this quantity allowed us to optimise the grid configuration avoiding any initial test runs. This led to the reduction of the computational cost per run in about 2×10^3 CPU hours. Extrapolated to the total amount of simulations, involved an approximate reduction of $\sim 6 \times 10^4$ CPU hours.

- I have reduced the residual eccentricity by more than one order of magnitude for those cases were initially $e \sim 0.01$. To do so, I defined a simplified strategy based on [141] by determining the amplitude of the oscillations. Then, I related them with the λ correction to be applied to the physical tangential momentum p_t. I have found a trivial relation relying on the Newtonian two body problem to connect the NR eccentricity with PN-EOB deviations. This simplified estimator has been shown to be sufficient for an appropriate reduction ($e \sim 10^{-3}$) in one single step.

- The radiation of all these simulations have been extracted at finite radii using the Newman-Penrose formalism. I have carefully studied the extrapolation effects trying to minimise the gauge effects in our data. Then, all the waveforms have been converted to strain through the fixed-frequency integration (FFI) method [142], which involved a careful tuning of the cutoff frequency f_0 and through the Exponential Fit (EF) that I developed in this thesis and that avoids the tuning of any free parameter. The results between the two methods looked consistent.

- Also in Chapter 3 I show the basic equations for computing the final mass and the final spin. These have been computed in two ways; using horizon information by means of the `AHFinder` implemented in `BAM` and through radiation quantities. For the latter we had to compute the missing PN radiation using the analytic 3.5PN for the energy evolution until the initial orbital frequency of the NR runs. The results are shown in Chapter 4.

- The peak luminosity was computed using Equation 3.20 of Chapter 3. Then, for all the 23 cases I had to postprocess the ψ_4 and compute the maximum of the combined luminosity, i.e., with the higher modes (HM) included. Thus, the NR

quality studies were not applied only to the dominant quadrupolar radiation but they have been extended to the HMs.

- The `BAM` data set is not sufficiently large to populate the parameter space. This led us to collect data from three more BBH codes; `LAZEV` [85], `MAYA` [6] and `SpEC` [84] plus an extra set of 37 extreme-mass-ratio waveforms [95, 158] . Although it is clear that this helps to better calibrate the fits, it also includes an extra source of error driven by the particular NR systematics of each code. First I studied the contribution to the error of the extrapolation effects for the `SpEC`, `BAM` and `MAYA` codes (we did not have all the `LAZEV` data to do so). In general, we have seen that the extrapolation effects seem to dominate the resolution errors although still being smaller than the residuals obtained. To have a more reliable estimate of the error, I have compared the values between *twin* cases (cases with the same physical parameters). In general, we have seen that these errors are compatible with the residuals thus showing up as the dominant ones. However, I could not extrapolate these estimates across the parameter space due to the small number of *twin* cases found.

Phenomenological modelling

The results of the different NR codes have been essential to devise and further calibrate phenomenological fits for the final mass (energy radiated), final spin and peak luminosity while they will also play a key role for the further calibration of the PhenomD model. In this line, with my collaborators I have obtained the following results:

- We have devised a novel strategy for calibrating higher than two dimensional fits where the contributions can be separated in order of importance. We called that a *hierarchical data-driven fit methodology* and it has been used in the main publications obtained throughout this thesis [7, 8, 188] for the calibration of new fits for the energy radiated, final spin and peak luminosity. This is shown in Chapter 4.

- One of the key points of the new methodology has been the use of the information criteria (AICc, BIC) to better justify the ansatz selection and avoid overfitting. This allowed us to consider a wider range of ansätze than in the previous phenomenological calibrations [38] and which helped to gain statistical significance in relation to the old models. The robustness of the procedure was also tested by using different spin parametrizations and where the results were compatible with the optimal choice of S_{eff}.

- We calibrated the subdominant unequal-spin effects through a simple order two polynomial in $\Delta\chi$ where the linear influence has been clearly captured. We leave for the future a better calibration of the higher than linear perturbations when cleaner and larger data sets are expected.

- In addition, we have also constrained the extreme-spin approach thus avoiding any overshooting of the Kerr limit while the extreme mass-ratio limit has been accounted from two different perspectives: by adding the known analytic formulas (final spin and energy radiated) and including explicit extreme mass-ratio data [153, 154] (peak luminosity).

- All this machinery is being used for the imminent PhenomD re-calibration. The preliminary results look promising and compatible with the predictions obtained from the final state and peak luminosity peaks.

Outlook

Subdominant effects

One of the main achievements of this step by step hierarchical methodology is that it helped to understand how the subdominant effects may be included in future gravitational wave models. Thus, there are some other effects that act on the same level as precession and eccentricity and which could be now considered in a similar way as the unequal-spin terms. Although its calibration is highly tied to how populated is our parameter space, the number of publicly available BBH simulations is increasing rapidly.

Quantification of the errors on the Phenom coefficients and derived quantities

As we have referred to throughout this thesis, there was no quantification of the errors on the old phenom models. With this new detailed strategy the error estimates come out more naturally than in the old studies helped by the ranking statistics developed in this work. One immediate application would be its implementation into the waveform models that would also help to better understand the parameter estimation results and constrain the physical parameters of future observations.

NR data quality and future models

The detailed NR data quality studies helped us to better understand the requirements for the gauge and grid choices across the parameter space. This was not restricted to

only the dominant (22) mode but also for the higher modes (HM). This is relevant for the calibration and modelling of (HM) models where the contribution of the modes may be comparable with the NR uncertainties of the non-quadrupolar modes.

Bibliography

[1] A. Einstein. Nherungsweise Integration der Feldgleichungen der Gravitation. *K. Preus., Sitzungsber Akad. Wiss.*, 1:688–696, 1916.

[2] A. Einstein. Nherungsweise Integration der Feldgleichungen der Gravitation. *K. Preus., Sitzungsber Akad. Wiss.*, 1:154, 1918.

[3] B. P. Abbott et al. Observation of Gravitational Waves from a Binary Black Hole Merger. *Phys. Rev. Lett.*, 116(6):061102, 2016. doi: 10.1103/PhysRevLett.116.061102.

[4] The SXS Collaboration. SXS Gravitational Waveform Database, 2016. URL http://www.black-holes.org/waveforms/.

[5] M. Campanelli et al. The rit binary black hole simulations catalog. Technical Report LIGO-P1700035, 2017. URL https://dcc.ligo.org/LIGO-P1700035.

[6] Karan Jani, James Healy, James A. Clark, Lionel London, Pablo Laguna, and Deirdre Shoemaker. Georgia Tech catalog of binary black hole simulations, 2016. URL http://www.einstein.gatech.edu/catalog/.

[7] Xisco Jimnez-Forteza, David Keitel, Sascha Husa, Mark Hannam, Sebastian Khan, and Michael Prrer. Hierarchical data-driven approach to fitting numerical relativity data for non-precessing binary black holes, with an application to final spin and radiated energy. *Phys. Rev.*, D95(6):064024, 2017. doi: 10.1103/PhysRevD.95.064024.

[8] David Keitel et al. The most powerful astrophysical events: gravitational-wave peak luminosity of binary black holes as predicted by numerical relativity. 2016.

[9] A. Einstein. Grundgedanken der allgemeinen Relativittstheorie und Anwendung dieser Theorie in der Astronomie. *K. Preus., Sitzungsber Akad. Wiss.*, 1:315, 1915.

[10] A. Einstein. Zur allgemeinen Relativittstheorie. *K. Preus., Sitzungsber Akad. Wiss.*, 2:778786, 799801, 1915.

[11] A. Einstein. Erklrung der Perihelbewegung des Merkur aus der allgemeinen Relativittstheorie. *K. Preus., Sitzungsber Akad. Wiss.*, 2:831–839, 1915.

[12] A. Einstein. Feldgleichungen der Gravitation. *K. Preus., Sitzungsber Akad. Wiss.*, 2:844–847, 1915.

[13] B. P. Abbott et al. Properties of the Binary Black Hole Merger GW150914. *Phys. Rev. Lett.*, 116(24):241102, 2016. doi: 10.1103/PhysRevLett.116.241102.

[14] Carles Bona, Carlos Palenzuela-Luque, and Carles Bona-Casas. *Elements of Numerical Relativity and Relativistic Hydrodynamics*. Springer, 2009.

[15] Bernard Schutz. *A First Course in General Relativity*. Cambridge University Press, 2nd edition, 2009. ISBN 0521887054.

[16] Benjamin P. Abbott et al. Results of the deepest all-sky survey for continuous gravitational waves on LIGO S6 data running on the Einstein@Home volunteer distributed computing project. *Phys. Rev.*, D94(10):102002, 2016. doi: 10.1103/PhysRevD.94.102002.

[17] Benjamin P. Abbott et al. First search for gravitational waves from known pulsars with Advanced LIGO. 2017.

[18] Nathan K. Johnson-McDaniel and Benjamin J. Owen. Maximum elastic deformations of relativistic stars. *Phys. Rev.*, D88:044004, 2013. doi: 10.1103/PhysRevD.88.044004.

[19] Luc Blanchet. Gravitational Radiation from Post-Newtonian Sources and Inspiralling Compact Binaries. *Living Rev. Rel.*, 17:2, 2014. doi: 10.12942/lrr-2014-2.

[20] Alejandro Bohé, Sylvain Marsat, and Luc Blanchet. Next-to-next-to-leading order spinorbit effects in the gravitational wave flux and orbital phasing of compact binaries. *Class. Quant. Grav.*, 30:135009, 2013. doi: 10.1088/0264-9381/30/13/135009.

[21] Thibault Damour. Coalescence of two spinning black holes: an effective one-body approach. *Phys. Rev.*, D64:124013, 2001. doi: 10.1103/PhysRevD.64.124013.

[22] Alessandra Buonanno and Thibault Damour. Transition from inspiral to plunge in binary black hole coalescences. *Phys. Rev.*, D62:064015, 2000. doi: 10.1103/PhysRevD.62.064015.

[23] Nils Andersson et al. The Transient Gravitational-Wave Sky. *Class. Quant. Grav.*, 30:193002, 2013. doi: 10.1088/0264-9381/30/19/193002.

[24] B. P. Abbott et al. Binary Black Hole Mergers in the first Advanced LIGO Observing Run. 2016.

[25] J. M. Weisberg, J. H. Taylor, and L. A. Fowler. GRAVITATIONAL WAVES FROM AN ORBITING PULSAR. *Sci. Am.*, 245:66–74, 1981. doi: 10.1038/scientificamerican1081-74.

[26] LIGO-Virgo scientific collaboration. The lsc-virgo white paper on gravitational wave searches and astrophysics, 2016. URL https://dcc.ligo.org/public/0111/T1400054/007.

[27] B. P. Abbott et al. Astrophysical Implications of the Binary Black-Hole Merger GW150914. *Astrophys. J.*, 818(2):L22, 2016. doi: 10.3847/2041-8205/818/2/L22.

[28] LISA. Lisa, 2016. URL https://www.elisascience.org/articles/elisa-mission/lisa-mission-proposal-l3.

[29] C. Palomba. Searches for continuous gravitational wave signals and stochastic backgrounds in LIGO and Virgo data. In *Proceedings, 46th Rencontres de Moriond on Gravitational Waves and Experimental Gravity: La Thuile, Italy, March 20-27, 2011*, pages 27–34, 2012. URL https://inspirehep.net/record/1084679/files/arXiv:1201.3176.pdf.

[30] Edgard F. D. Evangelista and José C. N. de Araujo. Stochastic background of gravitational waves generated by compact binary systems. *Brazilian Journal of Physics*, 44(2):260–270, 2014. ISSN 1678-4448. doi: 10.1007/s13538-014-0178-x. URL http://dx.doi.org/10.1007/s13538-014-0178-x.

[31] Chiara Caprini. Stochastic background of gravitational waves from cosmological sources. *J. Phys. Conf. Ser.*, 610(1):012004, 2015. doi: 10.1088/1742-6596/610/1/012004.

[32] J. Aasi et al. Search for gravitational waves associated with γ-ray bursts detected by the Interplanetary Network. *Phys. Rev. Lett.*, 113(1):011102, 2014. doi: 10.1103/PhysRevLett.113.011102.

[33] Istituto Nazionale di Fisica Nucleare. Auriga (antenna ultracriogenica risonante per l'indagine gravitazionale astronomica). URL http://www.auriga.lnl.infn.it.

[34] LSC. Lsc-livingston. URL "https://www.ligo.caltech.edu/LA".

[35] ET project. Et (einstein telescope). URL http://www.et-gw.eu.

[36] M. Maggiore. *Gravitational Waves: Volume 1: Theory and Experiments*. OUP Oxford, 2007. ISBN 9780198570745. URL https://books.google.es/books?id=AqVpQgAACAAJ.

[37] J. Abadie et al. A Gravitational wave observatory operating beyond the quantum shot-noise limit: Squeezed light in application. *Nature Phys.*, 7:962–965, 2011. doi: 10.1038/nphys2083.

[38] Sascha Husa, Sebastian Khan, Mark Hannam, Michael Pürrer, Frank Ohme, Xisco Jiménez Forteza, and Alejandro Bohé. Frequency-domain gravitational waves from nonprecessing black-hole binaries. I. New numerical waveforms and anatomy of the signal. *Phys. Rev.*, D93(4):044006, 2016. doi: 10.1103/PhysRevD.93.044006.

[39] Sebastian Khan, Sascha Husa, Mark Hannam, Frank Ohme, Michael Pürrer, Xisco Jiménez Forteza, and Alejandro Bohé. Frequency-domain gravitational waves from nonprecessing black-hole binaries. II. A phenomenological model for the advanced detector era. *Phys. Rev.*, D93(4):044007, 2016. doi: 10.1103/PhysRevD.93.044007.

[40] M Punturo et al. The einstein telescope: a third-generation gravitational wave observatory. *Classical and Quantum Gravity*, 27(19):194002, 2010. URL http://stacks.iop.org/0264-9381/27/i=19/a=194002.

[41] S. Hild et al. Sensitivity Studies for Third-Generation Gravitational Wave Observatories. *Class. Quant. Grav.*, 28:094013, 2011. doi: 10.1088/0264-9381/28/9/094013.

[42] Benjamin P. Abbott et al. Exploring the Sensitivity of Next Generation Gravitational Wave Detectors. *Class. Quant. Grav.*, 34(4):044001, 2017. doi: 10.1088/1361-6382/aa51f4.

[43] LISA Pathfinder. Lisa pathfinder, 2016. URL http://sci.esa.int/lisa-pathfinder.

[44] Karl Gebhardt, R. Michael Rich, and Luis C. Ho. An Intermediate-mass black hole in the globular cluster G1: Improved significance from new Keck and Hubble Space Telescope observations. *Astrophys. J.*, 634:1093–1102, 2005. doi: 10.1086/497023.

[45] B. P. Abbott et al. GW151226: Observation of Gravitational Waves from a 22-Solar-Mass Binary Black Hole Coalescence. *Phys. Rev. Lett.*, 116(24):241103, 2016. doi: 10.1103/PhysRevLett.116.241103.

[46] Frans Pretorius. Evolution of binary black hole spacetimes. *Phys. Rev. Lett.*, 95: 121101, 2005. doi: 10.1103/PhysRevLett.95.121101.

[47] Geoffrey Lovelace et al. Modeling the source of GW150914 with targeted numerical-relativity simulations. *Class. Quant. Grav.*, 33(24):244002, 2016. doi: 10.1088/0264-9381/33/24/244002.

[48] B. P. Abbott et al. GW150914: The Advanced LIGO Detectors in the Era of First Discoveries. *Phys. Rev. Lett.*, 116(13):131103, 2016. doi: 10.1103/PhysRevLett.116.131103.

[49] P. C. Peters. Gravitational Radiation and the Motion of Two Point Masses. *Phys. Rev.*, 136:B1224–B1232, 1964. doi: 10.1103/PhysRev.136.B1224.

[50] Thibault Damour, Bala R. Iyer, and B. S. Sathyaprakash. A Comparison of search templates for gravitational waves from binary inspiral. *Phys. Rev.*, D63:044023, 2001. doi: 10.1103/PhysRevD.63.044023,10.1103/PhysRevD.72.029902. [Erratum: Phys. Rev.D72,029902(2005)].

[51] Etienne Racine. Analysis of spin precession in binary black hole systems including quadrupole-monopole interaction. *Phys. Rev.*, D78:044021, 2008. doi: 10.1103/PhysRevD.78.044021.

[52] Sylvain Marsat, Alejandro Bohé, Luc Blanchet, and Alessandra Buonanno. Next-to-leading tail-induced spinorbit effects in the gravitational radiation flux of compact binaries. *Class. Quant. Grav.*, 31:025023, 2014. doi: 10.1088/0264-9381/31/2/025023.

[53] P. Ajith et al. Inspiral-merger-ringdown waveforms for black-hole binaries with non-precessing spins. *Phys. Rev. Lett.*, 106:241101, 2011. doi: 10.1103/PhysRevLett.106.241101.

[54] L. Santamaria et al. Matching post-Newtonian and numerical relativity waveforms: systematic errors and a new phenomenological model for non-precessing black hole binaries. *Phys. Rev.*, D82:064016, 2010. doi: 10.1103/PhysRevD.82.064016.

[55] Vitor Cardoso, Edgardo Franzin, and Paolo Pani. Is the gravitational-wave ringdown a probe of the event horizon? *Phys. Rev. Lett.*, 116(17):171101, 2016. doi: 10.1103/PhysRevLett.117.089902,10.1103/PhysRevLett.116.171101. [Erratum: Phys. Rev. Lett.117,no.8,089902(2016)].

[56] Andrea Taracchini, Alessandra Buonanno, Gaurav Khanna, and Scott A. Hughes. Small mass plunging into a Kerr black hole: Anatomy of the inspiral-merger-ringdown waveforms. *Phys. Rev.*, D90(8):084025, 2014. doi: 10.1103/PhysRevD.90.084025.

[57] Juan Calderon-Bustillo. *Sub-dominant modes of the gravitational radiation from compact binary coalescences: construction of hybrid waveforms and impact on gravitational wave searches.* PhD thesis, Universitat de les Illes Balears, 2015.

[58] Luc Blanchet and Bala R. Iyer. Hadamard regularization of the third post-Newtonian gravitational wave generation of two point masses. *Phys. Rev.*, D71: 024004, 2005. doi: 10.1103/PhysRevD.71.024004.

[59] Luc Blanchet, Thibault Damour, Gilles Esposito-Farese, and Bala R. Iyer. Gravitational radiation from inspiralling compact binaries completed at the third post-Newtonian order. *Phys. Rev. Lett.*, 93:091101, 2004. doi: 10.1103/PhysRevLett.93.091101.

[60] Michael Boyle, Duncan A. Brown, Lawrence E. Kidder, Abdul H. Mroue, Harald P. Pfeiffer, Mark A. Scheel, Gregory B. Cook, and Saul A. Teukolsky. High-accuracy comparison of numerical relativity simulations with post-Newtonian expansions. *Phys. Rev.*, D76:124038, 2007. doi: 10.1103/PhysRevD.76.124038.

[61] K. G. Arun, Alessandra Buonanno, Guillaume Faye, and Evan Ochsner. Higher-order spin effects in the amplitude and phase of gravitational waveforms emitted by inspiraling compact binaries: Ready-to-use gravitational waveforms. *Phys. Rev.*, D79:104023, 2009. doi: 10.1103/PhysRevD.79.104023,10.1103/PhysRevD.84.049901. [Erratum: Phys. Rev.D84,049901(2011)].

[62] Luc Blanchet, Guillaume Faye, Bala R. Iyer, and Siddhartha Sinha. The Third post-Newtonian gravitational wave polarisations and associated spherical harmonic modes for inspiralling compact binaries in quasi-circular orbits. *Class. Quant. Grav.*, 25:165003, 2008. doi: 10.1088/0264-9381/25/16/165003,10.1088/0264-9381/29/23/239501. [Erratum: Class. Quant. Grav.29,239501(2012)].

[63] Andrea Taracchini et al. Effective-one-body model for black-hole binaries with generic mass ratios and spins. *Phys. Rev.*, D89(6):061502, 2014. doi: 10.1103/PhysRevD.89.061502.

[64] Yi Pan, Alessandra Buonanno, Andrea Taracchini, Lawrence E. Kidder, Abdul H. Mrou, Harald P. Pfeiffer, Mark A. Scheel, and Bla Szilgyi. Inspiral-merger-ringdown waveforms of spinning, precessing black-hole binaries in the effective-one-body formalism. *Phys. Rev.*, D89(8):084006, 2014. doi: 10.1103/PhysRevD.89.084006.

[65] Yi Pan, Alessandra Buonanno, Michael Boyle, Luisa T. Buchman, Lawrence E. Kidder, Harald P. Pfeiffer, and Mark A. Scheel. Inspiral-merger-ringdown multipolar waveforms of nonspinning black-hole binaries using the effective-one-body formalism. *Phys. Rev.*, D84:124052, 2011. doi: 10.1103/PhysRevD.84.124052.

[66] Alejandro Boh et al. Improved effective-one-body model of spinning, nonprecessing binary black holes for the era of gravitational-wave astrophysics with advanced detectors. *Phys. Rev.*, D95(4):044028, 2017. doi: 10.1103/PhysRevD.95.044028.

[67] Michael Pürrer. Frequency domain reduced order model of aligned-spin effective-one-body waveforms with generic mass-ratios and spins. *Phys. Rev.*, D93(6): 064041, 2016. doi: 10.1103/PhysRevD.93.064041.

[68] Parameswaran Ajith et al. Phenomenological template family for black-hole coalescence waveforms. *Class. Quant. Grav.*, 24:S689–S700, 2007. doi: 10.1088/0264-9381/24/19/S31.

[69] Mark Hannam, Patricia Schmidt, Alejandro Bohé, Lela Haegel, Sascha Husa, Frank Ohme, Geraint Pratten, and Michael Pürrer. Simple Model of Complete Precessing Black-Hole-Binary Gravitational Waveforms. *Phys. Rev. Lett.*, 113(15): 151101, 2014. doi: 10.1103/PhysRevLett.113.151101.

[70] Sebastian Khan. *Numerical Modelling Of Black-Hole-Binary Mergers*. PhD thesis, Cardiff University, School of Physics and Astronomy, 2015. URL https://orca.cf.ac.uk/93841/1/2016KhanSPhD.pdf.

[71] Miguel Alcubierre, Bernd Bruegmann, Peter Diener, Michael Koppitz, Denis Pollney, Edward Seidel, and Ryoji Takahashi. Gauge conditions for long term numerical black hole evolutions without excision. *Phys. Rev.*, D67:084023, 2003. doi: 10.1103/PhysRevD.67.084023.

[72] Bernd Bruegmann, Jose A. Gonzalez, Mark Hannam, Sascha Husa, Ulrich Sperhake, and Wolfgang Tichy. Calibration of Moving Puncture Simulations. *Phys. Rev.*, D77:024027, 2008. doi: 10.1103/PhysRevD.77.024027.

[73] Denis Pollney, Christian Reisswig, Erik Schnetter, Nils Dorband, and Peter Diener. High accuracy binary black hole simulations with an extended wave zone. *Phys. Rev.*, D83:044045, 2011. doi: 10.1103/PhysRevD.83.044045.

[74] Mark A. Scheel, Harald P. Pfeiffer, Lee Lindblom, Lawrence E. Kidder, Oliver Rinne, and Saul A. Teukolsky. Solving Einstein's equations with dual coordinate frames. *Phys. Rev.*, D74:104006, 2006. doi: 10.1103/PhysRevD.74.104006.

[75] Thibault Damour, Bala R. Iyer, and B. S. Sathyaprakash. A Comparison of search templates for gravitational waves from binary inspiral - 3.5PN update. *Phys. Rev.*, D66:027502, 2002. doi: 10.1103/PhysRevD.66.027502.

[76] Miguel Alcubierre. *Introduction to 3+1 Numerical Relativity.* Oxford Science Publications, 2008.

[77] H. Friedrich. *On the hyperbolicity of Einstein's and other gauge field equations.* Springer, 1985.

[78] David Garfinkle. Harmonic coordinate method for simulating generic singularities. *Phys. Rev.*, D65:044029, 2002. doi: 10.1103/PhysRevD.65.044029.

[79] Frans Pretorius. Numerical relativity using a generalized harmonic decomposition. *Class. Quant. Grav.*, 22:425–452, 2005. doi: 10.1088/0264-9381/22/2/014.

[80] T. Nakamura, K. Oohara, and Y. Kojima. General Relativistic Collapse to Black Holes and Gravitational Waves from Black Holes. *Prog. Theor. Phys. Suppl.*, 90: 1–218, 1987. doi: 10.1143/PTPS.90.1.

[81] C. R. Evans, L. S. Finn, and D. W. Hobill. *Frontiers in numerical relativity.* 1989.

[82] Masaru Shibata and Takashi Nakamura. Evolution of three-dimensional gravitational waves: Harmonic slicing case. *Phys. Rev.*, D52:5428–5444, 1995. doi: 10.1103/PhysRevD.52.5428.

[83] Thomas W. Baumgarte and Stuart L. Shapiro. On the numerical integration of Einstein's field equations. *Phys. Rev.*, D59:024007, 1998. doi: 10.1103/PhysRevD.59.024007.

[84] The SXS Collaboration. SpEC: Spectral Einstein Code, 2016. URL http://www.black-holes.org/SpEC.html.

[85] Manuela Campanelli, James Healy, Carlos Lousto, and Yosef Zlochower. CCRG@RIT Catalog of Numerical Simulations, 2016. URL http://ccrg.rit.edu/~RITCatalog/.

[86] Pedro J. Montero and Isabel Cordero-Carrion. BSSN equations in spherical coordinates without regularization: vacuum and non-vacuum spherically symmetric spacetimes. *Phys. Rev.*, D85:124037, 2012. doi: 10.1103/PhysRevD.85.124037.

[87] Thomas W. Baumgarte, Pedro J. Montero, Isabel Cordero-Carrion, and Ewald Muller. Numerical Relativity in Spherical Polar Coordinates: Evolution Calculations with the BSSN Formulation. *Phys. Rev.*, D87(4):044026, 2013. doi: 10.1103/PhysRevD.87.044026.

[88] General Relativity and Gravitation groupof the Balearic Islands University. GRG: General Relativity and Gravitation group, 2017. URL http://grg.uib.es.

[89] Abdul H. Mroue et al. Catalog of 174 Binary Black Hole Simulations for Gravitational Wave Astronomy. *Phys. Rev. Lett.*, 111(24):241104, 2013. doi: 10.1103/PhysRevLett.111.241104.

[90] Karan Jani, James Healy, James A. Clark, Lionel London, Pablo Laguna, and Deirdre Shoemaker. Georgia Tech Catalog of Gravitational Waveforms. 2016.

[91] James Healy, Carlos O. Lousto, and Yosef Zlochower. Remnant mass, spin, and recoil from spin aligned black-hole binaries. *Phys. Rev.*, D90(10):104004, 2014. doi: 10.1103/PhysRevD.90.104004.

[92] James Healy and Carlos O. Lousto. Remnant of binary black-hole mergers: New simulations and peak luminosity studies. *Phys. Rev.*, D95(2):024037, 2017. doi: 10.1103/PhysRevD.95.024037.

[93] Alessandro Nagar, Thibault Damour, and Angelo Tartaglia. Binary black hole merger in the extreme mass ratio limit. *Class. Quant. Grav.*, 24:S109–S124, 2007. doi: 10.1088/0264-9381/24/12/S08.

[94] Sebastiano Bernuzzi and Alessandro Nagar. Binary black hole merger in the extreme-mass-ratio limit: a multipolar analysis. *Phys. Rev.*, D81:084056, 2010. doi: 10.1103/PhysRevD.81.084056.

[95] Enno Harms, Sebastiano Bernuzzi, Alessandro Nagar, and Anil Zenginoğlu. A new gravitational wave generation algorithm for particle perturbations of the Kerr spacetime. *Class. Quant. Grav.*, 31(24):245004, 2014. doi: 10.1088/0264-9381/31/24/245004.

[96] Dieter R. Brill and Richard W. Lindquist. Interaction energy in geometrostatics. *Phys. Rev.*, 131:471–476, 1963. doi: 10.1103/PhysRev.131.471.

[97] C. Bona, J. Masso, E. Seidel, and J. Stela. First order hyperbolic formalism for numerical relativity. *Phys. Rev.*, D56:3405–3415, 1997. doi: 10.1103/PhysRevD.56.3405.

[98] Manuela Campanelli, C. O. Lousto, P. Marronetti, and Y. Zlochower. Accurate evolutions of orbiting black-hole binaries without excision. *Phys. Rev. Lett.*, 96:111101, 2006. doi: 10.1103/PhysRevLett.96.111101.

[99] John G. Baker, Joan Centrella, Dae-Il Choi, Michael Koppitz, and James van Meter. Gravitational wave extraction from an inspiraling configuration of merging

black holes. *Phys. Rev. Lett.*, 96:111102, 2006. doi: 10.1103/PhysRevLett.96.111102.

[100] A. Lichnerowicz. Lintgration des quations de la gravitation relativiste et le problme des n corps. *Journal de Mathmatiques Pures et Appliques. Neuvime*, Serie 23:37–63, 1944.

[101] James W. York, Jr. Gravitational degrees of freedom and the initial-value problem. *Phys. Rev. Lett.*, 26:1656–1658, 1971. doi: 10.1103/PhysRevLett.26.1656.

[102] James W. York, Jr. Role of conformal three geometry in the dynamics of gravitation. *Phys. Rev. Lett.*, 28:1082–1085, 1972. doi: 10.1103/PhysRevLett.28.1082.

[103] J. M. Bowen. General form for the longitudinal momentum of a spherically symmetric source. *General Relativity and Gravitation*, 11:227–231, October 1979. doi: 10.1007/BF00762132.

[104] Jeffrey M. Bowen and James W. York, Jr. Time asymmetric initial data for black holes and black hole collisions. *Phys. Rev.*, D21:2047–2056, 1980. doi: 10.1103/PhysRevD.21.2047.

[105] Steven Brandt and Bernd Bruegmann. A Simple construction of initial data for multiple black holes. *Phys. Rev. Lett.*, 78:3606–3609, 1997. doi: 10.1103/PhysRevLett.78.3606.

[106] Sergio Dain, Carlos O. Lousto, and Ryoji Takahashi. New conformally flat initial data for spinning black holes. *Phys. Rev.*, D65:104038, 2002. doi: 10.1103/PhysRevD.65.104038.

[107] Gregory B. Cook and James W. York, Jr. Apparent Horizons for Boosted or Spinning Black Holes. *Phys. Rev.*, D41:1077, 1990. doi: 10.1103/PhysRevD.41.1077.

[108] Mark A. Scheel, Matthew Giesler, Daniel A. Hemberger, Geoffrey Lovelace, Kevin Kuper, Michael Boyle, B. Szilgyi, and Lawrence E. Kidder. Improved methods for simulating nearly extremal binary black holes. *Class. Quant. Grav.*, 32(10):105009, 2015. doi: 10.1088/0264-9381/32/10/105009.

[109] Geoffrey Lovelace, Robert Owen, Harald P. Pfeiffer, and Tony Chu. Binary-black-hole initial data with nearly-extremal spins. *Phys. Rev.*, D78:084017, 2008. doi: 10.1103/PhysRevD.78.084017.

[110] Geoffrey Lovelace et al. Nearly extremal apparent horizons in simulations of merging black holes. *Class. Quant. Grav.*, 32(6):065007, 2015. doi: 10.1088/0264-9381/32/6/065007.

[111] Marsha J. Berger and Joseph Oliger. Adaptive Mesh Refinement for Hyperbolic Partial Differential Equations. *J. Comput. Phys.*, 53:484, 1984. doi: 10.1016/0021-9991(84)90073-1.

[112] Lages Norbert. *Apparent Horizons and Marginally Trapped Surfaces in Nu- merical General Relativity.* PhD thesis, Friedrich-Schiller-Universitat Jena, 2010.

[113] Ezra Newman and Roger Penrose. An Approach to gravitational radiation by a method of spin coefficients. *J. Math. Phys.*, 3:566–578, 1962. doi: 10.1063/1.1724257.

[114] Nigel T. Bishop and Luciano Rezzolla. Extraction of Gravitational Waves in Numerical Relativity. 2016. doi: 10.1007/lrr-2016-2,10.1007/s41114-016-0001-9.

[115] R. Gomez, L. Lehner, P. Papadopoulos, and J. Winicour. The eth formalism in numerical relativity. *Class. Quant. Grav.*, 14:977–990, 1997. doi: 10.1088/0264-9381/14/4/013.

[116] Roger Penrose. Gravitational collapse and space-time singularities. *Phys. Rev. Lett.*, 14:57–59, 1965. doi: 10.1103/PhysRevLett.14.57.

[117] Robert P. Geroch. Asymptotic structure of space-time. 1977.

[118] Ian Hinder, Barry Wardell, and Eloisa Bentivegna. Falloff of the Weyl scalars in binary black hole spacetimes. *Phys. Rev.*, D84:024036, 2011. doi: 10.1103/PhysRevD.84.024036.

[119] Juan Calderón Bustillo, Alejandro Bohé, Sascha Husa, Alicia M. Sintes, Mark Hannam, and Michael Pürrer. Comparison of subdominant gravitational wave harmonics between post-Newtonian and numerical relativity calculations and construction of multi-mode hybrids. 2015.

[120] Hiroyuki Nakano, James Healy, Carlos O. Lousto, and Yosef Zlochower. Perturbative extraction of gravitational waveforms generated with Numerical Relativity. *Phys. Rev.*, D91(10):104022, 2015. doi: 10.1103/PhysRevD.91.104022.

[121] S. W. Hawking and G. F. R. Ellis. *The Large Scale Structure of Space-Time.* Cambridge Monographs on Mathematical Physics. Cambridge University Press, 2011. ISBN 9780521200165, 9780521099066, 9780511826306, 9780521099066. doi: 10.1017/CBO9780511524646.

[122] Masaru Shibata. *100 Years of General Relativity: Numerical Relativity.* WSPC, 2015.

[123] Olaf Dreyer, Badri Krishnan, Deirdre Shoemaker, and Erik Schnetter. Introduction to isolated horizons in numerical relativity. *Phys. Rev.*, D67:024018, 2003. doi: 10.1103/PhysRevD.67.024018.

[124] Abhay Ashtekar and Badri Krishnan. Isolated and dynamical horizons and their applications. *Living Rev. Rel.*, 7:10, 2004. doi: 10.12942/lrr-2004-10.

[125] Jonathan Thornburg. Event and apparent horizon finders for 3+1 numerical relativity. *Living Rev. Rel.*, 10:3, 2007.

[126] Michael I. Cohen, Harald P. Pfeiffer, and Mark A. Scheel. Revisiting Event Horizon Finders. *Class. Quant. Grav.*, 26:035005, 2009. doi: 10.1088/0264-9381/26/3/035005.

[127] Badri Krishnan. Quasi-local black hole horizons. In Abhay Ashtekar and Vesselin Petkov, editors, *Springer Handbook of Spacetime*, pages 527–555. 2014. doi: 10.1007/978-3-642-41992-8_25. URL http://inspirehep.net/record/1224254/files/arXiv:1303.4635.pdf.

[128] Emanuele Berti, Vitor Cardoso, Jose A. Gonzalez, Ulrich Sperhake, Mark Hannam, Sascha Husa, and Bernd Bruegmann. Inspiral, merger and ringdown of unequal mass black hole binaries: A Multipolar analysis. *Phys. Rev.*, D76:064034, 2007. doi: 10.1103/PhysRevD.76.064034.

[129] Manuela Campanelli, Carlos O. Lousto, Yosef Zlochower, Badri Krishnan, and David Merritt. Spin Flips and Precession in Black-Hole-Binary Mergers. *Phys. Rev.*, D75:064030, 2007. doi: 10.1103/PhysRevD.75.064030.

[130] S. W. Hawking. Gravitational radiation from colliding black holes. *Phys. Rev. Lett.*, 26:1344–1346, 1971. doi: 10.1103/PhysRevLett.26.1344.

[131] D. Christodoulou. Reversible and irreversible transforations in black hole physics. *Phys. Rev. Lett.*, 25:1596–1597, 1970. doi: 10.1103/PhysRevLett.25.1596.

[132] Maya Fishbach, Daniel E. Holz, and Ben Farr. Are LIGO's Black Holes Made from Smaller Black Holes? *Astrophys. J.*, 840(2):L24, 2017. doi: 10.3847/2041-8213/aa7045.

[133] Emanuele Berti and Marta Volonteri. Cosmological black hole spin evolution by mergers and accretion. *Astrophys. J.*, 684:822–828, 2008. doi: 10.1086/590379.

[134] Tullio Regge and John A. Wheeler. Stability of a Schwarzschild singularity. *Phys. Rev.*, 108:1063–1069, 1957. doi: 10.1103/PhysRev.108.1063.

[135] C. T. Cunningham, R. H. Price, and V. Moncrief. Radiation from collapsing relativistic stars. I - Linearized odd-parity radiation. *Astrophys. J.*, 224:643, 1978. doi: 10.1086/156413.

[136] M. J. Benacquista. Gravitational radiation from black hole binaries in globular clusters. *Class. Quant. Grav.*, 19:1297–1302, 2002. doi: 10.1088/0264-9381/19/7/309.

[137] Duncan A. Brown and Peter J. Zimmerman. The Effect of Eccentricity on Searches for Gravitational-Waves from Coalescing Compact Binaries in Ground-based Detectors. *Phys. Rev.*, D81:024007, 2010. doi: 10.1103/PhysRevD.81.024007.

[138] E. A. Huerta, Prayush Kumar, Sean T. McWilliams, Richard O'Shaughnessy, and Nicols Yunes. Accurate and efficient waveforms for compact binaries on eccentric orbits. *Phys. Rev.*, D90(8):084016, 2014. doi: 10.1103/PhysRevD.90.084016.

[139] Ian Hinder, Frank Herrmann, Pablo Laguna, and Deirdre Shoemaker. Comparisons of eccentric binary black hole simulations with post-Newtonian models. *Phys. Rev.*, D82:024033, 2010. doi: 10.1103/PhysRevD.82.024033.

[140] Nicolas Yunes, K. G. Arun, Emanuele Berti, and Clifford M. Will. Post-Circular Expansion of Eccentric Binary Inspirals: Fourier-Domain Waveforms in the Stationary Phase Approximation. *Phys. Rev.*, D80(8):084001, 2009. doi: 10.1103/PhysRevD.89.109901,10.1103/PhysRevD.80.084001. [Erratum: Phys. Rev.D89,no.10,109901(2014)].

[141] Michael Purrer, Sascha Husa, and Mark Hannam. An Efficient iterative method to reduce eccentricity in numerical-relativity simulations of compact binary inspiral. *Phys. Rev.*, D85:124051, 2012. doi: 10.1103/PhysRevD.85.124051.

[142] Christian Reisswig and Denis Pollney. Notes on the integration of numerical relativity waveforms. *Class. Quant. Grav.*, 28:195015, 2011. doi: 10.1088/0264-9381/28/19/195015.

[143] Jeffrey Winicour. Characteristic Evolution and Matching. 2008. doi: 10.12942/lrr-2009-3.

[144] C. Reisswig, N. T. Bishop, D. Pollney, and B. Szilagyi. Unambiguous determination of gravitational waveforms from binary black hole mergers. *Phys. Rev. Lett.*, 103:221101, 2009. doi: 10.1103/PhysRevLett.103.221101.

[145] H. Akaike. A new look at the statistical model identification. *IEEE Transactions on Automatic Control*, 19(6):716–723, 1974. doi: 10.1109/TAC.1974.1100705.

[146] G. E. Schwarz. Estimating the dimension of a model. *Annals of Statistics*, 6(2): 461–464, 1978. doi: 10.1214/aos/1176344136.

[147] Michal Dominik, Emanuele Berti, Richard O'Shaughnessy, Ilya Mandel, Krzysztof Belczynski, Christopher Fryer, Daniel E. Holz, Tomasz Bulik, and Francesco Pannarale. Double Compact Objects III: Gravitational Wave Detection Rates. *Astrophys. J.*, 806(2):263, 2015. doi: 10.1088/0004-637X/806/2/263.

[148] P. Ajith. Addressing the spin question in gravitational-wave searches: Waveform templates for inspiralling compact binaries with nonprecessing spins. *Phys. Rev.*, D84:084037, 2011. doi: 10.1103/PhysRevD.84.084037.

[149] Curt Cutler and Eanna E. Flanagan. Gravitational waves from merging compact binaries: How accurately can one extract the binary's parameters from the inspiral wave form? *Phys. Rev.*, D49:2658–2697, 1994. doi: 10.1103/PhysRevD.49.2658.

[150] Eric Poisson and Clifford M. Will. Gravitational waves from inspiraling compact binaries: Parameter estimation using second postNewtonian wave forms. *Phys. Rev.*, D52:848–855, 1995. doi: 10.1103/PhysRevD.52.848.

[151] Fabian Hofmann, Enrico Barausse, and Luciano Rezzolla. The final spin from binary black holes in quasi-circular orbits. *Astrophys. J.*, 825(2):L19, 2016. doi: 10.3847/2041-8205/825/2/L19.

[152] James M. Bardeen, William H. Press, and Saul A Teukolsky. Rotating black holes: Locally nonrotating frames, energy extraction, and scalar synchrotron radiation. *Astrophys. J.*, 178:347, 1972. doi: 10.1086/151796.

[153] S. A. Teukolsky and W. H. Press. Perturbations of a rotating black hole. III - Interaction of the hole with gravitational and electromagnet ic radiation. *Astrophys. J.*, 193:443–461, 1974. doi: 10.1086/153180.

[154] Ryuichi Fujita. Gravitational Waves from a Particle in Circular Orbits around a Rotating Black Hole to the 11th Post-Newtonian Order. *PTEP*, 2015(3):033E01, 2015. doi: 10.1093/ptep/ptv012.

[155] M. Davis, R. Ruffini, W. H. Press, and R. H. Price. Gravitational radiation from a particle falling radially into a schwarzschild black hole. *Phys. Rev. Lett.*, 27: 1466–1469, 1971. doi: 10.1103/PhysRevLett.27.1466.

[156] Scott A. Hughes and Roger D. Blandford. Black hole mass and spin coevolution by mergers. *Astrophys. J.*, 585:L101–L104, 2003. doi: 10.1086/375495.

[157] Alessandra Buonanno, Lawrence E. Kidder, and Luis Lehner. Estimating the final spin of a binary black hole coalescence. *Phys. Rev.*, D77:026004, 2008. doi: 10.1103/PhysRevD.77.026004.

[158] Sebastiano Bernuzzi, Alessandro Nagar, and Anil Zenginoğlu. Binary black hole coalescence in the large-mass-ratio limit: the hyperboloidal layer method and waveforms at null infinity. *Phys. Rev.*, D84:084026, 2011. doi: 10.1103/PhysRevD.84.084026.

[159] Enrico Barausse, Viktoriya Morozova, and Luciano Rezzolla. On the mass radiated by coalescing black-hole binaries. *Astrophys. J.*, 758:63, 2012. doi: 10.1088/0004-637X/786/1/76,10.1088/0004-637X/758/1/63. [Erratum: Astrophys. J.786,76(2014)].

[160] Andrew R Liddle. Information criteria for astrophysical model selection. *Mon. Not. Roy. Astron. Soc.*, 377:L74–L78, 2007. doi: 10.1111/j.1745-3933.2007.00306.x.

[161] Julian James Faraway. *Linear models with R*, volume 63 of *Texts in Statistical Science*, chapter 3.5, pages 41–44. CRC Press, Boca Raton, 2005.

[162] William H. Press. Long Wave Trains of Gravitational Waves from a Vibrating Black Hole. *Astrophys. J.*, 170:L105–L108, 1971. doi: 10.1086/180849.

[163] S. Chandrasekhar and Steven L. Detweiler. The quasi-normal modes of the Schwarzschild black hole. *Proc. Roy. Soc. Lond.*, A344:441–452, 1975. doi: 10.1098/rspa.1975.0112.

[164] Steven L. Detweiler. BLACK HOLES AND GRAVITATIONAL WAVES. III. THE RESONANT FREQUENCIES OF ROTATING HOLES. *Astrophys. J.*, 239: 292–295, 1980. doi: 10.1086/158109.

[165] Kostas D. Kokkotas and Bernd G. Schmidt. Quasinormal modes of stars and black holes. *Living Rev. Rel.*, 2:2, 1999. doi: 10.12942/lrr-1999-2.

[166] Alejandro Bohé, Mark Hannam, Sascha Husa, Frank Ohme, Michael Pürrer, and Patricia Schmidt. Phenompv2 – technical notes for the lal implementation. Technical Report LIGO-T1500602, LIGO Scientific Collaboration and Virgo Collaboration, 2016. URL https://dcc.ligo.org/T1500602.

[167] Alejandro Bohé, Michael Pürrer, Mark Hannam, Sascha Husa, Frank Ohme, Patricia Schmidt, et al. Imrphenompv2 publication. in preparation.

[168] Cedric G. Lacey and Shaun Cole. Merger rates in hierarchical models of galaxy formation. *Mon. Not. Roy. Astron. Soc.*, 262:627–649, 1993.

[169] B. F. Roukema, B. A. Peterson, P. J. Quinn, and B. Rocca-Volmerange. Merging history trees of dark matter halos: A Tool for exploring galaxy formation models. *Mon. Not. Roy. Astron. Soc.*, 292:835, 1997. doi: 10.1093/mnras/292.4.835.

[170] Marta Volonteri, Francesco Haardt, and Piero Madau. The Assembly and merging history of supermassive black holes in hierarchical models of galaxy formation. *Astrophys. J.*, 582:559–573, 2003. doi: 10.1086/344675.

[171] Tamara Bogdanovic, Christopher S. Reynolds, and M. Coleman Miller. Alignment of the spins of supermassive black holes prior to merger. *Astrophys. J. Lett.*, 661: L147, 2007. doi: 10.1086/518769.

[172] Wolfgang Tichy and Pedro Marronetti. The Final mass and spin of black hole mergers. *Phys. Rev.*, D78:081501, 2008. doi: 10.1103/PhysRevD.78.081501.

[173] Enrico Barausse. The evolution of massive black holes and their spins in their galactic hosts. *Mon. Not. Roy. Astron. Soc.*, 423:2533–2557, 2012. doi: 10.1111/j.1365-2966.2012.21057.x.

[174] A. Sesana, E. Barausse, M. Dotti, and E. M. Rossi. Linking the spin evolution of massive black holes to galaxy kinematics. *Astrophys. J.*, 794:104, 2014. doi: 10.1088/0004-637X/794/2/104.

[175] A. Klein, E. Barausse, A. Sesana, A. Petiteau, E. Berti, S. Babak, J. Gair, S. Aoudia, I. Hinder, F. Ohme, and B. Wardell. Science with the space-based interferometer eLISA: Supermassive black hole binaries. *Phys. Rev.*, D93(2):024003, 2016. doi: 10.1103/PhysRevD.93.024003.

[176] Jeffrey E. McClintock, Ramesh Narayan, Shane W. Davis, Lijun Gou, Akshay Kulkarni, Jerome A. Orosz, Robert F. Penna, Ronald A. Remillard, and James F. Steiner. Measuring the Spins of Accreting Black Holes. *Class. Quant. Grav.*, 28: 114009, 2011. doi: 10.1088/0264-9381/28/11/114009.

[177] Alex B. Nielsen. On the distribution of stellar-sized black hole spins. *J. Phys. Conf. Ser.*, 716(1):012002, 2016. doi: 10.1088/1742-6596/716/1/012002.

[178] Laura Brenneman. *Measuring the Angular Momentum of Supermassive Black Holes*. SpringerBriefs in Astronomy. Springer, 2013. doi: 10.1007/978-1-4614-7771-6.

[179] Christopher S. Reynolds. The Spin of Supermassive Black Holes. *Class. Quant. Grav.*, 30:244004, 2013. doi: 10.1088/0264-9381/30/24/244004.

[180] B. M. Peterson. Measuring the Masses of Supermassive Black Holes. *Space Science Reviews*, 183:253–275, sep 2014. doi: 10.1007/s11214-013-9987-4.

[181] Sascha Husa, Jose A. Gonzalez, Mark Hannam, Bernd Bruegmann, and Ulrich Sperhake. Reducing phase error in long numerical binary black hole evolutions with sixth order finite differencing. *Class. Quant. Grav.*, 25:105006, 2008. doi: 10.1088/0264-9381/25/10/105006.

[182] Yosef Zlochower and Carlos O. Lousto. Modeling the remnant mass, spin, and recoil from unequal-mass, precessing black-hole binaries: The Intermediate Mass Ratio Regime. *Phys. Rev.*, D92(2):024022, 2015. doi: 10.1103/PhysRevD.92.024022.

[183] Yosef Zlochower and Carlos O. Lousto. Erratum: Modeling the remnant mass, spin, and recoil from unequal-mass, precessing black-hole binaries: The intermediate mass ratio regime [Phys. Rev. D 92, 024022 (2015)]. *Phys. Rev.*, D94(2):029901 [Erratum], jul 2016. doi: 10.1103/PhysRevD.94.029901.

[184] Luciano Rezzolla, Enrico Barausse, Ernst Nils Dorband, Denis Pollney, Christian Reisswig, Jennifer Seiler, and Sascha Husa. On the final spin from the coalescence of two black holes. *Phys. Rev.*, D78:044002, 2008. doi: 10.1103/PhysRevD.78.044002.

[185] Nathan K. Johnson-McDaniel et al. Determining the final spin of a binary black hole system including in-plane spins: Method and checks of accuracy. Technical Report LIGO-T1600168, LIGO Scientific Collaboration and Virgo Collaboration, 2016. URL https://dcc.ligo.org/LIGO-T1600168/public.

[186] B. P. Abbott et al. An improved analysis of GW150914 using a fully spin-precessing waveform model. 2016.

[187] Deirdre Shoemaker et al. private communication, 10 2016.

[188] Xisco Jiménez Forteza, David Keitel, Sascha Husa, Mark Hannam, Sebastian Khan, Lionel London, and Michael Pürrer. Phenomenological fit of the peak luminosity from non-precessing binary-black-hole coalescences. Technical Report LIGO-T1600018-v4, LIGO Scientific Collaboration and Virgo Collaboration, 2016. URL https://dcc.ligo.org/LIGO-T1600018-v4/public.

[189] B. P. Abbott et al. Tests of general relativity with GW150914. *Phys. Rev. Lett.*, 116(22):221101, 2016. doi: 10.1103/PhysRevLett.116.221101.

[190] D. D. Frederiks et al. The ultraluminous GRB 110918A. *Astrophys. J.*, 779:151, 2013. doi: 10.1088/0004-637X/779/2/151.

[191] Jeremy D. Schnittman. Astrophysics of Super-massive Black Hole Mergers. *Class. Quant. Grav.*, 30:244007, 2013. doi: 10.1088/0264-9381/30/24/244007.

[192] Bence Kocsis and Abraham Loeb. Brightening of an Accretion Disk Due to Viscous Dissipation of Gravitational Waves During the Coalescence of Supermassive Black Holes. *Phys. Rev. Lett.*, 101:041101, 2008. doi: 10.1103/PhysRevLett.101.041101.

[193] Gongjie Li, Bence Kocsis, and Abraham Loeb. Gravitational Wave Heating of Stars and Accretion Disks. *Mon. Not. Roy. Astron. Soc.*, 425:2407–2412, 2012. doi: 10.1111/j.1365-2966.2012.21206.x.

[194] V. Connaughton et al. Fermi GBM Observations of LIGO Gravitational Wave event GW150914. *Astrophys. J.*, 826(1):L6, 2016. doi: 10.3847/2041-8205/826/1/L6.

[195] Pau Amaro Seoane et al. eLISA/NGO: Astrophysics and cosmology in the gravitational-wave millihertz regime. *GW Notes*, 6:4–110, 2013.

[196] Pau Amaro Seoane et al. The Gravitational Universe. 2013.

[197] Mohan Rajagopal and Roger W. Romani. Ultralow frequency gravitational radiation from massive black hole binaries. *Astrophys. J.*, 446:543–549, 1995. doi: 10.1086/175813.

[198] A. Sesana, A. Vecchio, and M. Volonteri. Gravitational waves from resolvable massive black hole binary systems and observations with Pulsar Timing Arrays. *Mon. Not. Roy. Astron. Soc.*, 394:2255, 2009. doi: 10.1111/j.1365-2966.2009.14499.x.

[199] Alberto Sesana and Alberto Vecchio. Measuring the parameters of massive black hole binary systems with Pulsar Timing Array observations of gravitational waves. *Phys. Rev.*, D81:104008, 2010. doi: 10.1103/PhysRevD.81.104008.

[200] F. Herrmann, Ian Hinder, D. Shoemaker, and P. Laguna. Unequal Mass Binary Black Hole Plunges and Gravitational Recoil. *Class. Quant. Grav.*, 24:S33–S42, 2007. doi: 10.1088/0264-9381/24/12/S04.

[201] Birjoo Vaishnav, Ian Hinder, Frank Herrmann, and Deirdre Shoemaker. Matched filtering of numerical relativity templates of spinning binary black holes. *Phys. Rev.*, D76:084020, 2007. doi: 10.1103/PhysRevD.76.084020.

[202] James Healy, Janna Levin, and Deirdre Shoemaker. Zoom-Whirl Orbits in Black Hole Binaries. *Phys. Rev. Lett.*, 103:131101, 2009. doi: 10.1103/PhysRevLett.103.131101.

[203] L. Pekowsky, R. O'Shaughnessy, J. Healy, and D. Shoemaker. Comparing gravitational waves from nonprecessing and precessing black hole binaries in the corotating frame. *Phys. Rev.*, D88(2):024040, 2013. doi: 10.1103/PhysRevD.88.024040.

[204] Y. Zlochower, J. G. Baker, Manuela Campanelli, and C. O. Lousto. Accurate black hole evolutions by fourth-order numerical relativity. *Phys. Rev.*, D72:024021, 2005. doi: 10.1103/PhysRevD.72.024021.

[205] John G. Baker, William D. Boggs, Joan Centrella, Bernard J. Kelly, Sean T. McWilliams, and James R. van Meter. Mergers of non-spinning black-hole binaries: Gravitational radiation characteristics. *Phys. Rev.*, D78:044046, 2008. doi: 10.1103/PhysRevD.78.044046.

[206] Bernard J. Kelly, John G. Baker, William D. Boggs, Sean T. McWilliams, and Joan Centrella. Mergers of black-hole binaries with aligned spins: Waveform characteristics. *Phys. Rev.*, D84:084009, 2011. doi: 10.1103/PhysRevD.84.084009.

[207] Larne Pekowsky, James Healy, Deirdre Shoemaker, and Pablo Laguna. Impact of higher-order modes on the detection of binary black hole coalescences. *Phys. Rev.*, D87(8):084008, 2013. doi: 10.1103/PhysRevD.87.084008.

[208] Juan Calderón Bustillo, Sascha Husa, Alicia M. Sintes, and Michael Pürrer. Impact of gravitational radiation higher order modes on single aligned-spin gravitational wave searches for binary black holes. *Phys. Rev.*, D93(8):084019, 2016. doi: 10.1103/PhysRevD.93.084019.

[209] Michael Boyle. Angular velocity of gravitational radiation from precessing binaries and the corotating frame. *Phys. Rev.*, D87(10):104006, 2013. doi: 10.1103/PhysRevD.87.104006.

[210] Michael Boyle, Lawrence E. Kidder, Serguei Ossokine, and Harald P. Pfeiffer. Gravitational-wave modes from precessing black-hole binaries. 2014.

[211] Michael Boyle. Transformations of asymptotic gravitational-wave data. *Phys. Rev.*, D93(8):084031, 2016. doi: 10.1103/PhysRevD.93.084031.

[212] Frank J. Zerilli. Effective potential for even parity Regge-Wheeler gravitational perturbation equations. *Phys. Rev. Lett.*, 24:737–738, 1970. doi: 10.1103/PhysRevLett.24.737.

[213] Olivier Sarbach and Manuel Tiglio. Gauge invariant perturbations of Schwarzschild black holes in horizon penetrating coordinates. *Phys. Rev.*, D64:084016, 2001. doi: 10.1103/PhysRevD.64.084016.

[214] Oliver Rinne, Luisa T. Buchman, Mark A. Scheel, and Harald P. Pfeiffer. Implementation of higher-order absorbing boundary conditions for the Einstein equations. *Class. Quant. Grav.*, 26:075009, 2009. doi: 10.1088/0264-9381/26/7/075009.

[215] Sebastiano Bernuzzi, Alessandro Nagar, and Anil Zenginoğlu. Binary black hole coalescence in the extreme-mass-ratio limit: testing and improving the effective-one-body multipolar waveform. *Phys. Rev.*, D83:064010, 2011. doi: 10.1103/PhysRevD.83.064010.

[216] Frank Ohme. *Bridging the Gap between Post-Newtonian Theory and Numerical Relativity in Gravitational-Wave Data Analysis*. PhD thesis, Potsdam, Max Planck Inst., 2012. URL https://inspirehep.net/record/1366224/files/ohme_diss.pdf.